University of Strathclyde
Department of Mechanical & Aerospace Engineering

A methodology for the experimental characterisation and computational modelling of Nitinol wires used in stent-graft devices

Alexandros Boukis

A thesis presented in fulfilment of the requirements
for the degree of Doctor of Philosophy

2020

To my parents

Declaration of Authenticity and Author's Rights

This thesis is the result of the author's original research. It has been composed by the author and has not been previously submitted for examination which has led to the award of a degree.

Alexandros Boukis

February 2020

Acknowledgments

I would like to thank my supervisor, Dr Marcus Wheel, for his support and patience during all these years.

A very big thank you to Terumo Aortic, and especially to Dr Robbie Brodie and Dr David Bow for their input in this project and great help.

I would also like to thank my partner Maria, for all the emotional support these past years, and my dear friend Mohamed for his great help throughout this academic journey.

Finally, a massive thank you to my parents for always believing in me, and to my sister who is always there for me no matter what.

Abstract

Stent-grafts are medical devices designed to treat abdominal aortic aneurysms (AAAs). These devices are usually composed of a Nitinol wireframe and a fabric graft. The design of next generation stent-grafts is directed towards a very low-profile when compacted. Such devices can treat narrow access vessels and tortuous anatomies while inducing less trauma to patients. Therefore, Nitinol stents are required to undergo greater deformations during manufacture without compromising the performance and durability of the medical device.

Experimental characterisation of the material is required to demonstrate its mechanical behavioural characteristics. Since Nitinol wires are subjected to multi-mode loading conditions, investigation should incorporate all loading modes and thermomechanical conditions that a device encounters during its life cycle. The resulting data can then enable the derivation of the material's constitutive properties which are necessary for computational analyses. Finite element analysis (FEA) has become an integral part of the design of medical devices and computational analyses reports are used nowadays as scientific evidence to support medical device submissions. The Nitinol constitutive model that is implemented in the finite element software Abaqus is considered the industry standard. However, its capabilities and limitations are not fully explored since there are no experimental data available for this purpose.

In the present work, a methodology was developed to characterise medical grade Nitinol wires in tension, compression, bending and torsion. The mechanical behaviour of the material was examined under high-strain tensile deformation. The relevant constitutive parameters were identified from the experimental results and the Abaqus Nitinol model was assessed, including its superelastic-plastic modelling capabilities, by simulating the mechanical tests of all loading modes. The key findings from the present work are summarised below.

High straining of the material during compaction results in decreased austenite stiffness, decreased load and unload plateaus and increased residual strain.

These features are more pronounced when multiple compaction attempts take place. A recommendation is made, to limit the compaction strain to 10%, if possible. This is because if more than one compaction attempts take place at 10% strain, the effect on the unload plateau, which influences the radial strength of the stent, will be small. In addition, up to 10% compaction strain there is only a small, gradual increase of residual strain. The bending response of the material is load-rate sensitive. Therefore, compaction should take place slowly in order to avoid potential rate effects. Sterilization is not expected to have a negative impact on the stress levels experienced by Nitinol wires during this process, since temperature sensitivity was not observed within the post-transformation region.

The Abaqus Nitinol model provided results that were in agreement with the experiments when modelling tension within the superelastic range, as only minor qualitative differences were identified between computational and experimental responses. However, the material model was incapable of forecasting the sensitivity of the unload plateau to the high strain loading. The present work shows that this limitation can be overcome by implementing Fortran subroutines that modify the transformation stresses during unloading as a function of the plastic strain reached during the simulation. Tension-compression asymmetry was also exhibited in the FEA results. The austenite stiffness and the start of the transformation during loading in compression agreed quantitatively with the experimental results, exhibiting negligible errors. However, the unloading transformation stresses in compression were underpredicted by up to 36.6% compared to the experimental data.

The flexural stiffness of austenite was also underestimated in the computational bending responses by up to 28.8%, although the transformation during loading started at the same force levels for FEA and experimental results. Results show that the loading path of the bending response can be improved if the flexural modulus of austenite is used as input parameter. However, the unloading path of the bending response was not captured correctly since it took place at lower forces compared to the experimental curves. The computational response in torsion was also not in agreement with the experimental results, as the torsional stiffness

was underestimated by 11.2% while the loading and unloading paths took place in lower load levels. The model however, was able to capture the qualitative features of the combined tension-torsion deformation.

Nomenclature

AAA	Abdominal Aortic Aneurysm
A_f	Austenitic finish temperature
CoC	Certificate of compliance
CSV	Comma Separated Variable file
DIC	Digital Image Correlation
DSC	Differential Scanning Calorimetry
EDM	Electro-Discharge Machining
EVAR	Endovascular Aneurysm Repair
FEA	Finite Element Analysis
FWM	Fort Wayne Metals
NiTi#1-SE	Nitinol#1 superelastic straight annealed wire manufactured by Fort Wayne Metals
SEM	Scanning Electron Microscope
USN®	ultra-stiff Nitinol wire manufactured by Fort Wayne Metals

Contents

Chapter 1 Introduction

1.1 Context

An aneurysm is defined as a permanent localised dilation of an artery to greater than one and a half times its normal diameter [1]. The abdominal aortic aneurysm (AAA), illustrated in Figure 1-1, is the localised widening of the abdominal aorta which is the largest artery of the human body. It is a cardiovascular disease that weakens the arterial wall jeopardizing its structural integrity and is associated with several risk factors including hypertension, atherosclerosis, smoking and advanced age [2, 3]. AAAs are usually discovered incidentally and may remain asymptomatic until they rupture. The mortality rate for patients with a ruptured AAA is approximately 90% [4].

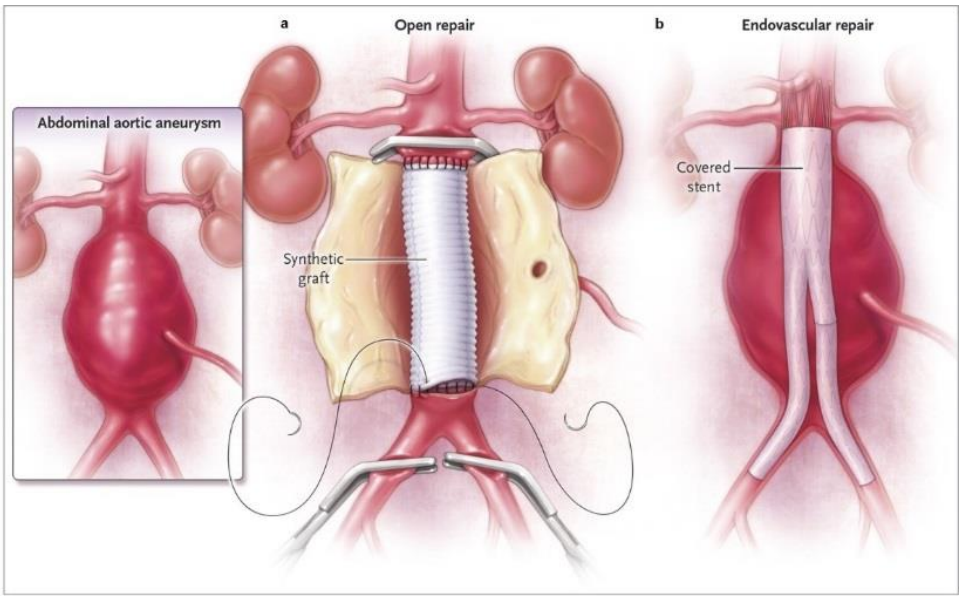

Figure 1-1 AAA and its treatment approaches: Open repair (a) and endovascular repair (b). Image reproduced with permission from Kent [5].

Open repair had been the sole approach for the treatment of AAAs for a long time. It is a surgical procedure during which the patient's abdomen is exposed and a

tubular synthetic membrane, known as graft, is sutured in the diseased aorta in order to by-pass the dilated segment as shown in Figure 1-1(a). Open repair is performed under general anaesthesia and it results in a month-long patient recovery [5, 6].

In the early 90's Parodi [7] and Volodos [8] introduced a minimally invasive treatment approach which is known today as the endovascular aneurysm repair (EVAR). This procedure utilises a tubular device known as stent-graft. It is formed by a rigid metal structure, the stent, which supports a flexible graft. After the stent-graft is manufactured, the whole device is compacted into a very small diameter sheath, which is part of the delivery system, and is sterilised. An illustration of a delivery system is shown in Figure 1-2. During the operation, the delivery system is advanced though the femoral artery into the aorta under radiological guidance, delivering the stent-graft in a collapsed state. The device is then deployed in the diseased aorta, excluding the aneurysm sac from the arterial circulation as illustrated in Figure 1-1(b).

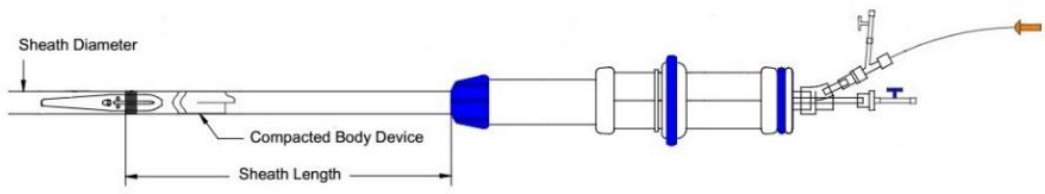

Figure 1-2 Illustration of the Vascutek Anaconda delivery system. Image adapted from [9].

EVAR can be carried out under local or general anaesthesia and it is followed by a week-long patient recovery [5, 6]. Today it is the most common approach for the treatment of AAAs. The smaller operative trauma and the decreased rehabilitation time compared to open repair, has allowed the treatment of patients with high surgical and anaesthetic risks [10]. Short-term mortality is also considered lower in patients undergoing EVAR although both treatment approaches result in similar long-term survival results [11-13].

The stent material of such devices is usually made of Nitinol, an alloy containing approximately 50% nickel and 50% titanium. It was named after the

elements it is composed of, and the place it was discovered. Hence, the word Nitinol is essentially an acronym for nickel, titanium and Naval Ordnance Laboratory [14]. Although it became a popular choice of material for a plethora of applications in the last twenty years, it has been over five decades since the alloy was first discovered by William Buehler [15].

Compared to a conventional metal, Nitinol's stress-strain response is notably different as seen in Figure 1-3. When stainless steel is deformed, the exhibited stress increases linearly with strain. The recoverable elastic strain is small and if exceeded, plastic deformation is induced. On the contrary, Nitinol exhibits a non-linear stress-strain response with a hysteretic profile. Its behaviour is characterised by two stress plateaus, one during loading and another during unloading. The material can accommodate large strains with minimal stress changes, hence undergoing large deformations without permanent strain. Thus, Nitinol is commonly referred to as a superelastic material. Similar responses, characterised by high elasticity and constant loads over a wide range of strains, are also exhibited by human tissue and bone [16].

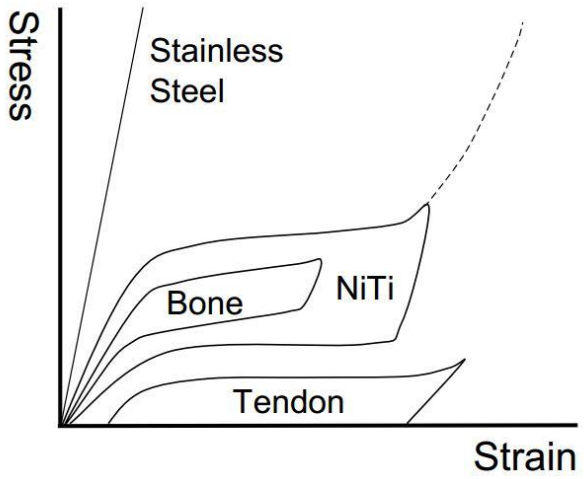

Figure 1-3 Stress-strain response of stainless steel, Nitinol (shown here as NiTi) and biological materials. Image reproduced with permission from Morgan [16].

Since the first Nitinol medical application, the orthodontic bridge wire, the material has been used in numerous biomedical devices [17]. Nitinol orthodontic wires apply a constant force over a prolonged period of treatment time, therefore

reducing the number of necessary re-adjustments and the patient's discomfort compared to stainless steel wires [18]. The compliance of Nitinol and its compatibility with biological materials, promotes bone healing in orthopaedic applications, by allowing the implant to share the loads with surrounding tissues [19].

Nitinol is the preferred material for the manufacture of stent-grafts due to its biocompatibility and its suitable compliance which allows the material to withstand compaction strains without permanent deformation, kinking and fractures [20-22]. Usually Nitinol stent-grafts are composed of a wire frame sewn onto a woven fabric graft. The most common wire frame configurations are the ring-stent and the z-stent. Commercial devices with a ring-stent include the Terumo Aortic Anaconda illustrated in Figure 1-4(a), and the Lombard Aorfix. Examples of the z-stent configuration currently in the market include the Medtronic Endurant shown in Figure 1-4(b), the Gore Excluder and the Terumo Aortic Treo.

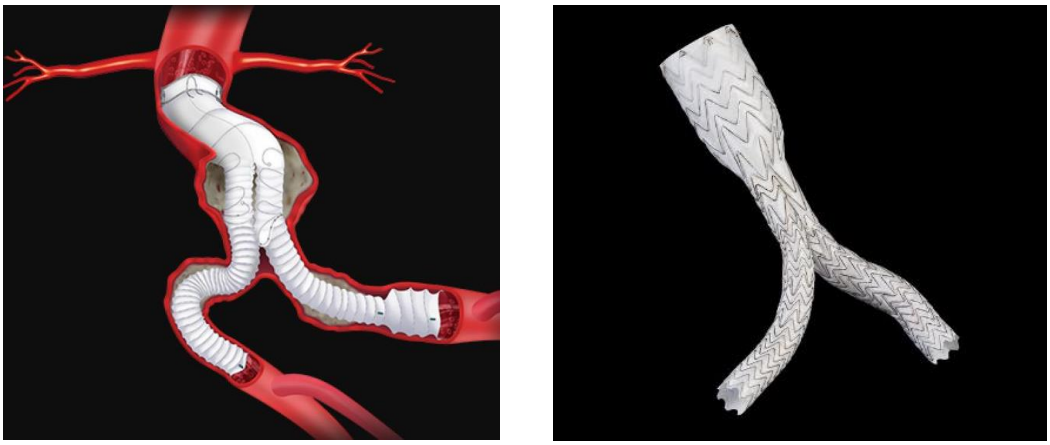

(a) (b)

Figure 1-4 Examples of commercial stent-graft devices: (a) The Vascutek Anaconda deployed in a tortuous abdominal aorta and iliac arteries. Illustration reproduced from [23]. (b) The Gore Excluder Endoprosthesis. Image reproduced from [24].

Since the early commercial applications, the stent-graft design has evolved in the last two decades leading to improved clinical results [25]. Post-operative complications commonly seen with first generation devices included the migration of the stent-graft in the blood vessel and the persistent blood flow in the aneurysm sac, also known as endoleak [26]. Migration has been overcome by adding fixation

mechanisms in the proximal, upper-end of the device. Such mechanisms included hooks and barbs that anchored in the vessel wall securing the device's position. Examples of anchoring mechanisms are seen in Figure 1-5 for three commercial stent-grafts. Stent-related endoleaks are usually prevented by oversizing the ends of the stent frame, which then act as a passive fixation and sealing mechanism.

(a) (b) (c)

Figure 1-5 Anchoring mechanisms of three commercial stent-grafts: Gore Excluder (a), Vascutek Anaconda (b) and Medtronic Endurant (c). Image reproduced with permission from Bosman et al. [27].

1.2 Objectives

Today, the design of stent-grafts is directed towards low-profile devices compacted into smaller diameter sheaths and delivery systems. These could allow the treatment of narrow and tortuous anatomies while reducing the patient's discomfort by inducing a smaller operative trauma. Therefore, next generation Nitinol stents are required to withstand greater deformations during manufacturing. Despite these design requirements, the high-strain behaviour of the material is not fully explored yet.

Moreover, finite element analysis (FEA) has become an integral part of the design of medical devices. Constitutive models implemented in FEA software are usually calibrated using uniaxial tensile data. Hence, the majority of Nitinol studies have been conducted in uniaxial tension. However, tensile data are often insufficient

to accurately predict the complex material behaviour. Data from other comparable studies exploring the behaviour of Nitinol wires in various loading modes are scarce.

Experimental characterisation is required to demonstrate the material's behavioural characteristics. Since Nitinol wires, which are the main structural component of stent-grafts, are subjected to multi-mode loading conditions, investigation should incorporate all loading modes and thermomechanical conditions that a device will encounter during its life cycle. The resulting data can then enable the quantitative derivation of the material's constitutive properties necessary for the development of new constitutive models or the evaluation of existing ones.

The present work seeks to:

1. Produce a complete set of experimental data by testing medical grade Nitinol wires in tension, compression, bending and torsion.

2. Examine the mechanical behaviour of the material under high-strain deformation, in order to investigate the effect of compaction on its properties.

3. Assess the capabilities and limitations of the constitutive model currently implemented in the finite element software Abaqus which is considered the industry standard for modelling Nitinol materials.

1.3 Thesis Outline

Chapter 2 provides a brief summary of the major Nitinol characteristics, in order to introduce the reader into the essential background for understanding the phenomena and terminology discussed later. Chapter 3 presents background information regarding the fabrication of Nitinol components and the stent life-cycle,

and also the literature review which is essentially divided into two parts. The first explores experimental characterisation studies and seeks to identify: unique material characteristics relevant to the present work, considerations associated with the mechanical testing of superelastic Nitinol specimens, and gaps in the literature.

The second part of the literature review provides a short overview of the constitutive modelling approaches developed to describe the behaviour of Nitinol materials. It then introduces the constitutive model currently implemented in the finite element software Abaqus. At the end of Chapter 3, the main literature findings are highlighted to reinforce the motives behind the initial objectives. These, are subsequently expanded into more detailed action plans.

Chapter 4 presents the methods adopted to approach the aforementioned objectives and is divided into two parts; the first details the experimental protocols designed to characterise the material and the second describes the methodology developed to perform the computational analyses. Both sections examine loading conditions in tension, compression, bending and torsion. Chapter 5 and Chapter 6 follow the same structure to present experimental and computational results respectively, both conducted according to the test methods.

In Chapter 7, the methodology of the present work is assessed by analysing its strengths and limitations. Results are discussed and compared with available findings in the literature and stent-design considerations are proposed. Suggestions for future work are also provided within this chapter. Chapter 8 presents an overview of the findings and their implications, and summarises the main recommendations for future investigations.

Chapter 2 Thermomechanical Characteristics of Nitinol

Following the discovery of Nitinol, research was driven by the need to understand the unusual thermomechanical behaviour of the material. Investigations were focused on the microstructural and metallurgical characteristics governing its macroscopic response. Physical, mechanical, and crystallographic properties were reported and research has been ongoing since then. A plethora of works has been published including technical reports, journal articles and books. Among others, the works of Jackson et al. [28], Duerig et al. [29], Humbeeck et al. [30], Otsuka and Wayman [31], Otsuka and Ren [32], and Lagoudas [33] have been established as textbooks in this field of research.

The following paragraphs present a brief summary of the major material characteristics based on the aforementioned books and journal articles. This is considered necessary, in order to introduce the reader into the essential background required to understand the phenomena and terminology discussed later in the present work.

2.1 Martensitic transformation

Nitinol materials usually have two phases: austenite and martensite. The transition between the two phases occurs through a non-diffusional solid state transformation known as martensitic transformation. Austenite is considered the initial, parent phase of the material and is stable at high temperatures. Martensite is stable at low temperatures and can adopt two different crystal structures, known as twinned and detwinned martensite. The typical states seen in Nitinol are illustrated in Figure 2-1. The martensitic state depends on the thermomechanical conditions. Usually twinned martensite is formed due to thermal loading whereas detwinned martensite is formed due to mechanical loading.

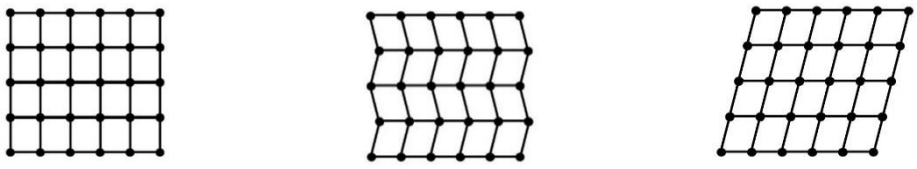

(a) (b) (c)

Figure 2-1 Illustration of the typical crystal structures observed in Nitinol: austenite (a), twinned martensite (b) and detwinned martensite (c).

Upon cooling in the absence of stress, austenite starts transforming to twinned martensite when temperature is reduced below the martensitic start temperature M_s. Transformation ends at the martensitic finish temperature M_f, with no macroscopic shape change observed in the Nitinol specimen. This transition is often termed forward transformation. If the material is heated, reverse transformation takes place. Twinned martensite starts transforming back to austenite when temperature is raised above the austenitic start temperature A_s. The transition ends at the austenitic finish temperature A_f with again negligible macroscopic shape change. The above process, which is the simplest form of the martensitic transformation, is illustrated in Figure 2-2.

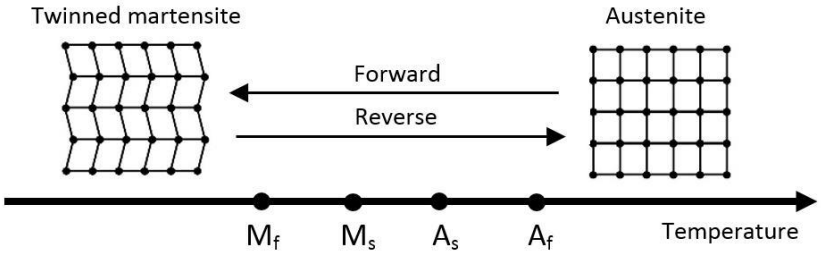

Figure 2-2 Temperature-induced transformations in Nitinol in the absence of external mechanical loads.

Note that the transformation temperatures are material properties that differ during the forward and reverse transformations. The difference between the transformation temperatures is known as the hysteresis temperature. The transformation of the material as a function of temperature is shown in Figure 2-3. The hysteresis temperature is defined as the difference between the temperature at

which the material is 50% transformed to austenite and the temperature at which the material is 50% transformed to martensite, upon heating and cooling respectively.

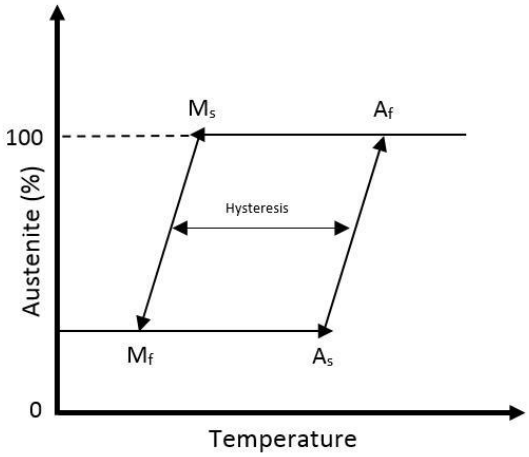

Figure 2-3 Austenite fraction against temperature in Nitinol materials.

2.2 Shape memory effect

The atomic boundaries of the twinned state have low energy, hence they are easily moved. If a twinned martensitic specimen is subjected to a mechanical load, its crystal structure will change adopting the detwinned form as seen in Figure 2-4. This process takes place when the induced load exceeds the stress level σ_{Ds} required to start detwinning. It is accompanied by a macroscopic shape change and is completed when the induced stress reaches the stress level σ_{Df}. The process of transforming the austenitic form to twinned martensite and subsequently deforming it into detwinned martensite is illustrated in Figure 2-5(a).

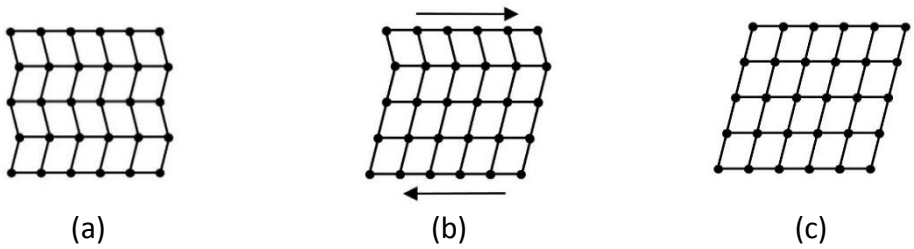

Figure 2-4 Detwinning in Nitinol materials. Twinned martensite (a) is transformed under the influence of an applied load (b) to detwinned martensite (c).

If the detwinned state is unloaded at temperatures below M_f, no change takes place in the crystal structure and macroscopic shape of the Nitinol specimen. Heating the material to temperatures above A_f, causes its transformation back to austenite as seen in Figure 2-5(b). Consequently, the shape of the deformed specimen is recovered. Subsequent cooling to temperatures below Mf does not result in any shape change and the whole process can be repeated by deforming the material again. This series of thermomechanical transitions is known as the shape memory effect. Therefore, Nitinol materials are also known as shape memory alloys.

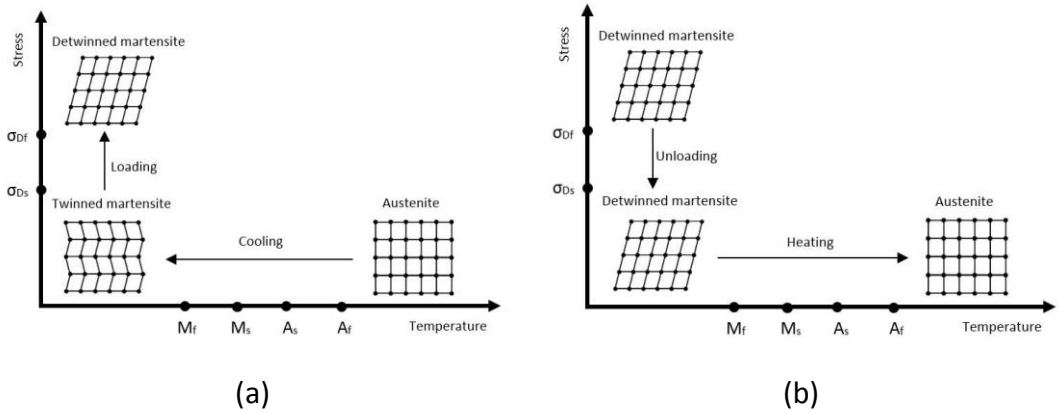

Figure 2-5 Thermomechanical paths presenting Nitinol's shape memory effect. The initial austenitic material is tranformed to detwinned martensite by cooling and subsequent loading (a) and then it is transfromed back to austenite by load removal and heating (b).

Figure 2-6 presents the above process in the stress-strain space, assuming the material is already in the twinned martensitic state. Upon loading, the initial linear part of the curve corresponds to the elastic deformation of the twinned martensite. When the σ_{Ds} stress level is reached, detwinning takes place characterised by an almost flat plateau. This region of the stress-strain curve ends at the σ_{Df} stress level. Further loading leads to the elastic deformation of the detwinned martensite until plastic deformation is induced. The material can be elastically unloaded and then heated to temperatures higher than A_f to recover its original shape, in the absence of permanent strain.

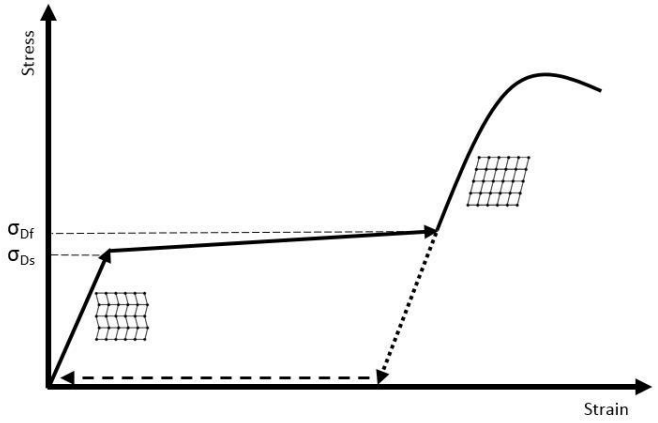

Figure 2-6 Typical stress-strain response for a martensitic Nitinol material with shape memory characteristics. Note that upon unloading residual strain is exhibited which can be recovered by transforming the material to austenite through heating.

2.3 Superelastic effect

Detwinned martensite can also be produced directly from the austenitic state through the application of a mechanical load. Figure 2-7 graphically explains the loading conditions for such a transition. The path A-B corresponds to the loading sequence of an austenitic Nitinol specimen and is characterised by two stress levels: the stress required to start the transformation during loading σ_L^S and the stress σ_L^E at which the transformation during loading ends. This type of transformation is accompanied by a macroscopic shape change of the tested specimen. Similarly, the unloading path C-D is defined by the stress required to start the transformation during unloading σ_U^S and the stress σ_U^E at which the transformation during unloading ends. All transformation stresses vary almost linearly with ambient temperature.

The load-unload sequence described above is known as the superelastic effect. The detwinned martensite produced during loading is often termed stress-induced martensite (SIM). If this process takes place at temperatures above A_f, reverse transformation results in the complete recovery of the initial austenitic structure and shape. Note that the highest temperature at which martensite can be

stress-induced is often denoted by M_d. Beyond that temperature level, Nitinol experiences ordinary elastic-plastic deformation.

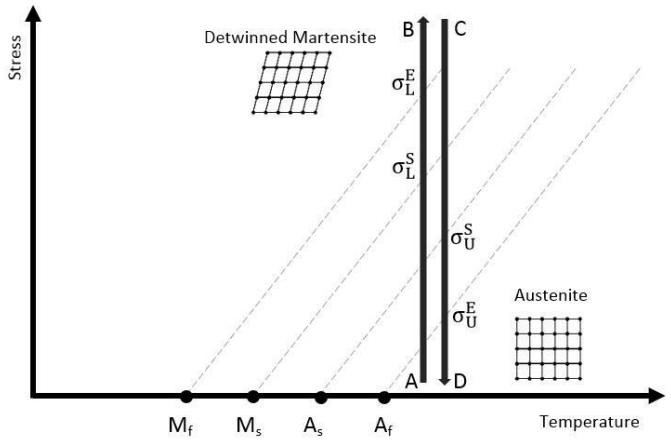

Figure 2-7 Loading and unloading paths representing the transition between austenite and detwinned martensite in superelastic Nitinol.

Figure 2-8 shows a typical stress-strain response of a superelastic Nitinol material. Upon loading, stress increases linearly with strain as the austenitic material is deformed elastically. The initial slope of the curve corresponds to the elastic modulus of austenite. Stress continues to increase linearly with strain until the σ_L^S stress level at which point the martensitic transformation is initiated. This is depicted by the upper, load plateau of the macroscopic response as stress increases only minimally with strain. The transformation during loading is considered complete at the σ_L^E stress level. Deformation beyond the superelastic plateau results in the post-transformation loading of the material. Detwinned martensite is then elastically loaded until plastic deformation is induced. The slope of the curve corresponds to the elastic modulus of the martensitic state of the material.

Upon unloading, stress decreases linearly with strain until the σ_U^S stress level. Subsequently, the material starts transforming back to austenite and the response is characterised by the lower, unload plateau. The transition is completed at the σ_U^E stress level followed by the elastic unloading of the austenitic state. In the absence of plastic deformation, unloading at temperatures above A_f produces a stress-strain curve with a closed loop, showing no residual strain. The hysteresis of the response represents the dissipated energy during the load-unload cycle.

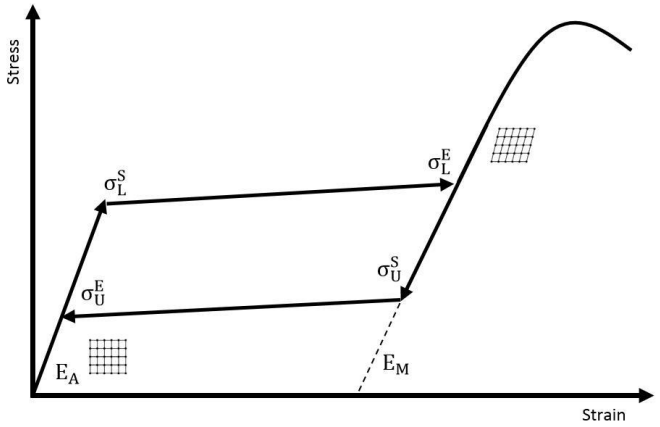

Figure 2-8 Typical stress-strain response of a superelastic Nitinol material characterised by nearly flat stress plateaus during loading and unloading.

2.4 R-phase transformation

Nitinol materials often adopt another microstructural state, known as R-phase. The R-phase is considered an intermediate state between austenite and martensite, as summarised in Figure 2-9. Its transition can be induced by a thermal or a mechanical load in a manner similar to the martensitic transformation. The temperature-induced transition takes place when cooling the austenitic state and is characterised by start and finish temperatures, R_S and R_F respectively, such as the ones described earlier for austenite and martensite.

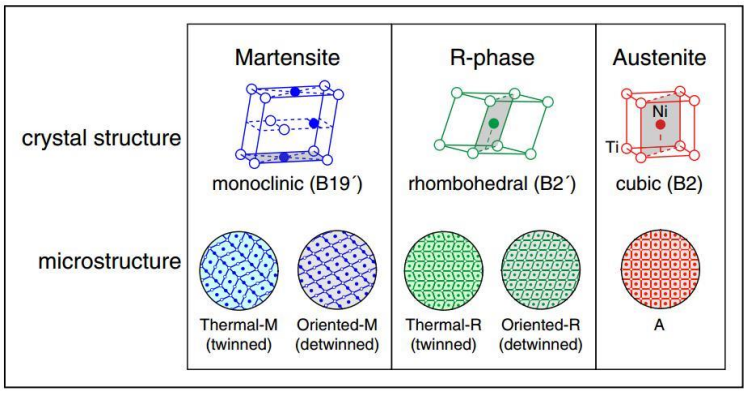

Figure 2-9 Illustration of the various phases and crystal structures seen in Nitinol materials. Image reproduced with permission from Shaw et al. [34].

The R-phase transformation temperatures of superelastic materials, often fall in-between the austenitic start and finish temperatures. Consequently, austenite and R-phase can co-exist at a wide range of temperatures. When such a Nitinol material is subjected to a mechanical load its behaviour is influenced by the R-phase, as austenite transforms first to R-phase and then to martensite. This two-step transition is manifested macroscopically by a reduction of the initial elastic stiffness upon loading, as seen in Figure 2-10.

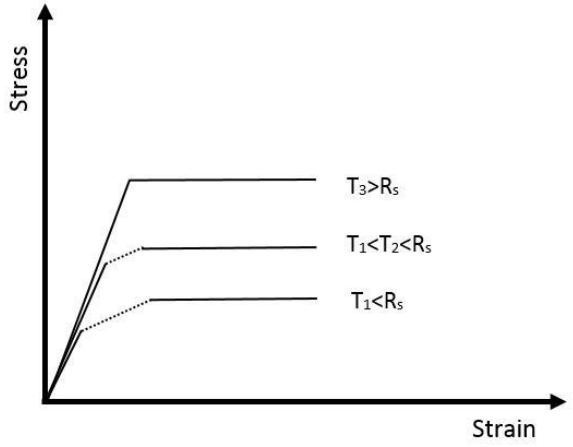

Figure 2-10 Illustration of Nitinol's stress-strain response upon loading, with and without R-phase present in the material.

At temperatures T_1 lower than R_S, the material is initially comprised of both austenite and R-phase. Upon loading, austenite is elastically deformed until the stress level that corresponds to the R-phase transition. The slope of the curve is then reduced and the material transforms to R-phase until the stress level required for the martensitic transformation is reached. At higher temperatures T_2, the R-phase content is decreased and the volume fraction of austenite is increased. Therefore, upon loading the region of the stress-strain curve that corresponds to the elastic loading of the austenitic state increases. When the presence of the R-phase is negligible at temperatures T_3, the material transforms directly from austenite to martensite as discussed earlier.

Chapter 3 Background and Literature Review

This chapter presents background information regarding the manufacturing of Nitinol components and the stent life-cycle. It also explores experimental characterisation studies and provides an overview of the modelling approaches developed to describe the behaviour of Nitinol materials.

3.1 Overview of stent life-cycle

3.1.1 Fabrication and processing of Nitinol

The two most common methods for producing Nitinol ingots are the vacuum-induction melting (VIM) and the vacuum-arc melting (VAR) [35]. After melting, the Nitinol ingot is forged and rolled into a bar which is then drawn down into a smaller diameter. The as-drawn material is then subjected to a series of cold drawing and annealing steps to fabricate the final wire component with the desired diameter.

Drawing at room temperature adds cold work to the material. Cold work is essentially the strengthening of a material though plastic deformation. Properties such as the ultimate tensile strength increase with cold work. However, this happens at the expense of ductility. The typical amount of cold work in Nitinol ranges between 30% and 50%, calculated in terms of reduction of the cross-sectional area [36]. Nitinol work-hardens quickly, so cold drawing is usually done in multiple steps with heat treatments (annealing) in-between, as illustrated in Figure 3-1. Annealing heat treatments restore some of the ductility of the Nitinol material. Wires are typically subjected to a final heat treatment to exhibit superelastic behaviour.

Shape setting is part of the heat treatments and refers to the process used to form a Nitinol wire into a specific geometry. This is done by constraining the wire into the desired new shape using special fixtures and then performing a heat treatment. Temperatures and treatment times are based on the desired mechanical

specifications. Aging is also another form of heat treatment that can be used to tune the properties of the final Nitinol component. Since some degree of aging will occur during shape setting, the two processes (aging and shape setting) are usually done simultaneously. Generally higher heat treatment temperatures result in higher transformation temperatures and lower ultimate tensile strength [37].

Wires can be sold in a straight annealed or cold worked (as-drawn) state. Final components are manufactured to specific requirements and specifications. Since the material properties are sensitive to thermomechanical processing, the conditions under which the various manufacturing steps take place are carefully chosen based on the final desired properties.

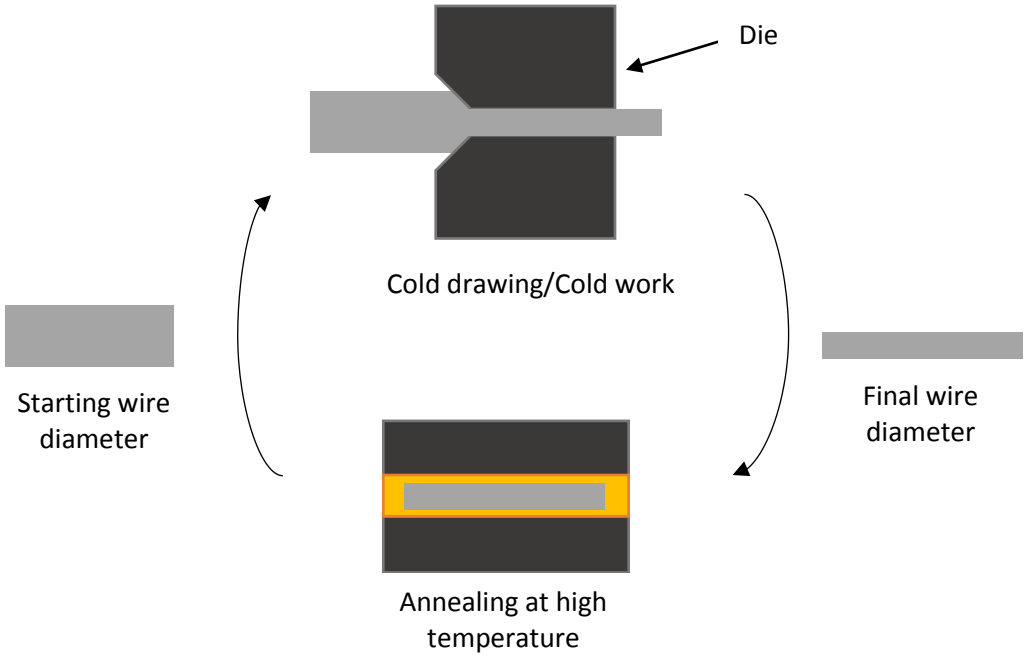

Figure 3-1 Illustration of the series of cold and hot work steps required to manufacture a final Nitinol wire component.

For the manufacture of Nitinol tubing, the ingot is forged and rolled into a bar followed by gun-drilling to create the initial tube. The tube is then subjected to a series of cold and hot work steps to produce the final component with the desired dimensions and properties. Tubes are usually supplied in a straight annealed condition. Similarly, the Nitinol ingot can be forged and rolled accordingly to manufacture sheets. The wrought sheet is then formed into the desired final

component by a series of cold and hot work steps. Sheets are usually supplied in a flat annealed condition.

In theory, Nitinol contains only Nickel and Titanium. However, impurities such as carbon and oxygen can be found in the raw materials. The impurities are dissolved during melting and can form particles, like carbides and oxides during the solidification of the melt. These particles have a different chemical composition and structure from the base metal and are called inclusions. Inclusions are known to act as sites for the initiation and propagation of fatigue cracks [38]. Therefore, the size and volume of inclusions in Nitinol components should be controlled. The ASTM standard F2063 [39] specifies the acceptable inclusion size in Nitinol alloys. Lately, research has focused on the manufacture of low inclusion Nitinol in order to improve the fatigue life of Nitinol components [40-46]. Low inclusion Nitinol, also known as extra low inclusion (ELI) Nitinol, can be particularly beneficial for long-term implanted devices that are subjected to a high number of load-unload cycles.

3.1.2 Introduction to ring-stents

The results of the present work are mainly discussed with the 'ring-stent' technology in mind. Ring-stents are employed in the design of endovascular devices made by Terumo Aortic Glasgow. The Anaconda Stent Graft System is an example of such a device, as mentioned earlier. It is a modular device comprised of a main body device and two leg devices which 'dock' to the main body. The main body and the leg devices are made in a range of different sizes. Each device is composed of a polyester woven graft that is supported by ring-stent structures which are made of multiple turns of straight-annealed Nitinol wire.

The three modular parts of the Anaconda One-Lok system are shown in Figure 3-2. The proximal rings of the body device provide radial force to seal against the vessel wall, thus exculding the anerysm sac from the circulation and preventing endoleaks. The proximal end of the body device also contains the hooks that

penetrate the vessel wall anchoring the device in place. All ring-stents are required to hold the fabric graft open providing a patent lumen for the blood flow.

The ring-stents are manufactured from straight annealed Nitinol wire which is turned multiple times to create a 'bundle' of wires. The two ends of the wire are then joined together with a tantalum crimp. The wire diameters used for the manufacture of Terumo Aortic ring-stents range from 0.10mm to 0.24mm. When the wire is turned, to form the ring, it is subjected to a small amount of mean strain, as seen in Figure 3-3 which depicts the deformation life-cycle of a ring-stent.

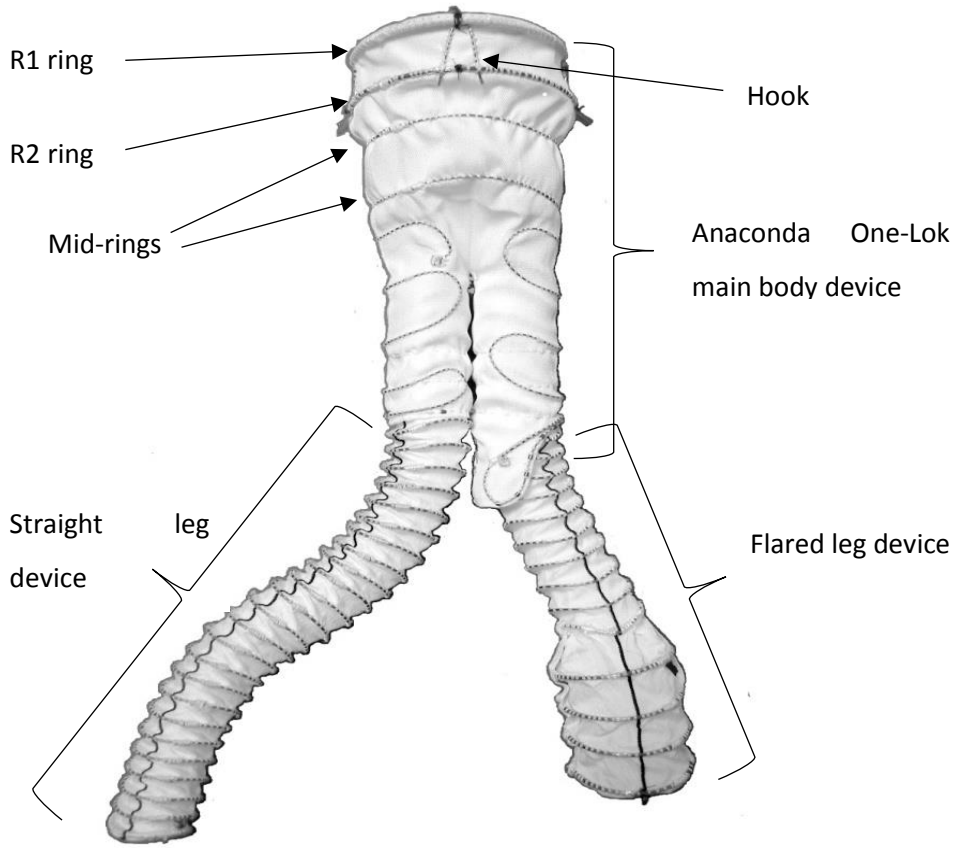

Figure 3-2 Image of the modular Anaconda stent-graft system which is comprised of the main body device and two leg devices. The image is reproduced by courtesy of Terumo Aortic Glasgow.

The ring-stents are designed to fold down into a steep 'saddle' shape when the device is compacted into the delivery system. During compaction, there are regions of the ring-stent where Nitinol will experience a high-strain deformation. This is shown as step 2 in Figure 3-3. Depending on the stent regions, there will also be

untransformed austenitic material that will be subjected only to elastic straining during this process. It is good practice to investigate the high-strain deformation considering it a worst-case scenario.

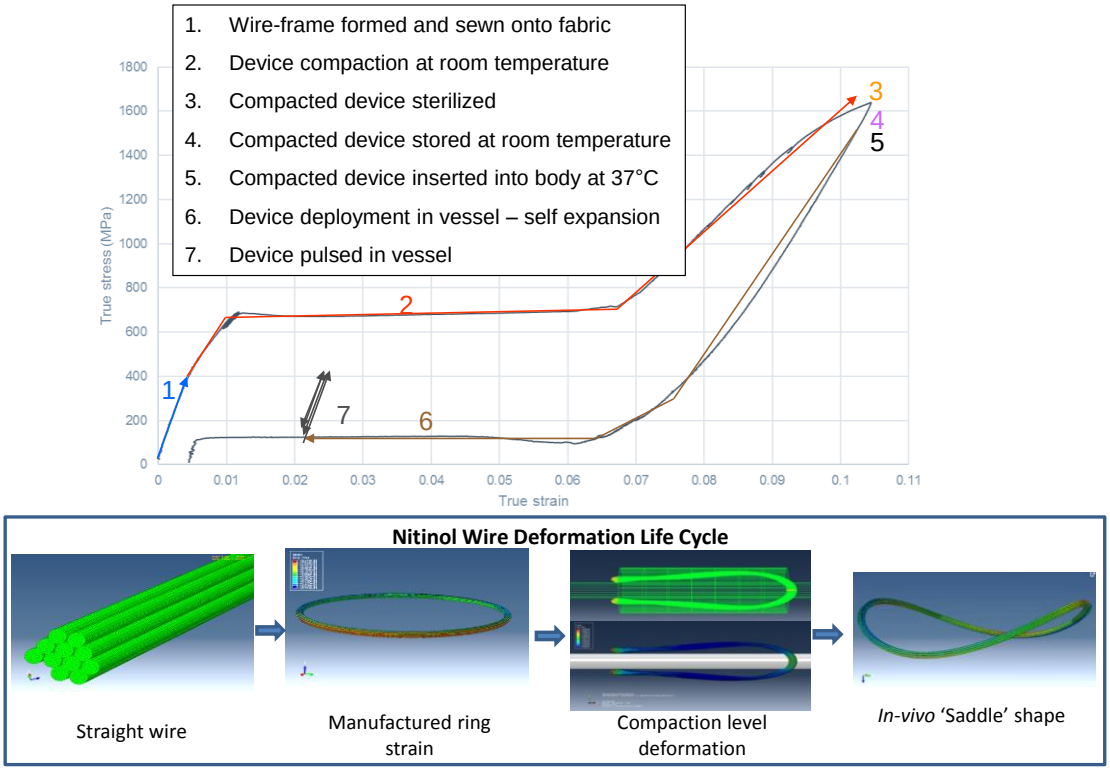

Figure 3-3 The deformation life-cycle of a ring-stent includes the wire being formed into a ring, compaction into a delivery sheath, sterilization, deployment to artery and pulsatile motion due to the cardiac cycle. The FEA images depict a ring-stent in its manufactured 'flat' position, approximation of the compacted state and a typical in-vivo 'saddle shape' deformation. The FEA Images are reproduced by courtesy of Terumo Aortic Glasgow.

Following compaction, the stent-graft is usually sterilised by ethylene oxide which can penetrate multiple layers of complex assembled devices and is compatible with materials that do not tolerate radiation or very high temperatures [47]. During this process the temperature is raised to approximately 55°C.

When the device is deployed into the diseased blood vessel, the ring-stents will try to 'self-expand' towards their original shape due to Nitinol's superelasticity. The rings will expand until they reach the aortic wall, but they will not return completely to their initial 'flat' shape. Clinical practice and medical device manufacturers suggest oversizing the device. Therefore, the ring-stents will assume

a ‘saddle’ shape which is characterised by two ‘peaks’ and two ‘valleys’. The saddle height of the ring will depend on the initial ring diameter, the diameter of the artery and the oversizing.

The ring-stents will apply a continuous radial force towards the vessel wall, also known as chronic outward force [48], to create a seal at the proximal and distal regions of the aneurysm. This will provide a new sealed path for blood to flow excluding the aneurysm sac. The outward radial force is also required to ensure the embedding of the proximal hooks into the vessel wall. Nitinol’s deformation during deployment is represented by step 6 in Figure 3-3. Note that the radial force of the ring-stent will be influenced by the unload plateau stress.

The stents will then be subjected to cycling due to the physiological systolic-diastolic pressure (step 7 in Figure 3-3). Cycling will take place within a small strain amplitude. Nitinol’s stiffness during cycling will resist any external deformation from the vessel wall. The cyclic elastic modulus is often termed radial resistive force [48].

Due to the complex deformation paths described above, Nitinol materials employed in stent-design should be investigated by considering all loading modes and thermomechanical conditions a device encounters during its life-cycle. The following sections identify some notable experimental studies that examine the behaviour of Nitinol under tension, compression, three-point bending and torsion.

3.2 Mechanical characterisation of superelastic specimens

3.2.1 Tension

Tensile testing has been established as the preferred choice for materials characterisation due to its simplicity. Several material properties and constitutive parameters can be determined using tensile data. Standards have been formed in order to provide engineers with recommendations and guidelines when conducting such experimental tests. Various researchers have investigated different aspects of

Nitinol's behaviour under tensile deformation including the temperature sensitivity, the load rate effects and the load history effects.

Ng and Sun [49] examined the temperature sensitivity of Nitinol tubes subjected to tension. Specimens were submerged into a water bath and deformed under displacement control at a strain rate of 5.6 x 10^{-5}/s. The transformation temperatures determined by differential scanning calorimetry (DSC) were: M_s=5.5°C, M_f=-32.7°C, R_s=52.1°C, R_f=28.2°C, A_s=23.3°C and A_f =57.1°C. Results presented in Figure 3-4 can be divided in three groups.

At 23°C and 28°C the material is mainly comprised of R-phase. Therefore, the initial part of these curves corresponds to the elastic deformation of R-phase. With subsequent loading, stress plateaus are formed as the material is transformed to martensite. Between R_f and R_s the material is comprised of both austenite and R-phase since A_s=23.3°C. There is a two-step stress-induced transformation as the material transforms from austenite to R-phase and then to martensite. The characteristic reduction of the initial elastic slope due to the R-phase can be observed in the curves of 34°C, 40°C, 46°C and 51°C. At temperatures above A_f=57.1°C, the material is austenitic and exhibits complete superelasticity with no residual strain present upon unloading. The transformation stresses also increase with temperature.

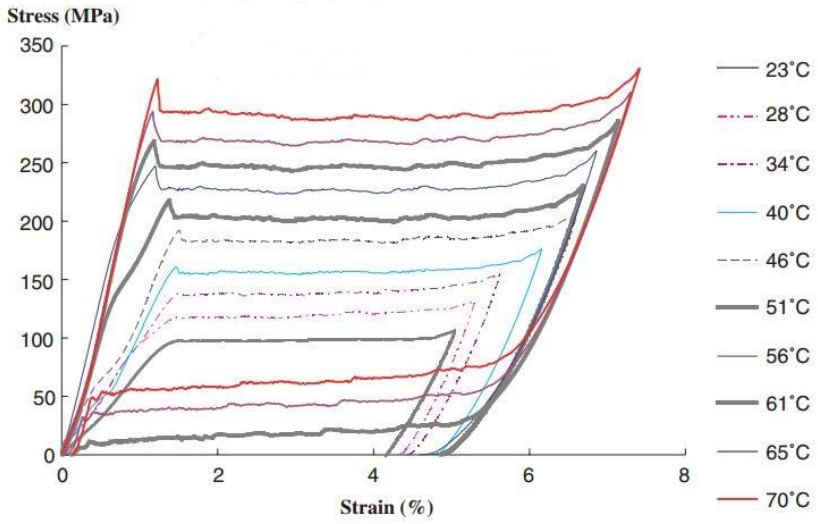

Figure 3-4 Temperature sensitivity of Nitinol tubes with an Af temperature of 57.1°C. Image reproduced with permission from Ng and Sun [49].

At a stable ambient environment, temperature changes are induced if testing is conducted under high strain rates. Tobushi et al. [50] examined the rate sensitivity of 0.75 mm diameter wires while recording their surface temperature. Specimens were pulled to 8% strain measured by an extensometer. The A_f of the material was 50°C, thus testing was conducted at 70°C, 80°C and 100°C using an environmental chamber. At low strain rates, maximum and minimum specimen temperatures were very close as seen in Figure 3-5(a). At high rates however, the temperature difference increased.

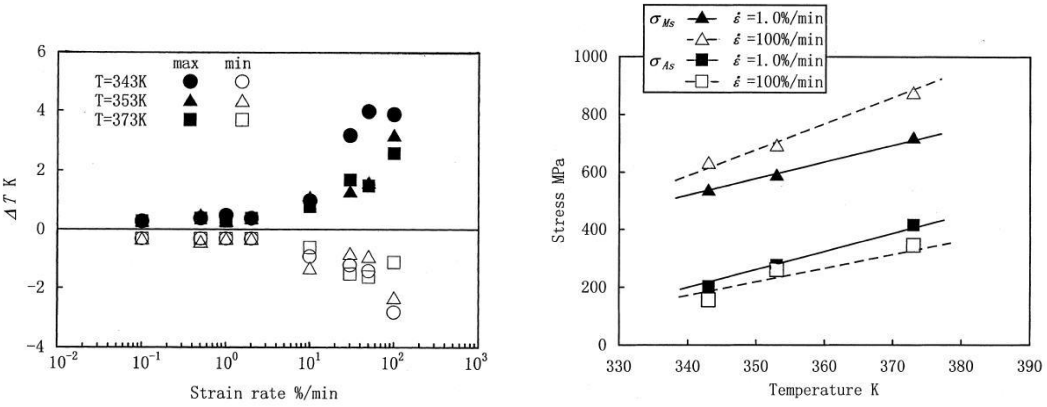

(a) (b)

Figure 3-5 Effect of strain rate on specimen temperature during loading and unloading (a). Evolution of transformation stresses during loading and unloading as a function of strain rate and temperature (b). Images adapted with permission from Tobushi et al. [50].

Figure 3-5(b) shows the evolution of the transformation stresses upon loading and unloading as a function of strain rate and temperature. Here, σ_{Ms} is the stress required to start the martensitic transformation during loading and σ_{As} is the stress at which reverse transformation to austenite starts taking place upon unloading. At low rates, transformation lines are almost parallel, increasing in a similar manner as the ambient temperature is increased. At high strain rates, the forward transformation line is shifted upwards towards higher stress levels, whereas the reverse transformation line is shifted slightly downwards.

Macroscopically these observations are portrayed with steep stress-strain curves shifted towards higher stress levels, as seen in Figure 3-6. Results are from the study of Dayananda and Rao [51] who tested 0.6mm diameter wires at various strain

rates. Testing was conducted at room temperature and the A_f of the material was 17.7 ^oC.

The need to understand the phenomena underlying the behaviour above, encouraged researchers to study the phase transition of the material by simultaneous full-field monitoring of deformation and temperature. Zhang et al. [52] used high speed and infrared cameras to record the surface morphology and temperature field respectively, of Nitinol strips subjected to tension. Testing was conducted under various strain rates, at room temperature in air. Figure 3-7 shows the nominal stress-strain response (a) and surface morphology (b) at a strain rate of 3.3 x 10^{-4}/s.

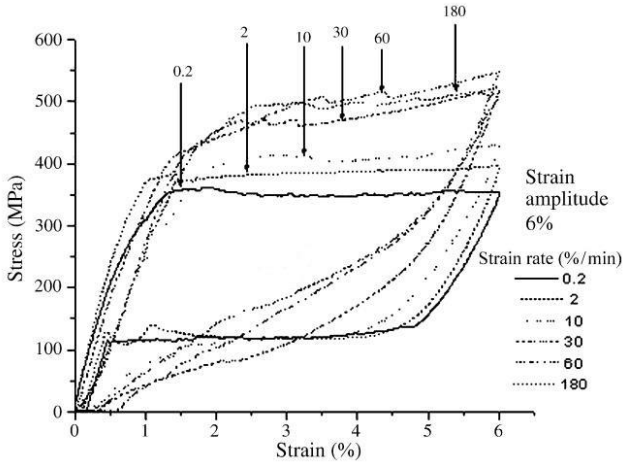

Figure 3-6 Stress-strain curves of superelastic Nitinol wire subjected to tension at various strain rates. Image adapted with permission from Dayananda and Rao [51].

Initially upon loading, linear elastic deformation of austenite takes place and the temperature distribution, not shown here, is considered uniform. With subsequent loading, a stress drop is exhibited following the nucleation of a martensite domain at the top end of the specimen (point b). Two fronts are formed separating martensite and austenite domains. One of the fronts is soon stopped at the top end while the other starts propagating down the specimen (point d). Temperature is then increased causing a stress increase (point e). Martensite is nucleated at a second region at the bottom end of the specimen followed by a stress drop. One of the two new fronts is soon stopped at the bottom end, leaving the two remaining fronts to propagate towards each other (point i) while temperature is further increased. The whole section is soon transformed to martensite (point l).

Reverse transformation to austenite during unloading takes place in a similar manner. Initially stress is decreased almost linearly with strain. With subsequent unloading, austenite domains are formed at the ends of the specimen and thereafter two fronts start propagating towards each other almost simultaneously (point p). Soon the whole specimen is transformed to austenite which is then unloaded elastically.

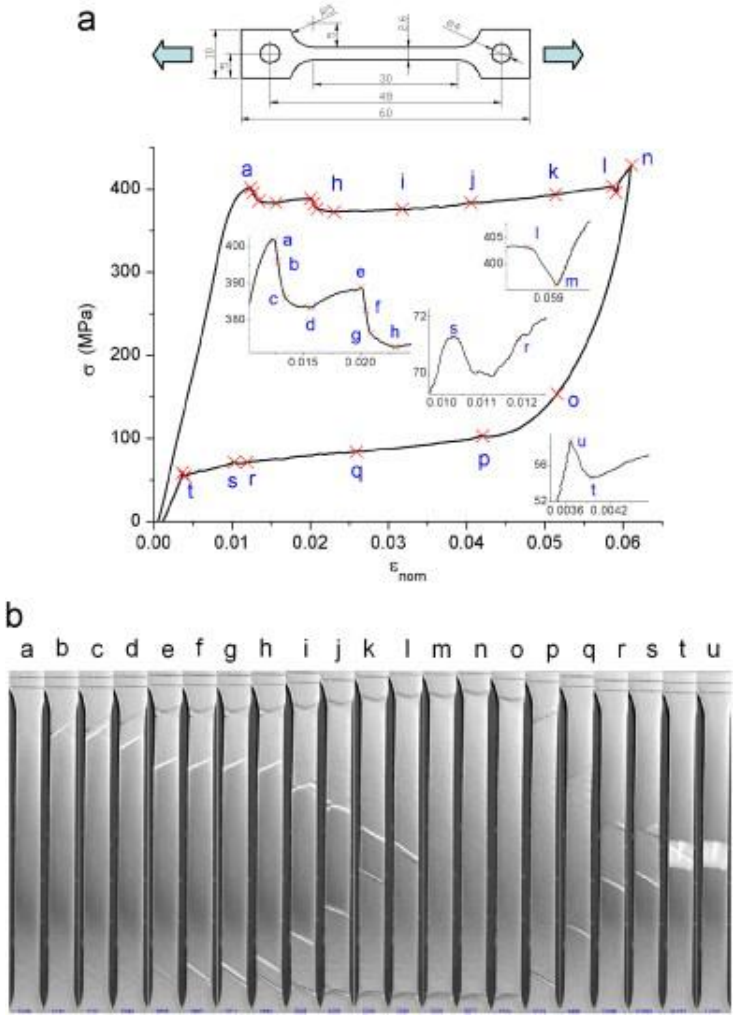

Figure 3-7 Stress-strain curve (a) and surface morphology (b) of Nitinol strips subjected to tensile deformation at a strain rate of 3.3 x 10^{-4}/s. Images adapted with permission from Zhang et al. [52].

At higher strain rates the above process differs as seen in Figure 3-8 which presents the nominal stress-strain response (a) and surface morphology (b) at a strain rate of 3.3 x 10^{-3}/s. Martensite nucleates at the top and bottom ends of the specimen almost simultaneously (point a). The upper front is stopped at the top end and the

lower front is stopped at the bottom end leaving two fronts to propagate towards each other (point b). Temperature is increased as heat cannot be transferred quickly to the environment at this loading rate. Consequently, stress increases and martensite nucleates at another region near the mid-section of the specimen (points c-d). With subsequent loading, two more martensite domains are formed (points e-f and g-h). The whole specimen is soon transformed as the transformation fronts merge. During unloading, transformation to austenite takes place in a similar manner incorporating the formation of multiple fronts.

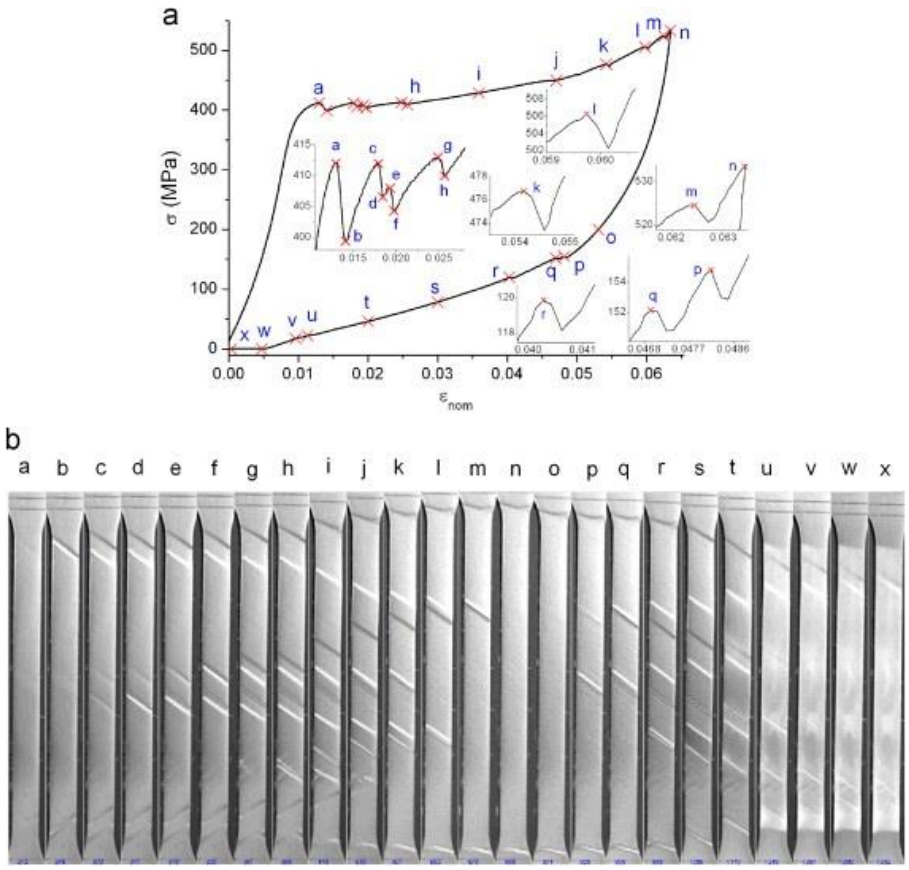

Figure 3-8 Stress-strain curve (a) and surface morphology (b) of Nitinol bone-shaped specimen at a strain rate of 3.3 x 10^{-3}/s. Images adapted with permission from Zhang et al. [52].

Therefore, at high strain rates the overall stress-strain response is shifted towards higher stress levels. Macroscopically, it seems that the formation of SIM cannot keep up with the increased rate. Elastic deformation of the already formed detwinned martensite could be taking place before the martensitic transformation is

complete. At even higher rates, multiple domain nucleation takes places and transformation becomes nearly homogeneous.

Note that the stress required for the nucleation of martensite is higher than the stress to continue the transformation. Similarly, nucleation of austenite requires a stress lower than the one to propagate the reverse transformation. Therefore, upon loading a stress overshoot or peak is often observed and upon unloading a stress undershoot or valley is seen. At low rates during loading there is enough time for the domains to move after nucleation and therefore the high stress is relaxed and the stress drop observed. However, at high rates the domains move quickly after nucleation, there is not enough time for relaxation and macroscopically the stress drop is not seen.

Shaw and Kyriakides [53, 54] also investigated the tensile response of Nitinol as a function of temperature, strain rate and ambient medium. They tested 1.07mm diameter wires at various strain rates, in air and water. Deformation and specimen temperature were monitored by miniature extensometers and thermocouples respectively. At high strain rates, specimens exhibited higher stresses during loading and lower stresses during unloading when testing took place in air. This is because water was a more efficient heat exchange medium compared to air. It acted as a heat sink and heat source during loading and unloading respectively, thus minimizing temperature changes caused by heat released from the specimen during loading and heat absorbed during unloading.

A similar study was conducted by He et al. [55] who subjected sheet specimens to tension at vari s strain rates and environ ntal conditions. The latter included still air, flowing air with velocity of 2m/s and flowing air with velocity of 17m/s. Heat transfer was improved as the air flow velocity increased. At high rates in flowing air, the stress-strain curves exhibited well-defined upper plateaus with smaller differences compared to the quasi-static loading, as seen in Figure 3-9(c). On the contrary, at high rates in still air, stress-strain curves had steep upper transformation regions, shifted towards high stress levels, according to Figure 3-9(a).

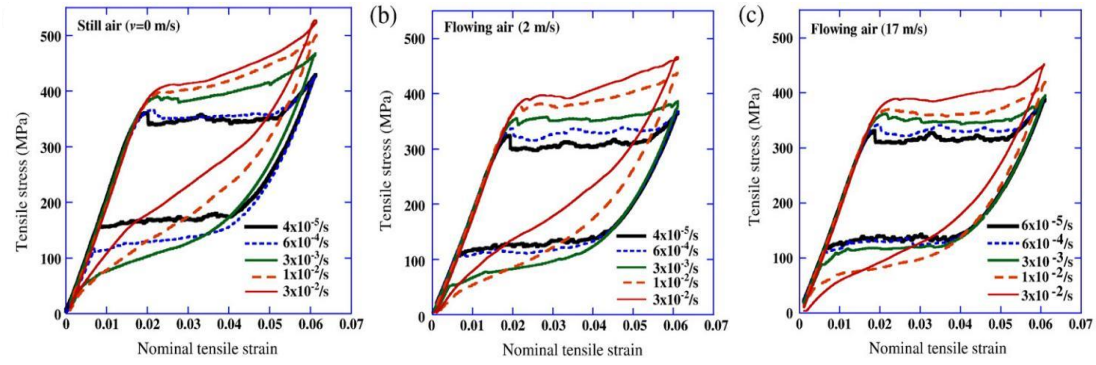

Figure 3-9 Stress-strain response of Nitinol sheet specimens at various strain rates and environmental conditions: still air (a), flowing air with velocity of 2m/s (b) and flowing air with velocity of 17m/s (c). Images adapted with permission from He et al. [55].

Several researchers have also investigated the cyclic deformation of Nitinol since the in-vivo response of medical devices is usually cyclic in nature due to the pulsatile blood flow. Brinson et al. [56] cycled superelastic sheet specimens to 2% strain under displacement control. Strain was calculated based on the machine's crosshead movement. According to Figure 3-10, the stress required to start the transformation during loading is decreased with increasing number of cycles. The slope of the upper transformation region becomes steep as the curve takes a hardening-like form. However, transformation stresses during unloading are less affected with cycling. Residual strain is accumulated and the overall behaviour, depicted as a gradual degradation of the material properties, is expected to stabilize after a certain number of cycles.

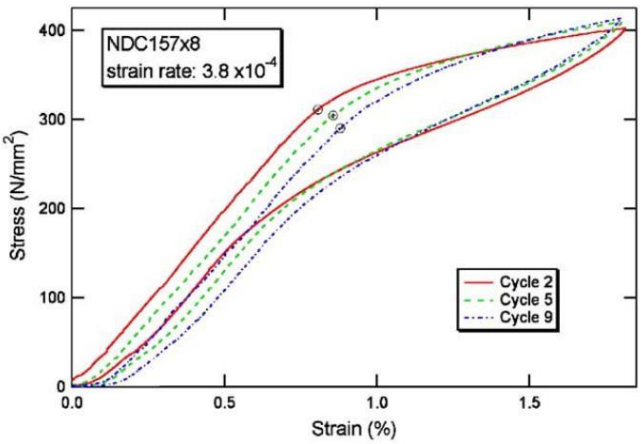

Figure 3-10 Effect of cycling on the tensile stress-strain response of Nitinol sheet specimens. The circled points on the curves indicate the start of the transformation during loading. Image reproduced with permission from Brinson et al. [56].

The authors also incorporated a digital camera and an optical microscope in their experimental configuration to examine features of the phase transformation during cycling. Microscope images at the end of cycles 1, 5, 10 and 15 are shown in Figure 3-11 for the same material grains. Localised plastic deformation is exhibited by cycle 5 within the grains, increasing over the following cycles. Consequently, remnant fields of increased stress are generated within the material structure which upon loading assist the phase transition. Thus, the stress required to initiate the transformation becomes lower as cycling progresses, explaining the changes of the macroscopic stress-strain response.

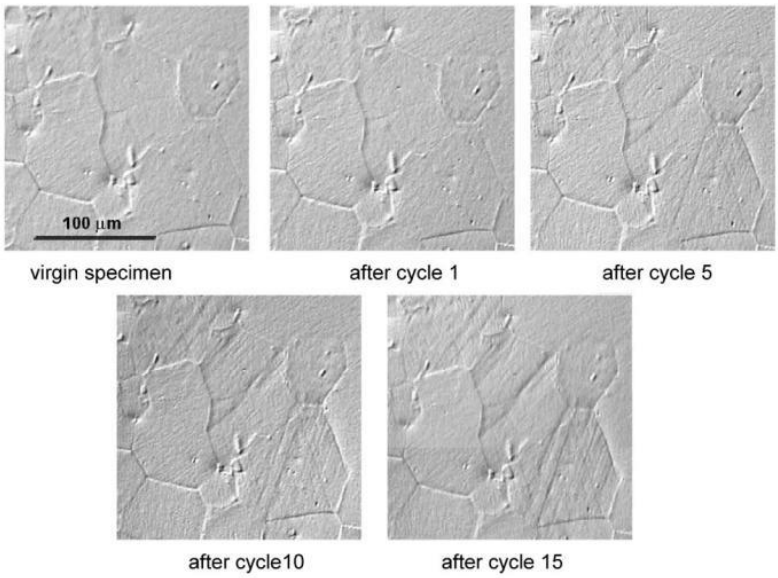

Figure 3-11 Accumulation of localised plastic deformation within the material grains under cyclic loading. Image reproduced with permission from Brinson et al. [56].

Similar stress-strain results were presented by DesRoches et al. [57] who cycled 1.8mm diameter superelastic wires to 6% strain. Iadicola and Shaw [58] examined the cyclic properties of Nitinol wires as a function of temperature. They subjected 0.765mm diameter specimens to tensile cycling at two different temperatures, namely 16.5°C and 24.6°C. The material was superelastic at both temperatures since the A_f was 12°C. The effect of cycling on the macroscopic stress-strain response was more pronounced at the higher temperature experiment. This was probably due to the greater stresses involved during deformation. The response was also stabilised faster at 24.6°C, requiring 30 cycles instead of 46 cycles at 16.5°C.

Schlun et al. [59] showed that when cyclic deformation takes place at high strains, only two cycles are enough to produce significant changes in the material properties. Superelastic Nitinol tubing was loaded and unloaded twice, up to 9% strain which was measured by a video extensometer. According to the authors, performing one or two load-unload cycles up to 6% strain did not alter the material response. Therefore, results were presented for cases between 6% and 9% strain which are reproduced here in Figure 3-12.

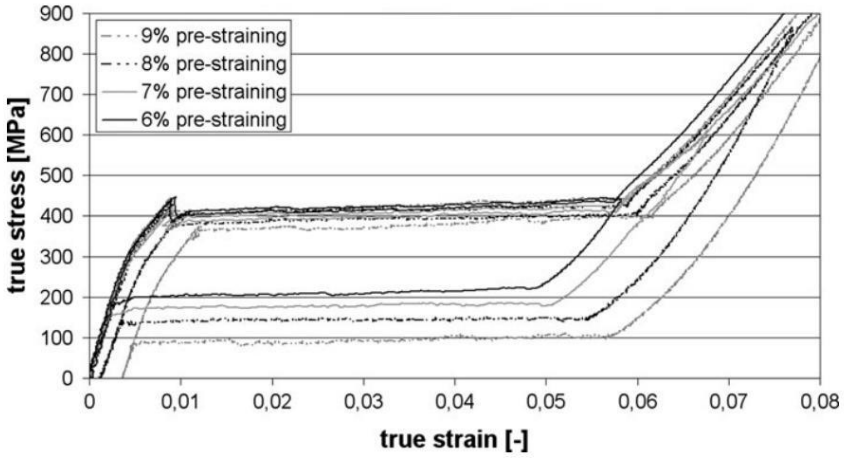

Figure 3-12 Effect of high-strain cycling on the tensile stress-strain response of Nitinol. Image reproduced with permission from Schlun et al [59].

By comparing the first cycles from every case, it is shown that unloading from progressively higher strains, results in a decrease of the unload plateau stresses while a significant amount of residual strain is exhibited. With subsequent loading, the upper, load plateau of the second cycle is shifted towards lower stress levels for the 8% and 9% strain cases. The unloading path of the second cycle was not presented in the published results. Also, the strain level required to induce such marked changes in the tensile response was not identified.

3.2.2 Compression

Compression testing is often required to obtain relevant constitutive parameters and/or to produce experimental results that will be used in comparisons with computational data. Evidence in the literature also suggests that Nitinol materials exhibit an asymmetry between tension and compression. Hence, research is driven by the interest to identify the differences between the two uniaxial deformation modes which could affect the behaviour of the material in multi-mode loading conditions. Since Nitinol characterisation requires the testing of specimens at superelastic strains, uniaxial compression becomes challenging due to issues such as buckling and barrelling. Different approaches have been adapted by researchers in order to explore the compressive behaviour of Nitinol specimens, although the available studies are still relatively scarce.

Orgeas and Favier [60] examined the tensile and compressive behaviour of Nitinol sheet specimens. Buckling during compression was prevented by using a custom-made gripping device attached on a thin groove that was machined on the specimens. The tensile specimen was pulled up to 8% strain and the compressive specimen was deformed up to 6% strain measured by a local clip-on extensometer. Testing was conducted at strain rate of 10^{-3}/s. A comparison between the tensile and compressive response of the material is presented in Figure 3-13. Note that both results here are plotted with positive values and the material was superelastic since its A_f was 55^{o}C.

Upon loading the deformation is initially linear elastic in both cases with a somewhat higher elastic modulus for compression. At a stress level of approximately 400MPa, the tensile curve displays a clear flat plateau which extends to 7% strain. On the contrary, a stress value of almost 600MPa is required in order for the compressive curve to form a positive slope transformation region. Beyond 4% strain, compressive stress increases quickly up to 800MPa at the end of the loading path. Upon unloading the compressive curve exhibits again a positive slope transformation region which

takes place at higher stress levels compared to the flat plateau in tension. Residual strain is higher in compression although the specimen was subjected to a lower maximum strain during loading.

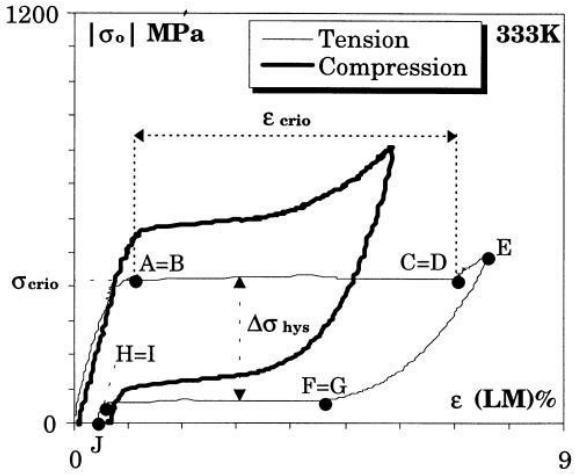

Figure 3-13 Tension-compression asymmetry of Nitinol sheet specimens. Image adapted with permission from Orgeas and Favier [60].

This tension-compression asymmetry was also observed by Reedlunn et al. [61] who tested Nitinol tubes using DIC to monitor the strain distribution on the specimens. Testing was conducted under a strain rate of $2x10^{-5}$/s at room temperature and since their material had an A_f of 19°C, all specimens were superelastic. In order to address the issues of buckling during compression, the authors used two steel cylinders as grips. A hole was machined into the cylinders to house the specimens providing them with lateral support during testing. The specimen surface was lubricated to allow them to slide within the grips minimizing friction effects.

The asymmetric behaviour of the material is demonstrated in the macroscopic stress-strain curves of Figure 3-14. Results here show the tensile specimen being deformed to 7% strain and the compressive one loaded up to 4% strain. The vertical axis of the graph is the engineering stress averaged over the cross-sectional area of the specimen and the horizontal axis is the strain along the tube axis averaged over the DIC gauge length. The tensile response exhibits clear flat plateaus

whereas the compressive response, shown here with negative values of stress and strain, is manifested by a steep curve shifted towards higher stress levels. Transformation stresses during loading and unloading are higher in compression and stress increases quickly beyond 3% compressive strain.

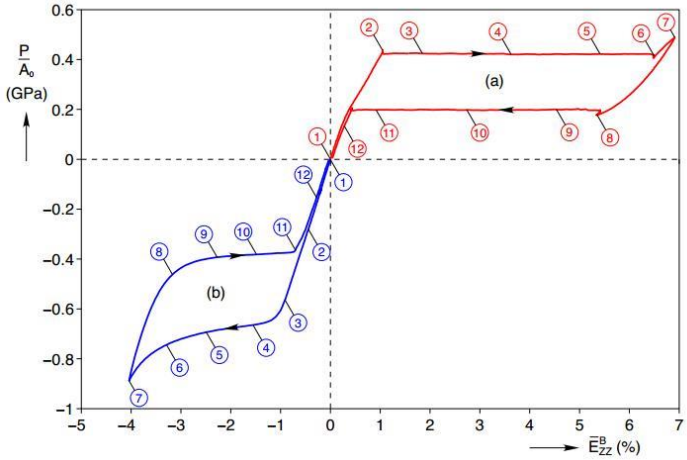

Figure 3-14 Tensile (a) and compressive (b) stress-strain curves of Nitinol tubes. The numbers on the curves correspond to the strain images seen in Figure 3-14. Image reproduced with permission from Reedlunn et al. [61].

The numbers on the above curves correspond to strain field images obtained by DIC. These are presented in Figure 3-15(a) for tension and Figure 3-15(b) for compression. Transformation in tension is non-homogeneous and it progresses through a martensite front which is formed near the bottom grip and propagates along the specimen upon loading. On the contrary, transformation in compression is homogenous. Strain fields are nearly uniform apart from small fluctuations near the grips. The difference observed in image 10 is attributed to specimen bending according to the authors.

Henderson et al. [62] also examined the tension-compression asymmetry of 1.8mm diameter superelastic wires. These specimens were thicker than conventional wires in order to accommodate the requirements of compression testing. However, they had undergone processing similar to medical grade materials. Custom grips were employed, made of solid steel cylinders with a hole machined into them in order to hold and support the specimens minimizing any buckling effects. The grips limited the maximum compressive strain to 4% measured by the machine's crosshead

displacement. The A_f of the examined material was -5°C and testing was conducted at 25°C. Results from this study, in the form of stress-strain data, are shown in Figure 3-16.

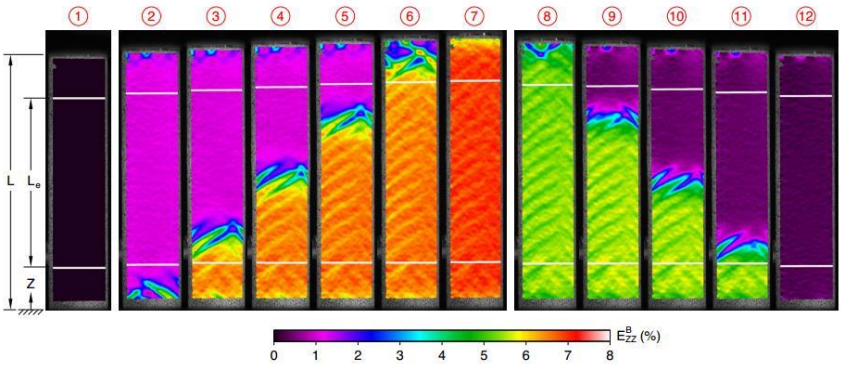

(a)

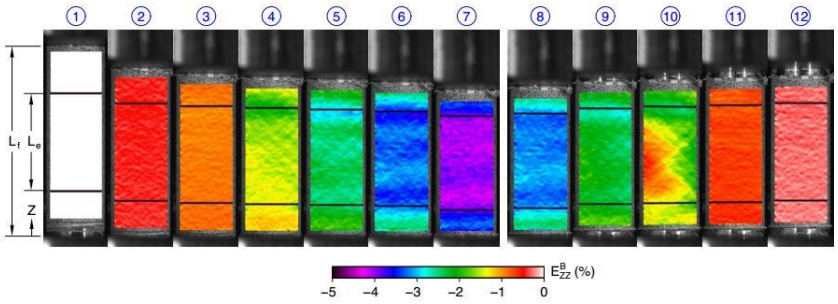

(b)

Figure 3-15 Tensile (a) and compressive (b) strain field images obtained by DIC. Le corresponds to the DIC gauge length. Images reproduced with permission from Reedlunn et al. [61].

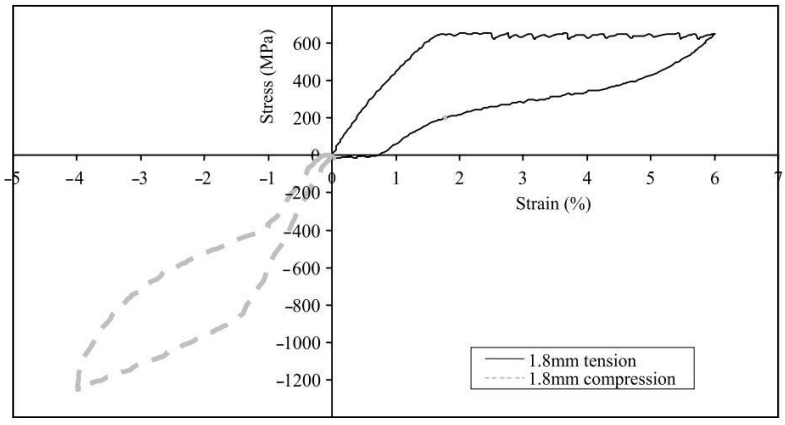

Figure 3-16 Tension-compression assymmetry of 1.8mm Nitinol wire. Image reproduced with permission from Henderson et al. [62].

The overall asymmetry features are in agreement with the previously mentioned studies. The tensile curve here is characterised by an oscillation in the upper plateau which is also seen in the tensile results of Kim and Daly [63]. It is associated with the continuing nucleation of martensite domains that cause small stress rises and drops. A significant residual strain is presented in tension upon unloading which could be associated with the fact that strain was calculated based on crosshead movement.

Siddons and Moon [64] showed that the asymmetry between tension and compression is maintained when subjecting superelastic Nitinol tubes to cyclic loading. Custom grips were used, composed of pin chucks with flat ends, between which the specimens were compressed. Strain was calculated using the machine's crosshead displacement. Results showed that the material's response was altered in a similar manner for both loading modes. Asymmetry between tension and compression has also been reported for martensitic Nitinol bars [65, 66].

3.2.3 Bending

The predominant deformation mode in stent-grafts, during compaction and in-vivo, is usually bending. Therefore, experimental characterisation is required in order to investigate the material's bending properties. The following paragraphs revolve mainly around the three-point bend test due to its simplicity and ease of reproducibility that makes comparisons between studies easy.

Three-point bending has been established as a standardised experimental method in the field of orthodontics [67]. Thus, the vast majority of studies regarding three-point bending of Nitinol wires often addresses the needs of such applications. The requirements of orthodontic applications differ from those of endovascular devices. However, these studies provide an insight into the complex material behaviour.

Pelton et al. [68] examined the three-point bending behaviour of superelastic Nitinol wires. The mid-region of 1.5mm diameter specimens was deflected by 3.5mm, between supports that were 20mm apart. Further information regarding the supports was not provided. The resulting macroscopic load-deflection curve of the wire is shown in Figure 3-17. The bending response is manifested with positive slope transformation regions during loading and unloading, implying a near homogeneous transformation. These are considered typical features exhibited by Nitinol wires when subjected to bending.

The authors attempted to directly compare the bending results with data from uniaxial tension. Converting the load-deflection results to stress-strain using conventional beam theory formulations led however to a prediction of unusually high stresses. The mechanical behaviour of Nitinol, unlike beam theory assumptions, is characterised by an asymmetry between the tensile and the compressive response. Consequently, this feature also dictates the bending behaviour of the material since part of a deflected specimen is deformed under tension and another part under compression.

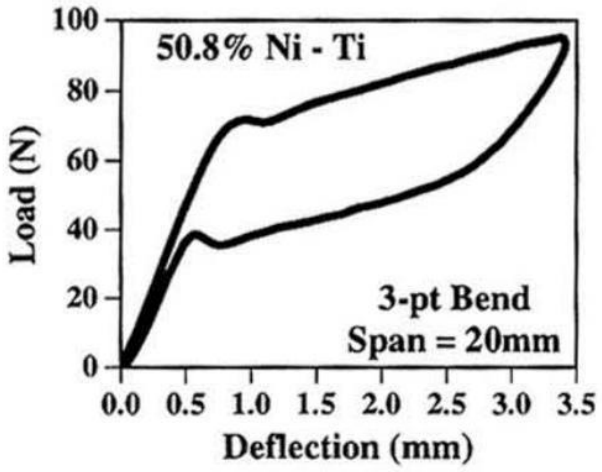

Figure 3-17 Load-deflection curve of a Nitinol wire subjected to three-point bending. Image reproduced from Pelton et al. [68].

Iijima and his co-workers [69] investigated the phase transformation of three different Nitinol wires subjected to three-point bending using micro x-ray diffraction

(XRD). The wires had rectangular cross-sections with dimensions of 0.41mm x 0.56mm. The supports were round bars with a diameter of 3mm and their span was 14mm. XRD spectra were obtained at three bending angles of 135, 146 and 157 degrees which corresponded to 3.5mm, 2.5mm and 1.6mm of deflection respectively. Results from their study are presented in Figure 3-18 which shows the changes of the martensite to austenite ratio for the three bending angles and test temperatures. Figure 3-18(a) presents the changes of the martensite to austenite ratio within the region of the tensile strain whereas Figure 3-18(b) presents the changes of the same ratio within the region of the compressive strain.

In Figure 3-18(a), as the bending angle becomes smaller at greater deflections, the martensite to austenite ratio increases since more material transforms to martensite. As the temperature increases the ratio decreases since austenite becomes more stable. Under very little load only the wire with an A_f of 37^{o}C exhibits changes in the martensite to austenite ratio with increasing temperature. This is because at 25^{o}C there is still a significant martensite fraction in the wire. Thus, when the temperature is increased the ratio decreases as the material further transforms to austenite. In Figure 3-18(b) the same features can be observed for the compression side of the wires. However, the amount of transformation is much lower confirming an asymmetric behaviour during bending.

Reedlunn et al. [61] measured the strain distribution on Nitinol tubes subjected to four-point bending by using DIC. Results showed strain localisations on the tensile side associated with the nucleation of martensite domains during the transformation. The strain on the outer fibers of the specimen exceeded the superelastic range. In agreement with the findings of the previous section, transformation on the compressive side of the specimen proceeded in a near-homogeneous manner without strain localisations. The authors considered the compressive deformation as the reason behind the positive slope transformation regions of the macroscopic load-deflection response in bending.

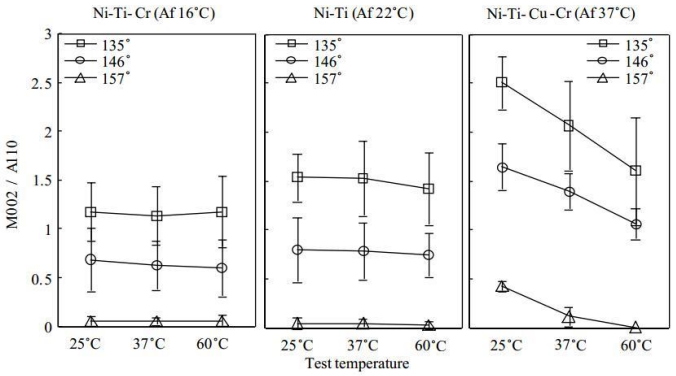

(a)

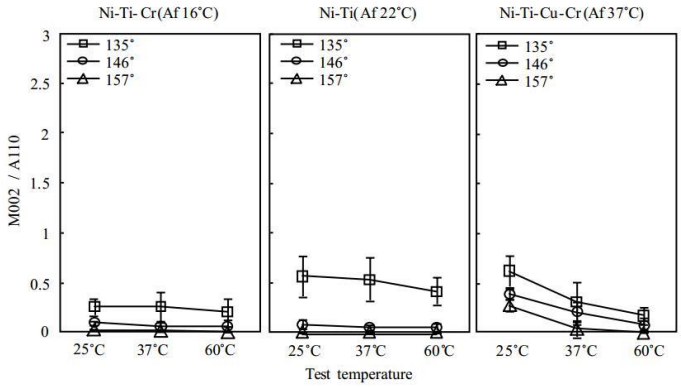

(b)

Figure 3-18 Evolution of the martensite to austenite ratio within the tensile (a) and compressive (b) region of Nitinol wires subjected to three-point bending. Results are shown for three different test temperatures and bending angles. Images reproduced with permission from Iijima et al. [69].

The temperature sensitivity of Nitinol wires subjected to three-point bending was extensively studied by Tonner and Waters [70]. Ten different brands of commercial Nitinol wires were tested at various temperatures from 5°C to 50°C. Testing was conducted with the specimens rested on knife-edge supports inside an environmental chamber. Results showed an almost linear relationship between the exhibited forces of the upper transformation region and the test temperature for all examined specimens. Additionally, forces varied significantly between different Nitinol wires of the same nominal dimensions.

3.2.4 Torsion

Numerous Nitinol applications require a multi-mode deformation of their components. Materials used in orthodontic applications, actuators and cardiovascular devices are often subjected to torsional loads. Stent-grafts are also expected to experience torsional deformations during compaction. Conclusions derived from tensile data cannot be used directly to describe the behaviour of the material in torsion and to obtain the relevant constitutive properties. Therefore, independent experiments are needed to fully characterise the material. However, relatively little work has been done to characterise the torsional properties of Nitinol.

Sun and Li [71] examined the tensile and torsional behaviour of superelastic Nitinol tubes using an optical microscope to examine the surface morphology of the specimens during testing. Experiments were conducted at room temperature utilizing custom grips to eliminate stress concentrations on the specimens. Tensile strain was measured by an extensometer while shear strain was calculated using rotation measurements from the testing machine. The tensile and torsional responses of the tube specimens are presented in Figures 3-19(a) and 3-19(b) respectively.

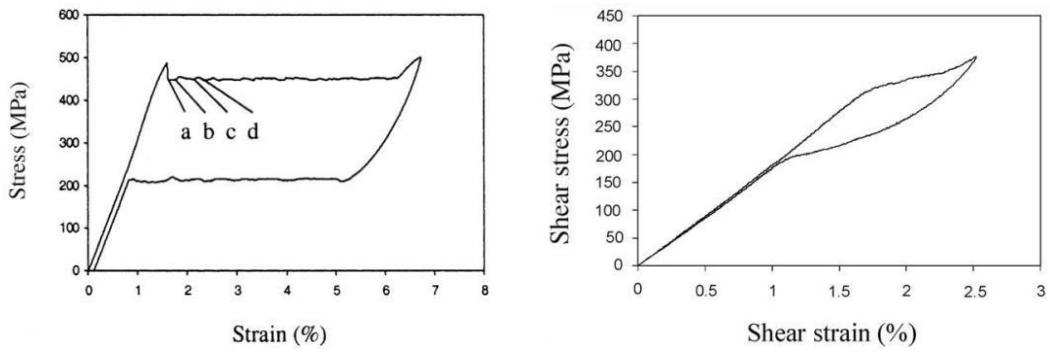

(a) (b)

Figure 3-19 Stress-strain response of Nitinol tubes under tension (a) and torsion (b). Images adapted with permission from Sun and Li [71].

The macroscopic tensile stress-strain curve is characterised by flat plateaus as transformation during loading proceeds with the nucleation and propagation of

martensitic domains. The points (a) to (d) correspond to surface morphology images, not shown here, which confirmed the non-homogeneous nature of the tensile transformation. The torsional response is characterised by positive slope transformation regions and an overall small hysteresis. Microscope surface observations indicated a homogenous transformation across the specimen without the localised nucleation of martensitic domains. Note that transformation during loading in torsion is initiated at approximately 1.6% shear strain and 320MPa shear stress whereas the equivalent transformation region in tension takes place at approximately 1.4% tensile strain and 450MPa tensile stress.

The authors also performed a series of tensile tests under different pre-applied shear stress levels to further investigate the differences between the two loading modes. According to the results shown in Figure 3-20, the overall deformation is similar to pure tension at low shear stress levels. A stress overshoot is exhibited upon loading indicating the nucleation of martensite domains. However, with increasing shear to tension ratio, transformation becomes homogeneous and the exhibited stresses during loading decrease.

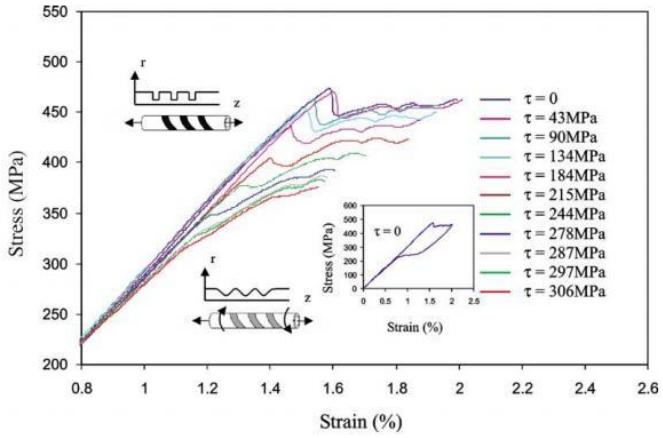

Figure 3-20 Tensile stress-strain response under different applied shear loads. Image reproduced with permission from Sun and Li [71].

Orgeas and Favier [60] compared the transformation stresses during loading in tension, compression and shear. They presented the stresses as a function of temperature, as seen in Figure 3-21. The lowest transformation stress is exhibited in shear and the highest in compression. The tensile transformation stress falls in-

between the values recorded for the other two loading modes. Temperature dependence in an almost linear manner is observed for all cases. Testing was performed with sheet specimens at strain rates in the order of 10^{-3}/s for all loading modes.

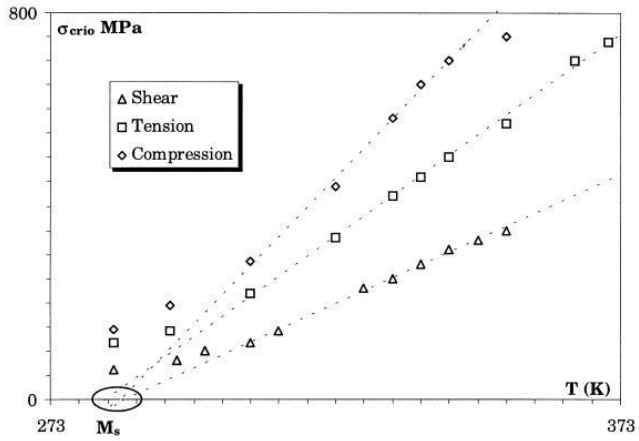

Figure 3-21 Transformation stresses as a function of loading mode and temperature. Image reproduced with permission from Orgeas and Favier [60].

Adler et al. [72] came to similar conclusions by testing superelastic Nitinol tubes in tension and torsion at a strain rate of 10^{-3}/sec. Engineering strain was measured in tension and rotational displacement in torsion. Results were presented in the form of equivalent stress and strain for a more direct comparison between the two loading modes. The torsional response was depicted by positive slope transformation regions and small hysteresis. Transformation during loading was initiated at approximately 2% equivalent strain in torsion and at 1.2% equivalent strain in tension.

An overall small influence of the loading rate on the torsional response has been reported. Doare et al. [73] found that the macroscopic response was changed when 2mm diameter, superelastic Nitinol wires were subjected to torsion at high rates. However, Dolce and Cardone [74] and Predki et al. [75] observed negligible rate effects in torsion. The same researchers also examined the cyclic behaviour of Nitinol under torsional loading. Similar to tensile cyclic loading, the accumulated residual

strain increased and the transformation stress during loading decreased with increasing cycle number.

Fewer researchers have examined the behaviour of Nitinol specimens under combined tension-torsion loading conditions. Most studies were usually driven by the interest in the development of constitutive models to describe the multi-mode deformation of the material. Experimental studies usually investigated three main loading patterns: simultaneous loading [76-79], triangular loading [76, 78, 79] and box loading [77-81] conditions. These are illustrated in Figure 3-22. Triangular loading, seen in Figure 3-22(b), is of interest to the present work as it allows the investigation of the torsional response in a pre-strained, predominantly transformed specimen.

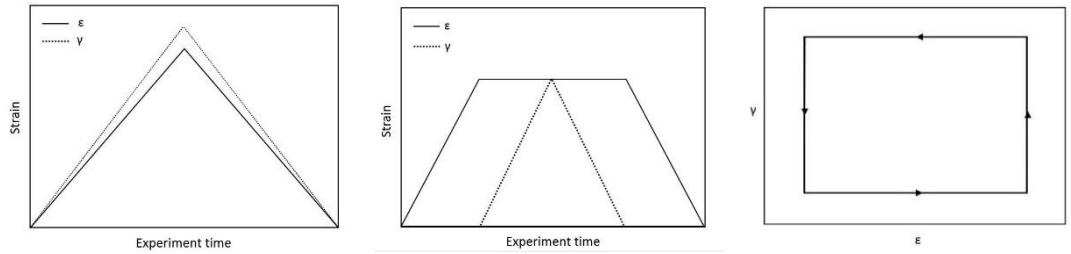

(a) (b) (c)

Figure 3-22 Simultaneous loading (a): Axial and rotational displacements are applied and removed on the specimen at the same time. Triangular loading (b): Upon loading tension is applied on the specimen followed by torsion. Subsequently, unloading proceeds in the reverse order. Box loading (c): Tension is followed by torsion during both loading and unloading. Note that the loading patterns (b) and (c) can also be applied with tension following torsion instead.

Mehrabi et al. [79] examined such a loading path of combined tension and torsion. Superelastic thin-wall tubes were employed in order to minimize the variation of shear strain in the specimen's cross-section. The A_f temperature of the material was 13°C and testing was conducted at a room temperature of 23°C. Axial displacement and rotation were measured and used to calculate stress-strain values. The strain rate of both loading modes was in the order of 10^{-3}/s. The tensile and shear stress-strain responses from these experiments are illustrated in Figures 3-23(a) and 3-23(b) respectively.

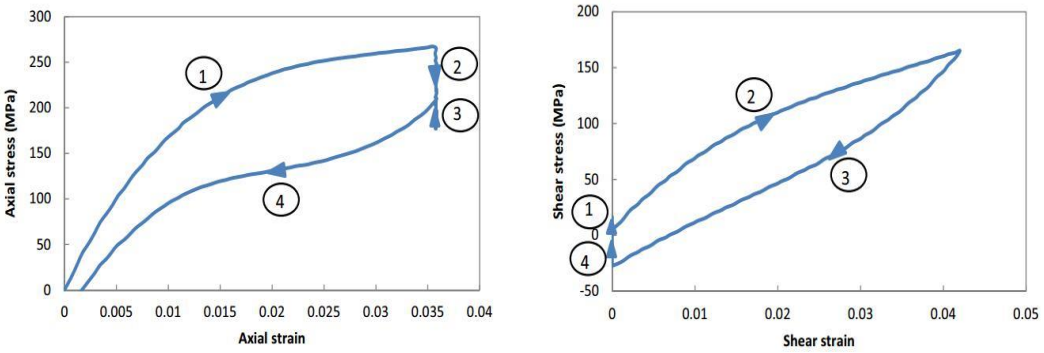

(a) (b)

Figure 3-23 Tensile (a) and torsional (b) stress-strain responses under triangular combined loading. Images adapted with permission from Mehrabi et al. [79].

In step 1, a tensile strain of 3.5% is applied on the specimen. Transformation from austenite to martensite is initiated and the tensile stress-strain curve exhibits a plateau-like transformation region upon loading. In step 2, the tensile displacement is kept constant while a 4.2% shear strain is applied. Note that different pre-tension levels were examined and results showed that at low tensile pre-strains, the overall behaviour is similar to pure torsion. However, here the modulus of the shear curve is reduced compared to a pure torsion test and hysteresis is decreased.

A small stress drop is also seen in the tensile response at the end of step 2. According to the authors, this behaviour is associated with further transformation of the material to martensite as strain increases. The elastic modulus is decreased causing the observed small stress drop. In step 3 the shear load is removed as the specimen is rotated back to its initial position while the tensile displacement is still constant. Consequently, a small increase is exhibited in the tensile load. A small amount of residual shear strain is recovered when the axial displacement becomes zero during step 4.

McNaney et al. [76] also came to the same conclusions when examining the mechanical behaviour of superelastic tubes subjected to combined tension-torsion under a triangular loading pattern. Andani and Elahinia [78] carried out similar experiments to evaluate a constitutive model for capturing the tension-torsion response of superelastic materials. Although distinct qualitative features of the

tension-torsion behaviour can often be identified, the complex microstructural mechanisms responsible for these are not yet fully understood.

3.3 Computational modelling of Nitinol materials

3.3.1 Phenomenological constitutive models

FEA is a computational method that is employed to obtain approximate solutions to a wide range of engineering problems. It has become an essential product development tool as it allows engineers to explore different design options, examine how a device performs and optimize their designs. FEA is widely used in the medical device industry to estimate the stress-strain state of devices.

Constitutive models are essentially mathematical equations intended to describe the principal features of a material behaviour in an idealized form [82]. The most common constitutive models are those that belong in the class of phenomenological models. They take into account only the macroscopic behaviour of the material and their advantage over other classes of constitutive models is that their material parameters are measurable quantities that can be identified by experimental tests. Therefore, these models are suitable for engineering practice and are implemented in FEA software.

Phenomenological constitutive models are usually built on macroscopic thermodynamics and on the common phase diagram of Nitinol that describes the experimentally identified transition regions from austenite to martensite and vice versa. The thermodynamic state of Nitinol can be determined by a combination of external and internal state variables. If the variables can be observed they are called external state variables otherwise they are called internal state variables [82].

A thermodynamic potential is a function that characterises a certain thermodynamic state of a material and depends on both external and internal state variables. The thermodynamic potentials commonly defined are: the specific internal

energy u, the specific enthalpy h, the specific Helmholtz free energy ψ and the specific Gibbs free energy G. All specific quantities are defined per unit mass and are represented usually be lower case letters. The exception is the Gibbs free energy, represented by a capital letter, according to standard notation in the literature of shape memory alloys [82].

When deriving constitutive equations, the most common choices for thermodynamic potentials are the Helmholtz and the Gibbs free energies. This is because the internal energy, which would appear as the first natural choice, depends on the entropy which is not an easily measured quantity. For the same reason the enthalpy is not commonly used either. The choice between the Helmholtz and Gibbs free energies depends on the state variable that can be controlled during experimental measurements, strain or stress.

Tanaka [83, 84], Liang and Rogers [85] and Brinson [86] were among the first to use such an approach to describe the behaviour of Nitinol materials. Using the martensitic fraction of the material as an internal variable and strain and temperature as control variables, a constitutive relation was derived. In this approach the second law of thermodynamics, expressed by the Clausius-Duhem inequality, was written in terms of the Helmholtz free energy. The uniaxial behaviour could then be described by:

$$\dot{\sigma} = E\dot{\varepsilon} + \Omega\dot{\xi} + \Theta\dot{T} \qquad \text{Equation 3-1}$$

with $$E = E_A + \xi(E_M - E_A) \qquad \text{Equation 3-2}$$

and $$\Theta = \Theta_A + \xi(\Theta_M - \Theta_A) \qquad \text{Equation 3-3}$$

In the above equations, σ and ε represent stress and strain respectively, E is the elastic modulus, Ω is the 'phase transformation tensor' and Θ is the coefficient of thermal expansion. The overdot denotes a time derivative and the subscripts A and M in Equation 3-2 and Equation 3-3 refer to the pure austenitic and martensitic phases of the material respectively.

Assuming the above material parameters constant, integration of Equation 3-1 results in the following constitutive relation:

$$\Delta\sigma = E\Delta\varepsilon + \Omega\Delta\xi + \Theta\Delta T \quad \text{Equation 3-4}$$

or $$\sigma - \sigma_0 = E(\varepsilon - \varepsilon_0) + \Omega(\xi - \xi_0) + \Theta(T - T_0) \quad \text{Equation 3-5}$$

where the subscript 0 refers to the initial state of the material.

Introducing the concept of the maximum residual strain ε^L allows the definition of a relationship between Ω and E. The maximum residual strain is a material constant which reflects the residual strain that is obtained when austenite is loaded to stress-induced martensite and then unloaded at temperature lower than A_S. Using initial conditions of $(\sigma_0 = \varepsilon_0 = \xi_0 = 0)$ and final conditions of $(\sigma = 0, \varepsilon = \varepsilon^L, \xi = 1)$ at $T = T_0$ $(M_s < T < A_s)$ in Equation 3-5, we get:

$$\Omega = -\varepsilon^L E \quad \text{Equation 3-6}$$

The essential difference in Brinson's work [86] is that the martensitic phase fraction was split into two parts: one part related to the martensite induced by stress and another part related to the martensite induced by temperature:

$$\xi = \xi_s + \xi_T \quad \text{Equation 3-7}$$

where ξ_s represents the fraction of the material that is stress-induced and ξ_T denotes the fraction of the material that has been transformed by temperature. This allowed the constitutive relation to be valid for both the supereleastic and shape-memory effects.

Different mathematical functions can be used to describe the evolution of the internal variable ξ during the phase transitions. The following equations, present the cosine functions developed by Liang and Rogers [85] and adapted by Brinson [86]. The transformation from austenite to martensite is described by Equation 3-8 and the transformation from martensite to austenite by Equation 3-9.

$$\xi = \frac{1-\xi_0}{2}\cos\left[a_M\left(T - M_f - \frac{\sigma}{C_M}\right)\right] + \frac{1+\xi_0}{2} \quad \text{Equation 3-8}$$

for $$C_M(T - M_s) < \sigma < C_M(T - M_f)$$

$$\xi = \frac{\xi_0}{2}\left\{cos\left[a_A\left(T - A_s - \frac{\sigma}{C_A}\right)\right] + 1\right\} \quad \text{Equation 3-9}$$

for $$C_A(T - A_f) < \sigma < C_A(T - A_s)$$

In the above equations, C_M and C_A are material properties that describe the relationship between the critical stress required to induce transformation and temperature. They are essentially the slopes of the stress-temperature plot, as shown in Figure 3-24. The austenite to martensite transformation is represented by C_M and the reverse transformation by C_A. The parameters a_M and a_A are defined in Equation 3-10 and Equation 3-11 respectively.

$$a_M = \frac{\pi}{M_s - M_f} \qquad \text{Equation 3-10}$$

$$a_A = \frac{\pi}{A_f - A_s} \qquad \text{Equation 3-11}$$

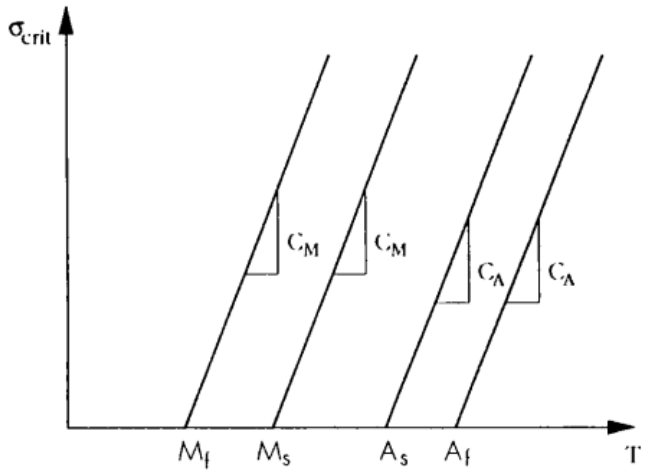

Figure 3-24 Relation between critical stresses for transformation and temperature. The slopes C_M and C_A here are equal. Image reproduced from Brinson [86].

A similar approach for the superelastic modelling of Nitinol was presented by Boyd and Lagoudas [87]. They proposed a constitutive model built on the Gibbs free energy that used the martensitic fraction of the material as an internal state variable. Prahlad and Chopra [88] compared the constitutive formulations of Tanaka, Liang-Rogers, Boyd-Lagoudas and Brinson and found that results from all models agreed well with the experimental tensile stress-strain response of a Nitinol wire. Brinson and Huang [89] also showed that different thermodynamics-based constitutive models can produce similar results when the same mathematical function that describes the evolution of the martensitic fraction (such as Equation 3-8) is adopted in all models.

3.3.2 Hysteresis, microplane and micromechanics constitutive models

Additionally, there are phenomenological constitutive models that describe the material behaviour without the introduction of internal state variables to represent the martensitic/austenitic fraction. These models were built directly on curve fitting experimental data, i.e. they sought to mathematically reproduce the experimental response of the material without considering any underlying events. The hysteresis models belong to this class. The aim of these models was to capture experimentally observed curves that involve high non-linearity and complex load-unload looping. Two main categories of hysteresis models can be found in the literature; models that were built on the Preisach algorithm and models that were developed on the Duhem-Madelung algorithm [90-93].

Another approach for the constitutive modelling of Nitinol is known as the microplane model. In this approach the macroscopic behavior is obtained by describing the material response along several planes of different orientations, called the microplanes [94]. A one-dimensional constitutive law on each micro-plane is sufficient to generate a macroscopic three-dimensional model when the multiaxial macroscopic behaviour is considered a superposition of the uniaxial responses within each mircroplane. There are two main formulations for microplane models [95]: the static constraint formulation, in which it is assumed that the stress vector acting on each microplane is the projection of the macroscopic stress tensor, and the kinematic constraint formulation in which the strain vector acting on each microplane is considered as the projection of the macroscopic strain tensor. Microplane models, initially introduced by Bazant [96], have been proposed by Brocca et al.[94] and Kadkhodaei et al. [95] among others.

Moreover there are microscopic models which are based on the micromechanics of a single crystal. These models mainly investigate the evolution of the martensitic phase transformation on a micro-scale. They sought to predict the response of the material by describing the crystallographic phenomena within the

material such as nucleation and propagation of transformation bands. The introduction of this modelling approach has been attributed to Patoor et al. [97]. Micromechanics models have also been developed by Fisher and Tanaka [98], Sun and Hwang [99, 100], Lexcellent et al. [101] and Huang and Brinson [102] among others. Most of these constitutive models however are more complicated than phenomenological models, therefore they are unsuitable for engineering practice.

3.3.3 Modelling Nitinol type materials with Abaqus

Due to the widespread use of FEA in the development of medical devices, computational analyses are also used nowadays as scientific evidence to support medical device submissions. Regulatory agencies, such as the Food and Drug Administration (FDA), require evidence of code verification activities that were performed to establish the correctness and fidelity of the numerical algorithms [103]. Code verification is accomplished through software quality assurance (SQA) and numerical code verification (NCV). SQA ensures the code is functioning correctly and produces repeatable results. NCV ensures the correct implementation of the numerical code, which is typically accomplished by performing benchmark problems.

This verification step is usually effortless for medical device manufacturers when a commercially available solver and its built-in material model database is used. Software developers comply with quality standards and they typically test their codes by running a wide range of benchmark problems, the results of which are available in the software documentation to reference. Code verification of a user-developed material model is time consuming and requires resources, which is why commercially available solvers such as Abaqus and Ansys (and their built-in Nitinol models) are so widely used by the medical device industry.

The superelastic model provided in Abaqus is intended for modelling Nitinol-type materials that exhibit a superelastic response [104-106]. It is based on the work of Auricchio and Taylor [107] who proposed one of the first phenomenological

models that included large deformations. The model is provided as a standard component in both Abaqus and Ansys, which are the most popular commercially available finite element solvers [108].

The superelastic model is based on the uniaxial behaviour shown in Figure 3-25 [105]. The material is considered to be in the austenite phase under zero loading conditions. Austenite is assumed to follow isotropic linear elasticity, characterised by the elastic modulus $\mathrm{E_A}$. Upon loading, the austenite phase starts transforming into martensite beyond a certain stress $\sigma_{\mathrm{L}}^{\mathrm{S}}$.

Martensite is also assumed to follow isotropic linear elasticity with a different elastic modulus $\mathrm{E_M}$. During unloading, martensite starts transforming back into austenite at a stress level $\sigma_{\mathrm{U}}^{\mathrm{S}}$, which is different from the stress at which the austenite to martensite transformation occurred. The transformation strain is fully recovered when the load is removed.

The parameters shown in Figure 3-25 are essentially the material data required by the model as inputs. These can be obtained from uniaxial tests and are explained in Table 3-1 [109]. The input parameters characterise the start and end of the phase transformation during loading and unloading. The different elastic properties of the austenite and martensite phases are accounted for.

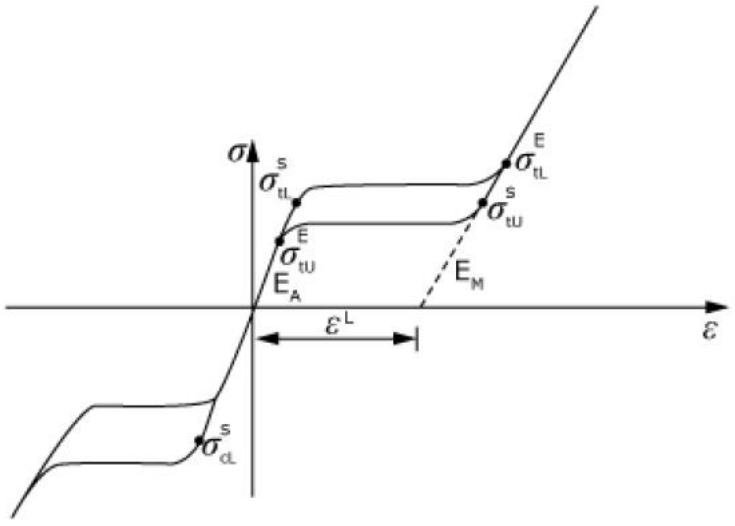

Figure 3-25 Stress-strain graph of the superelastic model implemented in Abaqus. Image reproduced from Simulia DS Support Knowledge Base [105].

Table 3-1 Input parameters of the Abaqus Nitinol model.

Input parameters		
No.	Symbol	Description
1	E_A	Austenite elasticity
2	ν_A	Austenite Poisson's ratio
3	E_M	Martensite elasticity
4	ν_M	Martensite Poisson's ratio
5	ε^L	Transformation strain
6	$\left(\frac{\delta\sigma}{\delta T}\right)_L$	$\delta\sigma/\delta T$ loading
7	σ_L^S	Start of transformation during loading
8	σ_L^E	End of transformation during loading
9	T_o	Reference temperature
10	$\left(\frac{\delta\sigma}{\delta T}\right)_U$	$\delta\sigma/\delta T$ unloading
11	σ_U^S	Start of transformation during unloading
12	σ_U^E	End of transformation during unloading
13	σ_{CL}^S	Start of transformation during loading in compression (as a positive value)
14	ε_V^L	Volumetric transformation strain
15	N_A	Number of annealings to be performed during the analysis
16	N_P	Number of stress-strain pairs to define the plastic curve
17	σ_{NP}^P, ε_{NP}	N number of stress-strain points in the plastic curve

Different behaviour in tension and compression can be specified. However, as seen in Figure 3-25 only one parameter is required: the start of transformation stress during loading in compression. This means that the rest of the transformation stresses in compression are estimated based on that value. The model also allows for user control of the volumetric transformation strain in case there is different behaviour in tension and in compression. Note that the slope of the elastic modulus of austenite is considered the same in tension and compression as shown in Figure 3-25.

Constitutive equations

During the phase transformation, the elastic properties of the material are calculated from the elastic constants of austenite and martensite, following the rule of mixtures [105]:

$$E = E_A + \xi_M (E_M - E_A) \qquad \text{Equation 3-12}$$

$$\nu = \nu_A + \xi_M (\nu_M - \nu_A) \qquad \text{Equation 3-13}$$

where ξ_M is the fraction of martensite, E_A is the elastic modulus of austenite, E_M is the elastic modulus of martensite, ν_A is the Poisson's ratio of austenite, and ν_M is the Poisson's ratio of martensite. Therefore, the deformation follows the elastic constants of austenite when the fraction of martensite is zero and follows the elastic constants of martensite when the fraction of martensite is one under full transformation.

The martensite and austenite fractions satisfy the following relation:

$$\xi_M + \xi_A = 1 \qquad \text{Equation 3-14}$$

The pressure dependency of the phase transformation is modelled by a Drucker-Prager loading function:

$$F = q + 3ap \qquad \text{Equation 3-15}$$

where $a = material\ parameter$

$$q = Mises\ equivalent\ stress$$

and $$p = \frac{Tr(\sigma)}{3} \qquad \text{Equation 3-16}$$

where $\sigma = stress\ tensor$

$Tr = trace\ operator$

The material parameter a characterizes the asymmetry between tension and compression. If tensile and compressive behaviours are the same, then $a = 0$. For a uniaxial tension-compression test, the parameter a is related to the initial value of austenite to martensite phase transformation in tension, σ_t^{AM} and compression, σ_c^{AM} as:

$$a = \frac{\sigma_c^{AM} - \sigma_t^{AM}}{\sigma_c^{AM} + \sigma_t^{AM}} \qquad \text{Equation 3-17}$$

The evolution of the martensite fraction is described by the following equations:

$$\dot{\xi_M} = \begin{cases} -H^{AM}(1-\xi_M)\dfrac{\dot{F}}{F - R_f^{AM}}, & for\ A \to M\ transformation \\ H^{MA}\xi_M \dfrac{\dot{F}}{F - R_f^{MA}}, & for\ M \to A\ transformation \end{cases} \qquad \text{Equation 3-18}$$

$$R_f^{AM} = \sigma_L^E(1 + a) \qquad \text{Equation 3-19}$$

$$R_f^{MA} = \sigma_U^E(1+a) \quad \text{Equation 3-20}$$

$$H^{AM} = \begin{cases} 1 \ \ if \ \ \begin{cases} R_s^{AM} < F < R_f^{AM} \\ \dot{F} > 0 \end{cases} \\ 0 \qquad\quad otherwise \end{cases} \quad \text{Equation 3-21}$$

$$H^{MA} = \begin{cases} 1 \ \ if \ \ \begin{cases} R_f^{MA} < F < R_s^{MA} \\ \dot{F} < 0 \end{cases} \\ 0 \qquad\quad otherwise \end{cases} \quad \text{Equation 3-22}$$

$$R_s^{AM} = \sigma_L^S(1+a) \quad \text{Equation 3-23}$$

$$R_s^{MA} = \sigma_U^S(1+a) \quad \text{Equation 3-24}$$

The stress-strain relationship can be written as:

$$\Delta\sigma = E\Delta\varepsilon \quad \text{Equation 3-25}$$

where strain is decomposed into two parts: a linear elastic component and a transformation component. The total strain increment $\Delta\varepsilon$, is then assumed to be the sum of the elastic strain increment $\Delta\varepsilon_{el}$, and the increment in transformation strain $\Delta\varepsilon_{tr}$:

$$\Delta\varepsilon = \Delta\varepsilon_{el} + \Delta\varepsilon_{tr} \quad \text{Equation 3-26}$$

where

$$\Delta\varepsilon_{tr} = \Delta\xi_M \varepsilon^L \frac{\partial F}{\partial \sigma} \quad \text{Equation 3-27}$$

Plasticity

If Nitinol is loaded in the post-transformation region, it exhibits a plastic behaviour. Plasticity effects were included in Abaqus for releases 6.10-1 and higher. The plasticity model for superelastic materials is based on the uniaxial stress-strain response shown in Figure 3-26 [110]. The deformation of martensite in the post-transformation region is assumed to follow an elastoplastic response, with elasticity characterized by the linear elastic model and the plastic behaviour represented by a Drucker-Prager model. In this case, the total strain increment $\Delta\varepsilon$ is assumed to be the

sum of the elastic strain increment $\Delta\varepsilon_{el}$, the increment in transformation strain $\Delta\varepsilon_{tr}$, and the increment in plastic strain $\Delta\varepsilon_{pl}$:

$$\Delta\varepsilon = \Delta\varepsilon_{el} + \Delta\varepsilon_{tr} + \Delta\varepsilon_{pl} \qquad \text{Equation 3-28}$$

Note that the unloading path of Figure 3-26 is the same as before (Figure 3-25). Although the material is loaded in the post-transformation region, the transformation stresses during unloading do not change. This means that the experimentally observed shift of the unload plateau towards lower stress levels is not accounted for. In addition, the modulus of martensite is the same in both loading and unloading.

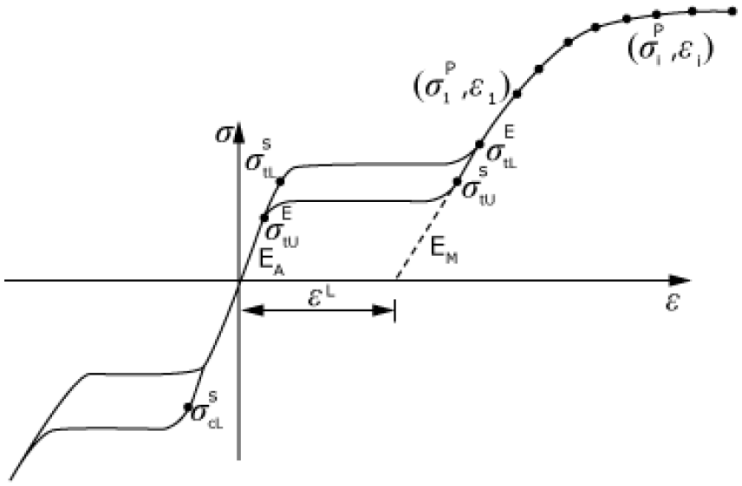

Figure 3-26 Stress-strain graph of the extended superelastic material model implemented in Abaqus that accounts for plastic deformation. Image reproduced from Simulia DS Support Knowledge Base [110].

Temperature effects

The material model also includes temperature effects [104]. The stress levels at which the transformation takes place at the reference temperature T_O are assumed to vary linearly with temperature, as shown in Figure 3-27. If the user specifies temperature-dependent material properties, i.e. if the sixth, ninth and tenth input parameters are non-zero, the solver shifts the transformation plateau by T_0 times the sixth, $\left(\frac{\delta\sigma}{\delta T}\right)_L$ and tenth, $\left(\frac{\delta\sigma}{\delta T}\right)_U$ input parameter value.

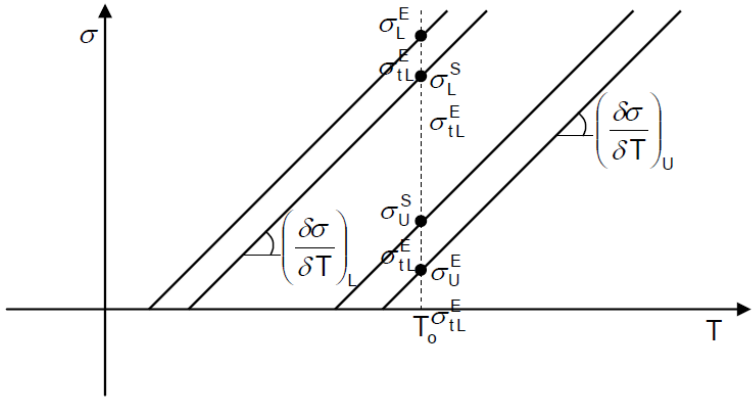

Figure 3-27 Stress-temperature properties of the Abaqus Nitinol model. Image reproduced from Simulia DS Support Knowledge Base [105].

Outputs

Apart from the default solver outputs, the material model also provides additional results in the form of solution-dependent state variables (SDVs), shown in Table 3-2 [109]. The model uses 24 SDVs in the superelastic case and 31 SDVs when plasticity is included. Note that true stresses and strains are used as inputs parameters as well as outputs values.

Table 3-2 Solution-dependent state variables of the Abaqus Nitinol model.

SDV	**Description**
SDV 1 – 6	Linear elastic strains
SDV 7 – 12	Transformation strains
SDV 19	Equivalent transformation strain
SDV 20	Volumetric transformation strain
SDV 21	Fraction of Martensite
SDV 22	Equivalent uniaxial tensile stress
SDV 23	Equivalent uniaxial tensile transformation strain
SDV 24	Equivalent uniaxial tensile total strain
SDV 25	Equivalent plastic strain
SDV 26 – 31	Plastic strains

Annealing

Abaqus provides the option of annealing the material during the analysis [104]. This is done by resetting the state variables to zero leading to a new strain-free element configuration. To enable this option the user needs to specify the number of

annealings (parameter N_A), followed by the step numbers in which the strain-free elements are required.

Strengths and limitations of the material model

The key strengths and limitations of the Abaqus Nitinol model are summarised below.

Strengths:

- Different elastic moduli and Poisson's ratios can be used for austenite and martensite. This allows the material model to differentiate the austenitic response from the martensitic response.
- The elastic properties are also calculated during the phase transformation of the material, based on the fraction of martensite.
- Four different transformation stresses are used as input parameters to describe all the start-finish transformations of the tensile superelastic behaviour of the material.
- The post-transformation loading behaviour can be described using additional stress-strain input parameters. During superelastic-plastic simulations, the material model can also estimate the plastic strain.

Limitations:

- The transformation stresses during unloading remain the same regardless of the strain level reached during loading. Therefore, the experimentally observed shift of the unload plateau towards lower stress levels is not accounted for, when modelling high-strain conditions.
- The elastic modulus of martensite remains the same during loading to, and unloading from the post-transformation region. However, this is not always correct according to experimental data.
- The behaviour of the material in compression is specified by only one transformation stress, while in tension four stress parameters are used. In compression, the other three transformation stresses are estimated by the

material model based on the material parameter a (Equation 3-17). Therefore, the predicted compression response may not be accurate, depending on the level of tension-compression asymmetry exhibited by the material.

- Since bending depends on both tension and compression, the bending response predicted by the material model is likely affected by the above limitation regarding compression modelling. Depending on the material's tension-compression asymmetry, the transformation forces/stresses in bending may not be estimated accurately, except for the start of transformation during loading.
- Additionally, due to Nitinol's asymmetric response the flexural modulus may not be equal to the elastic modulus in practice. Therefore, the flexural stiffness may not be estimated correctly, since the material model does not take into account the flexural modulus of austenite or martensite.
- The material model assumes that austenite and martensite follow isotropic linear elasticity and then uses the rule of mixtures to estimate the elastic moduli and Poisson's ratios during the phase transformation. Assuming that the same approach is used to estimate the shear stiffness, the torsional deformation of a solid wire specimen may not be predicted accurately since the strain distribution and thus the fraction of martensite, on the cross-section of a solid wire specimen subjected to torsion is non-uniform.

3.3.4 The Abaqus Nitinol model in the literature

The Abaqus Nitinol (Auricchio) model has been used in several studies. Gong and Pelton [111] demonstrated that the model can predict the mechanical behaviour of two medical devices including a self-expanding coronary stent. Simulation results showed good agreement with experiments in the superelastic range up to 5% strain. Kleinstreuer et al. [112] used Abaqus to investigate the impact of different Nitinol materials on the mechanical characteristics of a stent-graft. Load-deflection results

obtained through experimental testing agreed with simulations validating the finite element model. Other researchers have used the same superelastic model to study a Nitinol stent-mounted heart valve [113], to evaluate the performance of carotid artery stents [114], to investigate the bending behaviour of a commercially available AAA stent-graft [115] and to examine the deployment of a Nitinol self-expanding stent [116].

Gong et al. [117] used the Abaqus Nitinol model and the one developed by Qidwai and Lagoudas [118] to determine the radial force and crush characteristics of a self-expanding coronary stent. The Qidwai-Lagoudas model was implemented in Abaqus using user material subroutines and both constitutive models were calibrated based on the same uniaxial tensile data. The two material models produced very similar results regarding the load-deflection response of the stent, and represented the behaviour of the material well. Discrepancies existed at higher strain simulations since neither of the material models accounted for plasticity effects in their default configuration.

Zhu et al. [119] compared computationally the built-in Abaqus Nitinol model (Auricchio/Taylor), the model of Stebner and Brinson [120] and the constitutive model of Lagoudas et al. [121]. The last two models were implemented in Abaqus as user material subroutines. Subsequently, all three material models were calibrated from the same set of tensile data and were then used to simulate the responses of a single element cube in tension and a tube in torsion. The authors evaluated both the shape memory and the superelastic capabilities of each model.

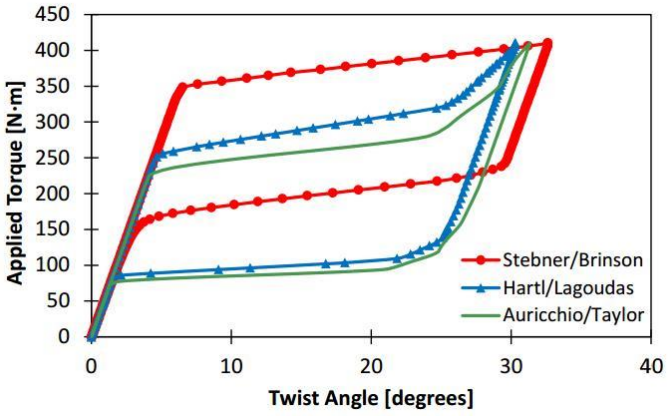

Figure 3-28 Comparison between torsional responses predicted by three different constitutive models. Image reproduced with permission from Zhu et al. [119].

The built-in Abaqus (Aurrichio) model is not recommended for shape memory effects, hence it was not included in that comparison. The predicted superelastic tensile responses differed only marginally among the three models. The torsional results however were different as seen in Figure 3-28. The Auricchio and Lagoudas models resulted in a similar response whereas the Stebner-Brinson one produced a curve which was shifted towards higher load levels. These results however were not compared with experimental data to fully assess the capabilities of each model.

Scalet et al. [122] compared the computational efficiency of the built-in Abaqus (Auricchio) and Lagoudas models mentioned above, by simulating the three-point bending of a rectangular superelastic Nitinol beam. The computer core runtime for the implicit analysis was approximately 45 minutes for both models although the Auricchio one displayed marginally greater wall-clock times. Note that in computing terms wall-clock time is the total elapsed time required for the completion of a task including all the necessary processes such as writing data to the disk. The core runtime for the explicit analysis was 20 and 22 hours for the Auricchio and Lagoudas models respectively. Core parallelization using 12 cores reduced the implicit and explicit computational times by factors of 6.2 and 8 for the Auricchio model respectively and by factors of 6 and 10 for the Lagoudas model.

3.4 Summary of literature findings and action plans

Many available studies in the literature have investigated the tensile properties of Nitinol. Its behaviour depends on the transformation temperatures and therefore on the crystallographic state during testing. Tensile transformation is non-homogeneous and proceeds with the localised formation of martensite domains. The material exhibits great temperature and strain rate sensitivity during mechanical testing. The unload plateau stresses seem load-path dependent, decreasing with increasing maximum strain beyond the superelastic plateau. However, there is little information on the post-transformation deformation and cycling of Nitinol wires, especially beyond 9% strain. Also, the temperature sensitivity of the material is unknown at such high strains.

Limited studies report on the compressive response of the material. Transformation under uniaxial compression is near homogeneous. Due to the inherent testing difficulties, a few different approaches have been adopted when examining superelastic specimens. One study was identified to subject Nitinol wire specimens to compression, but only to 4% strain.

The asymmetry between tension and compression also affects the bending behaviour. Research on the three-point bending properties of Nitinol wires, often addresses the needs of orthodontic applications. Studies usually examine the small deflection response within the superelastic range. No information has been published on the high load rate, large deflection bending of Nitinol wires, which is a loading condition often seen during the compaction of medical devices. Moreover, most studies examine the torsional response of Nitinol using only tube specimens at low deformation levels. To date, there is not a specific study available exploring the behaviour of Nitinol wires, which are the main structural component of stent-grafts, in tension, compression, bending and torsion.

Until recently, engineers and regulatory agencies were focused on investigating the axial and radial loading conditions of endovascular devices.

However, endovascular devices can be subjected to multiple loading modes during their life-cycle. Therefore, when developing test methods and designing a device, one should consider the different modes of deformation the device might be subjected to. For example, pulsatile loading caused by the cardiac cycle results in radial dilatation but can also produce non-radial deformation such as axial, bending and torsional. Depending on the device and the implantation site, non-radial deformation can also be induced by non-pulsatile loading such as loading from respiration or walking.

Regulatory agencies have also recognized the above and have updated their guidelines accordingly. The regulatory landscape of endovascular devices is now changing. The ISO 25539 standard already states that, if applicable, the structural integrity of an endovascular prosthesis should be evaluated under axial, bending and torsional loading [123]. Moreover, when submitting computational analyses reports it is required to confirm that the material model used for the simulations represents the behaviour of materials under the applicable loading mode.

FEA is often employed to assist the characterisation of a material and to replace costly and time-consuming experimental techniques. Researchers often focus their attention into developing new, mathematically advanced constitutive models to capture the behaviour of Nitinol materials. However, investing resources into the use of a new model not currently included in commercial finite element software is counter to common industry practice. Commercially available solvers and their built-in material model database are widely used by the medical device industry. This is because software developers comply with quality standards and the codes of commercial solvers are verified against benchmark problems.

The Nitinol model in Abaqus has been used in several academic and commercial studies. Despite being used for over a decade, its capabilities and limitations are not fully explored since there are no experimental data available for this purpose. Only a few studies compare FEA results to experimental data but none were identified to report on the accuracy of the model for representing the material across various loading modes. In addition, researchers often use input material

parameters that are published in other studies. There is also no available research that focuses on the elastic-plastic modelling capabilities of the material model.

The above findings confirm the initial objectives presented in Chapter 1. Therefore, the following Chapters seek to:

1. Produce a complete set of experimental data by testing medical grade Nitinol wires in tension, compression, bending and torsion.
    - Source wire specimens from a single manufacturer. The wires should be made from the same ingot type and they should all meet the same specifications. Their A_f must be lower than room temperature in order for the material to exhibit complete superelasticity at all testing conditions. The chemical composition of the specimens should also comply with the requirements of ASTM F2063.
    - Develop a new compression test method to allow the experimental characterisation of superelastic wire specimens.

2. Examine the mechanical behaviour of the material under high-strain deformation, in order to investigate the effect of stent-compaction on its properties.
    - Subject specimens to post-transformation deformation beyond 9% strain.
    - Perform multiple high-strain cycles to simulate the number of compaction attempts commonly found in industry.
    - Examine the post-transformation temperature sensitivity.
    - Examine the strain range within which the unload plateau stresses remains unaltered.
    - Investigate the load rate sensitivity of the bending response beyond the superelastic range.

3. Assess the capabilities and limitations of the Abaqus Nitinol model.

- Identify the relevant constitutive parameters from experimental data with minimal assumptions.
- Develop a methodology to simulate the mechanical tests.
- Investigate the model's superelastic-plastic modelling capabilities for capturing high-strain post-transformation loading conditions.

Chapter 4 Methodology of Experimental and Computational Procedures

This chapter describes the methods developed to accomplish the objectives of the present work. Experimental and computational procedures are explained in detail in the following sections. The strengths and limitations of the methodology adopted herein are discussed in Chapter 7.

4.1 Experimental methods

4.1.1 Nitinol wire specimens

Mechanical testing in the present study was conducted using superelastic Nitinol wires manufactured by Fort Wayne Metals (FWM). The commercial name of the material is Nitinol #1 super-elastic straight annealed (NiTi#1-SE) [124]. It is a medical grade Nitinol, suitable for use in applications such as stents, guidewires and orthodontic files. Specimens were sourced in the following diameters: 0.22mm, 0.45mm, 1mm, 1.8mm and 2.4mm.

Additionally, another type of FWM Nitinol wire was briefly examined. It is named ultra-stiff Nitinol (USN®) because it exhibits greater stiffness in the austenitic modulus region upon loading [125]. It is recommended by the manufacturer for applications such as guidewires that require increased initial resistance to deformation. USN® wires were made from the same FWM lot type of Nitinol as their NiTi#1-SE counterparts. Specimens with a diameter of 0.22mm were used to investigate potential benefits of using such materials in the design of stents.

The wire specimens used in this work are summarised in Table 4-1 below. The table includes the dimensions, the diameter tolerance (and the tolerance as a percentage of the nominal diameter), the condition and surface finish, as well as the

final 'active' A_f temperature of the Nitinol wires. The details of the cold work and heat treatment are not disclosed by the wire supplier for neither Nitinol type. A chemical etch finish was applied onto the wires to remove any oxide layer and leave a smooth surface. Note that the standard NiTi#1-SE material was predominantly used in this study and examined across all loading modes. Data involving the USN® material are only presented in section 5.5. The rest of the results including all computational data, refer only to the standard Nitinol material.

Table 4-1 Properties of the Nitinol wire specimens.

Wire Properties						
Dimensions	2.4mm x 46mm	1.8mm x 36mm	1.0mm x 300mm	0.22mm	0.45mm	0.22mm
Diameter Tolerance	±0.025mm (1.04%)	±0.025mm (1.38%)	±0.02mm (2.00%)	±0.0076mm (3.45%)	±0.0076mm (1.68%)	±0.0075mm (3.41%)
Condition	Straight Annealed	Straight Annealed	Straight Annealed	Straight Annealed	Straight Annealed	USN®
Surface finish	Etched	Etched	Etched	Etched	Etched	Etched
Lot Type	NiTi#1	NiTi#1	NiTi#1	NiTi#1	NiTi#1	NiTi#1
Active A_f (BFR)	2°C	13.60°C	14.10°C	13.50°C	14.3°C	11.90°C

The A_f temperature of the wires was measured by FWM using the bend and free recovery (BFR) technique. While DSC is used for characterising raw materials (ingots), the active A_f temperature of finished products is usually specified by a BFR test according to the ASTM standard test method for determination of transformation temperature of Nitinol alloys [126]. During this test, a sample is cooled into the martensitic region, deformed and then heated. The motion (and shape recovery) of the specimen is measured during heating and plotted versus the specimen temperature. The graph is then used to determine the A_f temperature at which shape recovery is complete. The FDA also recommends using the BFR method to identify the A_f temperature of components used in devices that are expected to be load bearing, since this method incorporates deformation [127].

The chemical composition of all the wires is stated to meet or exceed that set out by ASTM F2063 [39]. According to the standard, the percentage of Nickel in the alloy (per weight) should be between 54.5% and 57.0%, impurities should be lower

than those stated in Table 4-2, while the Titanium content should comprise the remaining balance.

Table 4-2 Nitinol chemical composition requirements according to ASTM F2063 [39]. The amount of Titanium is approximately equal to the difference between 100 % and the sum percentage of the other elements.

Element	Weight %
Nickel	54.5 - 57.0
Carbon	< 0.04
Cobalt	< 0.05
Copper	< 0.01
Chromium	< 0.01
Hydrogen	< 0.005
Iron	< 0.05
Niobium	< 0.025
Nitrogen	< 0.005
Oxygen	<0.04
Titanium	Balance

A number of tensile stress-strain characteristics are specified as basic requirements by Terumo Aortic for all Nitinol wires and were also used in the present work. These include: load plateau >560MPa; unload plateau >250MPa; permanent set after 8% strain <0.5%; elongation to failure >10% and ultimate tensile strength >1300MPa. Three wire samples were tested by the supplier from each batch according to the ASTM F2516-14 [128] guidelines and results were reported in each certificate of compliance (CoC). These results are reproduced here in Tables 4-3 to 4-8. For each sample the following parameters were measured: wire diameter, upper plateau stress (UPS), lower plateau stress (LPS), permanent set after unloading from 8% strain (Perm Set), ultimate tensile stress (UTS), uniform elongation (El_u) and elongation at failure (El_{break}). Note that the 2.4mm wire did not meet the required specifications in terms of LPS, permanent set and UTS. Therefore, this type of specimen was only used to identify qualitative features of the torsional response of the material as will be discussed in the following sections.

Only a single test was conducted with each specimen to avoid any load-path dependence effects. There are no clear recommendations on sample size according to Nitinol testing standards. In tension, the ASTM-F2516-14 [128] standard requires

three experiments for a given wire diameter and test method. This recommendation was also adopted for the rest of the experimental methods although since testing was carried out for characterisation purposes, sample size was usually decided on a case by case basis.

Table 4-3 Tensile results supplied with the 2.4mm diameter wire CoC.

Test at 37°C	Sample	Diameter	UPS	LPS	Perm Set	UTS	El_u	El_{break}
	1	2.414	629	218	0.72	1090.1	20.2	20.7
	2	2.414	649	226	0.66	1107.2	20.1	20.7
	3	2.414	633	234	0.64	1100.3	18.6	19.4
Mean		2.414	637.000	226.000	0.673	1099.200	19.633	20.267
Standard Deviation		0.000	10.583	8.000	0.042	8.603	0.896	0.751

Table 4-4 Tensile results supplied with the 1.8mm diameter wire CoC.

Test at 37°C	Sample	Diameter	UPS	LPS	Perm Set	UTS	El_u	El_{break}
	1	1.796	630	279	0.23	1421.6	18.4	18.6
	2	1.796	630	287	0.42	1432.5	20.1	20.3
	3	1.796	636	271	0.37	1420.9	19.3	19.4
Mean		1.796	632.000	279.000	0.340	1425.000	19.267	19.433
Standard Deviation		0.000	3.464	8.000	0.098	6.505	0.850	0.850

Table 4-5 Tensile results supplied with the 1mm diameter wire CoC.

Test at 37°C	Sample	Diameter	UPS	LPS	Perm Set	UTS	El_u	El_{break}
	1	0.999	638	304	0.45	1437.9	20.2	20.3
	2	0.999	648	307	0.35	1437.4	20.3	20.7
	3	0.999	668	325	0.22	1424.2	18.9	19.0
Mean		0.999	651.333	312.000	0.340	1433.167	19.800	20.000
Standard Deviation		0.000	15.275	11.358	0.115	7.769	0.781	0.889

Table 4-6 Tensile results supplied with the 0.45mm diameter wire CoC.

Test at 37°C	Sample	Diameter	UPS	LPS	Perm Set	UTS	El_u	El_{break}
	1	0.451	718	352	0.13	1496.0	17.5	17.9
	2	0.451	697	338	0.14	1496.7	17.1	17.3
	3	0.451	708	342	0.13	1497.3	16.9	17.0
Mean		0.451	707.667	344.000	0.133	1496.667	17.167	17.400
Standard Deviation		0.000	10.504	7.211	0.006	0.651	0.306	0.458

Table 4-7 Tensile results supplied with the 0.22mm diameter wire CoC.

Test at 37°C	Sample	Diameter	UPS	LPS	Perm Set	UTS	El_u	El_{break}
USN®	1	0.221	714	310	0.16	1363.4	14.4	14.4
	2	0.221	659	316	0.13	1370.3	14.3	14.3
	3	0.221	712	282	0.17	1363.6	14.4	14.4
Mean		0.221	695.000	302.667	0.153	1365.767	14.367	14.367
Standard Deviation		0.000	31.193	18.148	0.021	3.927	0.058	0.058

Table 4-8 Tensile results supplied with the 0.22mm diameter USN® wire CoC.

Test at 37°C	Sample	Diameter	UPS	LPS	Perm Set	UTS	El_u	El_{break}
	1	0.217	664	316	0.06	1567.6	15.5	15.5
	2	0.218	664	317	0.08	1579.3	15.4	15.4
	3	0.217	658	332	0.06	1563.2	15.4	15.4
Mean		0.217	662.000	321.667	0.067	1570.033	15.433	15.433
Standard Deviation		0.001	3.464	8.963	0.012	8.321	0.058	0.058

4.1.2 Tensile testing

Overview

Tensile testing was performed using the Instron 5965 testing machine and the Instron software Bluehill 3. The machine was fitted with a 2KN load cell which recorded the load carried by the wire specimens. These had a diameter of 0.22mm, 0.45mm and 1mm.

The thicker 1mm diameter wire was clamped by pneumatic side action grips. The fine wires were wrapped around horn-like pneumatic cord grips which can be seen in Figure 4-6. Due to their design, these grips make the transition from the free stressed region of the specimen to the clamped region gradually, while distributing the gripping force evenly. Thus, breakage near the jaws is minimized and specimen slippage is avoided.

Testing was conducted at room temperature, which was approximately 22°C, at 37°C and at 55°C. The Instron 3119-600 environmental chamber was employed for testing at 37°C and 55°C. Its temperature stability is ±2°C [129]. In addition, the probe of a calibrated external thermometer was placed in the temperature chamber to monitor the temperature within ±0.1°C increments. Sufficient time, approximately 15 minutes, was required in order for the temperature to stabilise before testing.

Measurement of strain based on crosshead movement is usually inaccurate in the strain range of interest. Moreover, using clip-on extensometers on wires can induce further testing difficulties [130]. Therefore, in the present study the Instron AVE2 non-contact video extensometer was employed to allow accurate testing up to high strains. Calibration was performed prior to the experiments using the Instron calibration plate seen in Figure 4-3.

The extensometer measured strain by tracking the displacement of 6mm round white markers placed on the wires, as seen in Figure 4-8. The distance between the markers corresponds to the gauge length of the extensometer. Before the video extensometer is configured, one needs to take into account the field of view considerations shown in Figure 4-1. The likely extension of the test specimen must be estimated in order to select the gauge length. Considering the anticipated significant extension due to the requirement of testing at high post-transformation strains, a gauge length of approximately 50mm was used here. This ensured that the markers were within the calibrated field of view at all times during the experiment.

Test plan

Two types of tensile tests were performed: Type I to derive key stress-strain parameters for the constitutive model that was used for FEA, and Type II to investigate the high-strain post-transformation behaviour of the material. During the first, specimens were deformed to 6% engineering strain, unloaded to 7MPa of stress, and then pulled to failure as described in the ASTM F2516-14 [128] standard.

During Type II tensile testing, three consecutive load-unload cycles were performed up to high strains in the post-transformation plastic region. Three cycles

were selected in order to represent the three potential attempts to compact the Anaconda stent-graft. Type II testing was conducted using the standard NiTi#1-SE 0.22mm and the USN® 0.22mm wires since this is the most common wire diameter used in the manufacture of the ring-stents. Following the principal investigation, additional single load-unload cycles to high strains were performed to complement the Type II results. Details of the test plan and the loading conditions are summarised in Table 4-9.

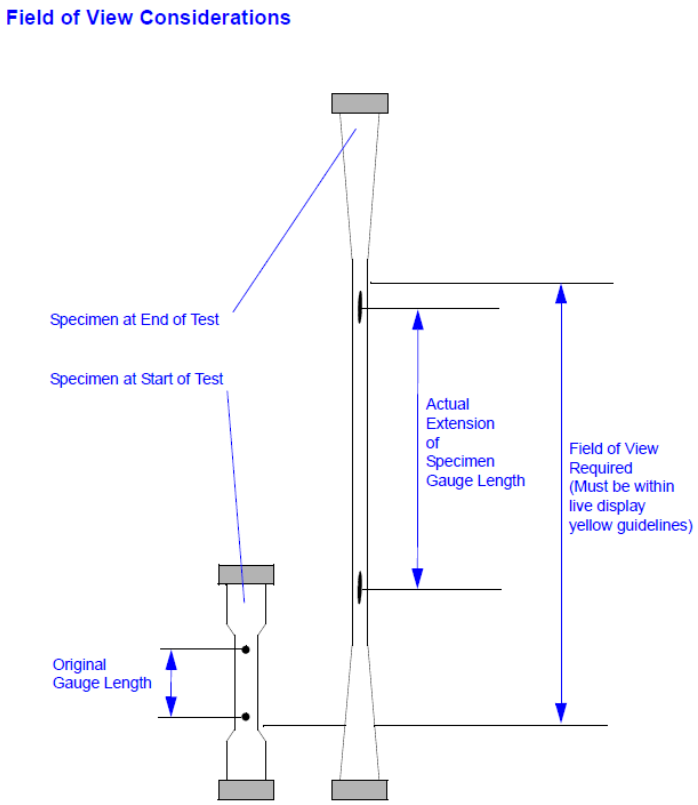

Figure 4-1 Field of view considerations when using a video extensometer to measure strain. Image reproduced from the Instron AVE manual [131].

The load rates used during the tensile tests are presented in Table 4-10. These were set according to the ASTM F2516-14 standard recommendations for the first cycle of Type I tests and for Type II tests. The resulting strain rates were in the order of 10^{-4}/s, thus slow enough to consider the experiment nearly isothermal. For the second cycle of Type I tests (i.e. loading to failure), a faster strain rate in the order of 10^{-3}/s is allowed according to the testing standard. However, in the present work the

rate was limited to only twice the magnitude of that used in the first cycle in order to avoid unnecessary rate effects.

Table 4-9 Loading conditions during tensile testing.

Specimen diameter (mm)	Loading conditions	Engineering Strain (%)	Temperature (°C)	Grip type
1	Type I - Load to 6% eng. strain, unload and then load to failure	N/A	22, 37	Pneumatic side action grips
0.45	Type I - Load to 6% eng. strain, unload and then load to failure	N/A	22, 37, 55	Pneumatic side action grips, Horn-like pneumatic cord grips
0.22	Type I - Load to 6% eng. strain, unload and then load to failure	N/A	22, 37	Horn-like pneumatic cord grips
	Type II - Load-unload for 3 cycles	7, 8, 9, 9.5, 10, 10.5, 11, 11.5, 12	37	
	Single load-unload cycle	10, 10.5, 11		
	Single load-unload cycle	9.5, 10, 10.5	22	
0.22 USN®	Type I - Load to 6% eng. strain, unload and then load to failure	N/A	37	Horn-like pneumatic cord grips
	Type II - Load-unload for 3 cycles	7, 8, 9, 10, 11		
	Single load-unload cycle	10.5, 11, 11.5, 12		

Table 4-10 Load rates used during the two types of tensile loading.

Wire diameter	Crosshead speed in mm/min per mm of initial length between grips	
	Type I - First cycle (load to 6 % strain and unload) and Type II	Type I - Second cycle (load to failure)
$0.2 < d \leq 0.5$	0.04	0.08
$0.5 < d \leq 2.5$	0.02	0.04

Test method

- The video extensometer is mounted onto the environmental chamber door as seen in Figure 4-2.

Figure 4-2 Video extensometer mounted on the environmental chamber door

- The calibration plate is gripped using the bottom side action pneumatic grip, as seen in Figure 4-3. The pneumatic grips are operated using the foot-pedals of the machine. Prior to that, any attached fixtures in the upper end of the environmental chamber are removed to ensure there is adequate space.
- The calibration settings of the video extensometer can be accessed in the Bluehill software by selecting the 'Calibrate' button. At this step, it is checked that the calibration plate is correctly aligned in the grips (black dot columns vertical), as seen in Figure 4-4. In addition, it is checked that the focus is good (shown by the green bars in Figure 4-4). The desired field of view for calibration is selecting by clicking and dragging on the window. Note that the calibration step can be skipped if a calibration has already been performed and saved on the system with no subsequent changes to the video extensometer.

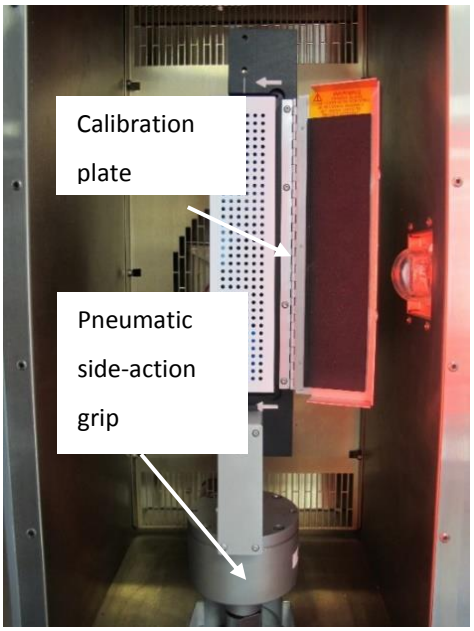

Figure 4-3 Calibration plate mounted on a pneumatic side-action grip inside the environmental chamber.

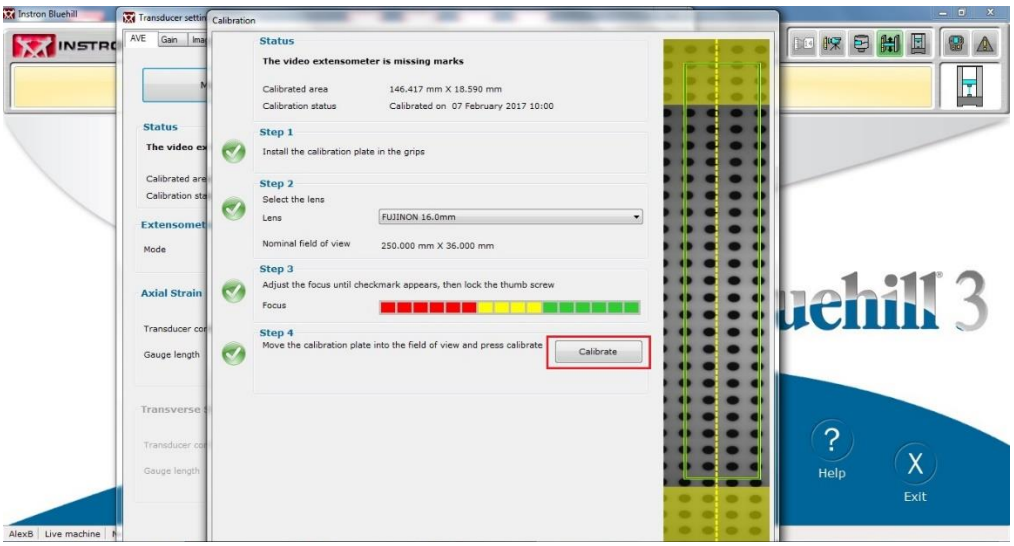

Figure 4-4 Video extensometer calibration window.

- The 2kN load cell is installed for testing (Figure 4-5(a)). The upper pneumatic cord grip is attached to the load cell using the attachment rod and then secured using the suitable pins (Figure 4-5(b)). Note: Although the cord grips are shown here, the process for attaching the side-action grips is exactly the same. The bottom pneumatic horn-like grip is attached to the frame using the

extension adapters (Figure 4-5(d)). The air hoses are then attached to both grips. The Instron machine prior to testing should look like Figure 4-6.

(a) (b)

(c) (d)

Figure 4-5 The 2kN load cell used for testing (a). Connection of the attachment rod to the load cell (b) and to the upper grip (c). Connection of the bottom grip to the frame using the extension adapters (d).

- Using the console soft keys, the upper grip is moved towards the bottom one until the two grips are in a just touching position. The extension is zeroed and then the upper grip is moved upwards by 110 mm. This gives an effective gauge length of 150mm when the wire is attached to the cord grips, as specified in ASTM F2516-14 [128]. Note that if the side action grips are used, that distance is set to 150mm from the beginning. The extension is zeroed again.
- The probe of the external thermometer is placed into the environmental chamber.

- Approximately 350mm of the Nitinol wire is cut using pliers. The wire is then wrapped around the upper horn-like grip first which is closed using the foot-pedals. The wire is pulled gently to remove the slack and then it is wrapped around the bottom grip.

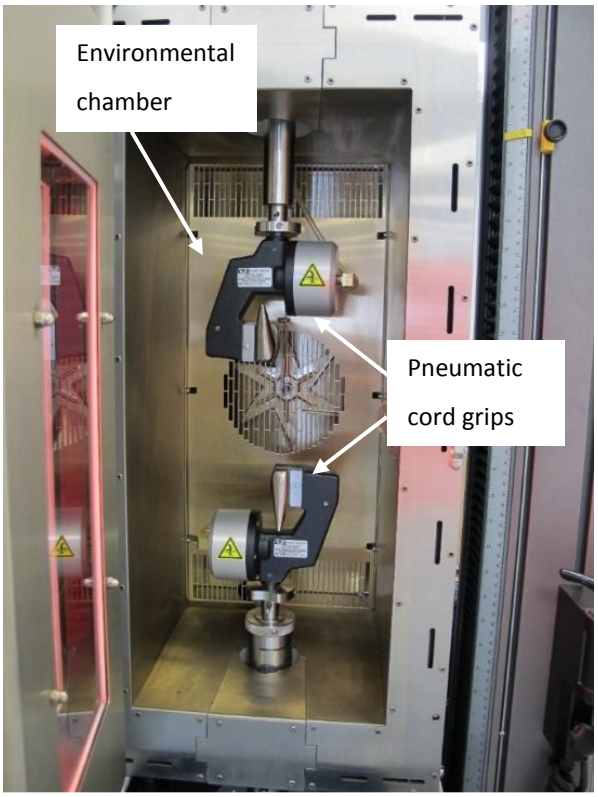

Figure 4-6 The environmental chamber and grips ready for specimen mounting and testing.

- A hole-puncher is used to cut through white labelling sticker in order to create small round markers which are 6mm in diameter, as seen in Figure 4-7.

(a)

(b)

Figure 4-7 Creating the video extensometer markers by punching through labelling sticker (a). The resulting round white markers are approximately 6mm in diameter (b).

- The markers are placed onto the wire at a distance that defines the video extensometer gauge length. The markers shown in Figure 4-8 are approximately 50mm apart.

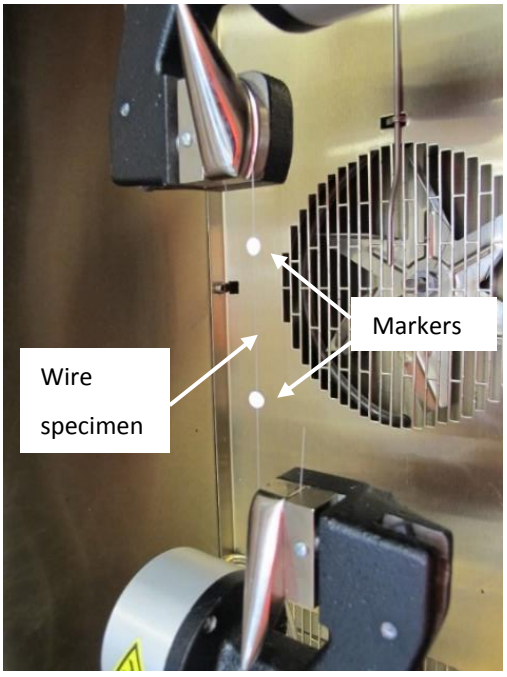

Figure 4-8 Placement of the video extensometer markers onto the wire specimen.

- Using a precision tip and the Loctite 4161 super-glue, a small amount of glue is placed onto the back of each marker to secure it onto the wire specimen.
- The fan, heating element and light of the environmental chamber are switched on and the desired temperature is selected.
- The 'Method' section of the Bluehill software (Figure 4-9) is then opened to load an existing test method or create a new one. The key features are mentioned here:
    - If stress output is required as raw data, the correct wire diameter must be entered in order for the software to calculate the tensile stress during testing. This is done via the 'Specimen' tab.
    - Under the 'Exports' tab, the 'Export raw data' option must be selected.

- The test parameters are then specified in the ‘Test Control’ tab.
- The ‘Strain 1’ option is selected under the ‘Strain’ tab. This means that strain will be measured using the video extensometer and not the crosshead displacement.
- The necessary ‘Absolute Ramp’ steps for the test are created under the ‘Test’ tab.
- The strain rate recommendations of ASTM-F2516 [128] are used to calculate the extension rates. For the 0.22mm diameter wire, this means an initial extension rate of 6mm/min.

- The temperature is checked to ensure that is stable (which takes approximately 15 minutes) and then the test is started.
- When the test finishes, the raw data file is saved when the ‘Finish’ button is pressed.

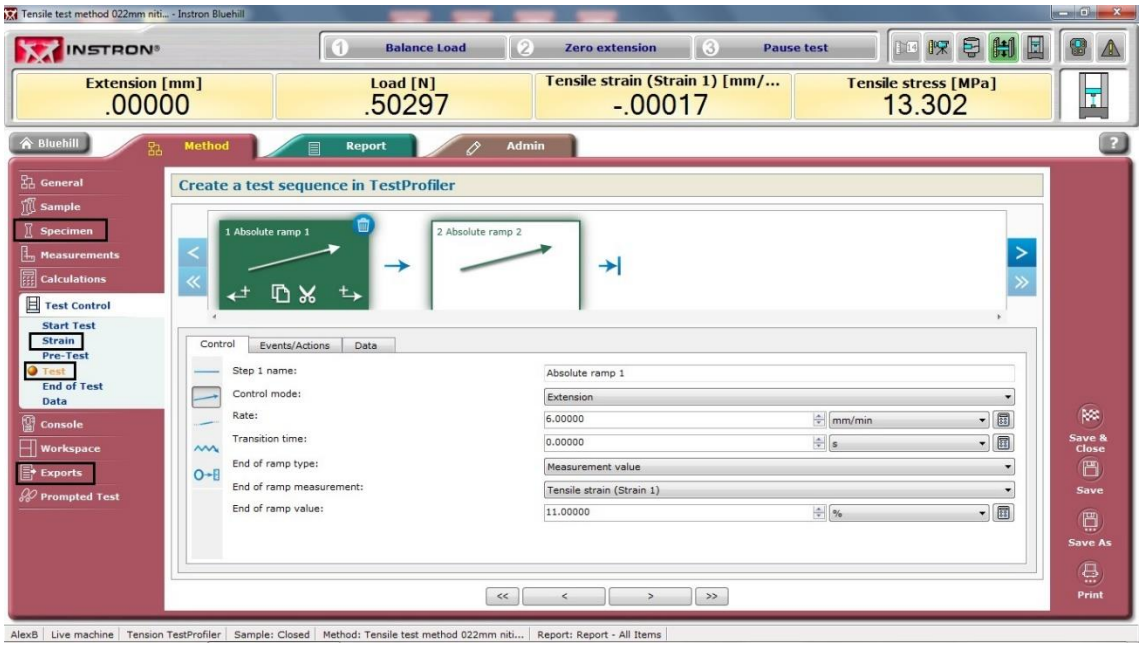

Figure 4-9 Method section of the Bluehill software with key tabs and options highlighted such as ‘Specimen’, ‘Strain’, ‘Test’ and ‘Export’.

Output

Load, extension, engineering stress and engineering strain were recorded as raw data in a comma separated variable (CSV) file. The file was later opened with

Microsoft Excel to process and plot the data. In the following chapter, all tensile results are presented in the form of true stress-strain graphs. True values were converted from the raw data using Equation 4-1 and Equation 4-2 seen below. The variables σ, ε, σ_τ and ε_τ represent the engineering stress, engineering strain, true stress and true strain respectively.

$$\sigma_\tau = \sigma(1 + \varepsilon) \qquad \text{Equation 4-1}$$

$$\varepsilon_\tau = \ln(1 + \varepsilon) \qquad \text{Equation 4-2}$$

The true stress-strain graphs were also used for calculating the strain energy density of the material. This served as an additional comparison between tension and compression and between experimental and computational results. When a material is subjected to a load, it absorbs energy. The area under the loading part of the stress-strain curve up to a given value of strain is then the strain energy per unit volume (U) absorbed by the material. The area can be calculated by integrating the curve within its limits as seen in Figure 4-10. The strain energy per unit volume, also referred to as the strain energy density is usually expressed in joules per cubic metre.

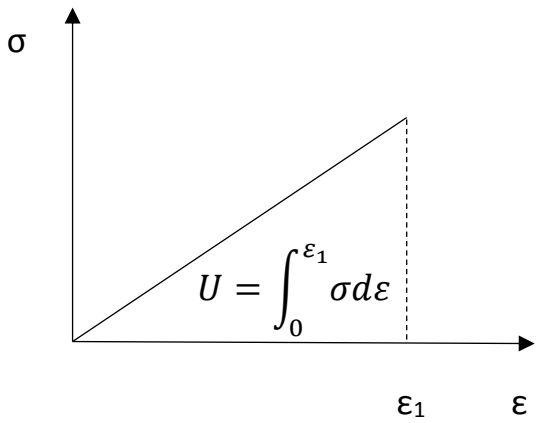

Figure 4-10 The area under a stress-strain curve up to a given value of strain is the strain energy per unit volume absorbed by the material and can be calculated by integrating the curve within its limits.

When the load is removed, the area under the unloading part of the stress-strain curve represents the energy released by the material. In the elastic range,

these two areas are equal and no energy is absorbed. If however the material is loaded into the plastic range or if the material exhibits hysteresis, i.e. loading and unloading do not follow the same path on the curve, the energy is not fully recovered. The energy loss is then the area under the stress-strain loop. In the present work the strain energy density was approximated from the raw data using the trapezoidal 'Riemann' summation method in Microsoft Excel.

4.1.3 Compression testing

Overview

Compression testing was conducted using a Deben Microtest miniature compression stage. The machine was equipped with a 2kN load cell which recorded the exhibited compressive force via the Deben Microtest software V6.0.113. The testing apparatus was mounted on a Hitachi S-3700N scanning electron microscope (SEM) seen in Figure 4-11(a), which served as a means of monitoring the real time specimen deformation through magnification.

Compressive specimens were manufactured by electro-discharge machining (EDM) the 1mm Nitinol wire into small specimens with a final length of 3mm. These were mounted onto the machine horizontally between a pair of compressive plattens as seen in Figure 4-11(b). Prior to testing, a small quantity of high load capacity lubricant was applied on the ends of the specimens to minimize any friction effects. A series of preliminary tests revealed an insufficient hardness of the initially used plattens. Visual examination showed indentation marks on the platten surface seen in Figure 4-12(a). Therefore, hardened plattens with polished faces (Figure 4-12(b)) were made to characterise the material in compression.

Test plan

Testing was conducted at room temperature under displacement control. Single load-unload cycles were performed up to 0.18mm displacement. The maximum displacement was chosen because it corresponds to 6% engineering strain

for the 3mm long specimen. A crosshead speed of 0.1mm/min was selected corresponding to a strain rate of 5.5 x 10^{-4}/s. The test method for compression is shown in Table 4-11.

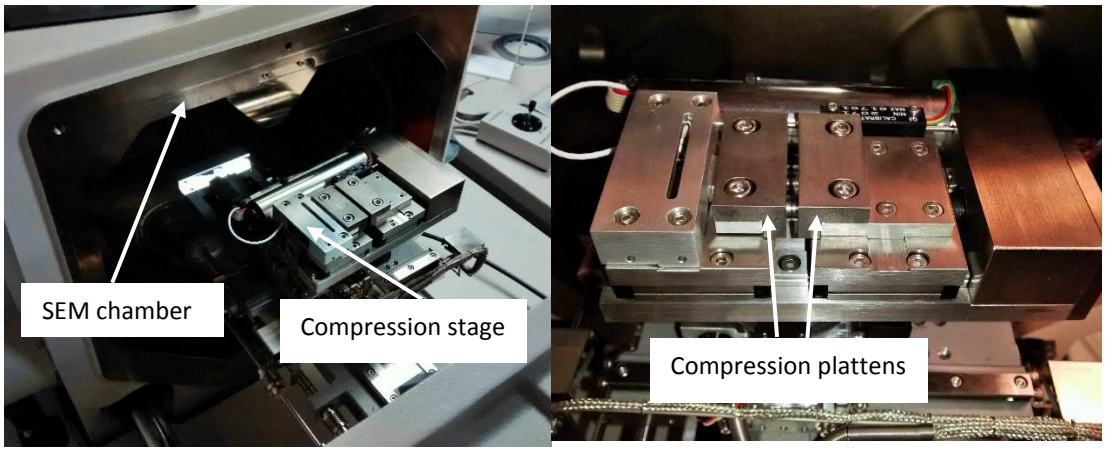

(a) (b)

Figure 4-11 The Deben Microtest machine mounted onto the SEM (a). Close-up image of the compression stage (b).

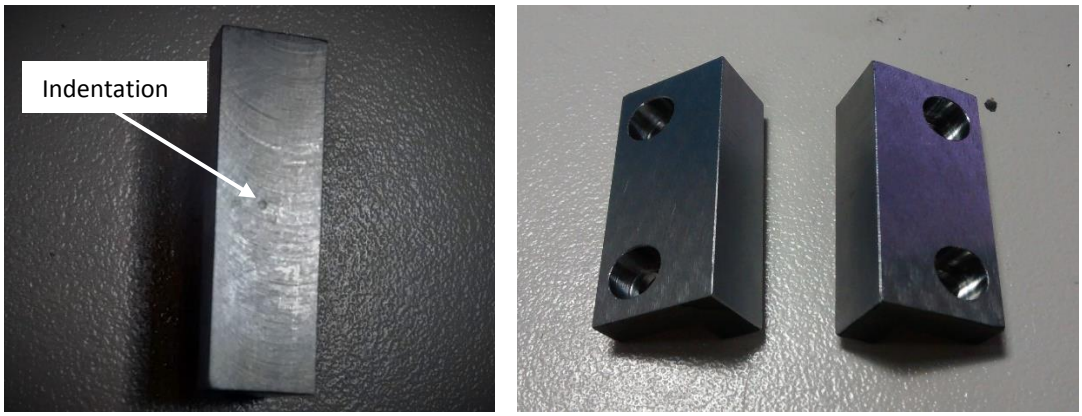

(a) (b)

Figure 4-12 Visual examination of the surface of the initial plattens showed that the specimen caused indentations (a). Hardened plattens with polished faces were then used in the experiments (b).

Table 4-11 Test method used for compression testing.

Specimen diameter (mm)	Loading description	Displacement (mm)	Crosshead speed (mm/min)	Strain rate (sec^{-1})
1	Single load-unload cycle	0.06, 0.09, 0.12, 0.15, 0.18	0.1	5.5 x 10^{-4}

Test method

- If the SEM is not required during testing, the experiment should be conducted outside the chamber for convenience. The stage can even be removed from the SEM and placed on the bench.
- The plattens are mounted and secured on the testing stage.
- The Deben Microtest software is launched (Figure 4-14). Using the 'Open jaws' and/or 'Close jaws' keys within the software, the plattens are moved to approximately 4mm apart. This gives just enough space to work with, while placing the specimen in-between the plattens.
- The specimen is gripped using high precision 'Dumont' tweezers (Figure 4-13(b)) and its two ends are lubricated with the high capacity 'Molykote BR2 plus' lubricant.
- Using the tweezers, the specimen is carefully placed horizontally in-between the two plattens (Figure 4-13(a)). Using the software keys again, the jaws are closed until they are in a 'just touching' position with the specimen. The specimen is inspected to ensure that it is aligned correctly and the extension is then zeroed by clicking on the 'Clear data' option in the Deben Microtest software.

(a) (b)

Figure 4-13 The compressive specimen was mounted horizontally between the plattens (a) using high precision tweezers (b).

- In the Deben software, under the 'Setup' options, the loading 'Mode' is set to 'Compression'.

- The load-unload sequence is specified by selecting the ‘Cyclic set’ option. A new window pops up which prompt the user to choose a control ‘Mode’, maximum and minimum values of loading and a number of cycles. The control ‘Mode’ is set to ‘Extension’ since the experiments are conducted under displacement control. The number of cycles is typically set to one for single load-unload tests. The minimum value of extension is zero while the maximum value can vary depending on the test.
- The crosshead speed is adjusted by clicking on the ‘MotorSpeed’ options. The load cell reading is zeroed by clicking on ‘Set Loadcell zero offset’ under the ‘Tools’ options.
- Experiments are conducted in the Advanced Materials Research Laboratory (AMRL) where the room temperature (approximately 22°C) is controlled by an air-conditioning system.
- The test is started and when the loading sequence is finished, the results are automatically saved in the specified work folder.

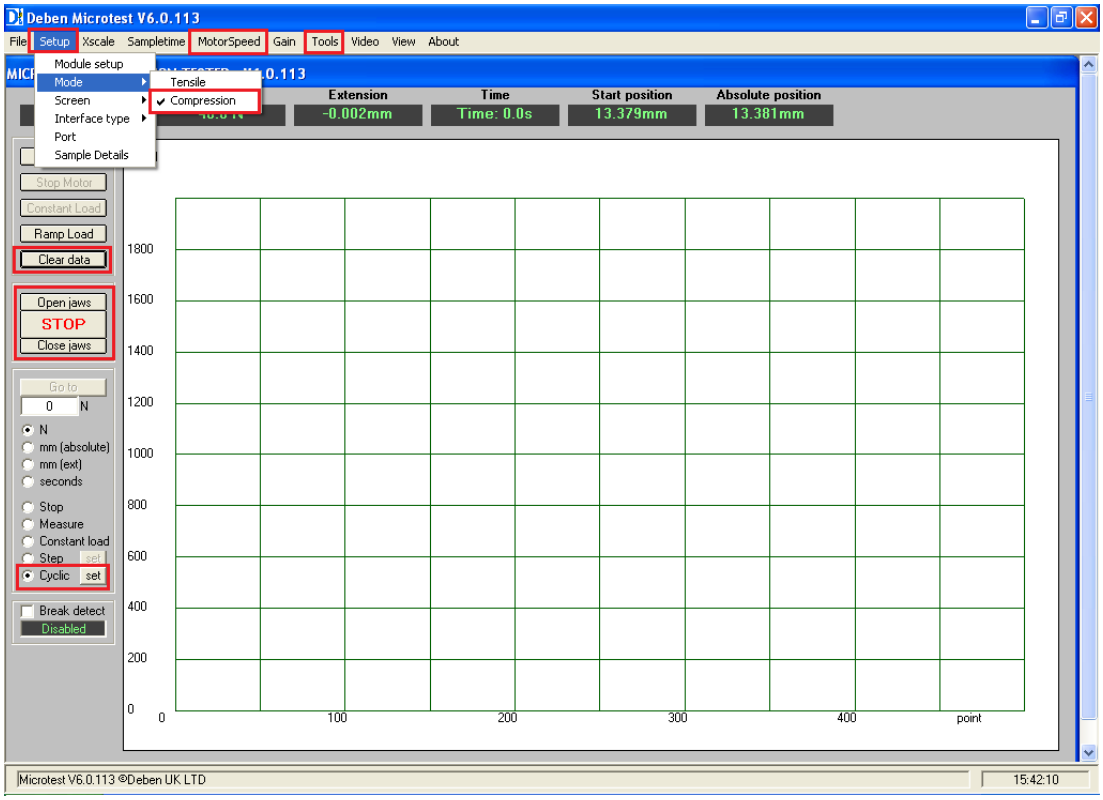

Figure 4-14 Main screen of the Deben Microtest software with key options highlighted such as: ‘Setup’, ‘MotorSpeed’, ‘Tools’, ‘Clear data’, ‘Open jaws’, ‘Close jaws’ and ‘Cycic set’.

Output

Force and displacement were recorded as raw data in the form of a CSV file. Engineering stress was calculated using the Equation 4-3 where F is the exhibited compressive force and A is the initial cross-sectional area of the specimen which is equal to πr^2. Engineering strain was calculated using the Equation 4-4 below where dl is the specimen's axial displacement and l_0 is the initial specimen length. Engineering values were subsequently used to calculate true stress and true strain using Equation 4-1 and Equation 4-2 as mentioned earlier. Compression results presented in the following chapters are in the form of true stress-strain graphs.

$$\sigma = \frac{F}{A} \qquad \text{Equation 4-3}$$

$$\varepsilon = \frac{dl}{l_0} \qquad \text{Equation 4-4}$$

4.1.4 Three-point bend testing

Overview

Three-point bend tests were performed using a Bose Electroforce 3200 testing machine and the Bose software WinTest 4.1. Testing was conducted using Nitinol wires with a diameter of 1mm and 0.45mm. The length of the specimens was approximately 34mm.

Each wire was placed on a podium consisting of two supports, as seen in Figure 4-16. The tips of the supports were formed into cylindrical bars with a diameter of 1.3mm. The span between the supports was 20mm. Grooves were machined onto the tips to prevent the wires from sliding laterally. The mid-span of the wire was displaced under the thrust of a deflection bar with a diameter of 1.3mm while a 450N load cell recorded the applied force.

Testing was performed at a room temperature of 22°C in air, and at 37°C in water when the apparatus was submerged into a temperature-controlled water bath, shown in Figure 4-20. Experiments were preceded by a waiting period of

approximately 5 minutes, to ensure all equipment had reached thermal equilibrium. In addition, testing was carried out at 22°C in water, to examine the effects different ambient media have on the bending behaviour of the wires.

Test plan

Each specimen was deformed under displacement control until the required deflection was produced, and then unloaded at the same crosshead speed. The testing machine was operated at various loading conditions and crosshead speeds according to the needs of each experiment. The 1mm wire was used for the majority of the tests due to its compatibility with the available 450N load cell. The 1mm wire also required small deflections to reach superelastic strain levels. Large deflections under three-point bending can cause a wire to slip on the supports and the displacement transducer to operate near its limits.

A detailed description of the test method is presented in Table 4-12. Single load-unload cycles were performed in order to investigate the bending characteristics of the material and its temperature sensitivity. Load rate effects were examined by testing at different crosshead speeds. The cyclic behaviour of the material in bending was investigated by performing up to 100 consecutive load-unload cycles within the superelastic range.

Test method

- The 450N load cell is attached onto the crosshead, as seen in Figure 4-15.

Figure 4-15 The 450N load cell attached to the moveable crosshead.

- The water bath is mounted and secured onto the frame of the testing machine.

Table 4-12 Test method used for three-point bend tests.

Specimen diameter (mm)	Specimen Length	Loading description	Support span (mm)	Deflection (mm)	Cross-head speed (mm/s)	Temperature (°C)	Ambient medium
1	34	Single load-unload cycle	20	2.5	0.01, 0.1, 1	22	Air
		Single load-unload cycle	20	6	0.1, 1	22	Air
		Single load-unload cycle with 10sec pause before unloading	20	6	1	22	Air
		Single load-unload cycle	20	6	1	22	Water
		Load-unload for 100 cycles	20	2.5	0.1	22	Air
		Single load-unload cycle	20	2.5	0.1	37	Water
		Load-unload for 100 cycles	20	2.5	0.1	37	Water
		Single load-unload cycle	20	6	0.1	37	Water
0.45	34	Single load-unload cycle	20	6	0.1, 1	22	Air

- The 1.3mm supports are attached onto the support podium at a span of 20mm (Figure 4-16).

Figure 4-16 Supports with a diameter of curvature of 1.3mm placed onto the support podium.

- The support podium is mounted on the 15mm diameter sealing rod which is placed in the water bath as seen in Figure 4-17. The lower end of the rod is attached to the frame of the testing machine.

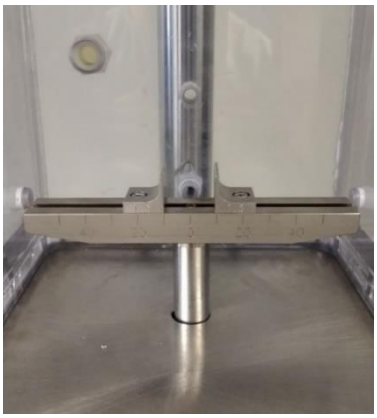

Figure 4-17 Support podium mounted onto the water bath rod.

- The 1.3mm deflection bar (indentor) is attached to the load cell using the attachment seen in Figure 4-18. At this point, the alignment between the support bars and the indentor is visually inspected.
- Approximately 34mm of the Nitinol wire is cut using pliers.
- The specimen is then placed onto the supports (Figure 4-19) where it should be able to move freely on the machined grooves of the supports.

Figure 4-18 Attaching the deflection bar (indentor) to the load cell using the attachment rod.

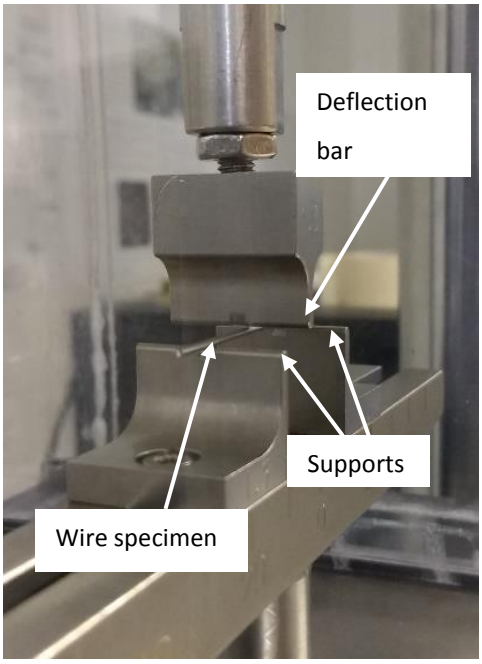

Figure 4-19 Close-up image of the 1mm wire specimen placed onto the supports.

- The front face of the water bath is closed and secured. The water bath is then filled with approximately 3.5 litres of water and the upper cover is placed onto the top of the bath. The experimental setup should now look like Figure 4-20.

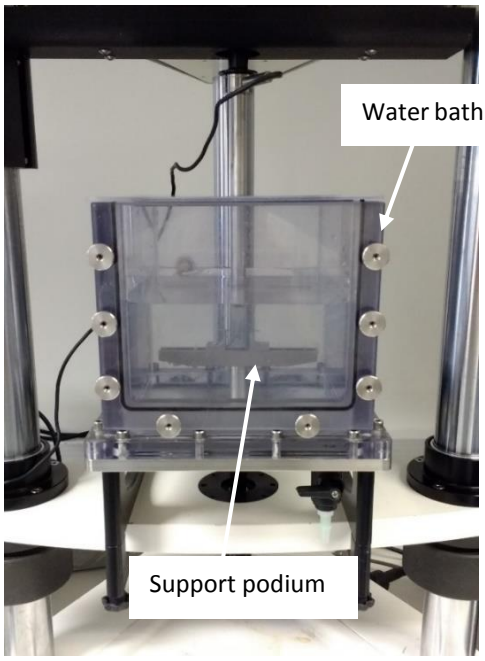

Figure 4-20 Completed three-point bending setup as the water bath is filled with water and the specimen is mounted onto the supports.

- The heating elements of the water bath are switched on using the external controller. The water bath is pre-configured to heat the water to 37°C.
- The Bose WinTest software (Figure 4-21) is launched in order to load an existing project file or to create a new one. The key features when creating a new file are mentioned here:
    - The test parameters are specified via the 'TuneIQ Waveform' tab in the main screen.
    - For single load-unload cycles, the 'Ramp' option is typically selected under the 'Block Type'. For cyclic loading, the 'Sine' option should be used instead.
    - Each individual ramp block can be configured by clicking on 'Edit'. In the 'Select Block Feedback' window that pops up, 'Disp' is selected for displacement controlled experiments. When the user hits 'Ok' a new window opens where the crosshead displacement and loading rate are entered.

- At this point the crosshead is still not powered on. This is done by clicking on ‘Local’ and then selecting ‘High’ in the window that pops up. The ‘Local’ button then turns green.
- Then the test can be started by clicking on ‘Run’.

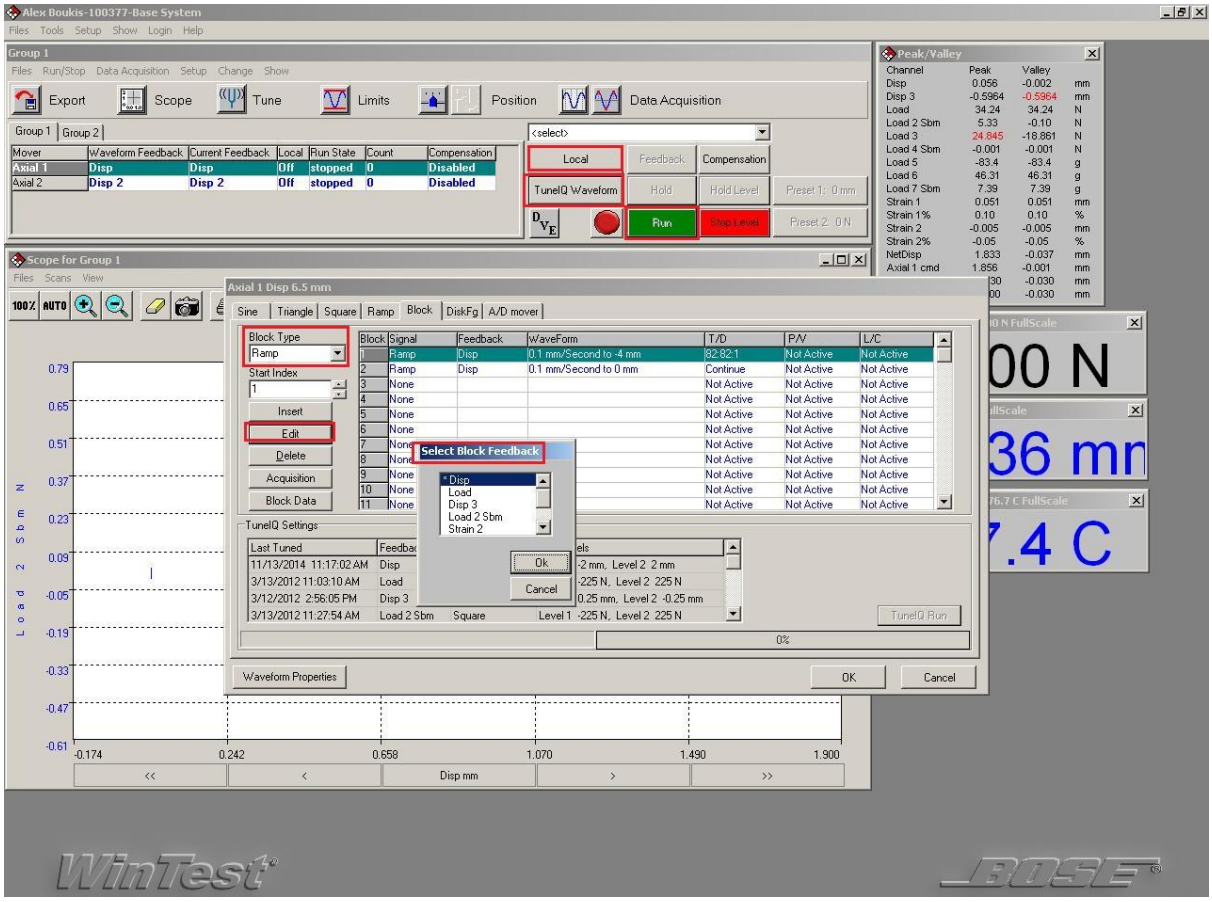

Figure 4-21 Main screen of the Bose WinTest software with key options highlighted such as ‘TuneIQ Waveform’, ‘Block Type’, ‘Select Block Feedback’ and ‘Local’.

- When the test ends, the crosshead returns to its initial position and the raw data are automatically saved.

Output

Force and displacement were recorded as raw data in the form of a CSV file.

4.1.5 Torsion testing

Overview

Torsion testing was performed using the Instron ElectroPuls E10000 Linear-Torsion machine (Figure 4-22(a)) and Instron software WaveMatrix V1.5 and Console V8.4. The machine was equipped with a bi-axial 1kN-25Nm load cell. Two different wire specimens were used with dimensions of: 1.8mm in diameter and 36mm in length for the first specimen and 2.4mm in diameter and 46mm in length for the second. One end of the specimen was rigidly clamped while the other was rotated using pneumatic wedge action grips seen in Figure 4-22(b). The resulting gauge length was approximately 16mm for the 1.8mm specimen and 20mm for the 2.4mm specimen.

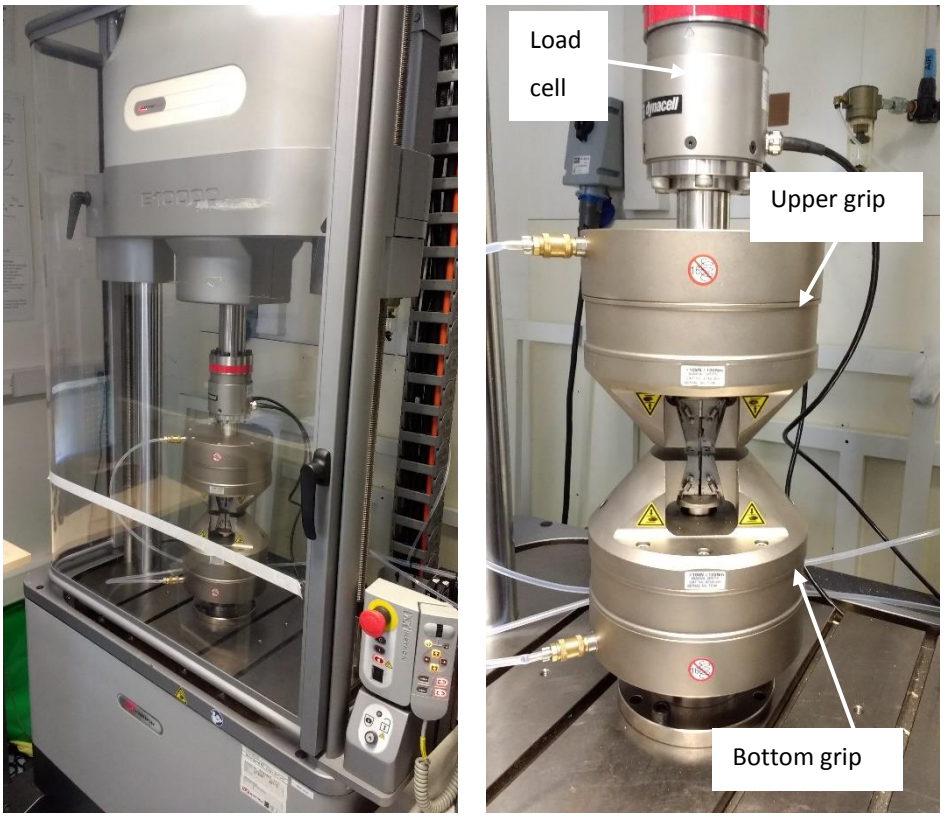

(a) (b)

Figure 4-22 The Instron E10000 testing machine used for torsion tests (a). The bottom grip was fixed onto the frame of the testing machine while the upper grip was allowed to rotate (b).

Test plan

The test plan is presented in Table 4-13. Tests were conducted at room temperature under displacement control. Single load-unload cycles were performed to 20, 40, 60 and 80 degrees of rotation, using the 1.8mm diameter specimen, to investigate the torsional response of the material and identify the relevant constitutive parameters. The crosshead speed was set to 0.5deg/sec corresponding to a strain rate of approximately $4.9x10^{-4}$/s.

The load rate sensitivity was investigated by performing single load-unload cycles to 80 degrees using the 2.4mm diameter specimen due to its better compatibility with the load cell. These tests were conducted at crosshead speeds of 0.5deg/sec and 5deg/sec, corresponding to a strain rate of $5.2x10^{-4}$/s and $5.2x10^{-3}$/s respectively.

Table 4-13 Test method used for torsional testing.

Specimen diameter (mm)	Specimen length (mm)	Gauge length (mm)	Loading description	Rotation (deg)	Crosshead speed (deg/sec)	Strain rate (sec^{-1})
1.8	36	16	Single load-unload cycle	20, 40, 60, 80	0.5	$4.9x10^{-4}$
2.4	46	20	Single load-unload cycle	80	0.5	$5.2x10^{-4}$
			Single load-unload cycle	80	5	$5.2x10^{-3}$

The same testing machine and software were used for combined tension-torsion experiments. However, different load cell and grips were employed since the anticipated force exhibited by the specimens would exceed the 1kN limit mentioned earlier. Therefore, 10kN-100Nm load cell and grips were used to accommodate the needs of the tensile part of the experiment. Testing was conducted at room temperature, under displacement control, using only the 2.4mm diameter specimen since the mismatch between the torque levels of the 1.8mm diameter wire and the new load cell would be even greater.

The loading sequence consisted of four steps. In step 1, axial displacement was applied. In step 2, axial displacement was kept constant while the specimen was rotated. In step 3, rotation was removed while the axial displacement was still constant. In step 4, the applied axial displacement was removed.

The test plan is presented in Table 4-14. Two cases of combined tension-torsion tests are examined here: small tensile displacement with large torsional displacement, and large tensile displacement with large torsional displacement. A crosshead speed of 0.2mm/min was used for the tensile part corresponding to a strain rate of $1.6x10^{-4}$/s. Axial strains were determined using the measured displacements. A crosshead speed of 0.5deg/sec was used for the torsional part corresponding to a strain rate of $5.2x10^{-4}$/s. Prior to tension-torsion testing, uniaxial tension was performed using the same experimental setup in order to define the force-displacement characteristics of the 2.4mm diameter specimen and identify the conditions used later during combined loading.

Table 4-14 Test method used for combined tension-torsion.

Specimen diameter (mm)	Loading description	Axial displacement (mm)	Crosshead speed (mm/min)	Strain rate (sec^{-1})	Rotation (deg)	Crosshead speed (deg/sec)	Strain rate (sec^{-1})
2.4	Loading in tension followed by torsion and unloading in reverse order.	0.1	0.2	$1.6x10^{-4}$	80	0.5	$5.2x10^{-4}$
		1			80		

Test method

- The suitable load cell is attached onto the crosshead of the testing machine.
- The upper grip is attached to the load cell, and the bottom grip is attached to the frame (Figure 4-22(b)). The air hoses are then attached to both pneumatic grips. Note that the user needs to ensure that there is adequate working space in-between the two grips. If not, the upper grip can be moved using the soft keys on the testing machine.

- Using a black ink pen, the 1.8mm diameter specimen is marked at a distance of 10mm from both ends. With this step, the user identifies the location where the specimen is going to be clamped. Subtracting 10mm from the top and bottom of the 36mm long specimen, results in a gauge length of 16mm. Similarly, the 2.4mm diameter specimen (46mm in length) is marked at a distance of 13mm from top and bottom, resulting in a gauge length of 20mm.
- The specimen is clamped by the bottom grip first at the marked location. A pair of high precision 'Dumont' tweezers is used to place the specimen between the clamps. Subsequently, the upper grip is moved downwards, using the soft keys, to clamp the upper end of the specimen. At this point, the specimen is visually examined from all sides to ensure it is aligned correctly when clamped (Figure 4-23).
- The 'Method' section of the Instron WaveMatrix software (Figure 4-24) is opened to load an existing test method or create a new one. This software is very similar to the Instron Bluehill that was introduced earlier in section. The key features are:
    - Under the 'Test' tab, the 'Sequence' option is selected to specify the test parameters.
    - The 'Absolute Ramp' option is typically selected as the 'Waveform' step type.
    - In 'Control Mode', the user selects whether the experiment is load controlled or displacement controlled. All tests were conducted under displacement control. For example, 'Rotation' is selected for torsion tests.
    - In 'Ramp Rate', the loading rate is entered in degrees/sec for torsion tests or mm/minute for axial tests.
    - The 'End Point' is set to the desired maximum displacement, e.g. 80 degrees for torsion.

- The above can be repeated for multiple steps if needed. The sequence of different steps will then appear at the top of the screen, as seen in Figure 4-24.

- Experiments were conducted in the Biomedical Engineering lab where the room temperature (approximately 22°C) was controlled by an air-conditioning system.
- When the test finishes, the raw data file is saved when the 'Finish' button is pressed.

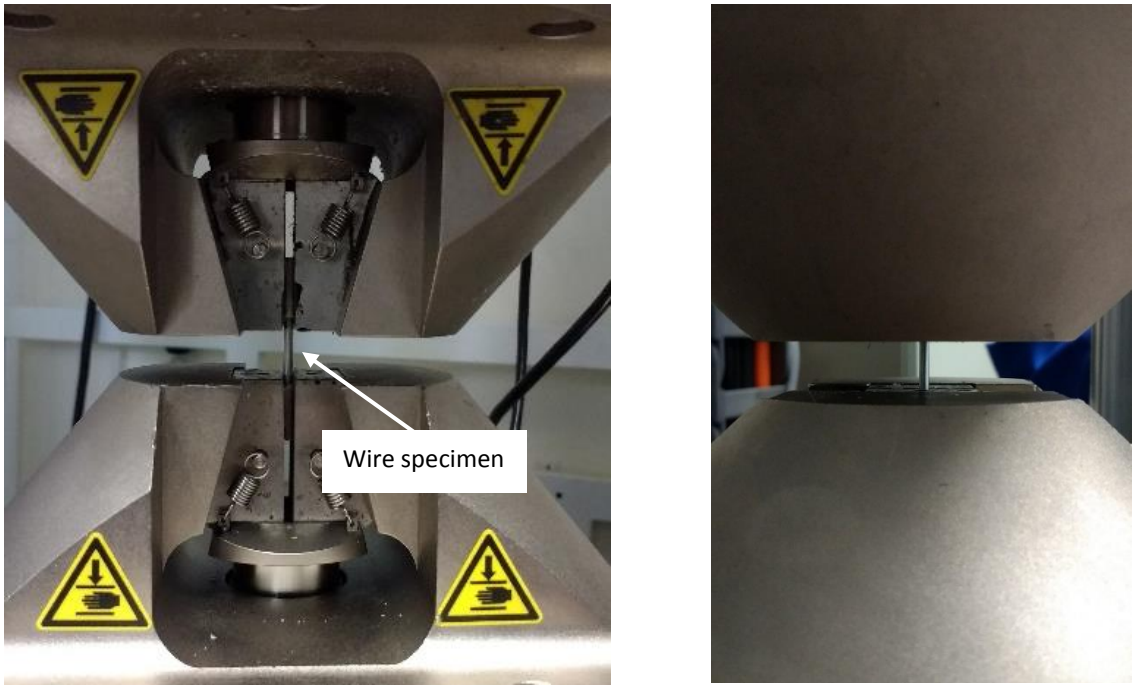

(a) (b)

Figure 4-23 Front (a) and side (b) close-up image of the gripped torsional specimen.

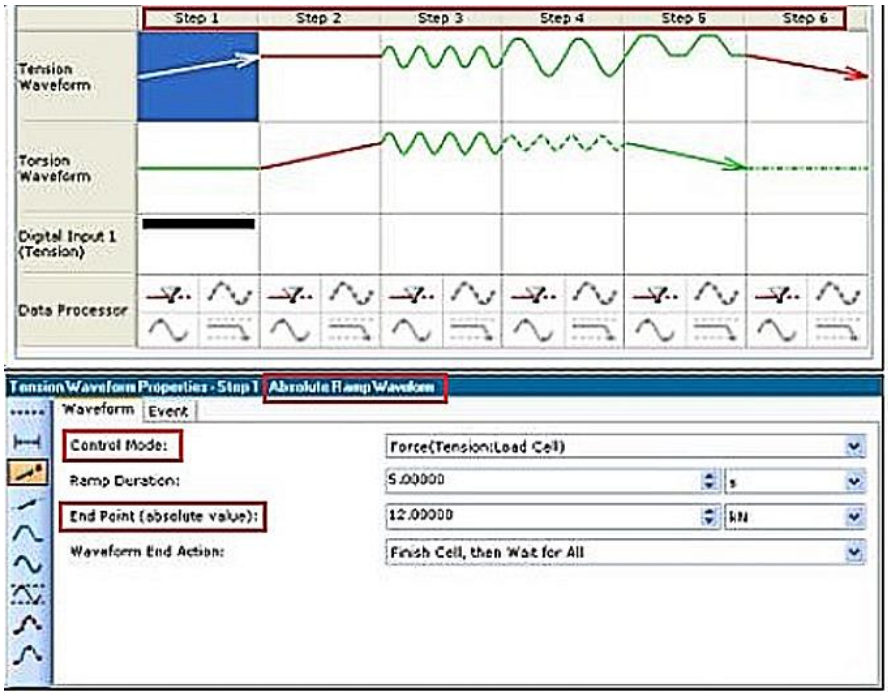

Figure 4-24 The 'Test' screen of the Instron WaveMatrix software with key features highlighted such as the multiple step sequence, the 'Absolute Ramp' Waveform type, the 'Control Mode' and the 'End Point'. Image adapted from the Instron WaveMatrix manual [132].

Output

Torque and rotational displacement were recorded during testing and saved in a CSV file. This was accessed using Microsoft Excel in order to process the data. Maximum shear stress and strain were also calculated from the raw data for comparison with results from other loading modes. Maximum shear stress was calculated using the Equation 4-5:

$$\tau = \frac{rT}{J} \qquad \text{Equation 4-5}$$

where τ, r, T and J are the shear stress, cross-sectional radius, exhibited torque and polar second moment of area respectively. The latter is equal to $\pi r^4/2$ for a circular cross-section. The maximum shear strain was calculated using the Equation 4-6:

$$\gamma_{max} = \frac{r\theta}{L} \qquad \text{Equation 4-6}$$

where γ_{max} is the maximum shear strain on the outer surface of the cross-section, θ is the relative rotation of the grips in radians and L is the gauge length. When combined tension-torsion tests were conducted, results included the exhibited force, torque, axial displacement and rotational displacement.

4.1.6 Error and uncertainty in experimental measurements

Quantities measured in experiments are subject to error. Usually errors are classified into two categories: random and systematic. Random errors, also known as precision or repeatability errors, cause scatter in experimental data and often result from fluctuating experimental conditions. Random errors are only associated with experimental results. Computational results usually have only round-off errors which are orders of magnitude less than experimental random errors and are typically ignored. Random errors can be identified using statistical analysis tools such as the standard deviation and the standard error [133]. The standard deviation s (Equation 4-8), is a measure of the dispersion of the data from the mean value $\bar{x}$ (Equation 4-7). The standard error $se(\bar{x})$ (Equation 4-9), is a measure of how precise the estimate of the mean is.

Mean (of n number of samples)	$\bar{x} = \frac{\sum_{i=1}^{n} x_i}{n}$	Equation 4-7
Standard deviation	$s = \sqrt{\frac{\sum_{i=1}^{n}(x_i - \bar{x})^2}{n-1}}$	Equation 4-8
Standard error of the mean	$se(\bar{x}) = \frac{s}{\sqrt{n}}$	Equation 4-9

Systematic errors, also known as bias errors, are also associated with experimental techniques and they can have many sources. These errors are not random in nature and they are reproduced in every repeat of a measurement. The

most common source of systematic error is the accuracy/calibration of a measuring instrument.

Therefore, testing systems are periodically assessed to ensure that they perform accurately and produce accurate and reliable data. Calibrations and verifications are conducted, typically annually, to internationally recognized standards such as the ASTM-E4 [134], ASTM-E2309 [135] and ASTM E83 [136]. Often testing machine manufacturers calibrate their systems to even exceed the requirements of the above standards.

The ASTM E4 standard [134] describes the procedures for the calibration and verification of the force measuring components of testing machines. The standard specifies that the testing machine should be accurate to 1% of the load reading over the verified range. The ASTM E2309 standard [135] describes the procedures for the calibration and verification of the displacement measuring components of testing machines. Displacement verification measures the actual travel of the machine's crosshead over a defined range of operation. The specified errors, according to ASTM E2309, are presented in Table 4-15 for various machine classifications. In addition, the ASTM E83 standard [136] details the process for calibrating and verifying strain extensometer systems. The errors in measuring strain according to ASTM E83 are shown in Table 4-16.

According to the Instron specifications, the load accuracy of the Instron 5965 [137] testing machine is ±0.5% of the reading. The Instron AVE2 video extensometer [138] is classified as a Class B-1 extensometer. Therefore, the allowable errors when measuring strain with this device should not exceed the values shown in Table 4-16, i.e. ±0.5% of the strain reading or ±0.0001 fixed strain error.

The load accuracy of the Deben testing machine [139] is reported as 1% and the displacement accuracy as a fixed value of 0.01mm. The specifications do not state whether the testing machine is calibrated to the ASTM or other standards. However, the fixed displacement accuracy of 0.01mm is lower than the requirement of the ASTM E2309 standard (fixed error of ±0.025mm), so it can be assumed that the Deben meets and even exceeds the specifications set by the standard.

Table 4-15 Classification of displacement measuring systems according to ASTM E2309.

Testing machine classification	Error not to exceed the greater of	
	Fixed error in mm	Relative error (% of displacement)
Class A	±0.025	±0.5
Class B	±0.075	±1.0
Class C	±0.125	±2.0
Class D	±0.25	±3.0

Table 4-16 Classification of extensometer systems according to ASTM E83.

Extensometer classification	Error of strain not to exceed the greater of	
	Fixed error	Relative error (% of strain)
Class A	±0.00002	±0.1
Class B-1	±0.0001	±0.5
Class B-2	±0.0002	±0.5
Class C	±0.001	±1
Class D	±0.01	±1
Class E	±0.1	±1

According to the Bose specifications, the displacement accuracy of the Bose Electroforce 3200 [140] exceeds the Class A testing machine accuracy as specified in the ASTM E2309 standard, i.e. ±0.5% of the displacement reading or a fixed error of ±0.025mm. The Bose load cell is stated to meet the requirements of the ASTM E4 standard.

According to the Instron specifications, the load accuracy of the Instron E10000 [141] testing machine is ±0.5% of the indicated load, or ±0.005 % of the load cell capacity, whichever is greater. The displacement accuracy is not reported in the Instron brochure. However, since all Instron testing machines are compliant with the ASTM standards, a maximum error of ±0.5% of the displacement reading can be assumed in this case.

When two different independent errors e_1 and e_2 are identified, they can be combined in quadrature (Equation 4-10) calculating the total or combined error e_c [133]. These reported errors are in essence estimates of the uncertainty associated with the experimental procedures. Combined errors are often multiplied by a coverage factor (k) to give a result which is called the expanded error or expanded

uncertainty [142]. Usually, a coverage factor k=2 is used to give a level of confidence of approximately 95%, assuming a normal distribution.

Combined error $$e_c = \sqrt{e_1^2 + e_2^2}$$ Equation 4-10

4.2 Computational analyses

4.2.1 Overview of the computational analyses

The commercially available Abaqus/Standard (v6.14) finite element solver was used for the computational analyses included in this work. This product has been extensively verified by the vendor (Dassault Systemes, Simulia Corp.) by running several benchmark analyses. The vendor of the software has implemented a quality management system which meets ISO 9001:2015 [143]. Therefore, additional verification of the software was not necessary.

Solution and convergence

A multistep, 'static general' structural analysis was implemented to simulate the physical tests. The nature of the performed analyses was non-linear due to: the non-linear material behaviour, the non-linear large displacements and the contact interactions that were enabled when necessary. The large displacement formulation was activated by the 'Nlgeom' option in Abaqus.

When an analysis problem is defined, it is usually divided into different steps. Abaqus breaks down any non-linear step into small increments which may require several iterations to find a solution. An iteration is an attempt at finding a solution in an increment. Newton's method is the iterative procedure which is applied in order to produce a converged solution for each increment [144].

For a body in equilibrium, the net force acting on it must be zero, i.e. the external forces P and the internal forces I must balance each other (Equation 4-11).

Consider now the non-linear response of a structure to a small load increment, ΔP, as shown in Figure 4-25. Abaqus uses the structure's stiffness K_0 at the start of the increment, also known as tangent stiffness at u_0, to calculate a displacement correction c_a for the structure. Using c_a the configuration is updated to u_a. The associated internal forces I_a in the 'updated configuration' of the system are subsequently calculated. The residual force for the iteration is then the difference between the total applied load P and I_a, and is used to assess the convergence (Equation 4-12).

$$P - I = 0 \qquad \text{Equation 4-11}$$

$$R_a = P - I_a \qquad \text{Equation 4-12}$$

If R_a is zero in the model, point a in Figure 4-25 would lie on the load-displacement curve and the structure would be in equilibrium. In reality however, the residual force in a nonlinear problem will never be exactly zero, so Abaqus compares it to a tolerance value. According to the default criterion, if R_a is smaller than 0.5% of the average force in the structure the solver accepts the solution as being in equilibrium. In this case, P and I_a are considered to be in equilibrium and u_a is considered a valid equilibrium configuration for the structure under the applied load.

Abaqus performs an additional convergence check before accepting the solution. The solver checks that the displacement correction c_a is smaller than a fraction, 1% by default, of the total incremental displacement $\Delta u_a = u_a - u_0$. If it is greater than 1% then another iteration is performed. When both convergence checks are satisfied the system is considered in approximate equilibrium and the next increment of loading can be started.

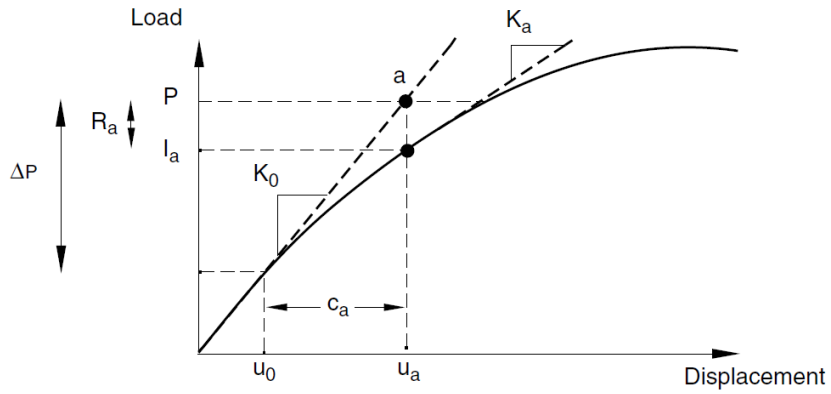

Figure 4-25 First increment of Newton's method. Image reproduced from the Abaqus Analysis User's Guide [144].

If the iteration described above is not converged, then the solver performs another iteration to bring the internal and external forces into equilibrium. A new stiffness matrix K_a is formed based on the updated displacement position u_a, as seen in Figure 4-26. If the solution is converging in this increment, the new residual force R_b and the new displacement correction c_b will be reduced. If they are within the acceptance criteria then the increment can be considered converged.

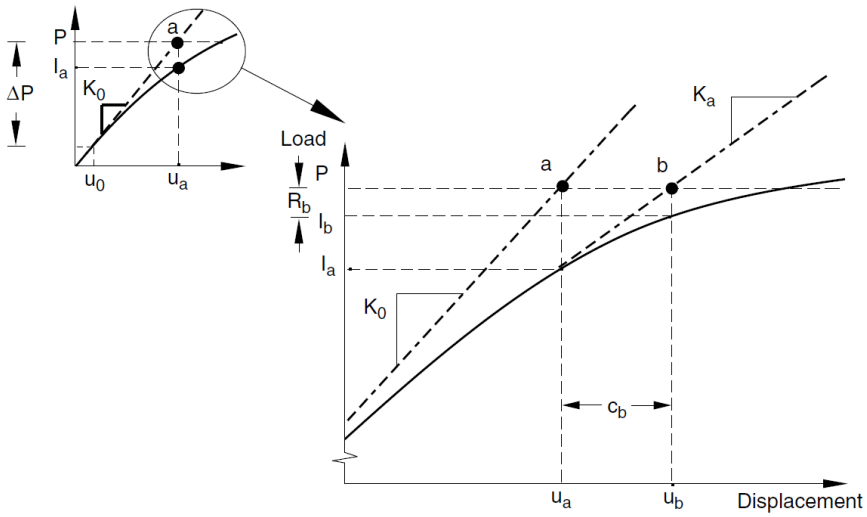

Figure 4-26 Second increment of Newton's method. Image reproduced from the Abaqus Analysis User's Guide [144].

Automatic Incrementation

The default arbitrary step time of one second was used for all steps, during which displacements and loads were applied linearly. Automatic incrementation was used, where the user suggests the size of the first increment in each step of the simulation and then Abaqus automatically adjusts the size of the subsequent time increments to solve the non-linear problem [144]. Automatic control is usually more efficient than manually enforcing the increment size. The user can also control the minimum and maximum allowable increment sizes.

The solution is usually obtained in several increments and multiple iterations are required to obtain approximate equilibrium for each increment. If the model is not in equilibrium at the end of the iteration, Abaqus tries another iteration. With every iteration the obtained solution should be closer to equilibrium. The number of required iterations for a time increment will vary depending on the degree of nonlinearity. The default incrementation procedure is based on the following criteria:

- If the solution has not converged within 16 iterations, the solver will abandon the increment. It will then attempt to find a solution again with the increment size set to 25% of its previous value.
- If the solution still fails to converge, Abaqus reduces the increment size again by the same amount. This process is continued until a solution is found.
- If the time increment becomes smaller than the minimum defined by the user or if more than 5 attempts are needed, the analysis will be stopped.
- If 2 consecutive increments require fewer than 5 iterations to obtain a converged solution, the solver will automatically increase the increment size by 50%.

When contact interactions are used, Abaqus runs severe discontinuity iterations to address any abrupt changes in the stiffness due to surfaces coming into contact (closing) or separating (opening) from each other. Severe discontinuity iterations are different from regular iterations in which the solution varies smoothly. When a severe discontinuity is detected, an iteration is started in which loads

representing contact pressures will either be applied or removed based on the specified contact pressure-overclosure relationship. The solver will continue these iterations until the severe discontinuities are sufficiently small or do not exist anymore. More details on this can be found in 'Analysis Solution and Control' of the Abaqus Analysis User's Guide. The default settings for the convergence criteria were used for all simulations discussed here.

4.2.2 Material parameters

The Abaqus Nitinol model requires 15 input parameters which are described in Table 4-17 [109]. As explained earlier, most of these parameters are identified from tensile data. The material behaviour is based on the stress-strain response illustrated in Figure 4-27. The material model can be extended to capture the post-transformation elastic-plastic loading if stress-strain points are entered to describe the region beyond the superelastic range.

Values for the elastic moduli of austenite and martensite (parameters 1 and 3 respectively) can be found by calculating the slope of the respective linear elastic parts of the tensile stress-strain curve. Similarly, the shear or torsional moduli can be found from experimental torque-rotation graphs or shear stress-strain curves. With the moduli values known, the Poisson's ratios can be calculated for austenite and martensite (parameters 2 and 4 respectively) assuming these states are isotropic using the Equation 4-13:

$$v = \left(\frac{E}{2G}\right) - 1 \qquad \text{Equation 4-13}$$

where v is the Poisson ratio, E is the elastic modulus and G is the shear or torsional modulus.

The transformation strain (parameter 5) can be found by tracing the $\mathrm{E_M}$ gradient from the end of the upper plateau down to the strain axis as shown in

Figure 4-27. The reference temperature (parameter 9) is set to zero for isothermal simulations. Consequently, parameters 6 and 10 are not used.

The start of transformation during loading (parameter 7) is the tensile stress at the end of the linear elastic region, just before the curve enters the plateau region. The end of transformation during loading (parameter 8) is the tensile stress at the end of the load plateau, right before the curve enters the post-transformation region, as shown in Figure 4-27. Similarly, the transformation stresses during unloading (parameters 11 and 12) are found from the lower, unload plateau of the tensile curve.

Table 4-17 Input parameters of the Auricchio constitutive model implemented in Abaqus.

Input parameters		
No.	Symbol	Description
1	E_A	Austenite elasticity
2	ν_A	Austenite Poisson's ratio
3	E_M	Martensite elasticity
4	ν_M	Martensite Poisson's ratio
5	ε^L	Transformation strain
6	$\left(\frac{\delta\sigma}{\delta T}\right)_L$	$\delta\sigma/\delta T$ loading
7	σ_L^S	Start of transformation during loading
8	σ_L^E	End of transformation during loading
9	T_o	Reference temperature
10	$\left(\frac{\delta\sigma}{\delta T}\right)_U$	$\delta\sigma/\delta T$ unloading
11	σ_U^S	Start of transformation during unloading
12	σ_U^E	End of transformation during unloading
13	σ_{CL}^S	Start of transformation during loading in compression (as a positive value)
14	ε_V^L	Volumetric transformation strain
15	N_A	Number of annealings to be performed during the analysis
16	N_P	Number of stress-strain pairs to define the plastic curve
17	σ_{NP}^P, ε_{NP}	N number of stress-strain points in the plastic curve

The stress at the start of transformation during loading in compression (parameter 13), is calculated from the experimental compression stress-strain curve. The value is entered in the parameters as a positive number. The volumetric transformation strain ε_V^L (parameter 14) is set equal to ε^L (parameter 5). This is considered the default approach during which parameter 14 is computed based on the difference between σ_L^S and σ_{CL}^S, thus allowing the software to define tension-

compression asymmetry. The number of annealings (parameter 15) is not of interest in the present analysis and it is set to zero. The input parameter values that were identified using experimental data are presented in Chapter 6, Section 6.1.

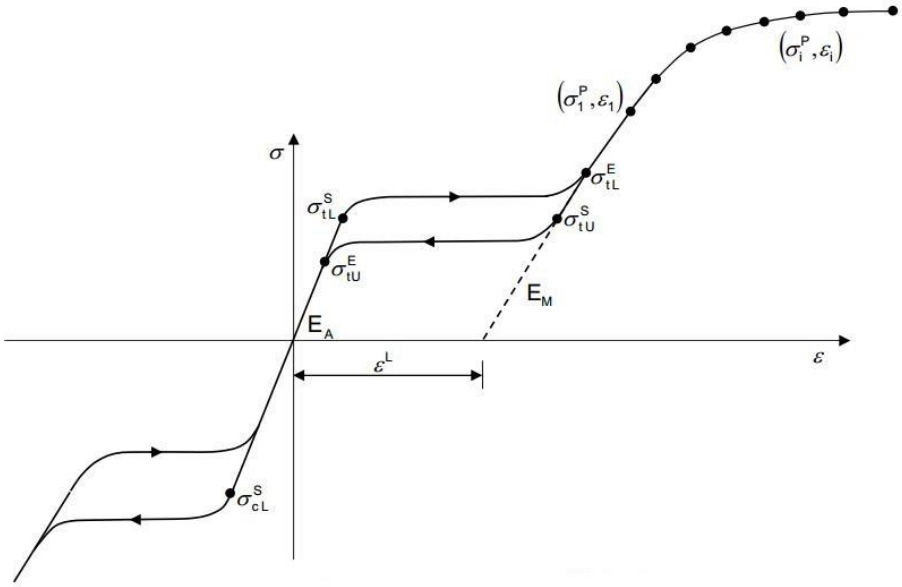

Figure 4-27 Stress-strain representation of the Abaqus Nitinol model. Image reproduced from Simulia DS Support Knowledge Base [110].

4.2.3 Tensile modelling

A simple cube model, comprised of just one element, was used in order to simulate uniaxial tension. A single element model is considered a valuable tool in FEA for validating complex nonlinear material models and user-defined subroutines, while minimizing convergence issues and excluding other factors that may influence the results. Thus, modelling in the present work was performed using a single element cube with dimensions 1mm x 1mm x 1mm. The geometry was designed as a 3D deformable part with a solid homogeneous section, using the 'solid extrude' function in Abaqus.

The boundary conditions (BCs) of the model were applied on the global/default coordinate system. The displacement of the base of the cube was constrained in the Y-direction, as shown in Figure 4-28. All other displacements on this face were unconstrained. The displacement of the left edge of the base, as seen

in Figure 4-29, was constrained in the X-direction. The other displacement BCs on this edge were unconstrained. The displacement of the top edge of the base was constrained in the Z-direction, as seen in Figure 4-30. All other displacements on this edge were unconstrained. In step 1 of the simulation, a displacement was applied on the upper face of the cube along the Y-direction, as shown in Figure 4-31, loading the structure. The other displacement BCs on this face were unconstrained. In step 2 of the simulation, the displacement of the upper face was reversed unloading the cube to its initial state. The above BCs are summarised in Table 4-18. Figure 4-32 also shows the BCs of the model with the 'wireframe' visualisation enabled.

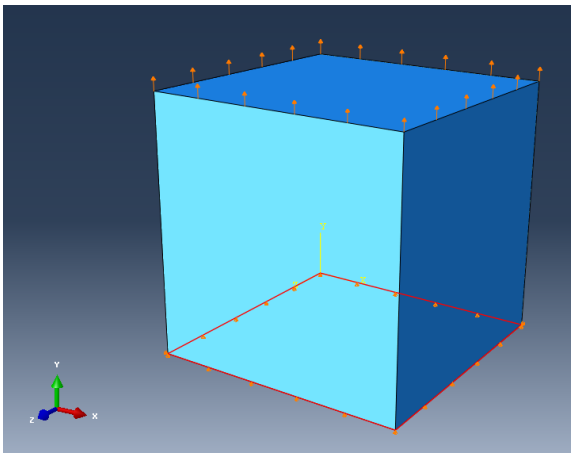

Figure 4-28 The base of the cube constrained in the Y-direction.

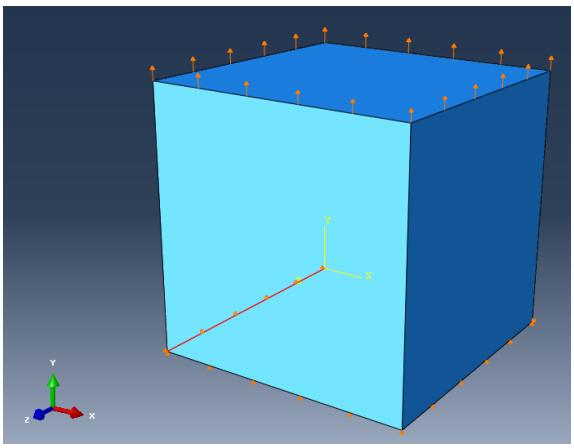

Figure 4-29 The left edge of the base constrained in the X-direction.

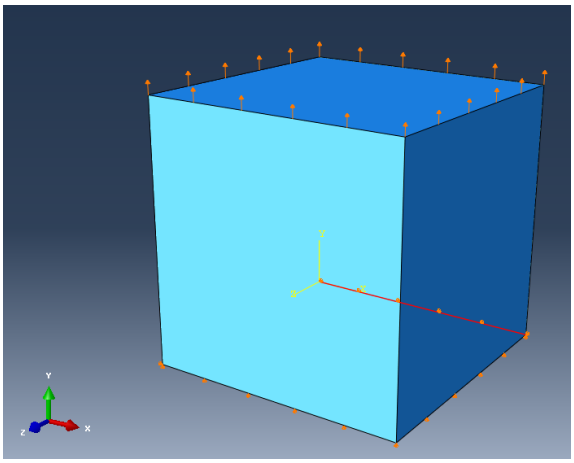

Figure 4-30 The top edge of the base constrained in the Z-direction.

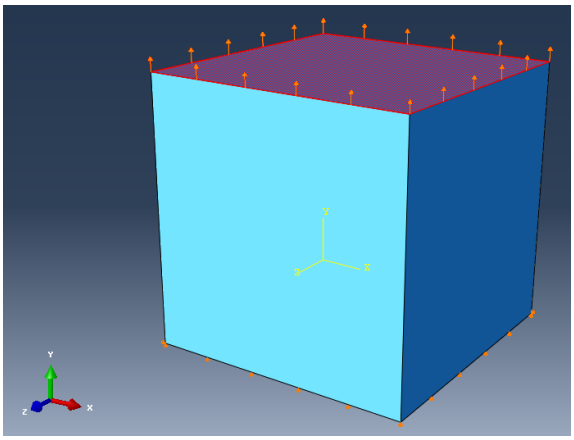

Figure 4-31 The upper face of the cube displaced in the Y-direction.

Table 4-18 Summary of the BCs used in the single element cube model.

Boundary condition	Simulation Steps		
	Initial	Step 1- Load	Step 2- Unload
Displacement of the base of the cube is constrained in the Y-direction. All other displacements on this face are unconstrained.	**Created**	Propagated	Propagated
Displacement is constrained in the X-direction for the left edge of the base (as seen in Figure 4-29). All other displacements on this edge are unconstrained.	**Created**	Propagated	Propagated
Displacement is constrained in the Z-direction for the top edge of the base (as seen in Figure 4-30). All other displacements on this edge are unconstrained.	**Created**	Propagated	Propagated
Displacement is applied in the Y-direction for the upper face of the cube. All other displacements on this face are unconstrained.		**Created**	**Modified:** Displacement is reversed

For best results when using only one element, a full integration, three-dimensional, 20-node quadratic hexahedral (brick) element (C3D20) was used to mesh the geometry. Plotting stress and strain after the analysis produced the true stress-strain results that were compared directly with experimental data.

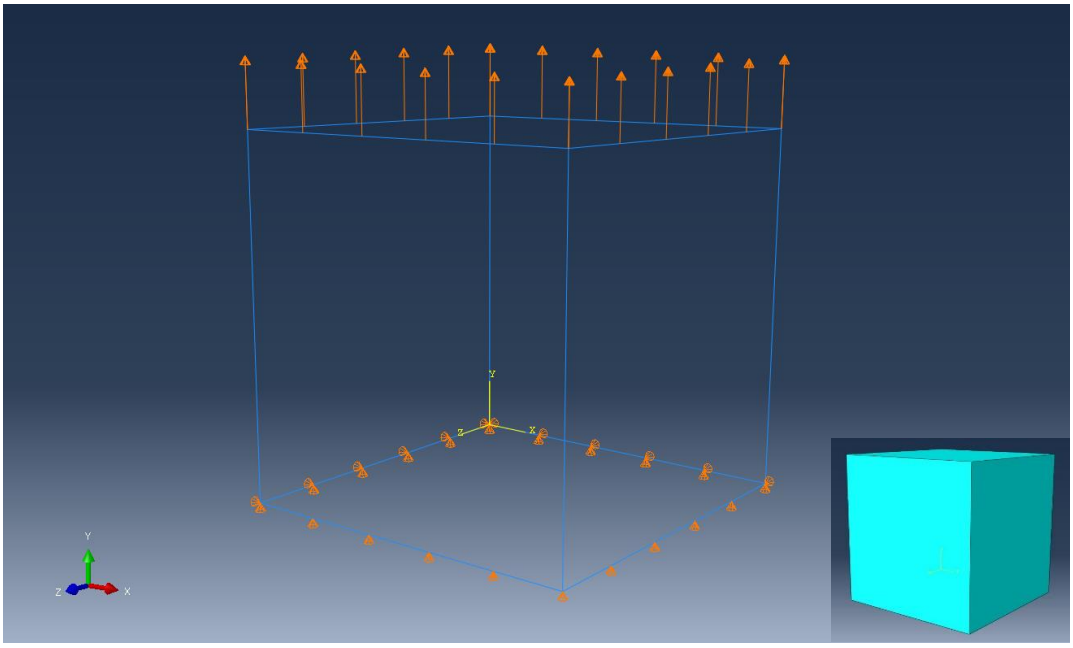

Figure 4-32 BCs of the single-element cube model. The meshed geometry is shown in the bottom right corner.

4.2.4 Compression modelling

Compression testing was simulated with a wire model which was created as a 3D deformable part with a solid homogeneous section, using the 'solid extrude' function in Abaqus. The dimensions of the wire were: 1mm in diameter and 3mm in length, like the specimen used in the physical tests. Using 'datum planes' in Abaqus, the cross-section of the wire was partitioned through the whole length to allow the use of a symmetrical mesh. Four quarters were created in the circular cross section as shown in Figure 4-33.

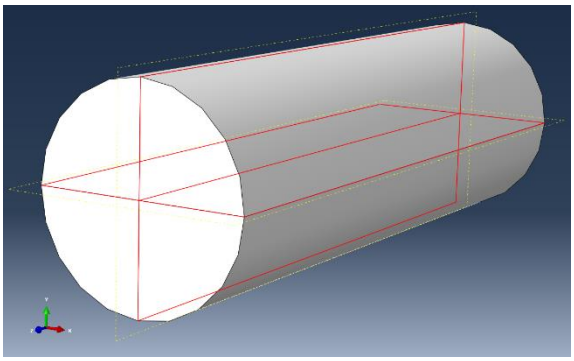

Figure 4-33 The wire cross-section was partitioned into four quarters.

The plates which compressed the wire were created as 3D analytical rigid parts with dimensions of 1.2mm by 1.2mm. In addition, 3D reference points were created to govern the behaviour of the plates. This was achieved by applying a 'rigid body' type constraint between the analytical rigid parts and their respective reference points.

Surface-to-surface contact with finite sliding was employed between the plates and the wire ends to simulate the experimental set-up. A low friction coefficient of 0.1 was used for the analysis since the specimen was lubricated on both ends during mechanical testing. The friction formulation was 'penalty', pressure-overclosure was set to 'hard contact' and separation after contact was allowed. The 'slave' surface of the contact interaction was the wire while the plates acted as the 'master' surfaces. Analytical rigid surfaces must always be the 'master' surface according to the Abaqus documentation [106].

The BCs of the model were applied on the global/default coordinate system. The displacement of the central line of the wire, seen in Figure 4-34, was constrained in the X-direction and in the Y-direction during all steps. The displacement in the Z-direction however was unconstrained. All displacements and rotations of the top reference point, shown highlighted in Figure 4-35, were constrained. All displacements and rotations were also constrained initially for the bottom reference point (Figure 4-36). This is the point that controlled the moving plate. In step 1 of the simulation, a known displacement was applied in the Z-direction, moving the plate and thereby compressing the wire. In step 2, the displacement was reversed

unloading the wire. The above BCs are summarised in Table 4-19. Figure 4-37 also shows the BCs of the model with the 'wireframe' visualisation enabled.

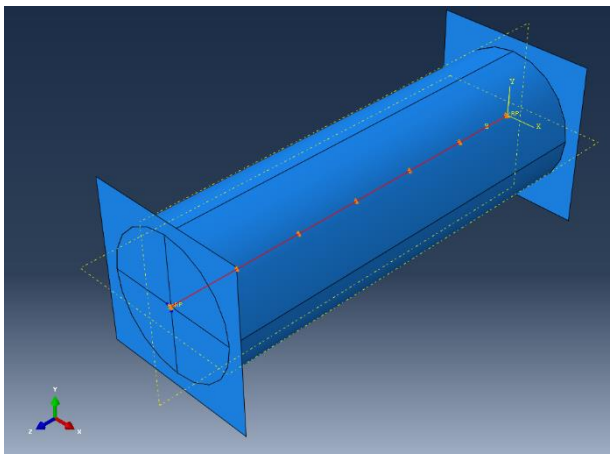

Figure 4-34 The central line of the wire was constrained in the X-direction and Y-direction.

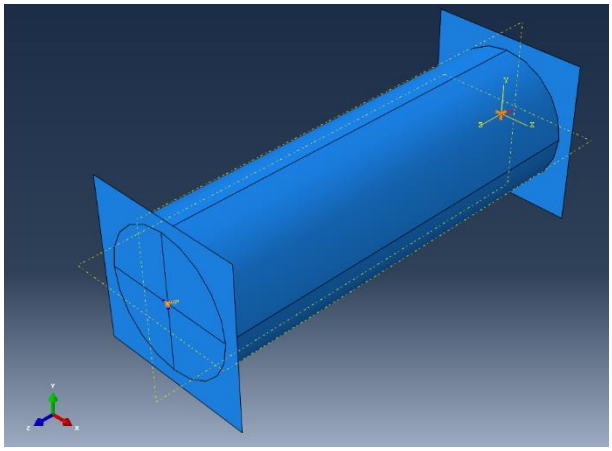

Figure 4-35 All displacements and rotations of the top reference point were constrained.

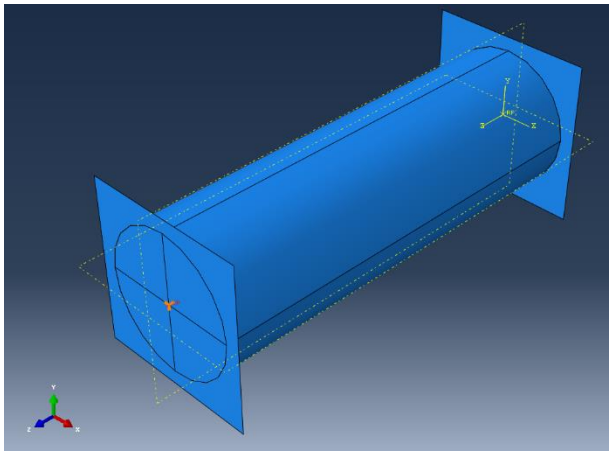

Figure 4-36 A known displacement was applied in the Z-direction of the bottom reference point in order to move the plate. All other displacements and rotations on this reference point were constrained.

Table 4-19 Summary of the BCs used in the compression model.

Boundary condition	Simulation Steps		
	Initial	Step 1- Load	Step 2- Unload
All displacements and rotations were constrained for the top reference point (as seen in Figure 4-35).	**Created**	Propagated	Propagated
All displacements and rotations were constrained for the bottom reference point (as seen in Figure 4-36).	**Created**	**Modified**: Displacement in the Z-direction was applied.	**Modified**: Displacement in the Z-direction was reversed.
Displacements in the X-direction and the Y-direction were constrained for the central line of the wire. Displacement in Z-direction was unconstrained for the central line.	**Created**	Propagated	Propagated

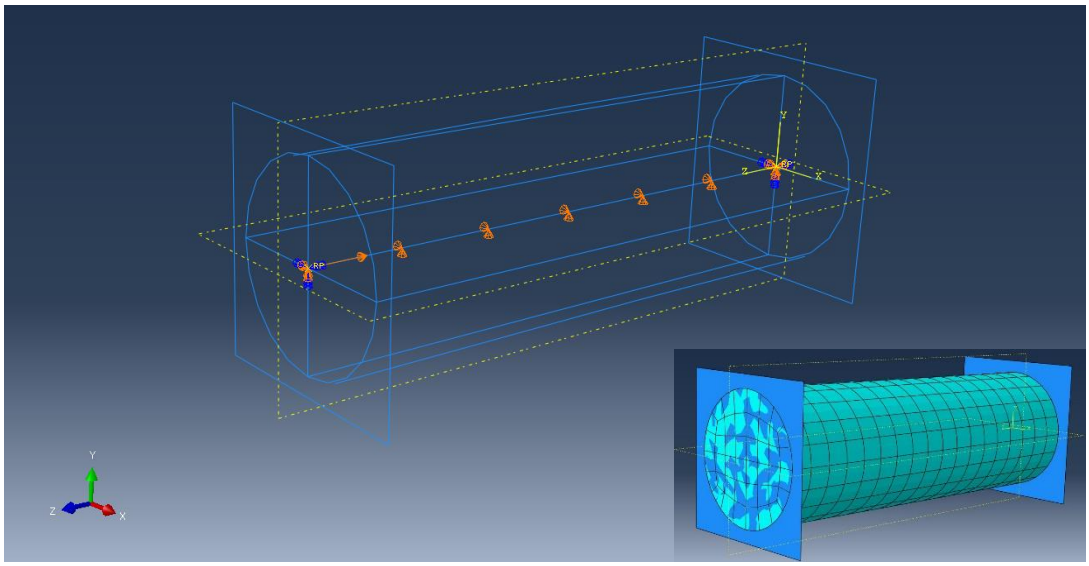

Figure 4-37 BCs of the compression model. The meshed geometry is shown in the bottom right corner.

Reduced-integration 20-node quadratic hexahedral (brick) elements C3D20R were used to mesh the wire. Reduced-integration elements use one integration point less in each direction compared to fully integrated elements [106]. However, they are not sensitive to mesh distortion and they can usually be used with a slightly coarser mesh. Therefore, they are generally the best choice for most simulations since they combine the capabilities of the fully integrated elements while being less computational demanding.

The mesh sensitivity was also examined prior to the final analysis in order to determine the suitable number of elements in the model. The number of elements in the cross-section was controlled by changing the seeding size on the partition edges. The number of elements in the longitudinal direction was separately controlled by the seeding size of the edges in that direction.

Mesh sensitivity results are shown in Table 4-20, which shows the number of elements that were used in each simulation, the maximum force and the percentage force difference between each simulation and the reference case. The force magnitude was used to assess the mesh during this study since it was of direct interest for extracting the final results. The reference simulation was the one with the highest number of elements. In Table 4-20, this is marked as simulation number 5. In addition, the wall-clock times are presented for each simulation as an indication of the required computational resources. All simulations were run on two 'Intel Xeon E5-1650 v3 3.50GHz' cores. Wall-clock times were extracted from the '.dat' output file of the simulation.

Due to the partitions, a symmetric mesh is automatically enforced in the cross-section. This is good practice for modelling structures with a circular cross-section but it also means that a very coarse mesh (in the cross-section) cannot be applied, if required. The initial number of elements in the cross-section of the wire was 32 which was later increased to 44, as seen in Table 4-20.

In Figure 4-38, force and wall-clock time were plotted against the number of elements. The solution became stable with increasing number of elements, which is shown as a 'plateau' in the force curve of Figure 4-38. On the contrary, the wall-clock time increased as the mesh became denser. This was expected since the solver was required to perform calculations for more elements. The mesh of case 3 was chosen for the final simulations despite requiring a longer wall-clock time compared to case 2. This is because its solution was more stable and finished with fewer increments and also the percentage force difference from the benchmark case (simulation 5) was smaller than 0.5% (absolute value).

If the 'mesh verify' function is used, Abaqus can also provide the user with information regarding the aspect ratio of the elements in the mesh. The aspect ratio is the ratio between the longest and shortest edge of an element. In an ideal mesh, the aspect ratio of the elements will be close to one. Hexahedral elements in Abaqus cannot have an aspect ratio greater than ten. For case 3, the average aspect ratio was 1.49. When the final simulation was finished, force and displacement data were extracted and then converted to stress and strain using the methodology of section 4.1.3.

Table 4-20 Results of the mesh sensitivity study for the compression model.

Simulation case	Number of elements			Force	Force diff	Wall-clock time (sec)	Time diff
	cross-section	length	total				
1	32	9	288	718	-1.37%	57	-63.92%
2	32	18	576	724	-0.55%	61	-61.39%
3	44	18	792	725	-0.41%	100	-36.71%
4	44	27	1188	727	-0.14%	129	-18.35%
5	44	36	1584	728	-	158	-

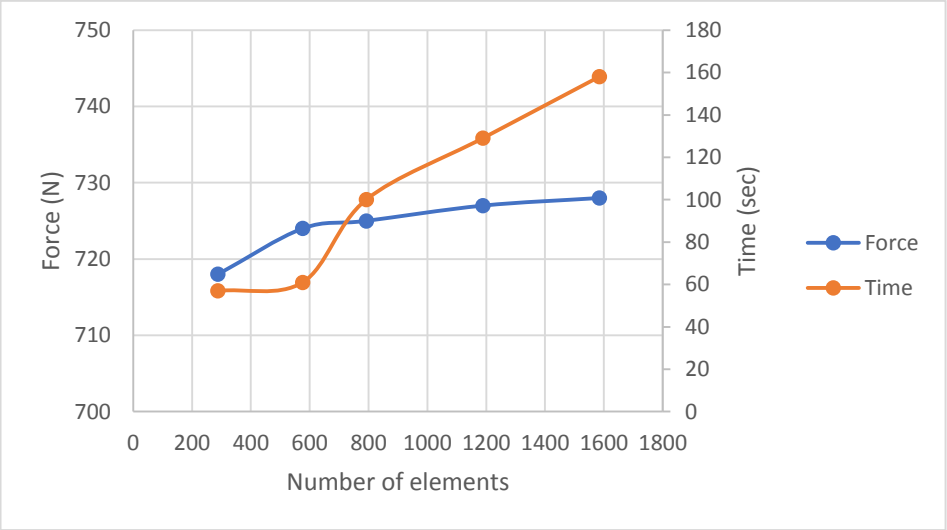

Figure 4-38 Force and wall-clock time plotted against the number of elements for the simulation cases of Table 4-20.

4.2.5 Three-point bend modelling

Three-point bending was simulated with a wire model which was created as a 3D deformable part with a solid homogeneous section, using the 'solid extrude' function in Abaqus. The dimensions of the wire were: 1mm in diameter and 34mm in length like the specimens used in the physical tests. The cross-section of the wire was partitioned into four quarters through the whole length, like the compression model described earlier.

The two supports and the indentor were designed as 3D analytical rigid parts with dimensions of 1.3mm in diameter and 1mm in length. The behaviour of these parts was controlled by 3D reference points. This was achieved by applying a 'rigid body' type constraint between the analytical rigid parts and their respective reference points.

Surface-to-surface contact interaction with finite sliding was enabled between the plates and the wire ends to simulate the experimental set-up. The friction coefficient was 0.22. This value was found by performing several trial and error simulations where the coefficient was fine-tuned until the load drop of the experimental bending response at 22°C was reproduced. The friction formulation was 'penalty', pressure-overclosure was set to 'hard contact' and separation after contact was allowed. The 'slave' surface of the contact interaction was the wire while the analytical rigid surfaces acted as the 'master' surfaces.

The BCs of the model were applied on the global/default coordinate system. The displacement of the central line of the wire was constrained in the Z-direction during all steps, as seen in Figure 4-39. The displacements in the other directions were unconstrained. All displacements and rotations of the two reference points that controlled the behaviour of the supports were constrained. The reference points are highlighted in Figure 4-40.

In step 1 of the simulation, a displacement in the Y-direction was applied on the reference point that controlled the indentor (Figure 4-41). Consequently, the

indentor moved downwards bending the wire. All other displacements and rotations were constrained on this reference point. In step 2, the displacement was reversed unloading the wire. The above BCs are summarised in Table 4-21. Figure 4-42 also shows the BCs of the model with the 'wireframe' visualisation enabled.

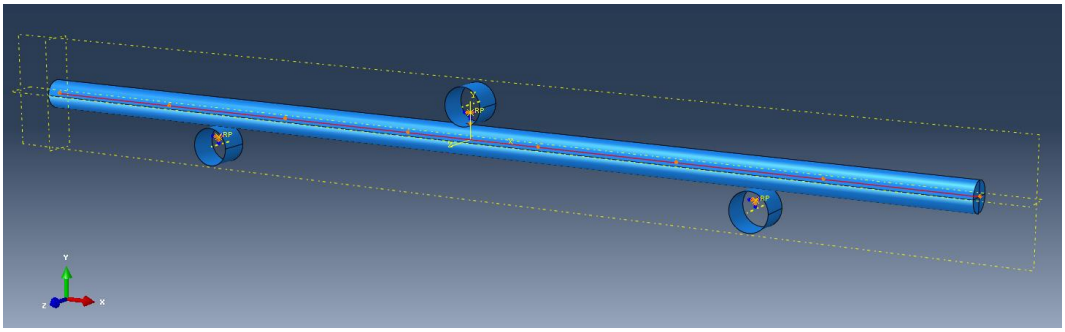

Figure 4-39 The central line of the wire was constrained in the Z-direction.

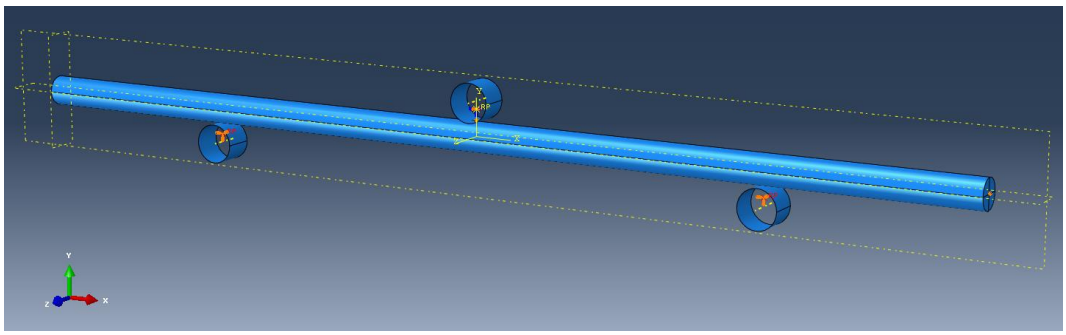

Figure 4-40 All displacements and rotations were constrained on the reference points of the supports.

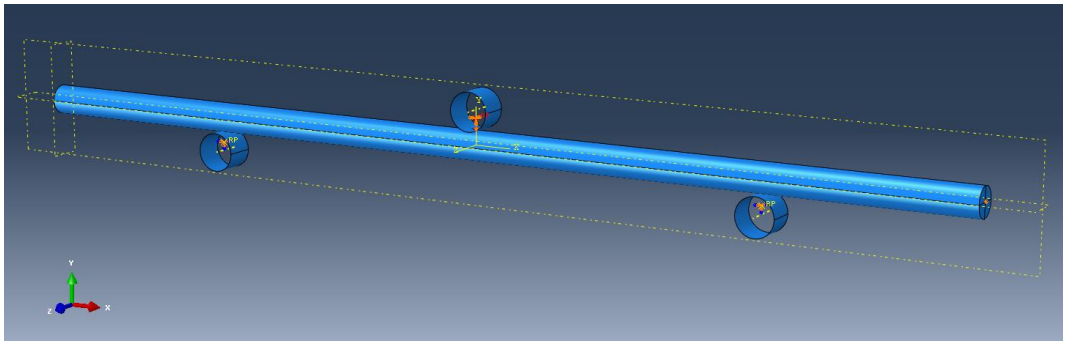

Figure 4-41 A known displacement was applied in the Y-direction of the reference point that controlled the indentor in order to bend the wire. All other displacements and rotations on this reference point were constrained.

Table 4-21 Summary of the BCs used in the three-point bend model.

Boundary condition	Simulation Steps		
	Initial	Step 1- Load	Step 2- Unload
Displacement in the Z-direction was constrained for the central line of the wire. All other displacements were unconstrained on the central line.	**Created**	Propagated	Propagated
All displacements and rotations were constrained for the reference points of the supports.	**Created**	Propagated	Propagated
Displacement in the Y-direction was applied for the reference point of the indentor. All other displacements and rotations were constrained for this reference point.		**Created**	**Modified:** Displacement in the Y-direction was reversed.

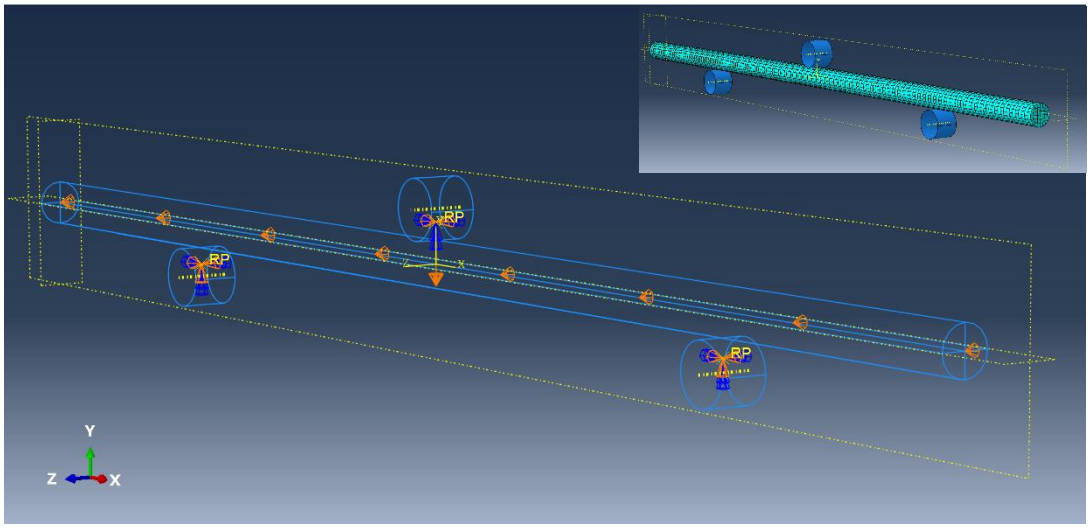

Figure 4-42 BCs of the three-point bend model. The meshed geometry is shown in the upper right corner.

The wire was meshed using incompatible mode, three-dimensional, 8-node, linear hexahedral (brick) elements (C3D8I). Incompatible mode elements were created in Abaqus in order to overcome the issues of shear locking in fully integrated linear solid elements subjected to bending [106]. Shear locking is described as the phenomenon which causes the elements to be overly stiff in bending resulting in under-predicted deflections. If used appropriately, in a relatively simple geometry with a fine mesh, incompatible mode elements produce results comparable to quadratic elements at a lower computational cost which becomes crucial when the number of elements is significantly large.

Prior to the final analysis, the mesh sensitivity was examined in order to determine the suitable number of elements in the model. The number of elements in the cross-section was controlled by changing the seeding size on the partition edges while the number of elements in the longitudinal direction was controlled by the seeding size of the edges in that direction. The force magnitude was initially used to assess the mesh sensitivity. However, the resulting force was the same for all simulations, giving a false 'sense' of convergence. This is not uncommon in FEA. In such cases, an additional criterion is selected to examine the mesh sensitivity. For the bending simulations discussed here, the maximum principal stress was chosen as the additional criterion.

The results of the mesh sensitivity study are shown in Table 4-22, which shows the number of elements that were used in each simulation, the maximum principal stress and the percentage stress difference between each simulation and the reference case. The reference simulation was the one with the highest number of elements (simulation number 5). The wall-clock times are also presented for all simulations which were run on two 'Intel Xeon E5-1650 v3 3.50GHz' cores. Wall-clock times were extracted from the '.dat' output file after each the simulation was finished.

Due to the partitions, a symmetric mesh is automatically enforced in the cross-section. The initial number of elements in the cross-section of the wire was 32 and it was later increased to 44, as seen in Table 4-22. The results of Table 4-22 are also presented in Figure 4-43, where maximum principal stress and wall-clock time were plotted against the number of elements. The mesh of case 3 was chosen for the final simulations due to the trade-off between computational time and percentage stress difference from the benchmark case.

As mentioned earlier, Abaqus can provide the user with information regarding the aspect ratio of the elements if the 'mesh verify' function is used. For case 3, the average aspect ratio was 1.75. When the final simulation was finished, force and displacement data were extracted and then compared with experimental results.

Table 4-22 Results of the mesh sensitivity study for the three-point bend model.

Simulation case	Number of elements			Max princ. stress	Max princ. stress diff	Wall-clock time (sec)	Time diff
	cross-section	length	total				
1	32	85	2720	666	1.99%	183	-75.63%
2	32	173	5536	662	1.38%	386	-48.60%
3	44	173	7612	657	0.61%	461	-38.62%
4	44	220	9680	654	0.15%	628	-16.38%
5	44	265	11660	653	-	751	-

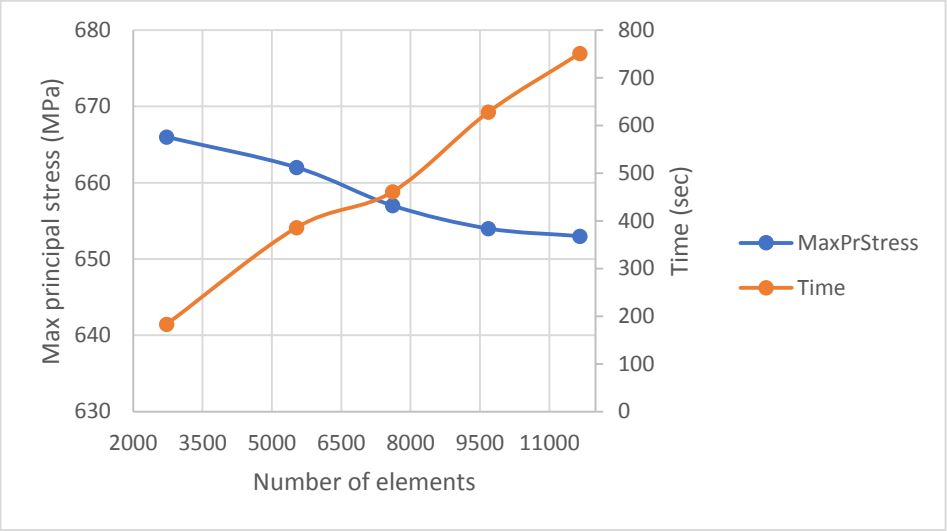

Figure 4-43 Max principal stress and wall-clock time plotted against the number of elements for the simulation cases of Table 4-22.

4.2.6 Torsion modelling

Torsion was simulated with two wire models which were created as 3D deformable parts with a solid homogeneous section, using the 'solid extrude' function in Abaqus. The dimensions of the modelled wires were: 1.8mm in diameter and 16mm in length for the first and 2.4mm in diameter and 20mm in length for the second wire. The cross-section of the wires was partitioned into four quarters through the whole length.

The movement of the right end of the wire which was rotated, was controlled using a 3D reference point. This was achieved by applying a 'kinematic coupling' type

constraint between the right end of the wire and the reference point, as shown in Figure 4-44.

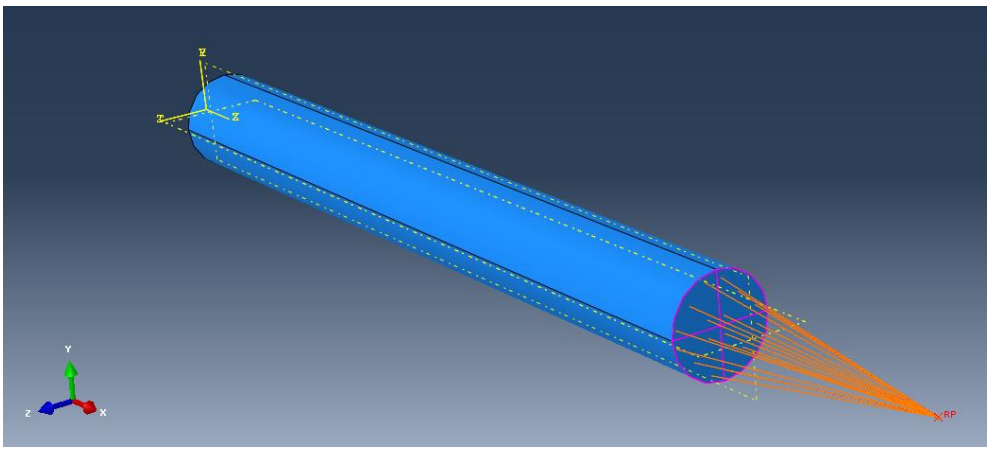

Figure 4-44 A 'kinematic coupling' type constrained was applied between the right end of the wire and a reference point.

The BCs of the model were applied on two coordinate systems: global and cylindrical. In the cylindrical coordinate system, the R-, Θ-, and Z- axes are interpreted as the 1-, 2- and 3- axes respectively, instead of the X-, Y- and Z-. The displacement of the central line of the wire was constrained in the R-direction during all steps (Figure 4-45). All other displacements were unconstrained. The displacement of the left end of the wire, as shown in Figure 4-46, was constrained in the Θ-direction and in the Z-direction. Any other displacements on this face were unconstrained.

In step 1 of the simulation, a rotation was applied in the X-direction (in the global coordinate system) of the reference point (Figure 4-47), causing the right end of the wire to rotate. The rotational displacement was reversed in step 2, unloading the wire. The above BCs are summarised in Table 4-23. Figure 4-48 also shows the BCs of the model with the 'wireframe' visualisation enabled.

The same model was also used to simulate combined tension-torsion. In this case two more steps were added between step 1 and step 2. During these two steps, an axial displacement was applied on the reference point to pull the right end of the wire in tension. The displacement was then reversed to remove the tensile load.

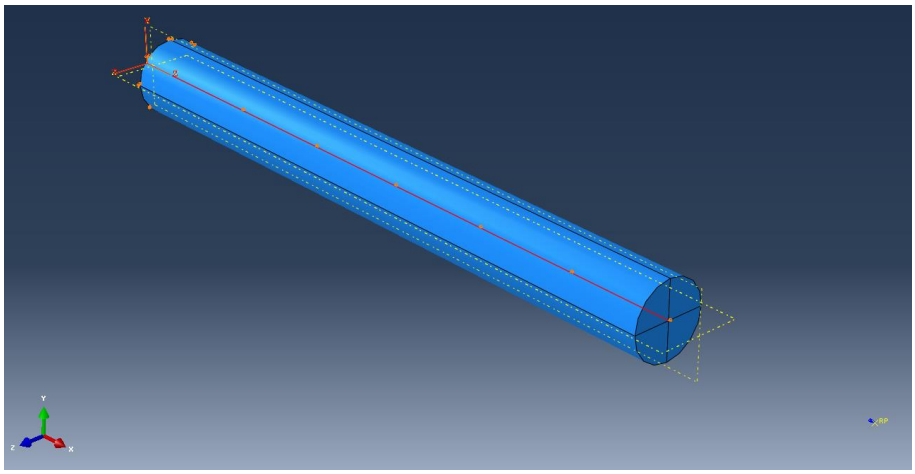

Figure 4-45 The central line of the wire was constrained in the R-direction.

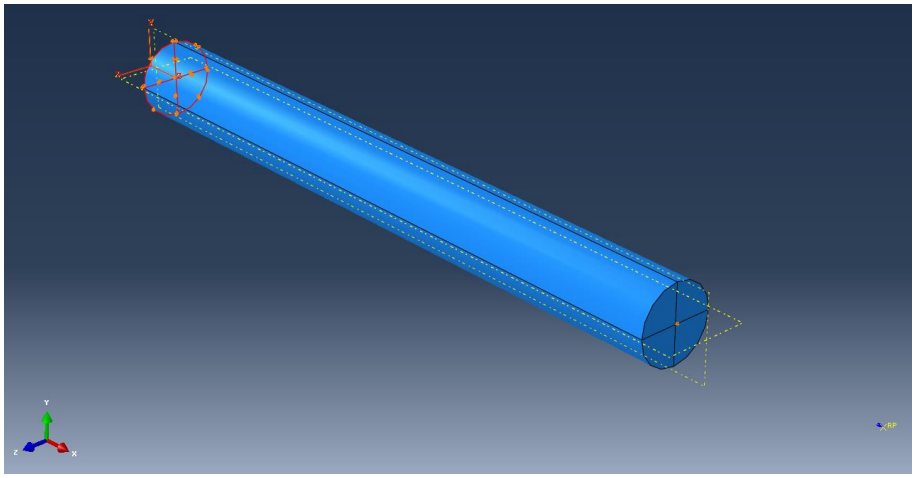

Figure 4-46 The left end of the wire was constrained in the Θ-direction and in the Z-direction.

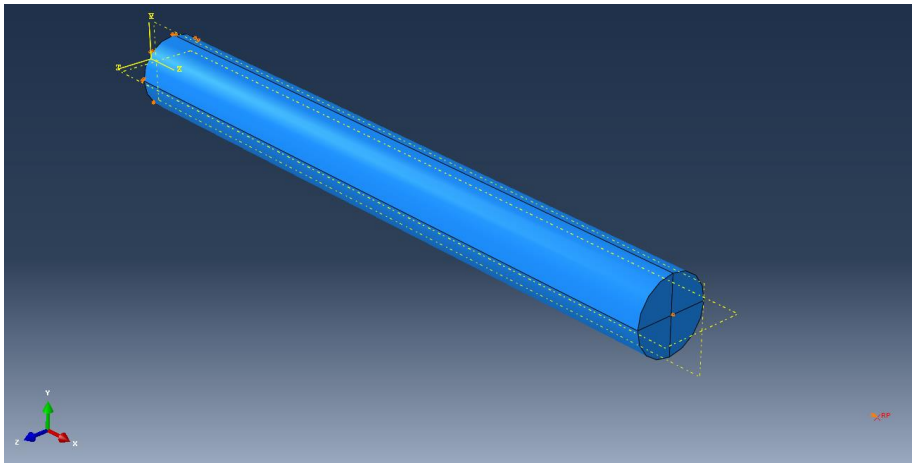

Figure 4-47 A rotational displacement in the X-direction (global coordinate system) was applied on the reference point which caused the right end of the wire to rotate.

Table 4-23 Summary of the BCs used in the torsional model.

Boundary condition	Simulation Steps		
	Initial	Step 1- Load	Step 2- Unload
Displacements in the Θ-direction and the Z-direction were constrained for the left face of the wire (as seen in Figure 4-46). All other displacements for this face were unconstrained.	**Created**	Propagated	Propagated
Displacement in the R-directions was constrained for the central line of the wire. All other displacements for the central line were unconstrained.	**Created**	Propagated	Propagated
Rotation in the X-direction (in the global coordinate system) was constrained for the reference point of the right face. All other displacements and rotations for the reference point were unconstrained.	**Created**	**Modified:** Rotation was applied in the X-direction.	**Modified:** Rotation was reversed.

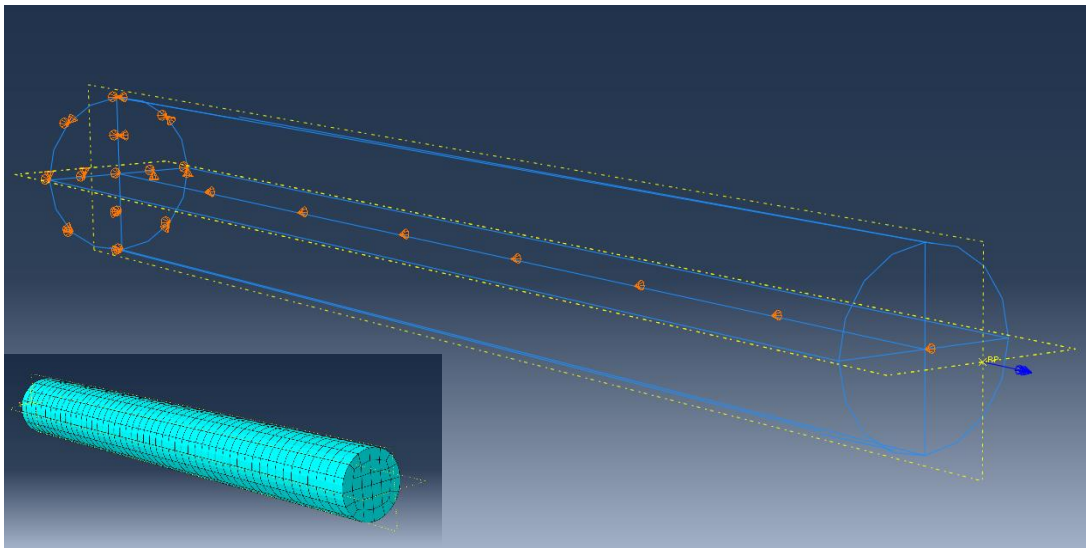

Figure 4-48 BCs of the torsional model. The meshed geometry is shown in the bottom left corner.

Reduced-integration 20-node quadratic brick elements C3D20R were used to mesh the geometries. The mesh sensitivity was examined prior to the final analysis in order to determine the suitable number of elements in the model. The number of elements in the cross-section was controlled by changing the seeding size on the partition edges. The number of elements in the longitudinal direction was separately controlled by the seeding size of the edges in that direction.

The torque magnitude was initially used to assess the mesh sensitivity. However, the resulting torque was the same for all simulations, giving a false 'sense'

of convergence. Therefore, the maximum shear stress was selected as the additional criterion. The results of the mesh sensitivity study are shown in Table 4-24, which shows the number of elements that were used in each simulation, the maximum shear stress and the percentage stress difference between each simulation and the reference case. The reference simulation was the one with the highest number of elements (simulation number 5). The wall-clock times are also shown for all simulations which were run on two 'Intel Xeon E5-1650 v3 3.50GHz' cores. Wall-clock times were extracted from the '.dat' output file after each the simulation was finished.

Due to the partitions, a symmetric mesh is automatically enforced in the cross-section. The initial number of elements in the cross-section of the wire was 32 and it was later increased to 44, as seen in Table 4-24. The same results are also presented in Figure 4-49, where maximum shear stress and wall-clock time were plotted against the number of elements. The mesh of case 4 was chosen for the final simulations due to the trade-off between computational time and percentage stress difference from the benchmark case. Using the 'mesh verify' function the average aspect ratio was identified to be 1.59. When the final simulation was finished, torque and rotation data were extracted and then compared with experimental results.

Table 4-24 Results of the mesh sensitivity study for the torsion model.

Simulation case	Number of elements			Max princ. stress	Max princ. stress diff	Wall-clock time (sec)	Time diff
	cross-section	length	total				
1	32	10	320	460	1.10%	33	-94.68%
2	32	25	800	459	0.88%	95	-84.68%
3	32	50	1600	461	1.32%	250	-59.68%
4	44	50	2200	454	-0.22%	390	-37.10%
5	44	70	3080	455	-	620	-

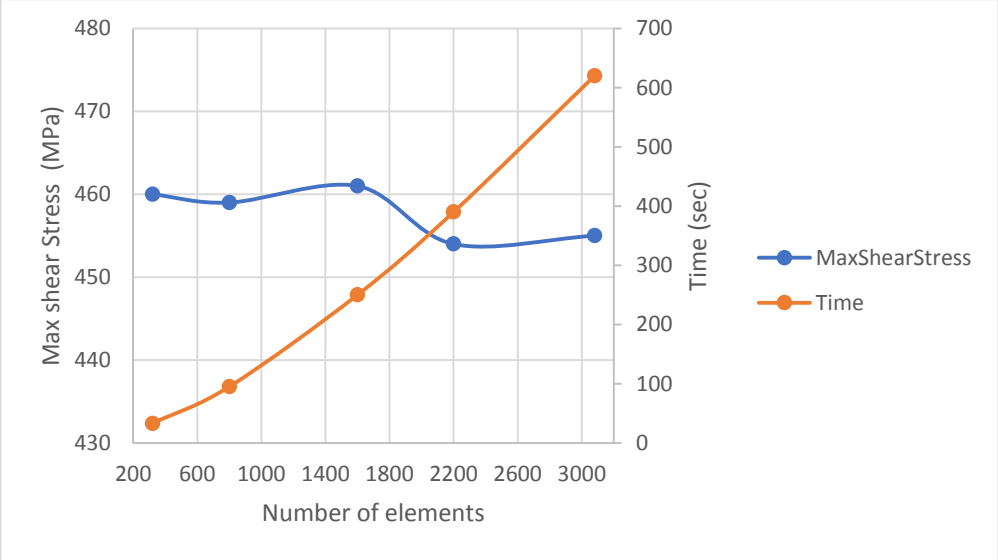

Figure 4-49 Max shear stress and wall-clock time plotted against the number of elements for the simulation cases of Table 4-24.

Chapter 5 Experimental Results

The following sections present the experimental results of this work. These were produced using the test methods described earlier in the previous Chapter. Observations and findings are discussed in Chapter 7.

5.1 Tensile response within the superelastic range

Figure 5-1 presents the tensile stress-strain response of the 1mm Nitinol wire when deformed within the superelastic range at 22°C and 37°C. Results correspond to the first cycle of Type I tensile testing as explained earlier in section 4.1.2. Both curves share the same characteristics. They are composed of essentially two linear regions and two nearly flat plateaus. Upon loading, the slope of the linear region represents the elastic modulus of austenite. It was calculated to approximately 44GPa at 22°C and 64GPa at 37°C by finding the equation for the linear trendline fitted to the raw data.

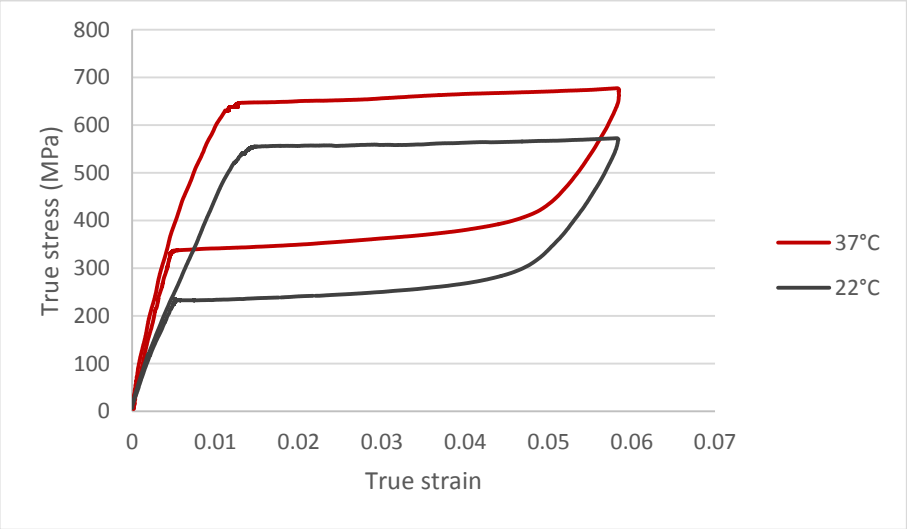

Figure 5-1 Stress-strain response of the 1mm Nitinol wire subjected to tension within the superelastic range at 22°C and 37°C.

The linear elastic region extends to approximately 1.4% strain at 22°C and to 1.25% strain at 37°C. The transformation from austenite to martensite is depicted by the upper plateau, as stress increases minimally with strain at both test temperatures. Transformation during loading takes place at approximately 540Mpa at 22°C and at 630MPa at 37°C. Loading in the results above ends at around 570MPa at 22°C and at 670Mpa at 37°C.

Upon unloading, the linear elastic region corresponds to the deformation of the material in the martensitic state assuming a complete transformation has been achieved. The slope of this region represents the elastic modulus of martensite which seems significantly less sensitive to temperature changes. Therefore, a similar value of approximately 31GPa can be adopted for both cases. This value was again obtained from the equation of the linear trendline fitted to the raw data. Transformation during unloading takes place at 300Mpa at 22°C and at 405MPa at 37°C. Transformation is completed at 200MPa at 22°C and at 280Mpa at 37°C, as the material reverts to its austenitic state. The final linear region of the curves corresponds to the elastic unloading of austenite. The quantitative data from the stress-strain responses of Figure 5-1 are also presented in Table 5-1.

Table 5-1 Tensile results obtained from the stress-strain curves of Figure 5-1.

	22°C	37°C
Austenite elastic modulus	44GPa	64GPa
End of linear loading region	1.4% strain	1.25% strain
Start of transformation during loading	540MPa	630MPa
Stress at 6% strain	570MPa	670MPa
Martensite elastic modulus	31GPa	31GPa
Start of transformation during unloading	300MPa	405MPa
End of transformation during unloading	200MPa	280MPa

5.2 Tensile loading beyond the superelastic region

Figure 5-2 presents the tensile stress-strain response of the 0.45mm Nitinol wire when deformed beyond the superelastic region, up to 10% true strain. Results

are derived from the second cycle of Type I tensile testing. During loading at 22°C, the slope of the curve changes abruptly at a stress level of approximately 220MPa, indicating the presence of R-phase in the material. As the ambient temperature is raised, the volume fraction of austenite in the material increases. The austenitic region of the stress-strain curve is then expanded, thus the above phenomenon is no longer seen.

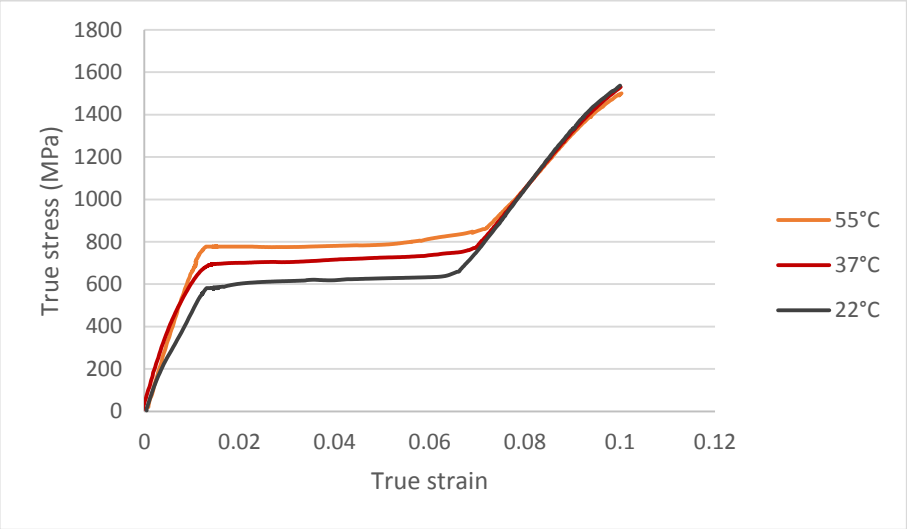

Figure 5-2 Tensile stress-strain response of the 0.45mm Nitinol wire when loaded beyond the superelastic range at different temperatures.

The elastic modulus of austenite is increased as temperature is raised from 22°C to 37°C. However, minimal difference is noted from 37°C to 55°C. Instead, the initial part of the curve becomes more linear at 55°C which is associated with the absence of R-phase at this temperature. Nevertheless, the transformation stresses keep increasing with temperature. Beyond the superelastic range, the three curves merge, following the same path into the post-transformation region. Loading at this point proceeds by ordinary martensite elastic-plastic deformation and not by phase transformation, hence the temperature sensitivity is suppressed.

Note that extrapolating the post-transformation curve gradients down to the strain axis leads to similar strain values. The transformation strain of the material, as defined in Abaqus, is approximately 0.0465 at 22°C and 0.048 at 37°C, values which

will be later used for computational modelling. The actual load plateau length however increases slightly with temperature.

5.3 High-strain tensile deformation

Figure 5-3 presents the stress-strain response of the 0.22mm standard Nitinol wire (NiTi#1-SE) when subjected to high-strain tensile deformation at 37°C for a single cycle. Results correspond to the first cycle of Type II tensile testing. In all curves illustrated below, the slope of the initial elastic region changes at approximately 450MPa indicating the presence of R-phase. A small stress overshoot is observed beyond the elastic loading at the onset of the upper plateau. Transition to the post-transformation region takes place at somewhat different strain level for each curve.

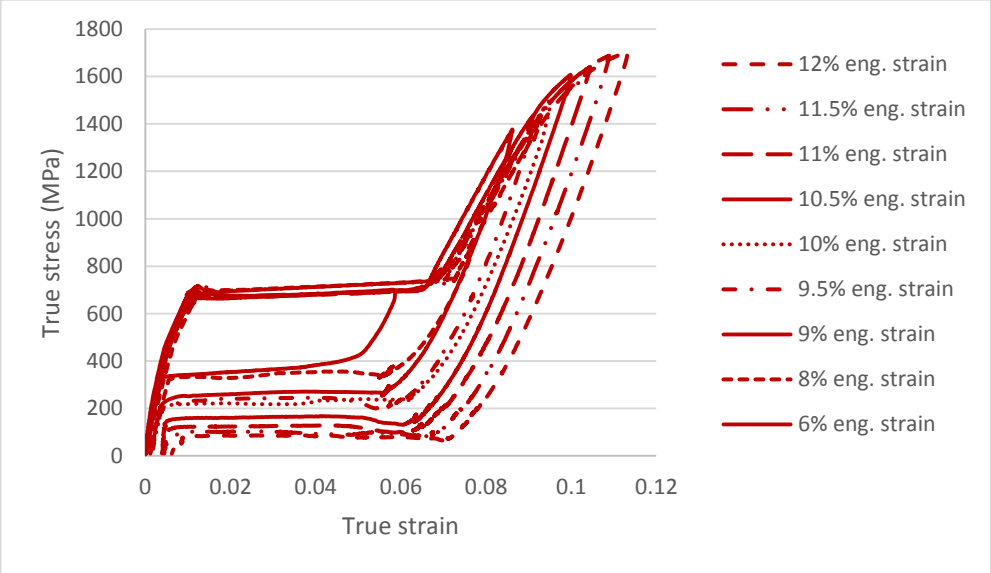

Figure 5-3 Stress-strain response of the 0.22mm NiTi#1-SE wire subjected to high-strain tensile deformation at 37°C.

During unloading, the slope of the region that corresponds to the unloading modulus of martensite is noticeably changed, depending on the applied post-transformation strain. Each curve does not follow its initial post-transformation loading path. This observation is better illustrated in Figure 5-4 which compares the

elastic modulus of martensite during high-strain loading and unloading. The unloading modulus is initially increased with maximum applied strain reaching a peak value of approximately 49.8GPa at 11% strain and is then decreased at higher strains. By comparison, the modulus during post-transformation loading remains almost the same. Detailed results extracted from each stress-strain curve are also presented in Table 5-2.

The lower, unload plateau is different for each curve depending on the maximum applied strain. With increasing deformation beyond 8% engineering strain, the unload plateau is shifted towards progressively lower stress levels. This is also seen in the values presented in Table 5-2. The unload plateau is also plotted against the applied engineering strain in Figure 5-5. The decrease of the unload plateau with increasing pre-strain seems to be almost linear. The strain range of interest in the present work is around 10% because of the interest in understanding the material properties during stent compaction.

The onset of the transformation during unloading takes place at approximately 270MPa, 180MPa and 130Mpa when unloading from 9.5%, 10.5% and 11.5% strain respectively. Correspondingly, the transformation ends at approximately 180MPa, 125MPa and 100MPa when unloading from 9.5%, 10.5% and 11.5% maximum strain respectively.

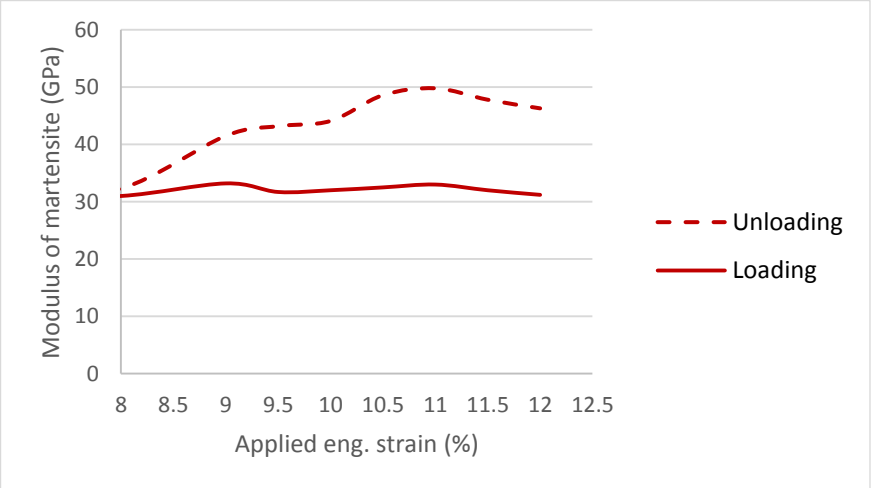

Figure 5-4 Elastic modulus of martensite, of the 0.22mm NiTi#1-SE wire, during loading and unloading against the applied engineering strain.

Unloading from 9.5% strain results in a lower plateau stress of 240MPa, measured at 3% strain. Similarly, unloading from 10.5% strain results in a lower plateau stress of 165MPa whereas unloading from 11.5% strain results in a lower plateau stress of only 105MPa. By comparison, the lower plateau stress when unloading within the superelastic range was approximately 360Mpa at 37°C.

Finally, residual strain varies greatly, depending on the pre-strain levels. The residual strain at the end of each load-unload cycle, is plotted against the applied pre-strain in Figure 5-6. There is only a small, gradual increase of residual strain with increasing pre-strain up to 10%. However, the residual strain appears to increase almost linearly with applied pre-strains greater than 10%. Unloading from 9.5% strain results in around 0.1% residual strain, whereas unloading from 10.5% and 11.5% strain results in 0.3% and 0.5% residual strain respectively. The residual strain values for each stress-strain curve are shown in Table 5-2.

Table 5-2 Tensile results obtained from the stress-strain curves of Figure 5-3.

	Loading strain							
	8%	9%	9.5%	10%	10.5%	11%	11.5%	12%
Unload plateau stress	360MPa	270MPa	240MPa	210MPa	165MPa	140MPa	105MPa	85MPa
Residual strain	0.05%	0.09%	0.1%	0.12%	0.3%	0.35%	0.5%	0.8%
Martensite modulus in loading	31GPa	33.2GPa	31.7GPa	32GPa	32.5GPa	33GPa	32GPa	31.2GPa
Martensite modulus in unloading	32.3GPa	41.5GPa	43.2GPa	44.1GPa	48.6GPa	49.8GPa	47.8GPa	46.3GPa

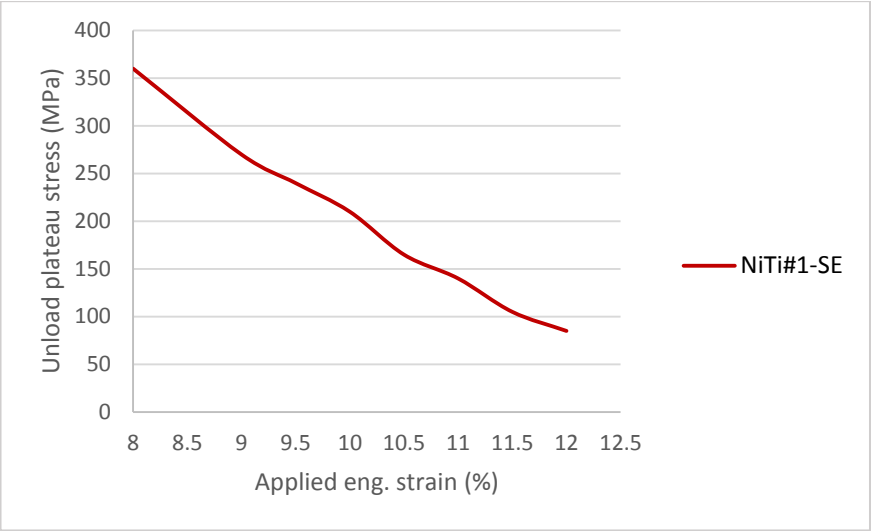

Figure 5-5 Unload plateau stress of the 0.22mm NiTi#1-SE wire against the applied engineering strain.

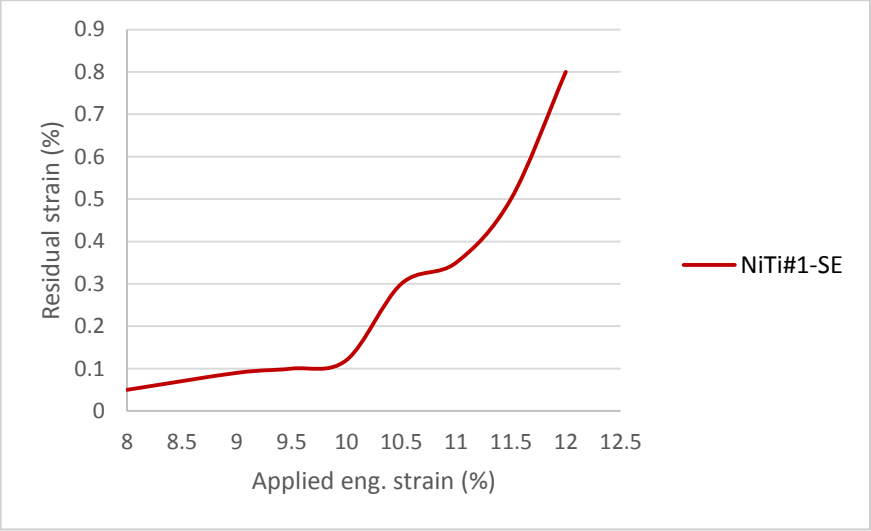

Figure 5-6 Residual strain of the 0.22mm NiTi#1-SE wire against the applied engineering strain.

5.4 Effect of high-strain cycling on the tensile response

Figure 5-7 presents the stress-strain response of the 0.22mm NiTi#1-SE wire subjected to high-strain deformation beyond the superelastic range for three cycles at 37°C. The motivation for investigating three cycles of loading is related to the practical compaction process. These curves correspond to the complete results of

Type II tensile testing for three different maximum strain levels, namely 10%, 10.5% and 11%.

With increasing cycles, the following qualitative features are noted in the illustrated responses: the elastic modulus of austenite is decreased, the transformation stresses during loading are decreased and the residual strain is increased. These are characteristics expected during cycling. However, the effect here is pronounced due to the marked initial strain present at the start of each cycle. In Figure 5-7(c), after pre-straining the material to 11% engineering strain, the elastic modulus of austenite is reduced to 35GPa and 26GPa in the second and third cycles respectively. By comparison its initial value during the first cycle was approximately 64GPa at 37°C. Transformation during loading takes place at 520MPa and 460MPa in the second and third cycles respectively, compared to 630MPa in the first cycle. Similarly, transformation during loading ends at approximately 600MPa and 540MPa during the second and third cycles respectively, compared to 710MPa in the first. The load plateau (measured at 3% strain) is decreased from approximately 700MPa in the first cycle to 477MPa in the third. The lower plateau is decreased by a smaller amount due to cycling. It is reduced from 140MPa during the first cycle to 80MPa in the third cycle. These results are also shown in Table 5-3 for each stress-strain curve of Figure 5-7. Residual strain increases from 0.35% in the first cycle to approximately 0.75% and 0.9% in the second and third cycles respectively.

The above phenomena are also noted in the graphs of Figures 5-7(a) and 5-7(b), yet less pronounced due to the lower level of initial strain present. When deforming the material to 10.5% strain, the elastic modulus of austenite is reduced to 44GPa and 34GPa in the second and third cycles respectively. Similarly, the load plateau is reduced to 572MPa in the second cycle and 500MPa in the third cycle. The lower plateau drops from 165MPa in the first cycle to 135MPa in the second, and to 125MPa in the third cycle. Residual strain is approximately 0.3% after completion of the first cycle and it increases to 0.6% and 0.7% after the second and third cycle respectively.

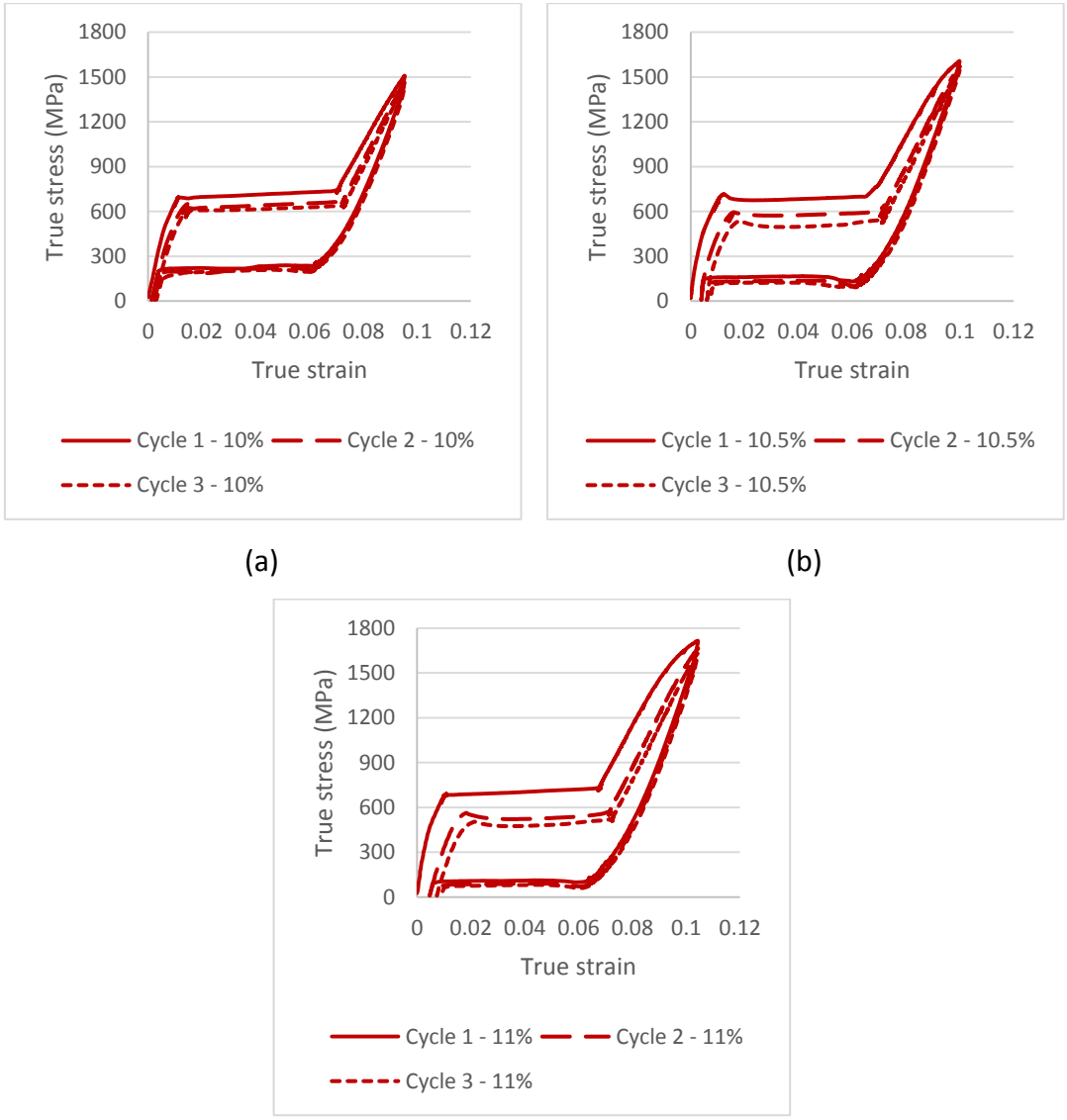

Figure 5-7 Stress-strain response of the 0.22mm NiTi#1-SE wire subjected to high-strain tensile cycling at 37°C.

When deforming the material to 10% strain, the elastic modulus of austenite is decreased to 52GPa in the second cycle and to 50GPa in the third. The load plateau is reduced only by 90MPa after three cycles of loading. The unload plateau is reduced from 210MPa in the first cycle to 200MPa in the second and to 190MPa in the third cycle. Finally, the accumulated residual strain was 0.12%, 0.23% and 0.3% at the end of the first, second and third cycles respectively.

Table 5-3 Tensile results obtained from the stress-strain curves of Figure 5-7.

	10% strain			10.5% strain			11% strain		
	Cycle 1	Cycle 2	Cycle 3	Cycle 1	Cycle 2	Cycle 3	Cycle 1	Cycle 2	Cycle 3
Austenite elastic modulus	64GPa	52GPa	50GPa	64GPa	44GPa	34GPa	64GPa	35GPa	26GPa
Load plateau stress	700MPa	630MPa	610MPa	680MPa	572MPa	500MPa	700MPa	523MPa	477MPa
Unload plateau stress	210MPa	200MPa	190MPa	165MPa	135MPa	125MPa	140MPa	90MPa	80MPa
Residual strain	0.12%	0.23%	0.3%	0.3%	0.6%	0.7%	0.35%	0.75%	0.9%

5.5 Tensile deformation of the USN® wires

Figure 5-8 presents the stress-strain response of the 0.22mm USN® wire when deformed within the superelastic range, at 37°C. The response of the USN® material is also compared with the one exhibited by the NiTi#1-SE wire. Detailed results are shown in Table 5-4. Upon loading, the USN® wire is clearly stiffer as the elastic modulus of austenite is approximately 85GPa. The load plateau is very similar for both wires and the elastic modulus of martensite is also practically the same. However, the unload plateau of the USN® wire is located at higher stress levels.

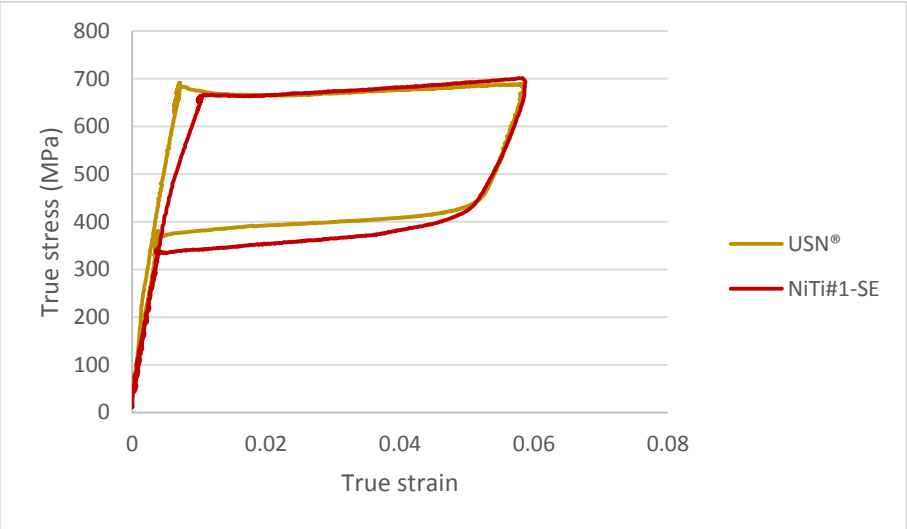

Figure 5-8 Stress-strain responses of the 0.22mm NiTi#1-SE and USN® wires subjected to tension within the superelastic range, at 37°C.

Table 5-4 Tensile results obtained from the stress-strain curves of Figure 5-8.

	USN®	NiTi#1-SE
Austenite elastic modulus	85GPa	64GPa
End of linear loading region	0.8% strain	1.25% strain
Start of transformation during loading	650MPa	630MPa
Stress at 6% strain	680MPa	670MPa
Martensite elastic modulus	31GPa	31GPa
Start of transformation during unloading	430MPa	405MPa
End of transformation during unloading	305MPa	280MPa

The post-transformation elastic-plastic deformation of the material is illustrated in Figure 5-9 which presents the stress-strain response of the 0.22mm USN® wire when subjected to high-strain tension at 37°C for a single cycle. The unload plateau stress depends on the maximum strain applied during loading and starts decreasing at lower strain levels compared to the NiTi#1-SE material (7% vs 8% strain). Because of this, between 8% and 9% pre-strain, the NiTi#1 wire exhibits higher unload plateaus. This can be seen in Figure 5-10, where the unload plateau stress is plotted against the applied pre-strain. The behaviour of the NiTi#1 wire is also plotted in the same graphs to allow for a direct comparison between the two different Nitinol specimens. The unload plateau of the USN® wire is altered more gradually and it remains at higher stress levels compared to the unload plateau of the NiTi#1-SE wire at the same conditions. The residual strain at the end of the load-unload cycles of the USN® wire, is greater compared to the standard Nitinol wire. In Figure 5-11, it can be seen that the residual strain of the USN® wire increases almost linearly with applied pre-strain, even at small pre-strain levels. The quantitative results for the above observations are presented in Table 5-5.

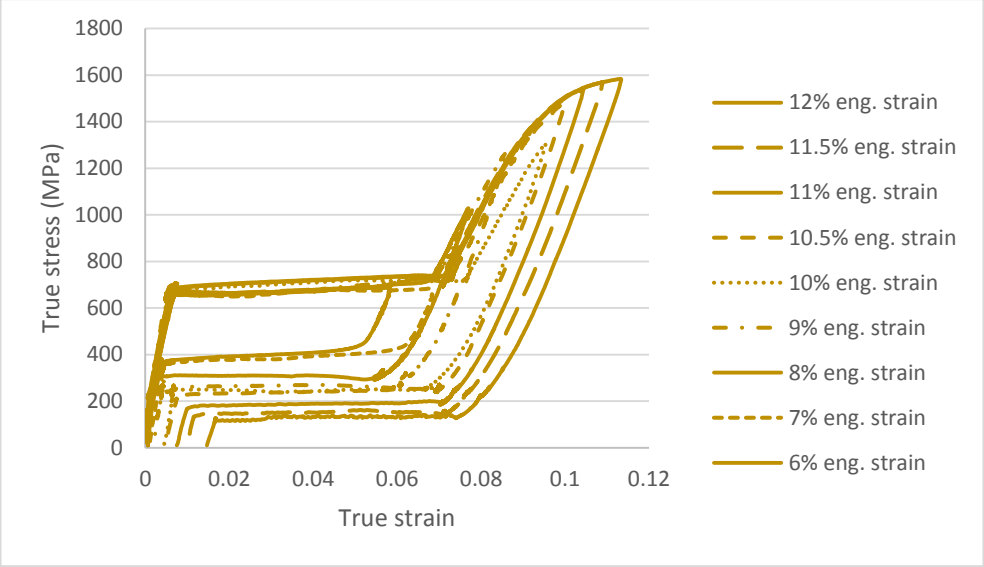

Figure 5-9 Stress-strain response of the 0.22mm USN® wire subjected to high-strain tensile deformation at 37°C.

Table 5-5 Tensile results obtained from the stress-strain curves of Figure 5-9.

	Loading strain								
	6%	7%	8%	9%	10%	10.5%	11%	11.5%	12%
Unload plateau stress	400	380	310	270	260	237	190	150	130
Residual strain	-	-	0.06%	0.2%	0.45%	0.52%	0.8%	0.98%	1.47%

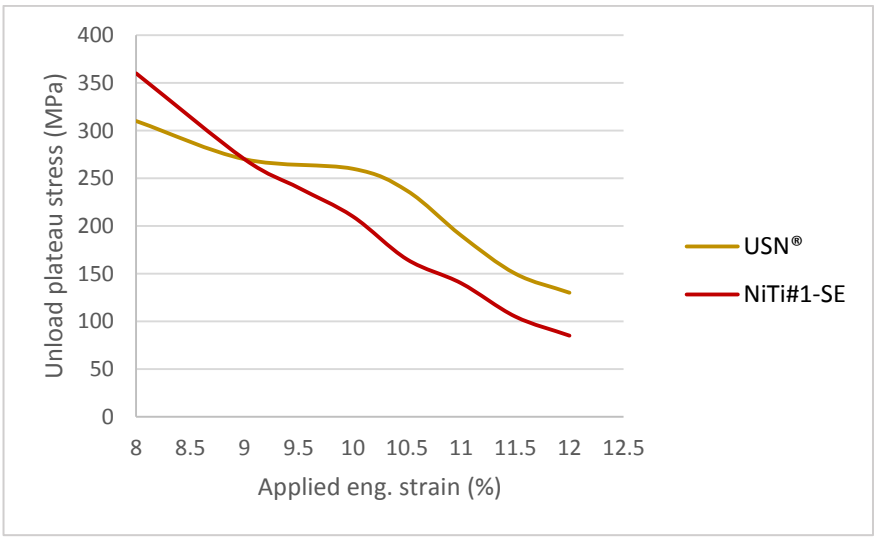

Figure 5-10 Unload plateau stress, of the 0.22mm USN® and NiTi#1-SE wires, against the applied engineering strain.

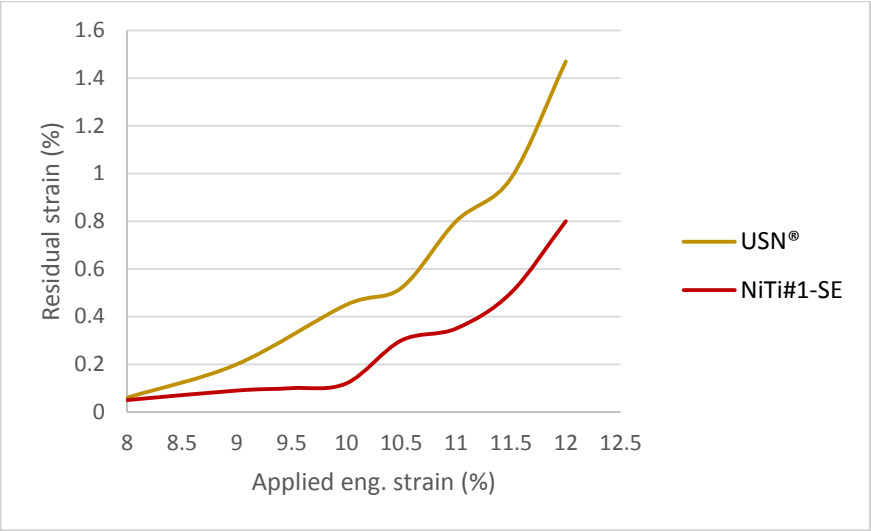

Figure 5-11 Residual strain, of the 0.22mm USN® and NiTi#1-SE wires against the applied engineering strain.

Figure 5-12 presents the stress-strain response of the 0.22mm USN® wire subjected to high-strain deformation beyond the superelastic range for three cycles at 37°C. The illustrated curves correspond to the complete results of Type II tensile testing for 10% and 11% maximum strain. The USN® specimen exhibits qualitative features similar to the ones discussed earlier for the NiTi#1-SE wire when subjected to cycling. However, a few differences are observed between the responses of the two materials regarding the initial stiffness, the unload plateau and the residual strain.

Although the elastic modulus of austenite is reduced in the second and third cycles as expected, it is always greater than its standard Nitinol counterpart in the same conditions, as seen in Table 5-6. When unloading the USN® wire from 10% strain, the lower plateau stress is approximately 260MPa (measured at 3% strain). The stress is considered the same in the second and third cycles since it is only marginally reduced. On the contrary, the NiTi#1-SE wire exhibited a lower plateau stress of 210MPa during the first cycle which was reduced to 190MPa in the third cycle. The accumulated residual strain of the USN® specimen was 0.45%, 1.4% and 1.55% at the end of the first, second and third cycles respectively. These values are considerably higher compared to the ones exhibited by the NiTi#1-SE wire during

unloading from 10% strain. This can be seen by comparing the results of Table 5-3 and Table 5-6.

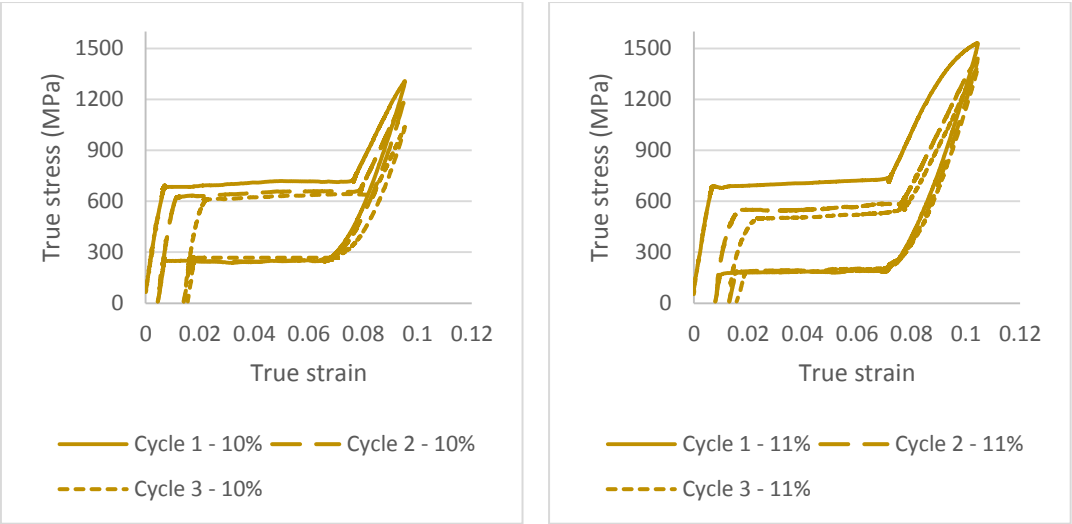

(a) (b)

Figure 5-12 Stress-strain response of the 0.22mm USN® wire subjected to high-strain tensile cycling at 37°C.

Table 5-6 Tensile results obtained from the stress-strain curves of Figure 5-12.

	10% strain			11% strain		
	Cycle 1	Cycle 2	Cycle 3	Cycle 1	Cycle 2	Cycle 3
Austenite elastic modulus	85GPa	85GPa	78GPa	85GPa	64GPa	52GPa
Load plateau stress	701MPa	640MPa	614MPa	700MPa	546MPa	500MPa
Unload plateau stress	~260MPa			~190MPa		
Residual strain	0.45%	1.4%	1.55%	0.8%	1.45%	1.6%

When unloading the USN® wire from 11% maximum strain, the lower plateau stress is approximately 190MPa which is again only marginally reduced in the following cycles. By comparison, the unload plateau stress of the standard wire was 140MPa in the first cycle and 80MPa in the third cycle. However, the accumulated residual strain of the USN® wire was 0.8%, 1.45% and 1.6% at the end of the first, second and third cycles respectively. Therefore, these values are again greater than those exhibited by the NiTi#1-SE wire at the same conditions. Interestingly, the load

plateau is reduced by a similar amount for the USN® and NiTi#1-SE wires, as it can be seen in Table 5-3 and Table 5-6.

5.6 Comparison between different diameter wires

Figure 5-13 illustrates the superimposed stress-strain responses of 0.22mm, 0.45mm and 1mm diameter wires subjected to tension within the superelastic range at 37°C. Although testing was performed in a temperature-controlled environmental chamber, using the same test method, results between the different specimens can vary. These differences could be attributed to the slightly different processing required for each specimen as explained later in Chapter 7. Upon loading, the elastic modulus of austenite is considered approximately the same for all specimens. The load plateau of the 1mm wire is placed at somewhat lower stress levels (656MPa) compared to the other two wires, as seen in Table 5-7.

Deformation to 6% engineering strain ends at approximately 670MPa, 690MPa and 700MPa for the 1mm, 0.22mm and 0.45mm specimens respectively. The unloading martensite modulus from 6% strain is similar for all examined wires. Smaller differences are seen in the unload plateau of the stress-strain curves. The final, linear elastic region during unloading is similar for all wires.

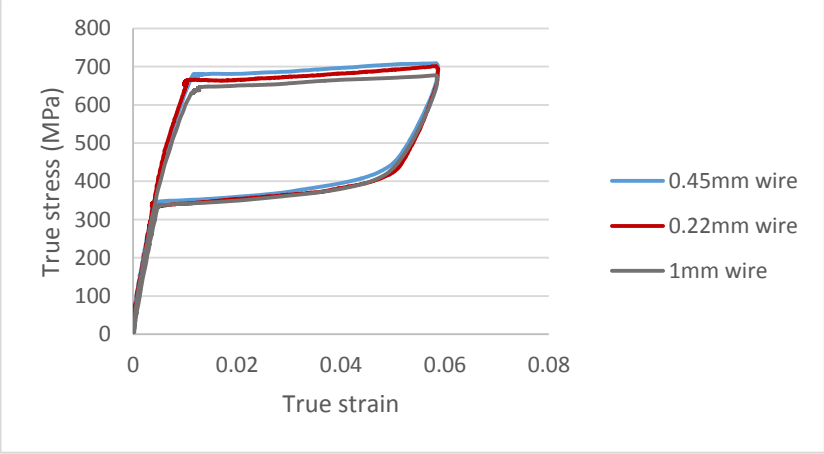

Figure 5-13 Superimposed stress-strain response of the 0.22mm (NiTi#1-SE), 0.45mm and 1mm Nitinol wires subjected to tension within the superelastic range at 37°C.

Table 5-7 Tensile results obtained from the stress-strain curves of Figure 5-13.

Wire diameter (mm)	UPS (MPa)	LPS (MPa)	Stress at 6% strain (MPa)
0.45	687	373	700
0.22	673	365	690
1	656	360	670

5.7 Uncertainty in the tensile tests

Three different 1mm diameter wires were subjected to tension within the superelastic range for a single cycle, and then pulled to failure as per ASTM F2516, at 22°C. The force recorded by the load cell during these tests was plotted against the engineering strain measured by the video extensometer, as shown in Figure 5-14. Force and engineering strain were selected here because these parameters are directly measured by the testing machine and reported in the raw data file. Macroscopically, only minor qualitative differences are seen between the illustrated curves.

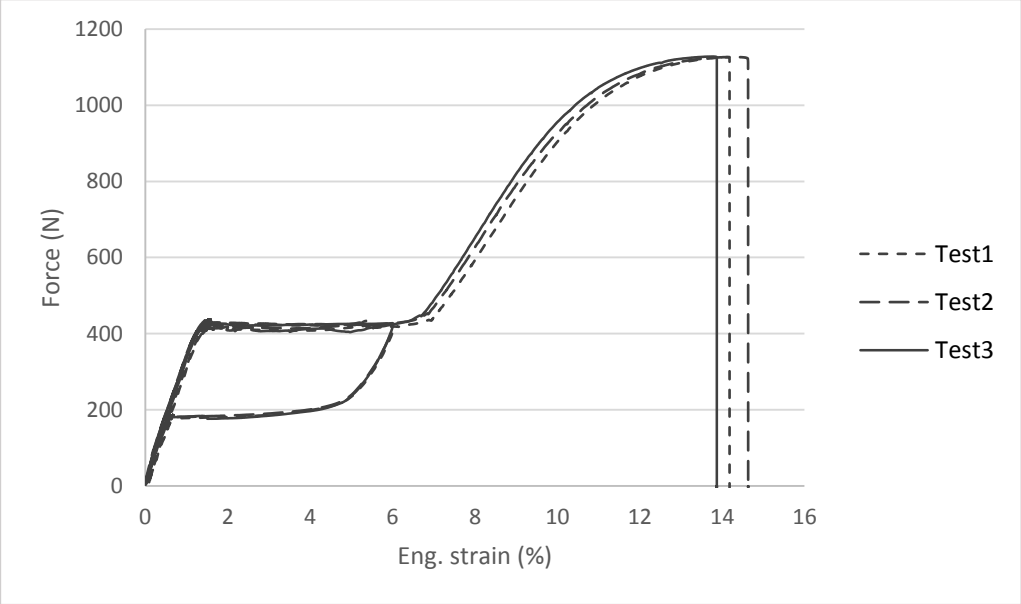

Figure 5-14 Force against engineering strain for three different 1mm wires subjected to tension within the superelastic range for a single cycle, and then pulled to failure, at 22°C.

From each test, values for the following parameters were extracted: upper and lower plateau forces, maximum force and uniform elongation (elongation at the maximum load). These parameters were chosen here because they are clearly identified in the results and do not depend on user-interpretation like the transformation forces/stresses. For each parameter, the mean value, standard deviation and standard error were calculated using the equations introduced in section 4.1.6. The calculations were performed using Microsoft Excel.

Table 5-8 Upper plateau force (UPF) at 3% strain, lower plateau force (LPF) at 3% strain, maximum force and uniform elongation (El_u) for the three different tensile tests of Figure 5-14. The following parameters were calculated for each result: mean value, standard deviation (STDEV), standard error (STError), systematic error (SysError), total error (TotError), relative error (RelError) and expanded error (ExpandErr).

Test	UPF (N)	LPF (N)	Max force (N)	El_u (% eng. strain)
1	423.32	186.94	1125.93	14.13
2	426.12	190.41	1126.43	14.25
3	421.42	184.79	1127.70	13.76
Mean	423.62	187.38	1126.69	14.05
STDEV	2.37	2.83	0.91	0.26
STError	1.37	1.64	0.53	0.15
SysError	2.12	0.94	5.63	0.07
TotError	2.52	1.88	5.66	0.16
RelError	0.59%	1.01%	0.50%	1.16%
ExpandErr	5.04	3.77	11.32	0.33

The results are shown in Table 5-8. The systematic error was also measured based on the accuracy specifications of the testing instruments that were mentioned earlier in section 4.1.6. For example, the systematic error for the upper plateau force was calculated by multiplying the mean value by 0.005 (since the load accuracy was 0.5% of the reading). The total or combined error was then estimated by adding the standard and systematic errors in quadrature using Equation 4-10 (section 4.1.6). Then, the expanded uncertainty was estimated based on the combined error multiplied by a coverage factor (k = 2), providing a level of confidence of

approximately 95%. The combined error was also used to calculate the percentage relative error, i.e. the combined error as a percentage of the mean value.

5.8 Compressive response at various strain levels

Figure 5-15 presents the compression stress-strain response of the EDM Nitinol specimens subjected to increasing strain increments, at 22°C. Compression to 2% strain results in a nearly linear curve with minor hysteresis. Beyond 2% strain, specimens are transformed to martensite at approximately 720MPa, exhibiting a positive slope transformation region during loading. Deformation beyond 4% strain results in a rapid increase of stress as features typical of post-transformation loading are shown in the macroscopic stress-strain response.

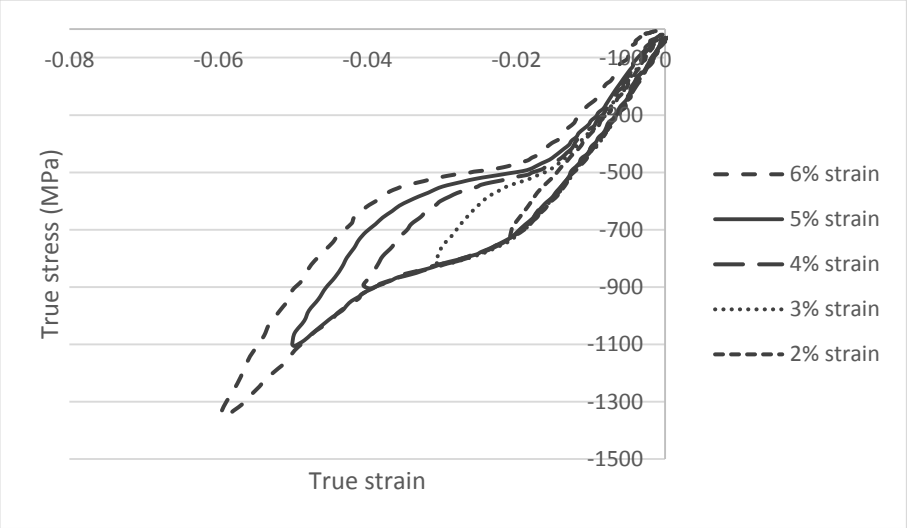

Figure 5-15 Compression stress-strain response of the 1mm Nitinol wire subjected to increasing strain increments at 22°C.

During unloading, the transformation stresses decrease progressively with applied strain beyond 4%. The lower plateau stress (measured at 3% strain) is approximately 600MPa when unloading from 4% maximum strain. By comparison, unloading from 5% and 6% strain results in a lower plateau stress of 550MPa and 520MPa respectively. Residual strain is negligible when unloading from a maximum

strain of 4%. However, unloading from 5% and 6% compressive strain results in approximately 0.1% and 0.15% residual strain respectively.

5.9 Tension-compression asymmetry

The compression stress-strain response differs from the tensile one, as seen in the previous section. The asymmetry is clearly illustrated when both results are plotted on the same graph in Figure 5-16. The two responses do not share the same characteristics; the tensile one is depicted by a flag-shaped curve whereas the compressive response is represented by a sigmoidal curve.

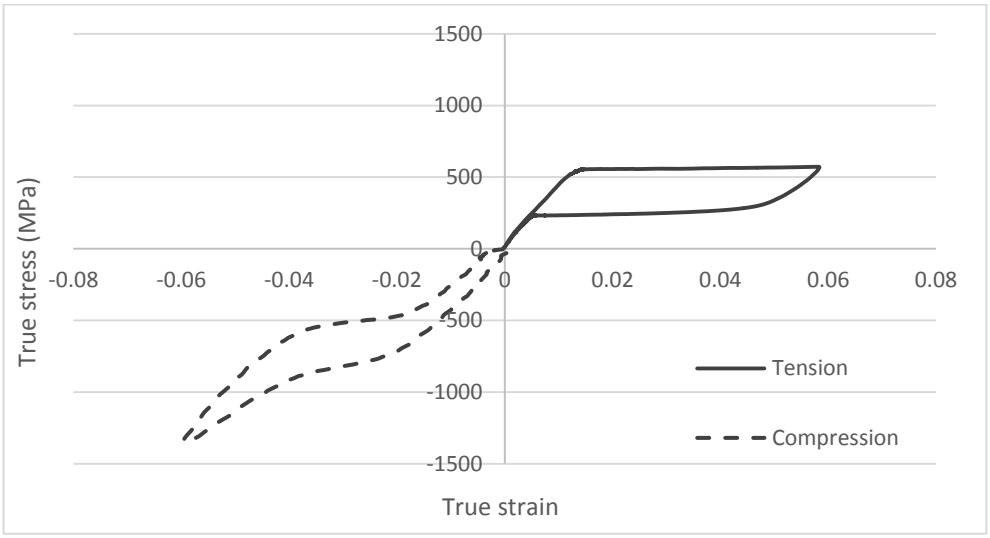

Figure 5-16 Tension-compression asymmetry: stress-strain response of the 1mm Nitinol wire subjected to 6% strain in tension and compression, at 22°C.

The linear elastic region upon loading extends to approximately 1.4% strain in tension and to 1.9% strain in compression. The elastic modulus of austenite is considered approximately the same in both responses. Transformation from austenite to martensite takes place at a stress level of approximately 540MPa in tension and 720MPa in compression. A nearly flat plateau is exhibited in tension extending to 6% strain and 570MPa of stress. On the contrary, a positive slope transformation region is seen during loading in compression extending to 4% strain

and 900MPa of stress. Beyond 4% compressive strain, the material enters the post-transformation region.

Upon unloading, the elastic modulus of martensite is considered the same for tension and compression. Reverse transformation takes place at 300Mpa in tension and at 575MPa in compression. Transformation is completed at 200MPa in tension and at 410Mpa in compression. No residual strain is present during the tensile deformation whereas compression results in approximately 0.15% residual strain. The energy loss of each curve was also calculated as explained in section 4.1.2. The percentage energy loss was approximately 46% in the tensile curve and 28% during the compression one. The above quantitative data are also presented in Table 5-9.

Table 5-9 Results obtained from the stress-strain responses of Figure 5-16.

	Tension	Compression
Austenite elastic modulus	44GPa	44GPa
End of linear loading region	1.4% strain	1.9% strain
Start of transformation during loading	540MPa	720MPa
Stress at 6% strain	570MPa	>900MPa
Martensite elastic modulus	31GPa	31GPa
Start of transformation during unloading	300MPa	575MPa
End of transformation during unloading	200MPa	410MPa
Residual strain	-	0.15%

5.10 Microscope images during compression

Figure 5-17 presents magnified SEM images of the EDM wire subjected to compression. Figure 5-17(a) shows the specimen mounted between the compression plattens prior to loading. It is appropriately aligned as it retains its original nominal dimensions. The post-deformation image of Figure 5-17(b) corresponds to the stress-strain response shown in Figure 5-16. The image was captured at the end of the loading path when the wire was being subjected to 6% compressive strain.

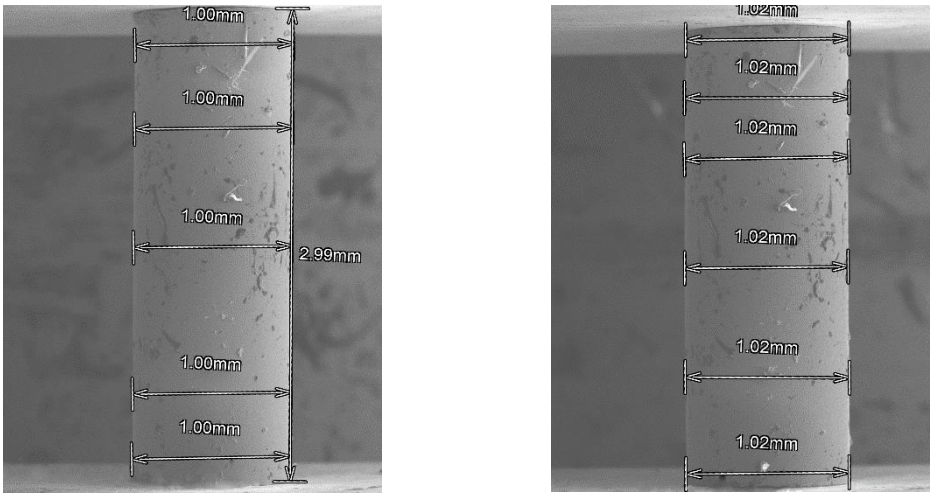

(a) (b)

Figure 5-17 SEM images of the 1mm Nitinol wire subjected to 6% compressive strain: prior to loading (a) and at the end of the loading path (b).

Its cross-section expanded radially in a uniform state by of 0.02mm throughout the specimen length. Barrelling effects are not observed. Note that the illustrated dimensions are not intended to act as accurate displacement measurements, since they depend on the SEM operator. Several user-dependent factors can influence these measurements such as the placement of the dimension cursor on the screen and the camera settings. Nevertheless, these images confirm the current methodology as a promising experimental procedure for compression testing of Nitinol wires.

5.11 Uncertainty in the compression tests

Figure 5-18 shows three different force-displacement curves derived from compression testing of the 1mm diameter wire. The samples were displaced to 0.18mm and then unloaded, at 22°C. From each curve, values for the following parameters were extracted: upper and lower plateau forces, maximum force and displacement at maximum force. Note that although the compressive responses do not exhibit clear plateaus, the term was still used here for continuity. These plateau

forces were measured at 0.09mm during loading and unloading. The parameters here were chosen because they are clearly identified in the results and do not depend on user-interpretation like the transformation forces. Force and displacement parameters were selected because these were directly measured and recorded by the testing machine.

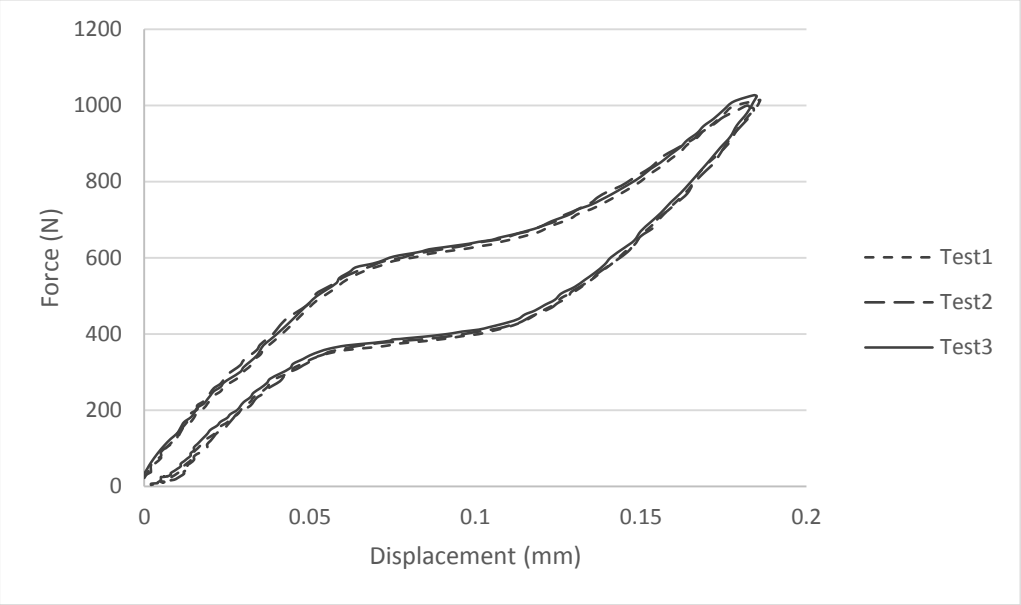

Figure 5-18 Force-displacement response of three different 1mm wires subjected to compression, at 22°C.

For each of the parameters mentioned above, the mean value, standard deviation and standard error were calculated using the equations introduced in section 4.1.6. The results are shown in Table 5-10. The systematic error was also measured for each parameter, based on the specifications of the testing instruments. The systematic error for force parameters was calculated by multiplying the mean value by 0.01 (since the load accuracy was 1% of the reading). The accuracy for displacement readings was a fixed error of 0.01mm. The total or combined error was then estimated by adding the standard and systematic errors in quadrature using Equation 4-10 (section 4.1.6). The combined error was then used to calculate the percentage relative error, i.e. the combined error as a percentage of the mean value. The expanded uncertainty was also estimated based on the combined error

multiplied by a coverage factor (k = 2), providing a level of confidence of approximately 95%.

Table 5-10 Upper plateau force (UPF) at 0.09mm, lower plateau force (LPF) at 0.09mm, maximum force, and displacement at maximum force for the three compression tests shown in Figure 5-18. The following parameters were calculated for each result: mean value, standard deviation (STDEV), standard error (STError), systematic error (SysError), total error (TotError), relative error (RelError) and expanded error (ExpandErr).

Test	UPF (N)	LPF (N)	Max force (N)	Displacement at max force (mm)
1	615.32	386.40	1014.49	0.186
2	622.26	391.59	999.56	0.182
3	627.03	398.19	1026.53	0.184
Mean	621.54	392.06	1013.53	0.184
STDEV	5.89	5.91	13.51	0.002
STError	3.40	3.41	7.80	0.001
SysError	6.22	3.92	10.14	0.010
TotError	7.08	5.20	12.79	0.010
RelError	1.14%	1.33%	1.26%	5.47%
ExpandErr	14.17	10.39	25.58	0.020

5.12 Bending response within the superelastic range

Figure 5-19 presents the bending response of the 1mm Nitinol wire when deformed within the superelastic range at 22°C and 37°C. Results correspond to testing conducted at a loading rate of 0.1mm/sec. Upon loading, the slope of the linear part of the curves represents the flexural stiffness of the material. For linear elastic deformation under three-point bending, the relationship between the applied force and the imposed deflection is given by Equation 5-1, where F is the force, E is the flexural modulus, I is the second moment of area of the cross-section, D is the deflection and L is the span between the supports.

$$F = 48\left(\frac{EID}{L^3}\right) \quad \text{Equation 5-1}$$

Therefore, the flexural modulus of austenite can be calculated to approximately 59GPa and 72GPa at 22°C and 37°C respectively. Note that the flexural modulus is significantly higher compared to the elastic modulus derived from the tensile data earlier. Usually, tensile and bend tests result in a similar modulus for conventional linear symmetric materials, unlike superelastic Nitinol.

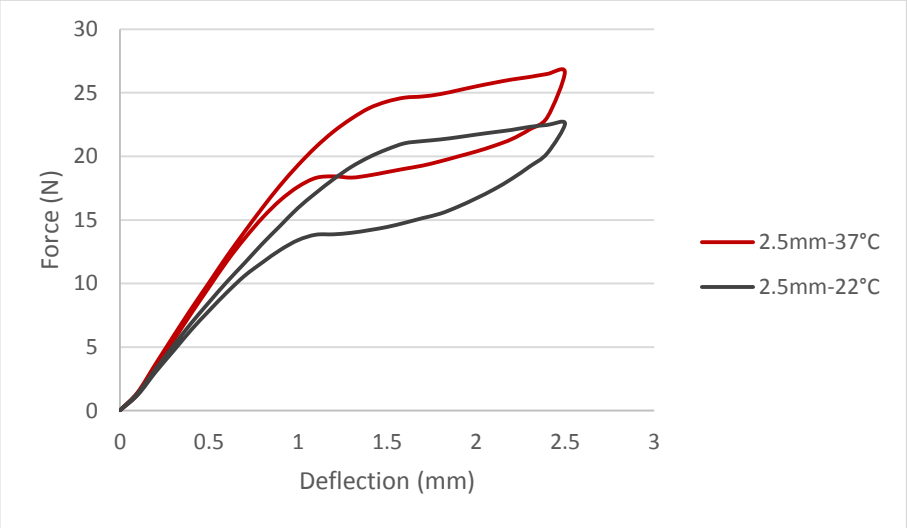

Figure 5-19 Force-deflection response of the 1mm Nitinol wire subjected to three-point bending within the superelastic range at 22°C and 37°C.

The bending response is characterised by a positive slope transformation region during loading which starts at approximately 21N and 23.8N at 22°C and 37°C respectively. A small load overshoot is observed in both curves before the upper transformation region is formed. The maximum force at the end of the loading path is 22.6N and 26.6N at 22°C and 37°C respectively.

Upon unloading, a small load drop is seen which is associated with the reversal of the frictional contact force between the wires and the supports. The load drop value is approximately 2.3N and 3.5N at 22°C and 37°C respectively. At 22°C, reverse transformation takes place at approximately 16N whereas at 37°C transformation during unloading starts at 22N. Both unload transformation regions have a positive slope and are followed by a small load undershoot. Transformation ends at approximately 13.5N and 18N at 22°C and 37°C respectively. No permanent

deformation is present at the end of the unloading paths. These results are also presented in Table 5-11.

Table 5-11 Bending results obtained from the force-deflection curves of Figure 5-19.

	22°C	37°C
Austenite flexural modulus	59GPa	72GPa
Start of transformation during loading	21N	23.8N
Max force at 2.5mm	22.6N	26.6N
Load drop upon unloading	2.3N	3.5N
Start of transformation during unloading	16N	22N
End of transformation during unloading	13.5N	18N

5.13 Load rate effects on the bending response within the superelastic range

Figure 5-20 presents the bending response of the 1mm Nitinol wire when deformed within the superelastic range at various load rates, namely 0.01mm/sec, 0.1mm/sec and 1mm/sec in air. Note that the load-deflection curve at 0.1mm/sec is the same as the one shown in Figure 5-19 at 22°C.Reducing the load rate by an order of magnitude to 0.01mm/sec, has little effect on the macroscopic bending response.

However, increasing the rate to 1mm/sec results in significant differences as the load-deflection curve is altered. The initial linear elastic region is only marginally changed. Transformation during loading takes place at the same deflection, yet at a higher force level of 22N. Subsequently, the curve enters the transformation region without the presence of a load overshoot. The loading path is then shifted towards higher force levels and is characterised by a steeper slope. The maximum force is 24.3N which is approximately 7.5% higher compared to the lower rate test. Upon unloading, the load drop is approximately the same and is followed by a steep curve with no plateau features. The whole unloading path is then shifted towards higher force levels and enters the linear elastic region, without any force undershoot. The above results are also presented in Table 5-12.

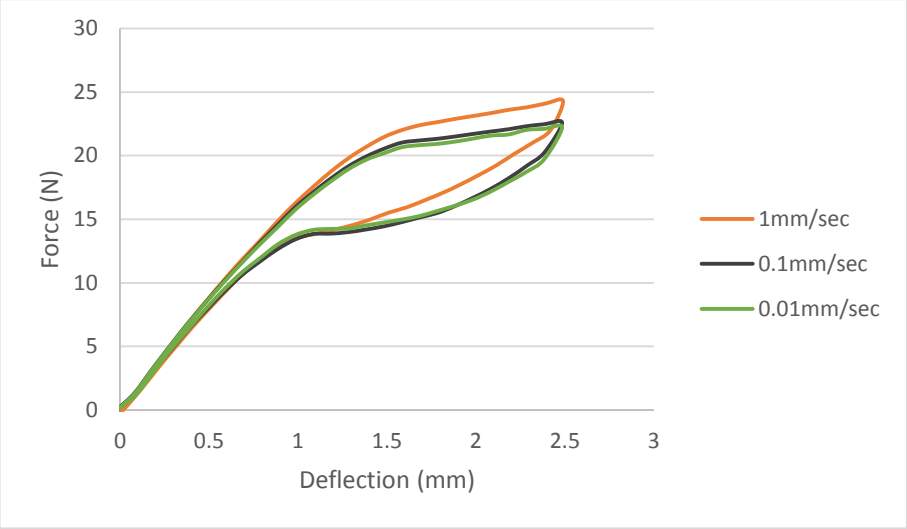

Figure 5-20 Load rate sensitivity of the 1mm Nitinol wire subjected to three-point bending within the superelastic range, at 22°C, in air.

Table 5-12 Bending results obtained from the force-deflection curves of Figure 5-20.

	Loading rate at 22°C	
	0.1mm/sec	1mm/sec
Start of transformation during loading	21N	22N
Max force at 2.5mm	22.6N	24.3N
Start of transformation during unloading	16N	-
End of transformation during unloading	13.5N	13N

5.14 Load rate effects on the bending response beyond the superelastic range

Figure 5-21 presents the bending response of the 1mm Nitinol wire when deformed beyond the superelastic range at load rates of 0.1mm/s and 1mm/s. Upon loading at 0.1mm/sec, the initial force-deflection characteristics are the same as those described earlier for the specimen deflected to 2.5mm. However, in this case force increases up to approximately 24.8N at a deflection of 4.3mm. Beyond that point, a negative slope is exhibited macroscopically which is associated with the sliding friction between the specimen and the supports at large deflections.

Upon unloading, the load drop is approximately 5.8N and is characterised by an almost vertical curve. Thereafter, a secondary small force drop is seen leading to the lower transformation region which begins at 15.3N and 5.3mm. The unloading path can then be divided into two parts. The first from 5.3mm to 3mm, and the second from 3mm until the final elastic region which takes place after a small force undershoot. The transformation during unloading ends at approximately 11.5N. Unloading from a maximum deflection of 6mm results in approximately 0.06mm permanent deformation.

Upon loading at 1mm/sec, the initial bending response is the same as the one exhibited by the specimen deflected to 2.5mm at high rates. With further loading in this case, force increases to approximately 26.8N at 4.2mm. Subsequently, a negative slope is exhibited macroscopically until the maximum deflection which is followed by a load drop of 5.2N. Although the unloading path is initially shifted towards higher force levels, it ends at lower forces compared to the 0.1mm/sec curve. The transformation during unloading in this case ends at 9N and the final linear elastic unloading results in an increased permanent deformation of 0.11mm. The comparison between the two bending curves can also be seen in Table 5-13.

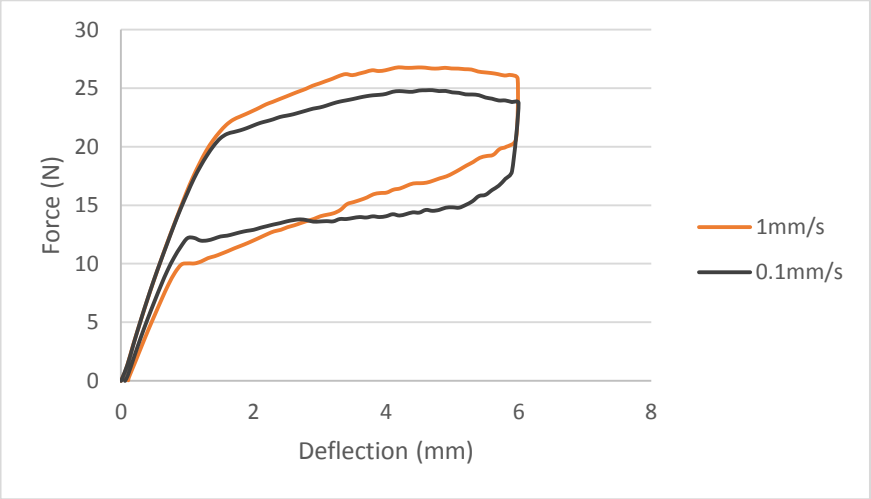

Figure 5-21 Load rate sensitivity of the 1mm Nitinol wire subjected to three-point bending beyond the superelastic range, at 22°C, in air.

Table 5-13 Bending results obtained from the force-deflection curves of Figure 5-21.

	Loading rate at 22°C	
	0.1mm/sec	1mm/sec
Start of transformation during loading	21N	22N
Max force	24.8N at 4.3mm	26.8N at 4.2mm
Load drop upon unloading	5.8N	5.2N
Start of transformation during unloading	15.3N	-
End of transformation during unloading	11.5N	9N
Permanent deformation	0.06mm	0.11mm

The effect of high-rate testing on the unloading path of the force-deflection curve, was further examined by adding a 10-second pause between loading and unloading. Results are presented in Figure 5-22, where the solid line corresponds to the high rate test described in Figure 5-21 and the dashed line to testing performed at the same rate with a 10-second pause before unloading. The loading part is the same in both curves, as expected. The load drop during the paused test is greater, almost matching the one observed in the 0.1mm/s curve of Figure 5-21. The unloading path is shifted towards lower force levels although its slope is the same in both curves. The quantitative results that correspond to the above observations can be seen in Table 5-14.

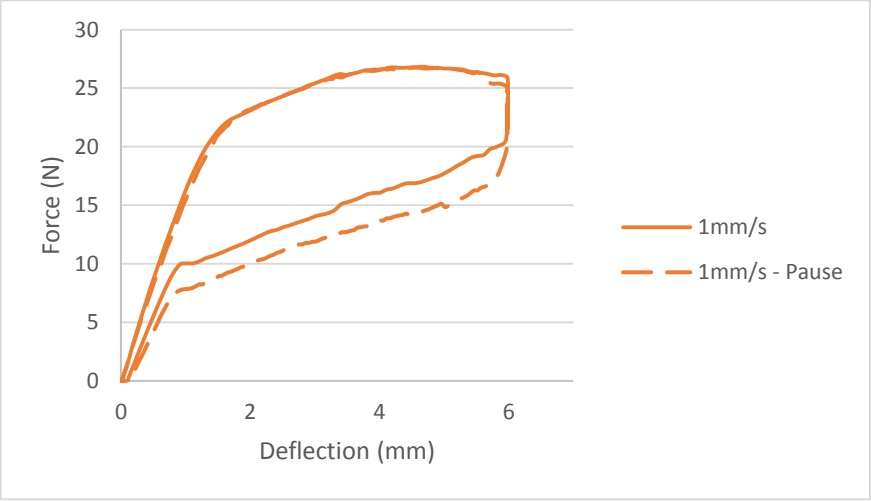

Figure 5-22: Effect of 10-second pause between loading and unloading, on the force-deflection curve of the 1mm wire subjected to high-rate bending.

Table 5-14 Bending results obtained from the force-deflection curves of Figure 5-22.

	Loading rate/condition at 22°C	
	1mm/sec	1mm/sec - pause
Start of transformation during loading	22N	22N
Max force	26.8N at 4.2mm	26.8N at 4.2mm
Load drop upon unloading	5.2N	6N
Start of transformation during unloading	-	-
End of transformation during unloading	9N	7N
Permanent deformation	0.11mm	0.12mm

The aforementioned results are summarised in Figure 5-23 which also shows the effect of the ambient medium on the load rate sensitivity of Nitinol. The 1mm diameter wire was subjected to high rate bending while submerged in water, at 22°C. In this case, the force-deflection response was almost unaffected by the increased rate. The load-unload path is very similar to the low rate test until approximately 3mm during unloading. This can also be seen in the results of Table 5-15. From that point until the onset of the final elastic unloading, the curve follows the path of the high rate test. These findings are discussed in Chapter 7 along with the rest of the results.

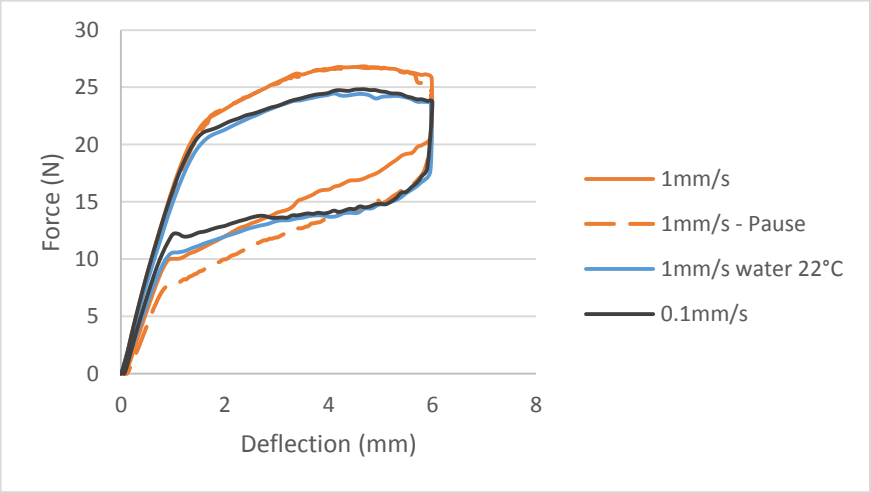

Figure 5-23 Effect of loading rate and ambient medium on the bending response of the 1mm Nitinol wire.

Table 5-15 Bending results obtained from the force-deflection curves of Figure 5-23.

	Loading rate/condition at 22°C	
	1mm/sec - air	1mm/sec - water
Start of transformation during loading	22N	20.5N
Max force	26.8N at 4.2mm	24.5N at 4.1mm
Load drop upon unloading	5.2N	5.8N
Start of transformation during unloading	-	15N
End of transformation during unloading	9N	10N
Permanent deformation	0.11mm	0.05mm

5.15 Load rate effects on the bending response of small diameter wires

Figure 5-24 presents the bending response of the 0.45mm Nitinol wire when deformed at load rates of 0.1mm/s and 1mm/s. As expected, the cross-sectional diameter has a significant effect on the exhibited forces. The maximum force when deforming the specimen at 0.1m/s is 1.85N. By comparison, the 1mm wire exhibited a force of approximately 24.8N at the same loading conditions and experimental configuration. A decrease in the wire cross-section results in lower forces as the second moment of area is proportional to the fourth power of the cross-sectional radius.

Note that results of Figure 5-24 are more comparable to the ones shown in Figure 5-20 (section 5.13) since the wire is strained within the superelastic range. Nevertheless, it is evident that the response of the smaller diameter specimen is less affected by the increased load rate. Both force-deflection curves follow the same path during loading and unloading. Some oscillation can be attributed to the mismatch between the exhibited forces and the sensitivity of the available load cell.

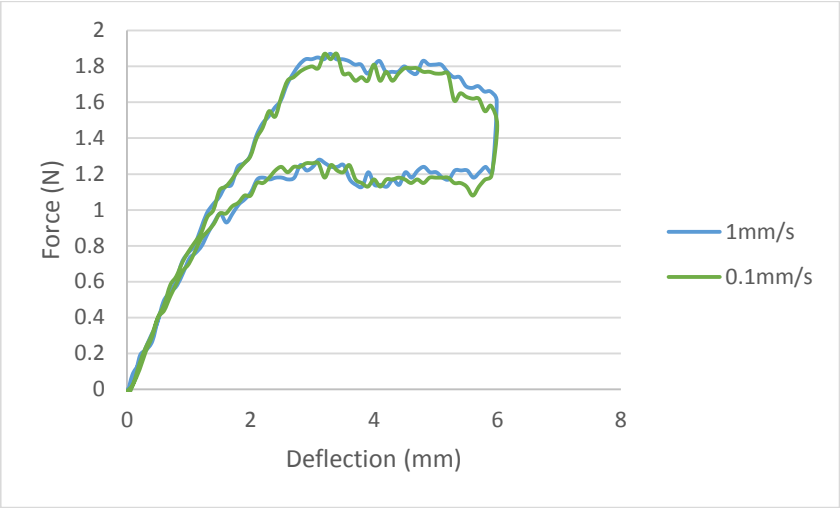

Figure 5-24 Load rate sensitivity of the 0.45mm Nitinol wire subjected to three-point bending within the superelastic range, at 22°C, in air.

5.16 Effect of cyclic loading on the superelastic bending response

Figure 5-25 presents the cyclic response of the 1mm Nitinol wire when subjected to three-point bending within the superelastic range at 22°C (a) and 37°C (b). Specimens were cycled 100 times to a maximum deflection of 2.5mm. For better image clarity, both graphs show cycles 1 to 10 and cycles 50, 90 and 100. Both responses exhibit similar qualitative features: the flexural stiffness is decreased, the forces at the onset of the upper transformation region are decreased and the residual deformation is increased. These changes are more pronounced during the first 10 cycles. At the 50th cycle, the behaviour starts stabilising at both test temperatures.

Figure 5-26 presents the evolution of the initial flexural stiffness of the material with increasing cycles. At 22°C, the flexural modulus is initially 59GPa, decreasing gradually during the first 30 cycles. It experiences another moderate decrease from cycle 60 to 90 and at the end of cycling its value is 56GPa. At 37°C, the modulus is initially 72GPa but is quickly reduced during the first 20 cycles to approximately 69GPa. Another small reduction is seen between cycles 50 and 60 and then the value of the flexural modulus is stabilised to approximately 67GPa.

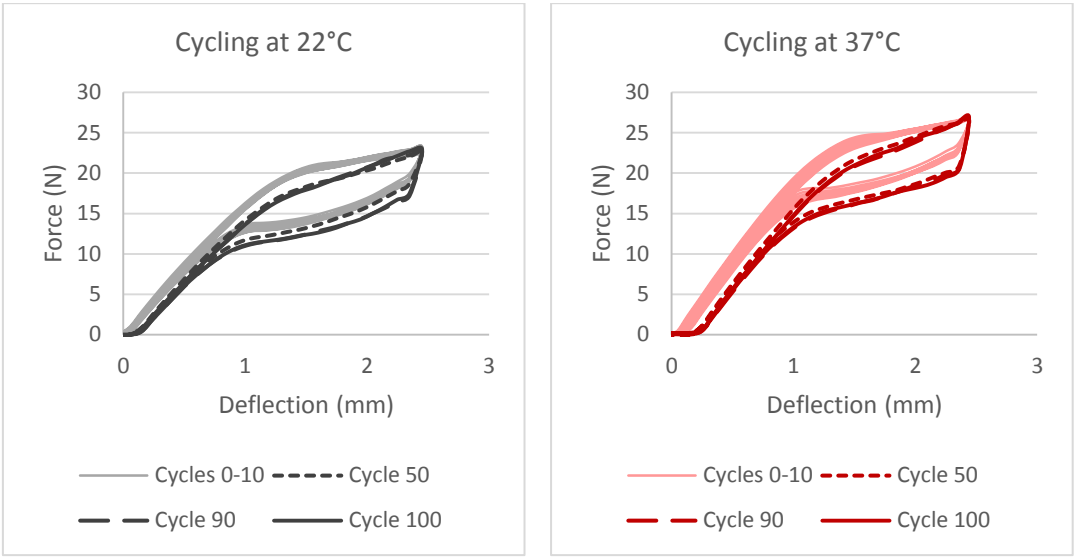

(a) (b)

Figure 5-25 Cyclic response of the 1mm Nitinol wire subjected to three-point bending within the superelastic range at 22°C (a) and 37°C (b).

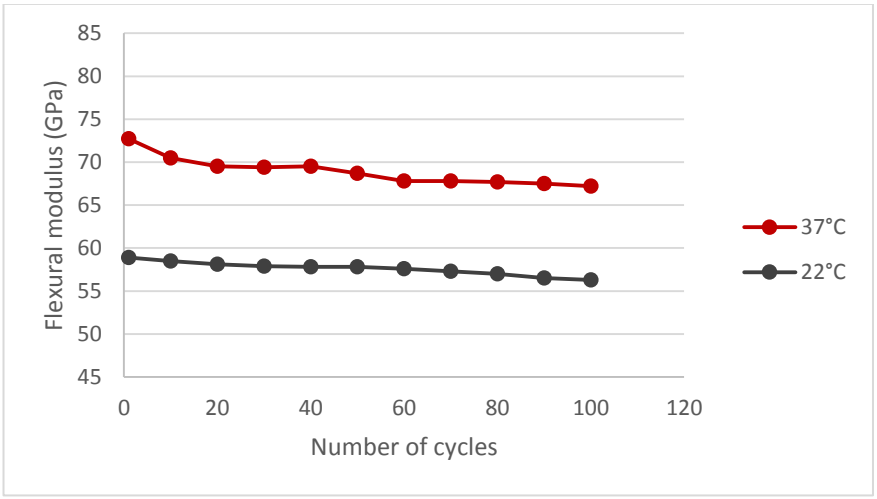

Figure 5-26 Austenite flexural modulus against increasing number of cycles under three-point bending. Results correspond to the force-deflection curves shown in Figure 5-25.

Similarly, the onset of the transformation region during loading is progressively shifted towards lower force levels at both test temperatures, as seen in Figure 5-27. At the 100th cycle, transformation during loading took place at 16.5N and 19N, at 22°C and 37°C respectively. By comparison, the initial values in the first cycle were 21N and 23.8N, at 22°C and 37°C respectively. The rate of that decrease was similar at both temperatures.

Additionally, the residual deformation was quickly increased in the first 10 cycles, especially at 37°C, as seen in Figure 5-28. From the 10th cycle onwards, that increase became more gradual at both temperatures, and by the end of cycling the accumulated residual deformation was approximately 0.15mm at 22°C, and 0.25mm at 37°C.

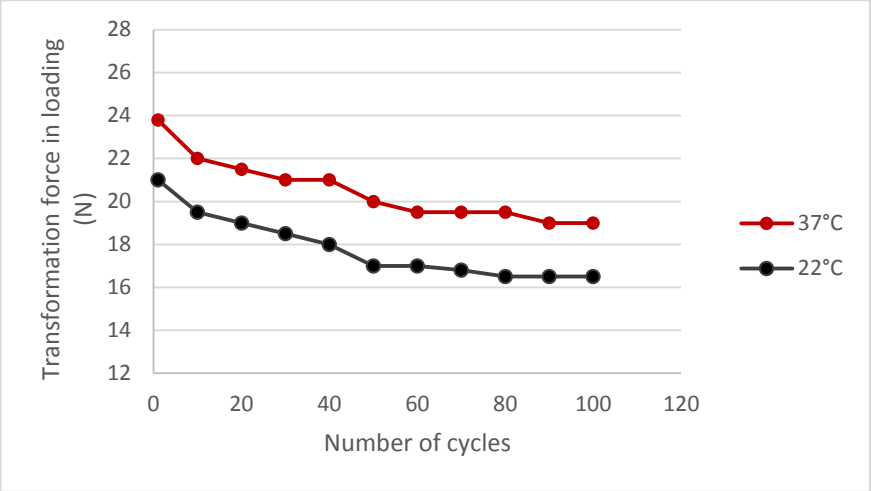

Figure 5-27 Transformation force during loading against increasing numbers of cycles under three-point bending. Results correspond to the force-deflection curves shown in Figure 5-25.

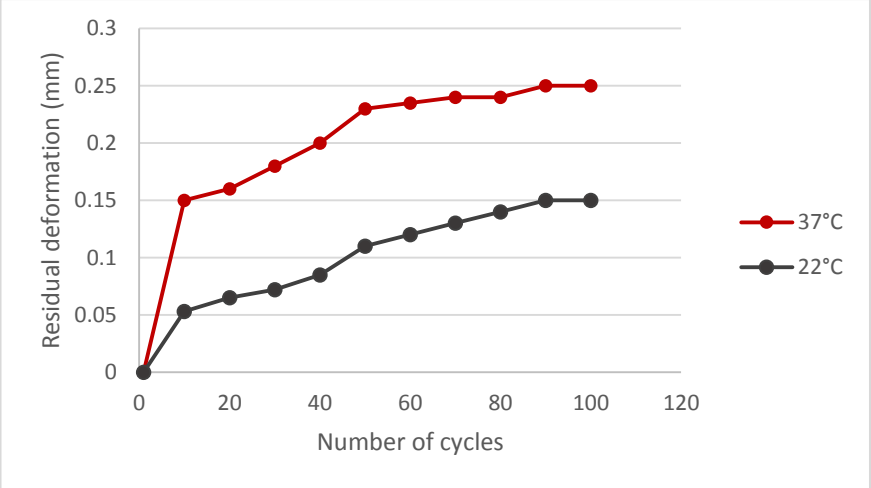

Figure 5-28 Residual deformation against increasing numbers of cycles under three-point bending. Results correspond to the force-deflection curves shown in Figure 5-25.

5.17 Uncertainty in the three-point bend tests

Figure 5-29 shows three different force-deflection curves derived from three-point bend testing of the 1mm diameter wire. The samples were deflected to 6mm and then unloaded, at 22°C. From each curve, values for the following parameters were extracted: upper and lower plateau forces, maximum force, and displacement at maximum force. Plateau forces were measured at 3mm during loading and unloading. These parameters were selected for this study because they are clearly identified in the results and do not depend on user-interpretation like the transformation forces.

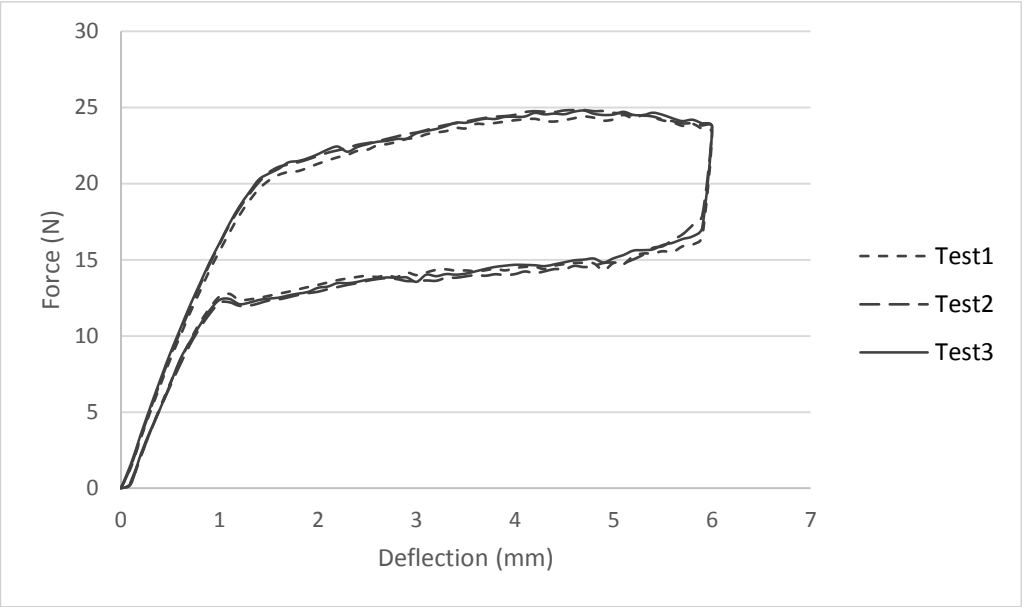

Figure 5-29 Force-deflection response of three different 1mm wires subjected to three-point bending at 22°C.

For each of the aforementioned parameters, the mean value, standard deviation and standard error were calculated using the equations introduced in section 4.1.6. The results are shown in Table 5-16. The systematic error was also measured for each parameter, based on the specifications of the testing instruments. The systematic error for force parameters was calculated by multiplying the mean value by 0.01 (since the load accuracy was assumed to be 1% of the reading). The

accuracy for displacement readings was found by multiplying the mean value by 0.005 (since the accuracy was assumed to be 0.5% of the displacement reading). Note that the systematic displacement error (0.023mm) is smaller than the fixed allowable error of 0.025mm which is reported in the ASTM standard. According to the standard guidelines, the greater of these two values should be considered the error of the measurement. The total or combined error was then estimated by adding the standard and systematic errors in quadrature using Equation 4-10 (section 4.1.6). Then, the expanded uncertainty was estimated based on the combined error multiplied by a coverage factor (k = 2), providing a level of confidence of approximately 95%. The combined error was also used to calculate the percentage relative error, i.e. the combined error as a percentage of the mean value.

Table 5-16 Upper plateau force (UPF) at 3m, lower plateau force (LPF) at 3mm, maximum force, and displacement at maximum force for the three bend tests shown in Figure 5-29. The following parameters were calculated for each result: mean value, standard deviation (STDEV), standard error (STError), systematic error (SysError), total error (TotError), relative error (RelError) and expanded error (ExpandErr).

Test	UPF (N)	LPF (N)	Max force (N)	Displacement at max force (mm)
1	23.00	13.99	24.40	4.700
2	23.35	13.61	24.82	4.300
3	23.30	13.55	24.72	4.601
Mean	23.22	13.72	24.65	4.534
STDEV	0.19	0.24	0.22	0.208
STError	0.11	0.14	0.13	0.120
SysError	0.23	0.14	0.25	0.023
				<0.025
TotError	0.26	0.19	0.28	0.123
RelError	1.11%	1.42%	1.12%	2.71%
ExpandErr	0.51	0.39	0.55	0.246

5.18 Torsional response at various rotation levels

Figure 5-30 presents the torque-rotation response of the 1.8mm Nitinol specimen when subjected to increasing rotation increments, at 22°C. Rotation to 20 degrees results in a nearly linear curve with minor hysteresis. The initial region upon loading represents the elastic deformation of the material in the austenitic state. If the curve is converted to shear stress and strain using the equations presented earlier in section 4.1.5, the torsional modulus of austenite can be identified by finding the equation for the linear trendline of the slope. Its value here is approximately 16.9GPa.

Beyond 20 degrees, the specimens are transformed to martensite at approximately 0.5Nm, exhibiting a positive slope transformation region. At 80 degrees, the maximum torque is 0.7Nm. The linear region that follows unloading from 80 degrees, corresponds to the deformation of the material in the martensitic state assuming a complete transformation has been achieved. The assumption should be valid considering the maximum shear strain of the specimen is approximately 7.85% at 80 degrees. Note that this value was calculated using Equation 4-6 (section 4.1.5) as explained earlier. The torsional modulus of martensite here is approximately 12.2GPa.

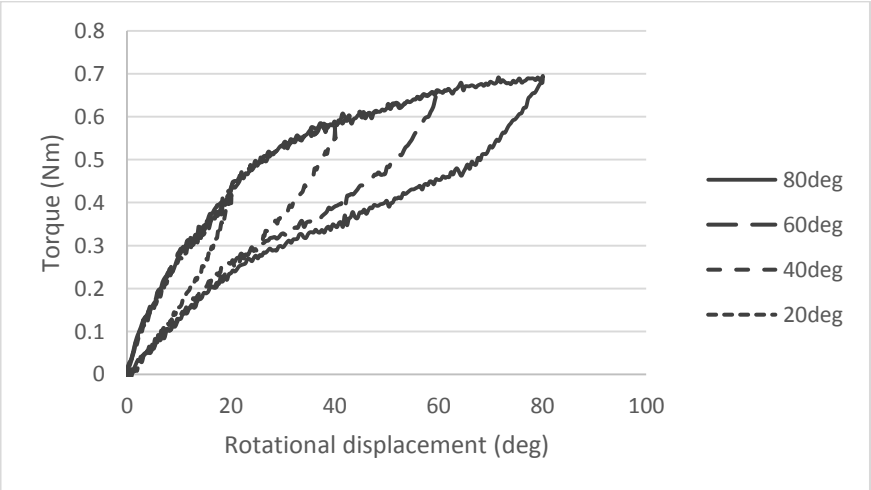

Figure 5-30 Torsional response of the 1.8mm Nitinol wire subjected to increasing rotation increments, at 22°C.

Transformation during unloading from 80 degrees, takes place at approximately 0.5Nm. The lower transformation region has a positive slope similar to the upper one. Unloading from 40 and 60 degrees of maximum rotation results in a slightly different path and hysteresis. However, the transformation region ends at approximately 0.25Nm in all curves. The final linear elastic unloading path is also the same in all cases although it is not the same as the loading one. Finally, there is negligible residual deformation at the end of the load-unload cycles. The above results are summarised in Table 5-17.

Table 5-17 Torsion results obtained from the torque-rotation curves of Figure 5-30.

Austenite torsional modulus	16.9GPa
Start of transformation during loading	0.5Nm
Max torque at 80 degrees	0.7Nm
Martensite torsional modulus	12.2GPa
Start of transformation during unloading	0.5Nm
End of transformation during unloading	0.25Nm

5.19 Load rate effects on the torsional response

Figure 5-31 presents the load rate effects on the torsional response of the 2.4mm Nitinol specimen. Increasing the load rate by an order of magnitude to 5deg/s, does not affect the linear elastic region which is only marginally changed. Transformation during loading takes place at a higher torque level compared to low rate testing (1.4Nm vs 1.3Nm). The upper transformation region is shifted towards higher load levels and is characterised by a steeper slope with even fewer plateau traits. Maximum torque is approximately 15% higher compared to that exhibited during testing at low rates (1.9Nm vs 1.65Nm).

Upon unloading, the slope of the region that corresponds to the torsional modulus of martensite is similar for both curves. Transformation during high rate unloading, takes place again at a greater torque level compared to the low rate

experiment (1.5Nm vs 1.3Nm). Moreover, the transformation region also ends at higher loads (0.9Nm vs 0.8Nm). The final linear elastic region is approximately the same in both curves. These results are summarised in Table 5-18.

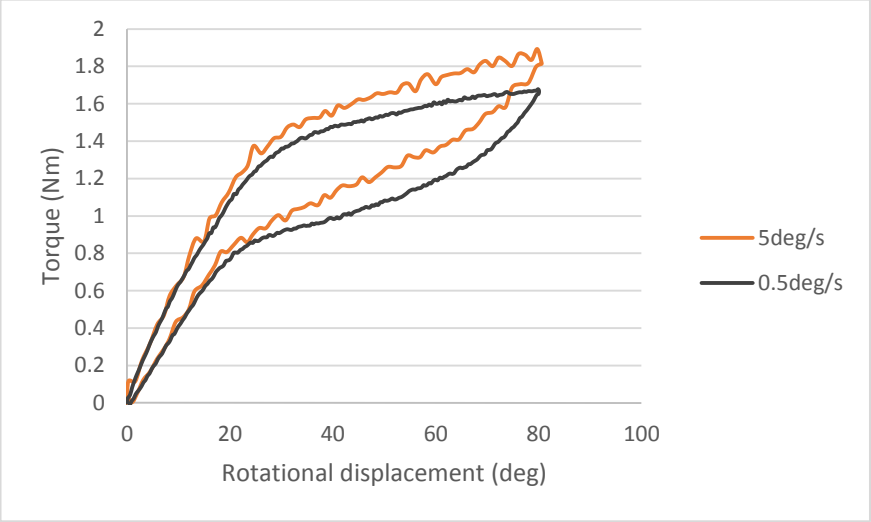

Figure 5-31 Load rate sensitivity of the 2.4mm Nitinol specimen subjected to torsion

Table 5-18 Torsion results obtain from the torque-rotation curves of Figure 5-31.

	Loading rate at 22°C	
	0.5deg/sec	5deg/sec
Start of transformation during loading	1.3Nm	1.4Nm
Max torque at 80 degrees	1.65Nm	1.9Nm
Start of transformation during unloading	1.3Nm	1.5Nm
End of transformation during unloading	0.8Nm	0.9Nm

5.20 Combined tensile and torsional deformation

The present section presents the qualitative features of the material's response under combined tension-torsion loading conditions. Figure 5-32 shows the response of the 2.4mm specimen when subjected to a low tensile deformation followed by a large torsional deformation. The force-displacement curve is illustrated in Figure 5-32(a) along with the pure tensile response for comparison. Similarly, the

torque-rotation curve is illustrated in Figure 5-32(b) along with the pure torsional deformation.

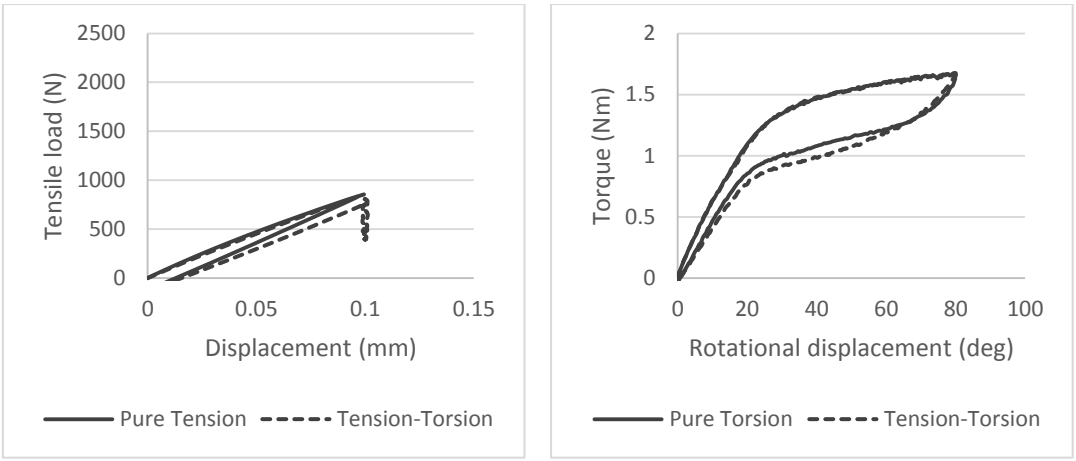

(a) (b)

Figure 5-32 Tensile (a) and torsional (b) response of the 2.4mm Nitinol wire subjected to combined low tensile deformation-large torsional deformation.

Initially, the specimen is displaced axially by 0.1mm. Subsequently, the axial displacement is kept constant while the specimen is rotated by 80 degrees. During this process, a small load drop is observed in the tensile response which is recovered when the rotational displacement is removed. Thereafter, the axial displacement is also removed completing the loading sequence.

Apart from the load drop, the force-displacement curve differs minimally from the pure tensile response. The loading path is the same in both curves although unloading during combined tension-torsion takes place at slightly lower force levels. Similarly, the torsional response during tension-torsion is similar to the one seen during pure torsion. The only difference is seen in the unload transformation region which is shifted to somewhat lower torque levels.

Figure 5-33 shows the response of the 2.4mm specimen when subjected to a large tensile deformation followed by a large torsional deformation. The force-displacement curve is illustrated in Figure 5-33(a) along with the pure tensile response for comparison. Similarly, the torque-rotation curve is illustrated in Figure 5-33(b) along with the pure torsional deformation.

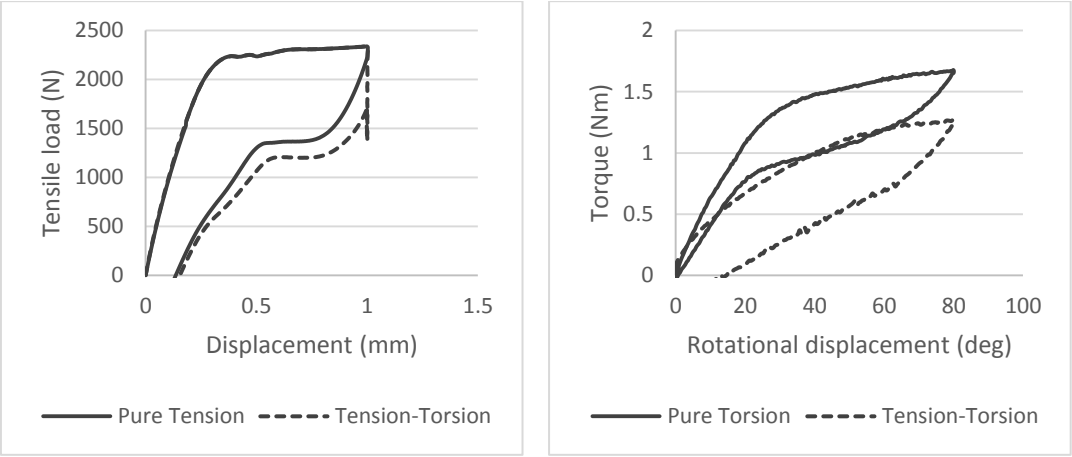

(a) (b)

Figure 5-33 Tensile (a) and torsional (b) response of the 2.4mm Nitinol wire subjected to combined large tensile deformation-large torsional deformation.

Initially, the specimen is displaced axially by 1mm. The response exhibits a linear elastic region followed by an almost flat load plateau. Subsequently, the axial displacement is kept constant while the specimen is rotated by 80 degrees. The torsional response is depicted by a nearly linear behaviour to approximately 65 degrees of rotation. The transformation region seems rather small, extending only from 65 to 80 degrees.

During this process, a load drop is again observed in the tensile response which is recovered when the rotational displacement is removed. Torsional unloading takes places in an almost linear manner, leading to a residual deformation of approximately 16 degrees. When the axial displacement is removed, tensile unloading takes place at lower force levels compared to pure tension. However, the tensile residual deformation is similar in both responses.

5.21 Uncertainty in the torsion tests

Figure 5-34 shows three different torque-rotation curves derived from torsion testing of the 1.8mm diameter wire. The samples were displaced to 80 degrees and then unloaded, at 22°C. From each curve, values for the following parameters were

extracted: upper and lower plateau torque (measured at 40 degrees of rotation), maximum torque and rotation at maximum force. These parameters were selected for this study because they are clearly identified in the results and do not depend on user-interpretation like the transformation forces.

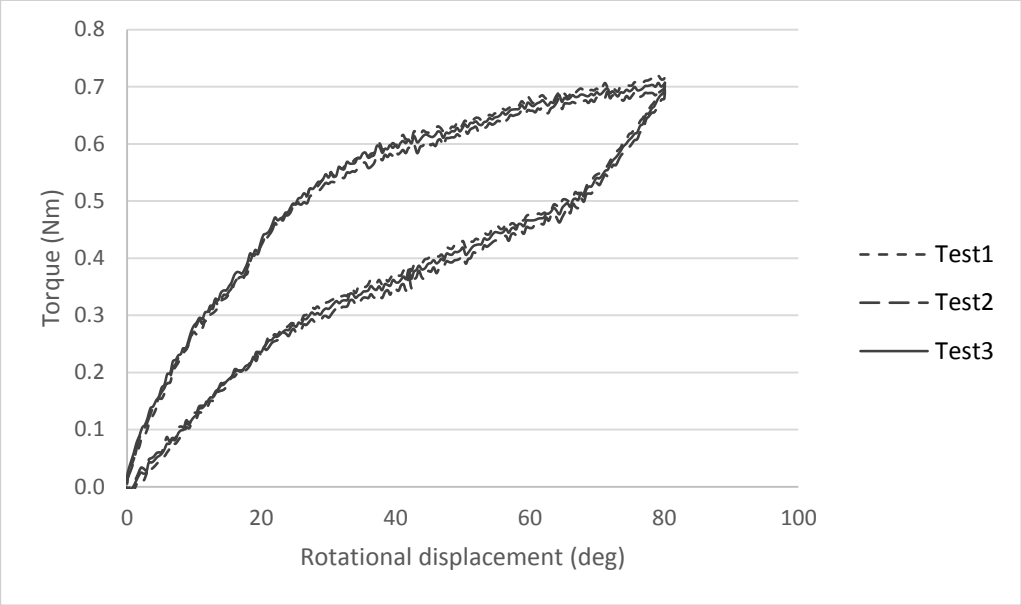

Figure 5-34 Torque-rotation curves of three different 1.8mm specimens subjected to torsion at 22°C.

For each of the parameters mentioned above, the mean value, standard deviation and standard error were calculated using the equations introduced in section 4.1.6. The results are shown in Table 5-19. The systematic error was also measured for each parameter, based on the specifications of the testing instruments. The systematic error for load parameters was calculated by multiplying the mean value by 0.005 (since the load accuracy was 0.5% of the reading). The accuracy for displacement readings was assumed to be 0.5%. The total or combined error was then estimated by adding the standard and systematic errors in quadrature using Equation 4-10 (section 4.1.6). The combined error was then used to calculate the percentage relative error, i.e. the combined error as a percentage of the mean value. The expanded uncertainty was also estimated based on the combined error

multiplied by a coverage factor (k = 2), providing a level of confidence of approximately 95%.

Table 5-19 Load torque at 40 degrees, unload torque at 40 degrees, maximum torque, and rotation at maximum torque for the three torsion tests shown in Figure 5-34. The following parameters were calculated for each result: mean value, standard deviation (STDEV), standard error (STError), systematic error (SysError), total error (TotError), relative error (RelError) and expanded error (ExpandErr).

Test	Load torque at 40deg (Nm)	Unload torque at 40deg (Nm)	Max torque (Nm)	Rotation at max torque (deg)
1	0.600	0.367	0.717	80.103
2	0.582	0.346	0.695	80.097
3	0.593	0.358	0.707	80.100
Mean	0.592	0.357	0.706	80.100
STDEV	0.009	0.011	0.011	0.003
STError	0.005	0.006	0.006	0.001
SysError	0.003	0.002	0.004	0.400
TotError	0.006	0.006	0.007	0.401
RelError	1.02%	1.78%	1.03%	0.50%
ExpandErr	0.012	0.013	0.015	0.801

Chapter 6 Computational Results

This chapter presents results derived from finite element simulations. These were conducted according to the methodology outlined in Chapter 4. Computational results are compared with the relevant experimental data here and findings are discussed in Chapter 7.

6.1 Input parameters selection

Nitinol is represented in Abaqus by 15 constitutive parameters which describe the superelastic state of the material. The present section summarizes the input parameters' values and reminds the reader of the way these are identified using the available experimental data. Figure 6-1 presents the stress-strain response of the 1mm Nitinol wire subjected to tension within the superelastic range for a single cycle, and then pulled to failure, at 22°C. The relevant constitutive parameters are identified on the experimental curve.

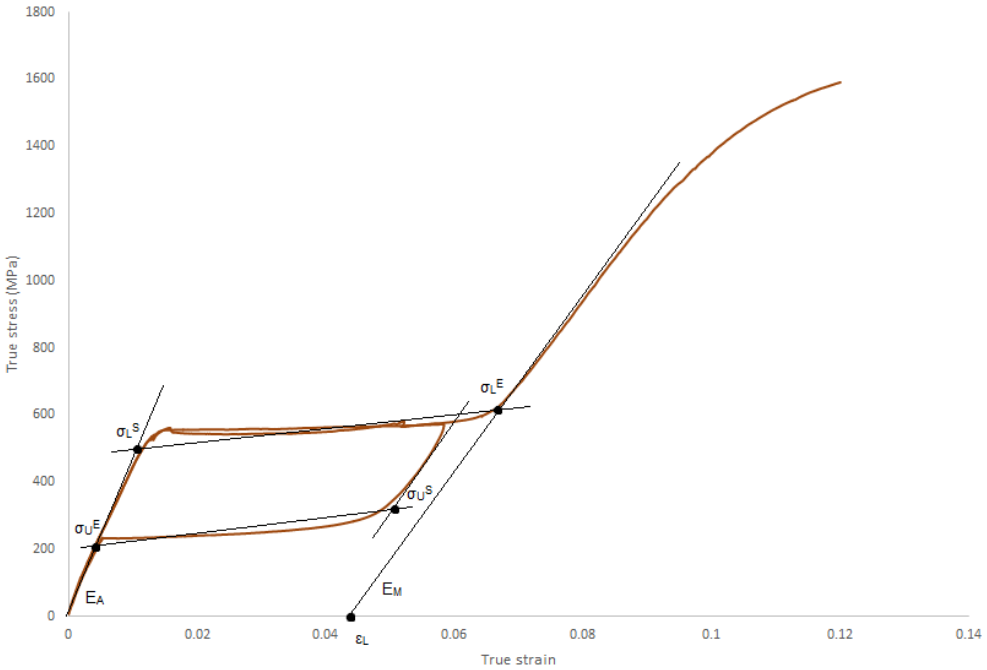

Figure 6-1 Identifying the relevant input parameters using experimental tensile data.

The linear elastic region upon loading is used to calculate the elastic modulus of austenite E_A by finding the equation for the linear trendline of the curve. The start of the transformation during loading σ_L^S is defined as the point where the slope of the stress-strain curve changes right before entering the upper plateau, as seen in Figure 6-1. The end of the transformation during loading σ_L^E is found at the point the curve enters the post-transformation region right after the load plateau. The post-transformation linear elastic region is used to calculate the elastic modulus of martensite E_M by finding the equation for the linear trendline of the curve. In practice, the martensite modulus can also be calculated using the unloading curve from 6% strain (to the unload plateau) since the slope of both curves shown in Figure 6-1 is similar.

The transformation strain is identified by extrapolating the post-transformation curve gradient down to the strain axis. The start of the transformation during unloading σ_U^S is defined as the point where the slope of the stress-strain curve changes right before the lower plateau, when unloading from 6% strain. The end of the transformation during unloading σ_U^E is found at the point where the curve enters the final linear elastic region, when unloading from 6% strain.

As explained in section 5.18, torsion data were used to calculate the relevant torsional moduli after converting the torque-rotation curve to shear stress-strain. The linear elastic region upon loading was used to calculate the torsional modulus of austenite by finding the equation for the linear trendline of the curve. The torsional modulus of martensite is calculated in a similar manner, using the unloading curve from 80 degrees (to the lower transformation region). Although these moduli are not directly used as input parameters, they are required to calculate the Poisson's ratios of austenite and martensite using Equation 4-13 (section 4.2.2). Additionally, compression results of section 5.8 are used to identify the start of the transformation during loading in compression. The parameter is defined as the point where the slope of the stress-strain curve changes before entering the upper transformation region. Note that the value is entered in the input parameters as a positive number.

Table 6-1 Input parameters used for FEA at 22°C and 37°C.

Input parameters			Test temperature	
No.	Symbol	Description	22°C	37°C
1	E_A	Austenite elasticity (GPa)	44000	64000
2	ν_A	Austenite Poisson's ratio	0.3	0.3
3	E_M	Martensite elasticity (GPa)	31000	31000
4	ν_M	Martensite Poisson's ratio	0.27	0.27
5	ε^L	Transformation strain	0.0465	0.048
6	$\left(\frac{\delta\sigma}{\delta T}\right)_L$	$\delta\sigma/\delta T$ loading	-	-
7	σ_L^S	Start of transformation loading (MPa)	540	630
8	σ_L^E	End of transformation loading (MPa)	605	710
9	T_o	Reference temperature	0	0
10	$\left(\frac{\delta\sigma}{\delta T}\right)_U$	$\delta\sigma/\delta T$ unloading	-	-
11	σ_U^S	Start of transformation unloading (MPa)	300	405
12	σ_U^E	End of transformation unloading (MPa)	200	280
13	σ_{CL}^S	Start of transformation stress during loading in compression, as a positive value (MPa)	720	840
14	ε_V^L	Volumetric transformation strain	0.0465	0.048
15	N_A	Number of annealings to be performed during the analysis	0	0
16	N_P	Number of stress-strain pairs to define the plastic curve	6	8
17	σ_{NP}^P, ε_{NP}	N number of stress (MPa) and strain points in the plastic curve	1592, 0.10 1660, 0.105 1705, 0.11 1734, 0.115 1743, 0.12 1750, 0.125	1362, 0.09 1491, 0.095 1590, 0.1 1660, 0.105 1706, 0.11 1737, 0.115 1756, 0.12 1764, 0.125

The values of the input parameters at 22°C are summarized in Table 6-1. Note that stress and strain are entered as true values. The above process was repeated to identify the input parameters at 37°C. Due to the lack of torsion and compression

data at 37°C, the Poisson's ratios of austenite and martensite were assumed to be the same at both temperatures.

In addition, the start of the transformation during loading in compression (720MPa) is 33.3% greater than the start of the transformation during loading in tension (540MPa), at 22°C. Therefore, the value for the start of the transformation during loading in compression at 37°C is estimated to satisfy the above relationship considering the start of the transformation during loading in tension is 630MPa at this temperature. Both sets of input parameters were extended using the stress-strain pairs shown in Table 6-1 (parameters No. 17), in order to capture the post-transformation superelastic-plastic behaviour of the material.

6.2 Superelastic tensile modelling

Figure 6-2 presents the computational and experimental responses of the material when subjected to tension within the superelastic range at 22°C and 37°C. The experimental stress-strain curves correspond to results presented earlier in section 5.1. Therefore, only the differences between FEA and experiments are identified here.

There is an excellent agreement between the computational forecasts and the experimental results when modelling tension. This is mainly because the input parameters were based directly on the tensile data. The transformation stresses during loading and unloading, as well as the elastic moduli of austenite and martensite, are practically the same in both FEA and experimental curves.

Only very minor differences can be identified, which are mostly of a qualitative nature. For instance, at both temperatures, the initial elastic region of austenite in the FEA curves is depicted by a straight line, whereas the slope in the experimental results is influenced by the presence of R-phase.

The hysteresis of the computational responses is also in agreement with the tensile results. The energy loss was calculated for each curve, as described in section

4.1.2. At 22°C, the energy loss is approximately 45.7% in the FEA result and 46.2% in the experimental curve. Similarly, at 37°C the energy loss is 38.7% and 38.9% in the computational and experimental curves respectively.

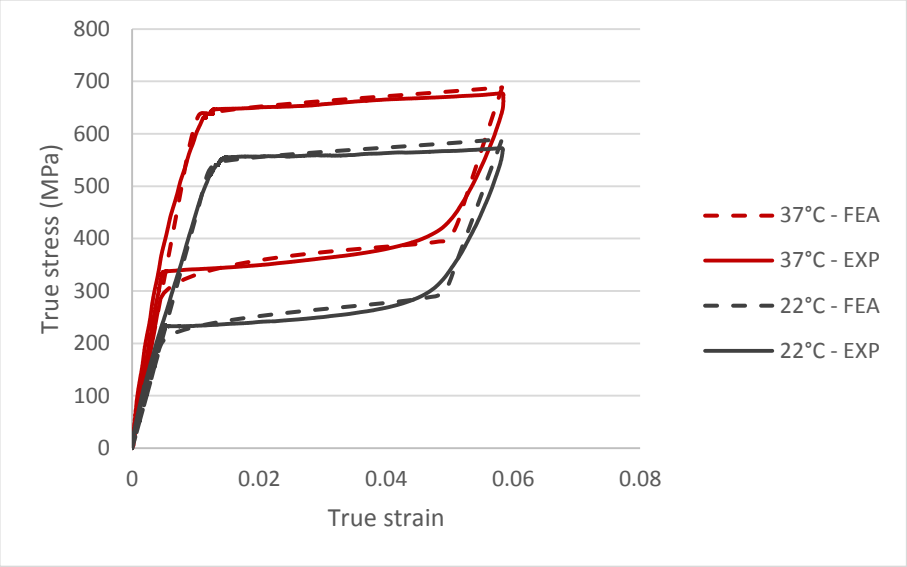

Figure 6-2 Comparison between computational and experimental responses of Nitinol subjected to tension within the superelastic range at 22°C and 37°C.

6.3 Post-transformation tensile modelling

Modelling Nitinol's high-strain deformation can allow engineers to predict the behaviour of the material during the compaction and deployment of a stent-graft. Therefore, simulations were performed to examine whether the high-strain tensile results can be reproduced computationally by Abaqus.

Figure 6-3 presents the computational and experimental responses of the material when subjected to high-strain tension at 22°C. Figure 6-4 also compares similar computational and experimental results at 37°C. Note that although the material at 22°C is superelastic, its deformation limits for a reversible phase transformation are lower. Therefore, testing at 22°C was conducted up to 10.5% strain.

In all FEA curves, the loading path within the superelastic range is in good agreement with the experimental results. This was expected, based on the findings of the previous section, and is not examined further. Instead, the focus of this section is on the post-transformation region and on the unloading path.

The transition to the post-transformation region is influenced by four parameters: the stress at the end of the transformation during loading (parameter 8), the transformation strain (parameter 5), the elastic modulus of martensite (parameter 3) and the stress-strain points that define the plastic region (parameter 17). Figures 6-3 and 6-4 show that the post-transformation deformation is predicted correctly as the loading path to high strains is the same for computational and experimental curves.

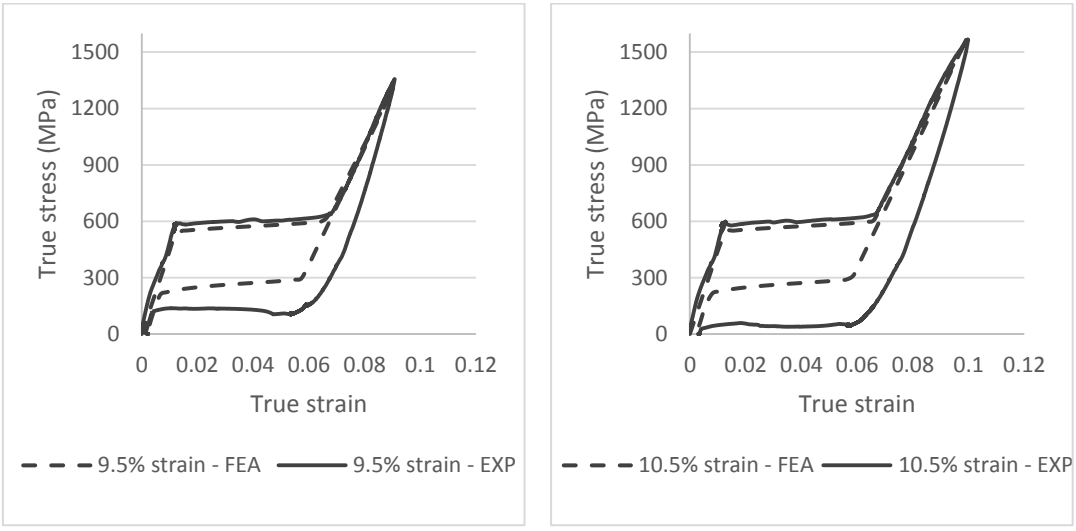

(a) (b)

Figure 6-3 Comparison between computational and experimental responses of Nitinol subjected to high-strain tension: 9.5% strain at 22°C (a) and 10.5% strain at 22°C (b).

When the material is unloaded from high strains, the unloading modulus changes in the experiments. However, this feature is not seen in the computational results, where the unloading modulus of martensite remains the same regardless of the applied maximum strain.

Moreover, the unload plateau also remains the same regardless of the applied strain. Transformation during unloading from 9.5% strain at 22°C, starts at 135MPa

and finishes at 105MPa experimentally, as seen in Table 6-2. When unloading from 10.5% strain at the same temperature, transformation starts at 70MPa and finishes at 20MPa. However, in both FEA curves the unload plateau starts at 300MPa and finishes at 200MPa. These values are the initial input parameters for the unload transformation stresses.

Table 6-2 Comparison between experimental (EXP) and computational (FEA) results obtained from Figure 6-3. The percentage difference between FEA and EXP results is shown in brackets, for the residual strains.

	Loading strain, at 22°C			
	9.5% - EXP	9.5% - FEA	10.5% - EXP	10.5% - FEA
Start of transformation during unloading	135MPa	300MPa	70MPa	300MPa
End of transformation during unloading	105MPa	200MPa	20MPa	200MPa
Residual strain	0.17%	0.15% (-11.8%)	0.34%	0.31% (-8.8%)

Similarly, transformation during unloading from 11% strain at 37°C, starts at approximately 150MPa and finishes at 120MPa in the experiments. Transformation during unloading from 11.5% strain starts at 130MPa and finishes at 100MPa. Finally, when unloading from 12% strain, the plateau starts at 95MPa and finishes at 60MPa. However, in the computational results transformation during unloading always starts at 405MPa and finishes at 280MPa. The above results are summarised in Table 6-3.

At the end of the unloading path, the computational responses exhibit residual strains. These values can be different from the experimental ones, as seen in Table 6-2 and Table 6-3. For instance, the predicted residual strain in the 11.5% strain case at 37°C, was the same in both FEA and experimental results. However, the residual strain in the 11°C strain curve at 37°C, was smaller by approximately 28.6% compared to the experiment.

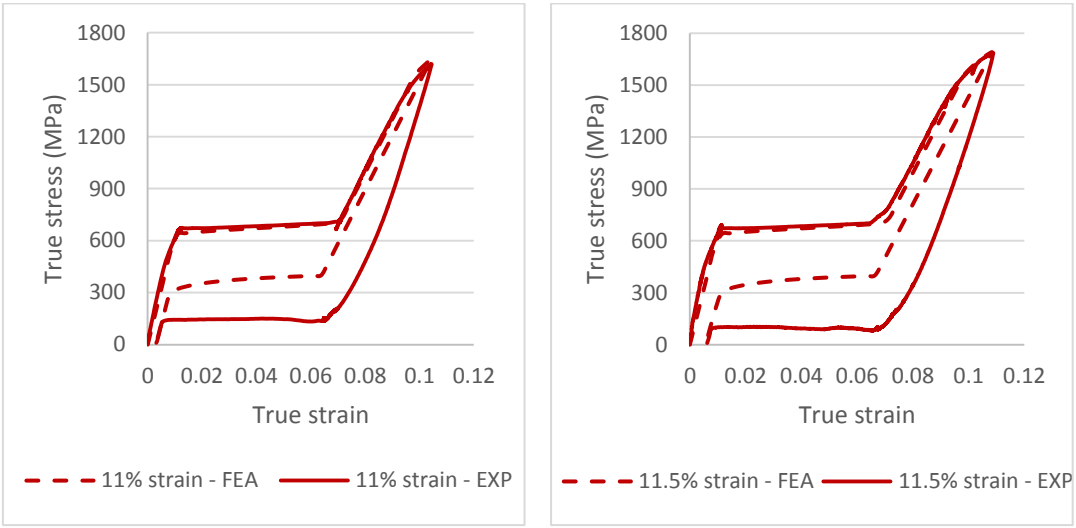

(a)

(b)

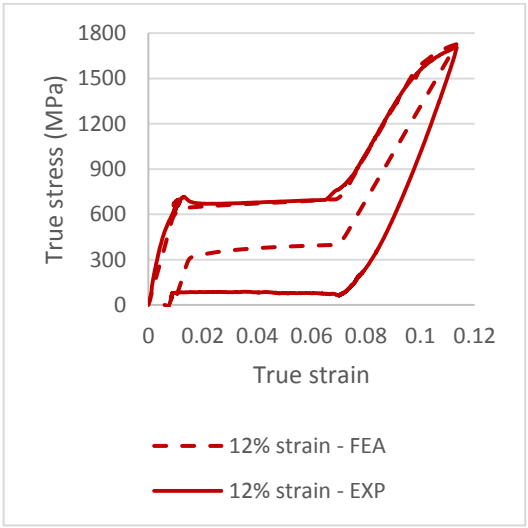

(c)

Figure 6-4 Comparison between computational and experimental responses of Nitinol subjected to high-strain tension: 11% strain at 37°C (a), 11.5% strain at 37°C (b) and 12% strain at 37°C (c).

Table 6-3 Comparison between experimental (EXP) and computational (FEA) results obtained from Figure 6-4. The percentage difference between FEA and EXP results is shown in brackets, for the residual strains.

	Loading strain, at 37°C					
	11% - EXP	11% - FEA	11.5% - EXP	11.5% - FEA	12% - EXP	12% - FEA
Start of transformation during unloading	150MPa	405MPa	130MPa	405MPa	95MPa	405MPa
End of transformation during unloading	120MPa	280MPa	100MPa	280MPa	60MPa	280MPa
Residual strain	0.35%	0.25% (-28.6%)	0.5%	0.5%	0.8%	0.84% (5%)

6.4 Post-transformation tensile modelling using subroutines

The results presented in the previous section showed that Abaqus is capable of capturing the post-transformation loading response of the material. However, the unloading plateau was not represented correctly in the FEA results as it was insensitive to the loading history.

Therefore, the use of subroutines was explored in the present work to examine if the computational forecasts can be improved in terms of the unload plateau. Two subroutines were written in Fortran, in order to modify the input material parameters during the simulations. The first subroutine was coupled with the input parameters at 22°C and the second was coupled with the input parameters at 37°C.

The purpose of the subroutines was to modify the transformation stresses during unloading (parameters 11 and 12) when called by the program. This was achieved by writing an 'if' statement in the subroutine code, which altered the transformation stresses as a function of the plastic strain that was reached during the simulation. The subroutine codes can be found in the Appendix. Each one was written based on available high-strain tensile data. Therefore, for the 22°C subroutine, tensile

tests to 9.5% and 10.5% strain were used. Similarly, for the 37°C subroutine, tensile tests to 11%, 11.5% and 12% strain were used.

The 'if' statement contains essentially two parts for both subroutines. At 22°C, the first part calculates the unload transformation stresses when the predicted plastic strain is lower than 0.2%. The constants used in this part of the subroutine were calculated as explained below in Equation 6-1 and Equation 6-2.

For plastic strain lower than 0.2% at 22°C:

$$135 \approx 300 - (x \cdot 0.0015) \quad \text{Equation 6-1}$$

$$105 \approx 200 - (y \cdot 0.0015) \quad \text{Equation 6-2}$$

In Equation 6-1, the left part (135) is the start of the transformation during unloading from 9.5% strain in MPa. In the right part of the equation, 300 is the initial start of the transformation during unloading in MPa, x is an unknown variable and 0.0015 is the predicted by FEA plastic strain after unloading from 9.5% strain. In Equation 6-2, the left part (105) is the end of the transformation during unloading from 9.5% strain in MPa. In the right part of the equation, 200 is the initial end of the transformation during unloading in MPa, y is an unknown variable and 0.0015 is again the predicted by FEA plastic strain after unloading from 9.5% strain. The above equations result in:

$$x=110000$$

$$y=64000$$

The second part of the 'if' statement, as shown in Appendix A.1, estimates the same stresses when the plastic strain is higher than 0.2% at 22°C. The parameters that were used are explained below in Equation 6-3 and Equation 6-4.

For plastic strain greater than 0.2% at 22°C:

$$70 \approx 300 - (110000 \cdot 0.002) - [\, a \cdot (0.0031 - 0.002)] \quad \text{Equation 6-3}$$

$$20 \approx 200 - (64000 \cdot 0.002) - [\, b \cdot (0.0031 - 0.002)] \quad \text{Equation 6-4}$$

In Equation 6-3 above, the left part (70) is the start of the transformation during unloading from 10.5% strain in MPa. In the right part of the equation, 300 is the initial start of the transformation during unloading in MPa, 110000 is the

unknown variable x that was found earlier, a is unknown and 0.0031 is the predicted by FEA plastic strain after unloading from 10.5% strain. In Equation 6-4, the left part (20) is the end of the transformation during unloading from 10.5% strain in MPa. In the right part of the equation, 200 is the initial end of the transformation during unloading in MPa, 64000 is the unknown y that was found earlier, b is an unknown variable and 0.0031 is again the predicted by FEA plastic strain after unloading from 10.5% strain at 22°C. From the above equations:

$$a=9091$$

$$b=47273$$

A similar method was applied for the 37°C subroutine. The 'if' statement contains again two parts. The first calculates the unload transformation stresses when the predicted plastic strain is lower than 0.3%. The constants were calculated as explained below in Equation 6-5 and Equation 6-6.

For plastic strain lower than 0.3% at 37°C:

$$150 \approx 405 - (x \cdot 0.0025) \qquad \text{Equation 6-5}$$

$$120 \approx 280 - (y \cdot 0.0025) \qquad \text{Equation 6-6}$$

In Equation 6-5, the left part (150) is the start of the transformation during unloading from 11% strain in MPa. In the right part of the equation, 405 is the initial start of the transformation during unloading in MPa, x is an unknown variable and 0.0025 is the predicted by FEA plastic strain after unloading from 11% strain. In Equation 6-6, the left part (120) is the end of the transformation during unloading from 11% strain in MPa. In the right part of the equation, 280 is the initial end of the transformation during unloading in MPa, y is an unknown variable and 0.0025 is again the predicted by FEA plastic strain after unloading from 11% strain. Solving the above equations for x and y we get:

$$x=102000$$

$$y=64000$$

The second part of the 'if' statement of the 37°C subroutine estimates the unload transformation stresses when the plastic strain is higher than 0.3%. The parameters were derived from the system of equations below.

For plastic strain greater than 0.3% at 37°C:

$$130 \approx 405 - a - [\, b \cdot (0.005 - 0.003)] \qquad \text{Equation 6-7}$$

$$100 \approx 280 - c - [\, d \cdot (0.005 - 0.003)] \qquad \text{Equation 6-8}$$

$$95 \approx 405 - a - [\, b \cdot (0.0084 - 0.003)] \qquad \text{Equation 6-9}$$

$$60 \approx 280 - c - [\, d \cdot (0.0084 - 0.003)] \qquad \text{Equation 6-10}$$

In Equation 6-7 above, the left part (130) is the start of the transformation during unloading from 11.5% strain in MPa. In the right part of the equation, 405 is the initial start of the transformation during unloading in MPa, a and b are unknowns and 0.005 is the predicted by FEA plastic strain after unloading from 11.5% strain. In Equation 6-8, the left part (100) is the end of the transformation during unloading from 11.5% strain in MPa. In the right part of the equation, 280 is the initial end of the transformation during unloading in MPa, c and d are unknowns and 0.005 is again the predicted by FEA plastic strain after unloading from 11.5% strain.

Similarly, in Equation 6-9, the left part (95) is the start of the transformation during unloading from 12% strain in MPa. In the right part of the equation, 405 is the initial start of the transformation during unloading in MPa, a and b are unknowns and 0.0084 is the predicted by FEA plastic strain after unloading from 12% strain. In Equation 6-10, the left part (60) is the end of transformation during unloading from 12% strain in MPa. In the right part of the equation, 280 is the initial end of the transformation during unloading in MPa, c and d are unknowns and 0.0084 is again the predicted by FEA plastic strain after unloading from 12% strain. From the above system of equations:

$$a=254$$

$$b=10294$$

$$c=156$$

$$d=11765$$

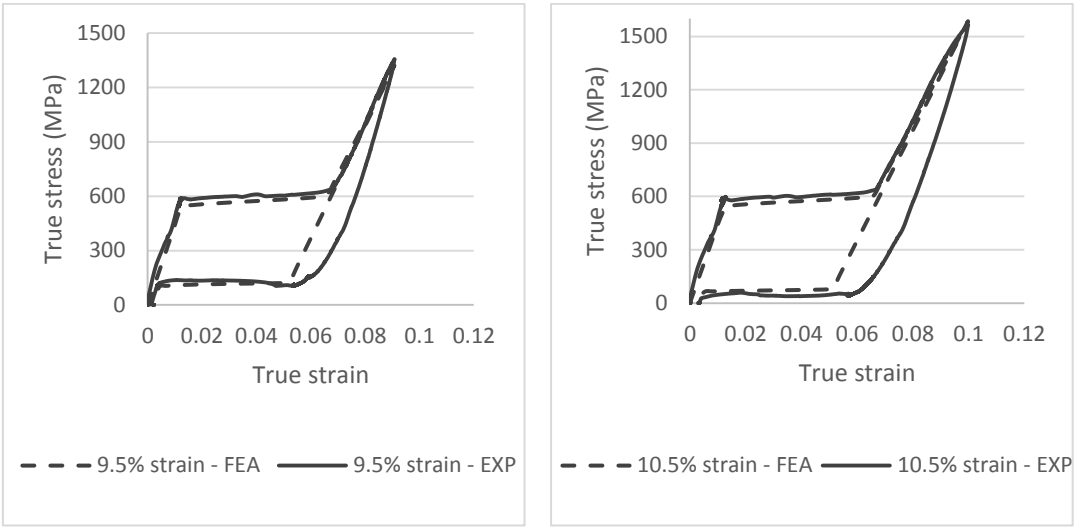

(a) (b)

Figure 6-5 Using subroutines to improve the computational response of Nitinol subjected to high-strain tension at 22°C: 9.5% strain (a) and 10.5% strain (b).

The effect of the subroutines on the computational responses is seen in Figure 6-5 and in Figure 6-6. Using exactly the same input parameters as earlier, the unload plateaus in all graphs are different compared to the previous section. During these simulations the subroutine was called to override the original input parameters for the unload plateau (parameters 11 and 12) based on the plastic strain that was produced during loading. New values were then assigned to the transformation stresses during unloading which were different in each case, as seen in Figures 6-5 and 6-6.

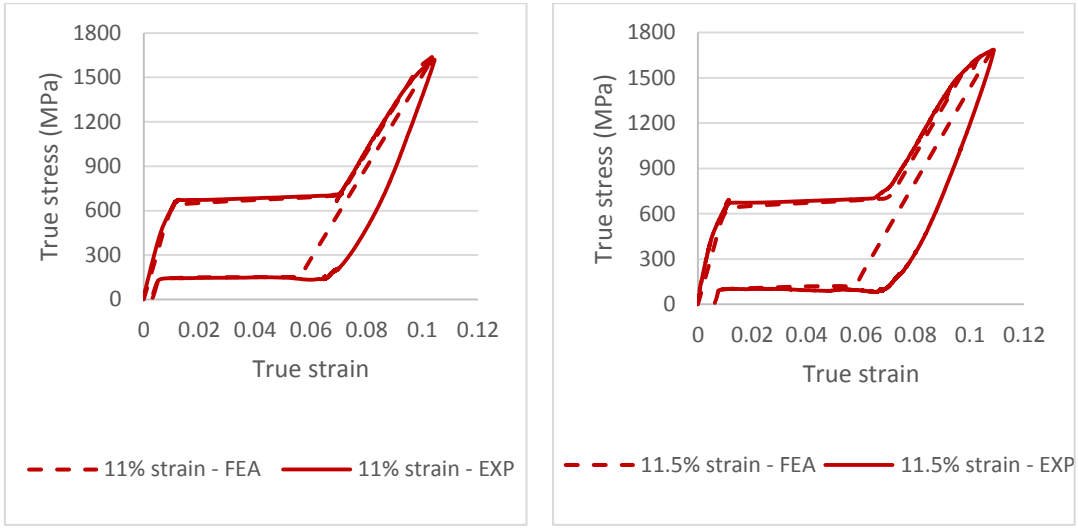

(a)

(b)

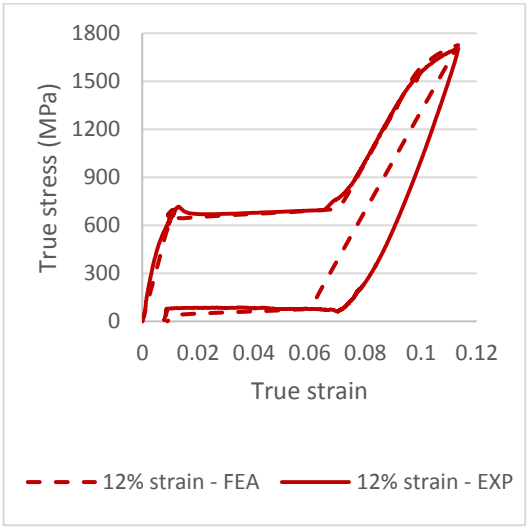

(c)

Figure 6-6 Using subroutines to improve the computational response of Nitinol subjected to high-strain tension at 37°C: 11% strain (a), 11.5% strain (b) and 12% strain (c).

Additional simulations were performed where increasing small strain increments were applied to the model. This was performed in order to identify the minimum applied tensile strain that was required to activate the subroutines. Results are shown in Figure 6-7 including the respective 6% strain responses for comparison. This sensitivity study showed that the unload plateau is changed when the material is loaded to 7% strain or higher at 22°C, and to 10.35% strain or higher at 37°C.

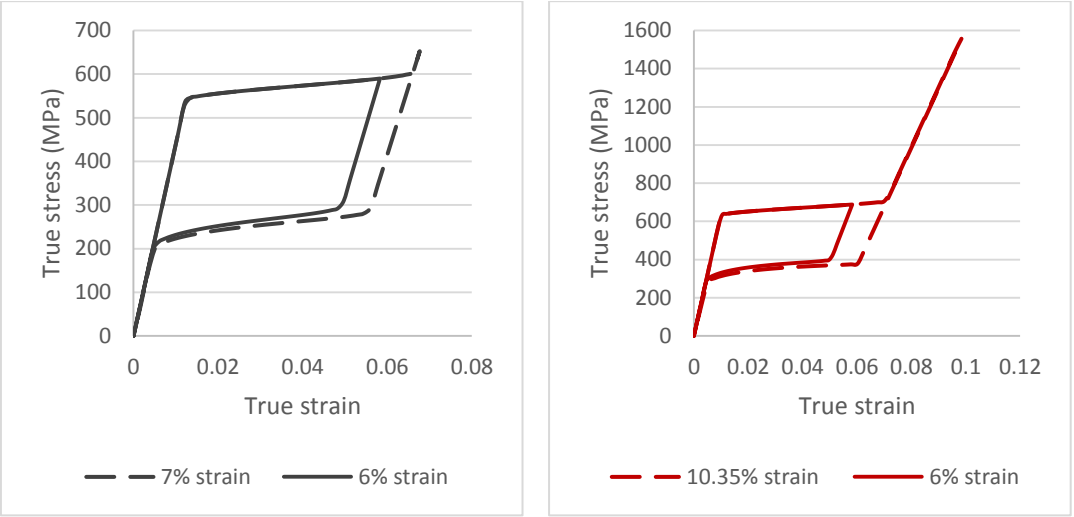

(a) (b)

Figure 6-7 Investigating the strain level required to activate the subroutines during tensile simulations at 22°C (a) and 37°C (b).

6.5 Modelling tension-compression asymmetry

Simulations were performed to investigate the asymmetry between tension and compression in the computational results and to assess whether the material model can represent the experimentally observed compressive behaviour. Figure 6-8 presents the computational and experimental responses of the material when subjected to 6% strain in both tension and compression at 22°C.

Upon loading in compression, the elastic modulus of austenite is equal to the one exhibited in tension. Transformation during loading takes place at 720MPa, which is the value defined in the input parameters. Thereafter, the transformation region has a positive slope where stress increases with strain, unlike tension. At the end of the loading path, the stress value is approximately 800MPa which is significantly higher compared to the 570MPa of tension. Therefore, asymmetry is clearly present in the FEA responses. These parameters are also compared in Table 6-4.

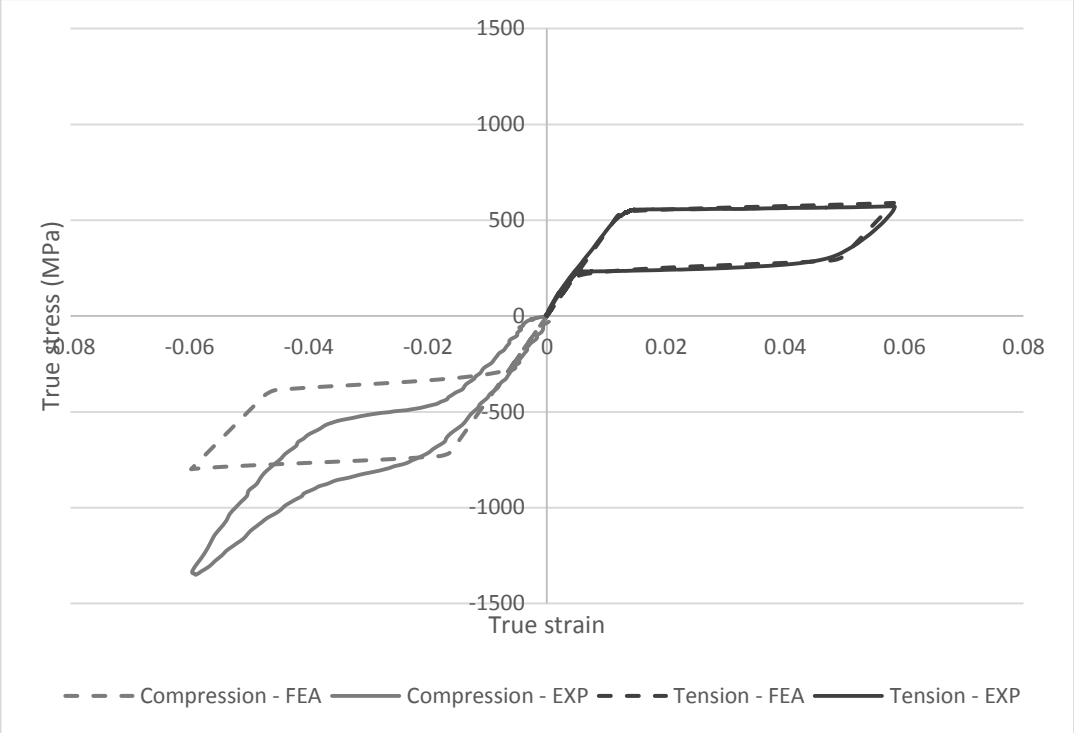

Figure 6-8 Comparison between computational and experimental responses of the 1mm Nitinol wire subjected to 6% strain in tension and compression, at 22°C.

Table 6-4 Comparison between computational (FEA) and experimental (EXP) results obtained from Figure 6-8. The percentage difference between FEA and EXP results is shown in brackets.

22°C			
	Tension FEA/EXP	Compression FEA	Compression EXP
Austenite elastic modulus	44GPa	44GPa	44GPa
Start of transformation during loading	540MPa	720MPa	720MPa
Stress at 6% strain	570MPa	800MPa	>900MPa
Martensite elastic modulus	31GPa	31GPa	31GPa
Start of transformation during unloading	300MPa	400MPa (-30.4% compared to compression EXP)	575MPa
End of transformation during unloading	200MPa	260MPa (-36.6% compared to compression EXP)	410MPa
Residual strain	-	-	0.15%

Upon unloading, the elastic modulus of martensite is again equal to the one exhibited in tension. The asymmetry between tension and compression continues in the unloading path. The unloading transformation region in compression starts at approximately 400MPa and finishes at 260MPa. These values are considerably higher compared to tension, as seen in Figure 6-8 and Table 6-4.

Although asymmetry is exhibited in the computational curves, it is not as pronounced as in the experimental results. Initially, the elastic modulus of austenite and the start of the transformation during loading are in agreement with the experimental results, as seen in Table 6-4. However, the load plateau in the computational response is extended towards the end of the loading path whereas in the experimental curve it ends at approximately 4% strain. Beyond that strain level in the experiment, the material enters the post-transformation region. The unloading modulus is also altered in the experiment when deforming the material to the plastic region. This feature is again not reproduced by the FEA response. The predicted unload plateau is also placed at significantly lower stress levels compared to the experimental curve, as seen in Table 6-4. Due to the above, the predicted by FEA stress-strain curve is not like the sigmoidal experimental response. Instead, it has a flag shape like the tensile response.

The residual strain that was exhibited in the experiment at the end of the load-unload cycle, is also not reproduced by the finite element model. Moreover, the hysteresis of the computational response does not agree with the experimental result. The energy loss within each hysteretic loop was calculated as mentioned in section 4.1.2. The energy loss was approximately 42% in the computational response and 28% in the experimental curve.

Additional compression simulations were also performed where increasing small strain increments were applied to the model. This was performed in order to identify the minimum compressive strain that was required to activate the subroutines. Results are shown in Figure 6-9 including the respective 6% strain responses for comparison. Both sets of input parameters (22°C and 37°C) were included, although the transformation stress during loading in compression at 37°C

was estimated. This sensitivity study showed that the unload plateau is changed when the material is loaded to 6.4% strain or higher at 22°C, and to 9.85% strain or higher at 37°C. If these results are compared against the values reported at the end of section 6.4, it can be seen that the subroutine effect is exhibited at lower strains in compression compared to tension. This was expected because the material is subjected to higher stresses in compression and enters the post-transformation region faster.

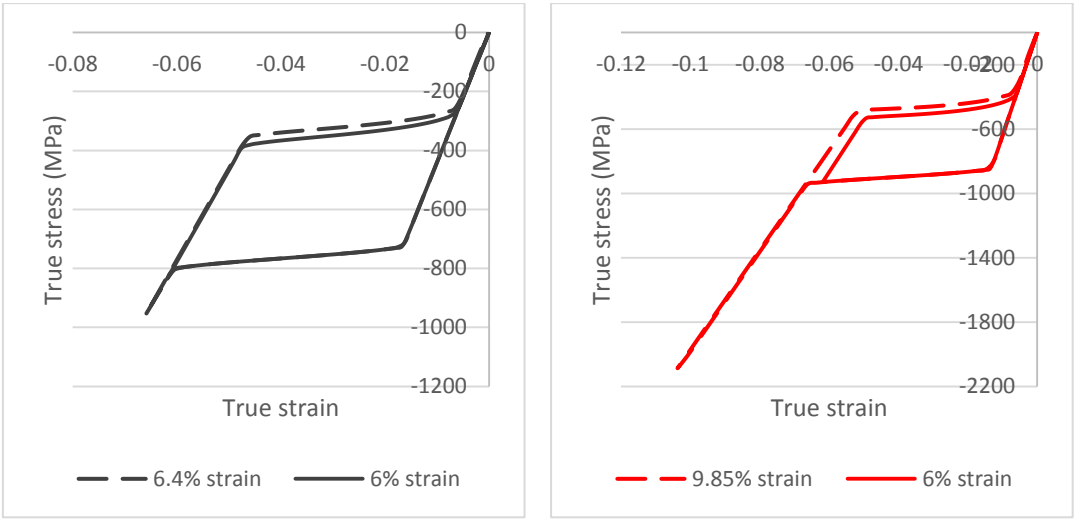

(a) (b)

Figure 6-9 Investigating the strain level required to activate the subroutines during compression simulations at 22°C (a) and 37°C (b).

6.6 Modelling three-point bending within the superelastic range

Figure 6-10 presents the computational and experimental responses of the 1mm Nitinol wire subjected to three-point bending within the superelastic range at 22°C and 37°C. For image clarity, two separate graphs were created. The experimental force-deflection curves correspond to the results presented earlier in section 5.12.

At both temperatures, the predicted flexural stiffness during loading is underestimated. As seen in Table 6-5 and Table 6-6, the flexural stiffness was smaller

by approximately 28.8% at 22°C, and by 13.9% at 37°C, compared to the experimental results. Note that the predicted flexural modulus at both temperatures is very similar to the elastic modulus that was used as input parameter.

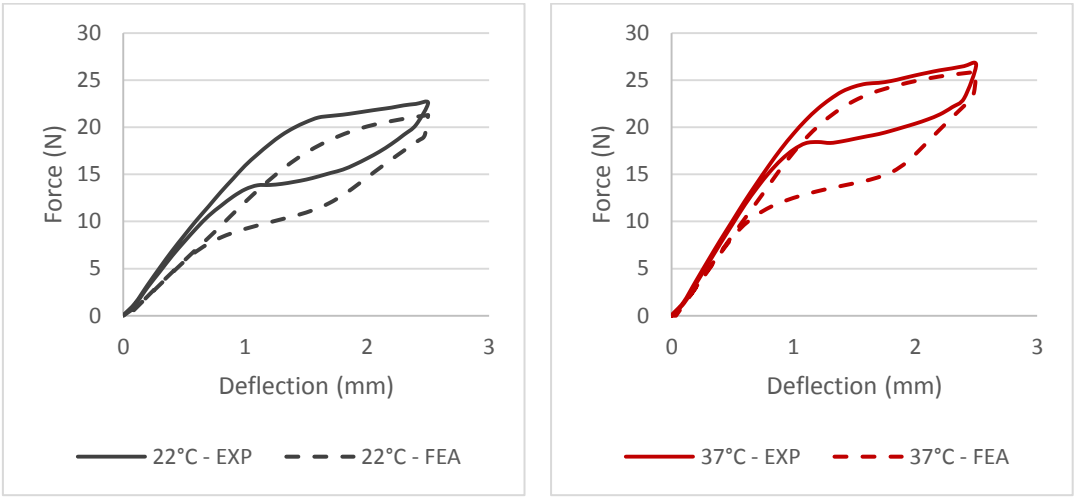

(a) (b)

Figure 6-10 Comparison between experimental and computational responses of the 1mm Nitinol wire subjected to three-point bending within the superelastic range at 22°C (a) and 37°C (b).

During loading at 22°C, the transformation region starts at approximately 21N and 2.1mm in the computational response, whereas the equivalent region in the experimental curve starts at the same force level but at a deflection of 1.6mm. The small load overshoot is also not seen in the FEA results. The loading path of the FEA curve has a positive slope and reaches a maximum force of 21.3N instead of 22.6N in the experiment.

During loading at 37°C, the transformation region in the computational response starts at approximately 23.8N and 1.7mm, whereas in the experimental curve it starts at the same force level but at a deflection of 1.4mm. The maximum exhibited force is 25.9N and 26.6 in FEA and experimental results respectively. These results

During unloading at 22°C, the load drop is approximately 2.3N in both computational and experimental curves, validating the friction properties that were selected in the model. The unload transformation region in the FEA response starts

at approximately 12N whereas the equivalent region during the experiment takes place at 16N. The unload transformation region is then completed again at different force levels: 7.5N and 13.5N, in FEA and experiment respectively.

Table 6-5 Comparison between computational (FEA) and experimental (EXP) results obtained from Figure 6-10(a). The percentage difference between FEA and EXP results is shown in brackets.

22°C	FEA	EXP
Austenite flexural modulus	42GPa (-28.8%)	59GPa
Start of transformation during loading	21N at 2.1mm	21N at 1.6mm
Max force at 2.5mm	21.3N (-5.8%)	22.6N
Load drop upon unloading	2.3N	2.3N
Start of transformation during unloading	12N (-25%)	16N
End of transformation during unloading	7.5N (-44.4%)	13.5N

Upon unloading at 37°C, the exhibited load drop in the FEA curve is 2.8N instead of 3.5N in the experimental force-deflection response. This could be attributed to the use of water as the ambient medium for bend testing at 37°C. The subsequent transformation region starts at 15.3N and 22N in computational and experimental curves respectively. The predicted unloading paths proceed at lower force levels compared to the experimental results. The transformation region ends at 11N in the FEA curve and 18N in the experimental one. The above results are summarised in Table 6-5 and Table 6-6.

Table 6-6 Comparison between computational (FEA) and experimental (EXP) results obtained from Figure 6-10(b). The percentage difference between FEA and EXP results is shown in brackets.

37°C	FEA	EXP
Austenite flexural modulus	62GPa (-13.9%)	72GPa
Start of transformation during loading	23.8N at 1.7mm	23.8N at 1.4mm
Max force at 2.5mm	25.9N (-2.6%)	26.6N
Load drop upon unloading	2.8N (-20%)	3.5N
Start of transformation during unloading	15.3N (-30.5%)	22N
End of transformation during unloading	11N (-38.9%)	18N

6.7 Modelling three-point bending beyond the superelastic range

Figure 6-11 presents the computational and experimental responses of the 1mm Nitinol wire subjected to three-point bending beyond the superelastic range at 22°C. The experimental force-deflection curve corresponds to the low-rate results presented earlier in section 5.14.

Upon loading, the initial force-deflection characteristics of the FEA curve, are the same as those described in the previous section. In this case, the loading path continues beyond 2.5mm, reaching a maximum force of 22.7N and 24.8N, in the computational and experimental results respectively. These force levels were achieved at approximately the same deflection of 4.3mm in both responses. With further loading, the loading path exhibits a negative slope in the experimental curve which is reproduced by the finite element model.

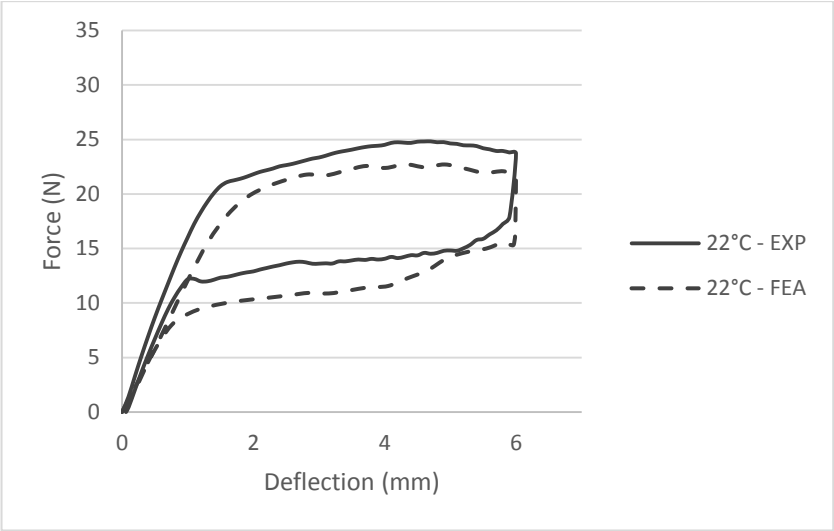

Figure 6-11 Comparison between experimental and computational responses of the 1mm Nitinol wire subjected to three-point bending beyond the superelastic range at 22°C.

Table 6-7 Comparison between computational (FEA) and experimental (EXP) results obtained from Figure 6-11. The percentage difference between FEA and EXP results is shown in brackets.

22°C	FEA	EXP
Max force	22.7N at 4.3mm (-8.5%)	24.8N at 4.3mm
Load drop upon unloading	6.2N (6.9%)	5.8N
Start of transformation during unloading	12N (-21.6%)	15.3N
End of transformation during unloading	7.5N (-34.8%)	11.5N
Permanent deformation	-	0.06mm

Upon unloading, the load drop is approximately 6.2N and 5.8N in the computational and experimental curves respectively. A secondary load drop is present in both curves leading to the unload transformation region which starts at 12N in the FEA response and at 15.3N in the experiment. This region ends at 7.5N and 11.5N in FEA and experiment respectively.

Note that the start/end force levels of the predicted unload transformation region, are equal to the ones seen earlier when modelling bending within the superelastic range at 22°C. Thus, the predicted unloading path is insensitive of the loading history. It also ends without any permanent deformation whereas a residual

deformation of 0.06mm is present in the experiment. The above quantitative results can also be seen in Table 6-7.

Due to the lack of residual deformation in the FEA curve, the strain level that was reached during the simulation was examined. Figure 6-12 shows the stress-strain response of an element located at the region of maximum tensile strain. The element is clearly deformed to 9% true strain in the post-transformation region. Note that FEA results are always plotted as true stress and strain values, since the input parameters are configured in the same manner.

The dashed line in Figure 6-12 corresponds to the stress-strain response of the same element when the subroutine was used during the analysis. This result shows that, if individual elements within the mesh are subjected to high strains, the input parameters at their respective integration points will be modified by the subroutine. This response compares well with the 9.5% tensile strain case of Figure 6-5 (section 6.4). The transformation stresses during unloading and the residual strain are the same.

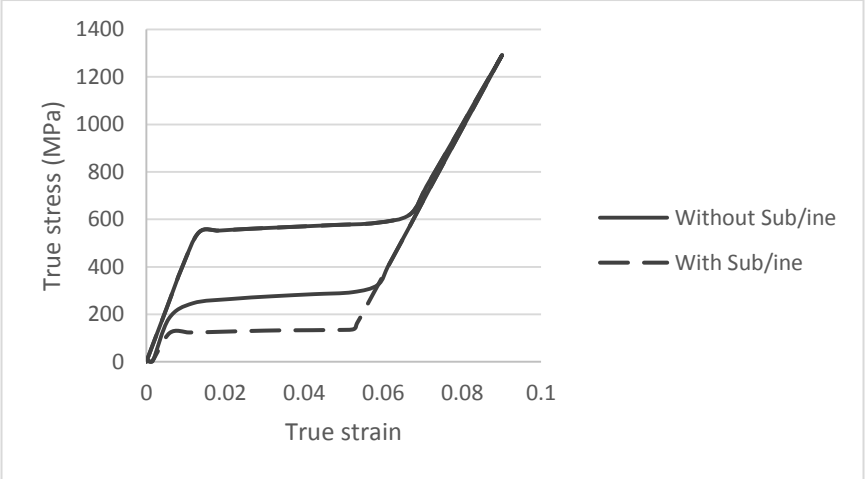

Figure 6-12 Tensile stress-strain response of an element at the region of maximum tensile strain, with- and without the subroutine that modifies the unload plateau.

Figure 6-13 shows the predicted force-deflection curve when the subroutine is used. The curve is also compared with the computational response presented previously in Figure 6-11. The only noticeable change is seen in the unloading path

from approximately 3.8mm to 1mm, which takes place at marginally lower force levels.

This finding confirms the description given in section 5.14, that the transformation regions of the force-deflection curve can be divided into two parts. The 'true' transformation regions in both loading and unloading paths are up to approximately 4mm. Beyond that point, the bending response is influenced by the sliding of the specimen over the supports.

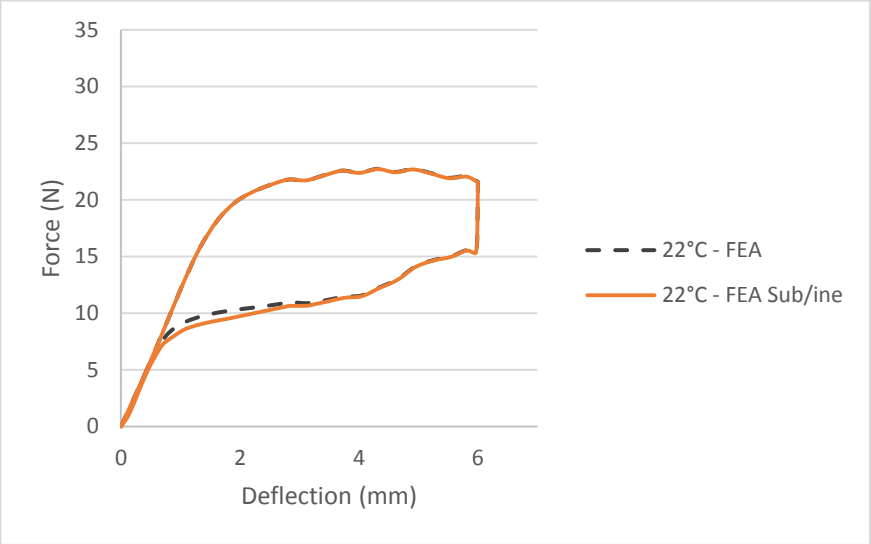

Figure 6-13 Comparison between computational bending responses, with- and without the subroutine that modifies the transformation stresses during unloading.

Differences between computational and experimental results are also seen when modelling large deflection bending at 37°C. Figure 6-14 presents the FEA and experimental responses of the 1mm Nitinol wire subjected to three-point bending beyond the superelastic range at 37°C. Upon loading, the initial force-deflection characteristics of the FEA curve, are the same as those described in the previous section 6.6.

In this case, the loading path continues beyond 2.5mm, reaching a maximum force of 27N and 30N, in the computational and experimental results respectively. These force levels were achieved again at approximately the same deflection of 4.3mm in both responses. With further loading to 6mm, the loading path exhibits a negative slope in both curves.

Upon unloading, the predicted load drop (7.2N) is significantly smaller compared to the experimental one (11.6N). The predicted unload transformation region is insensitive of the loading history. The transformation region starts at 15.3N and finishes at 11N. These values are equal to the ones exhibited in the superelastic case. This can be seen by comparing the parameters of Table 6-6 and Table 6-8. By comparison, the unload transformation region of the experimental response starts at 16.5N and finishes at 15N. Unloading ends without any permanent deformation in the FEA curve whereas a residual deformation of around 0.1mm is exhibited during the experiment. The above quantitative results are summarised in Table 6-8.

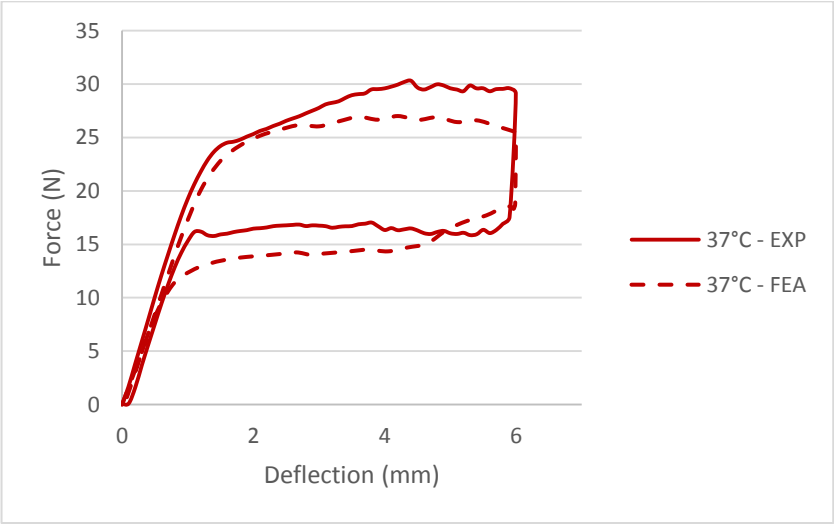

Figure 6-14 Comparison between experimental and computational responses of the 1mm Nitinol wire subjected to three-point bending beyond the superelastic range at 37°C.

Table 6-8 Comparison between computational (FEA) and experimental (EXP) results obtained from Figure 6-14. The percentage difference between FEA and EXP results is shown in brackets.

37°C	FEA	EXP
Max force	27N at 4.3mm (-10%)	30N at 4.3mm
Load drop upon unloading	7.2N (-37.9%)	11.6N
Start of transformation during unloading	15.3N (-7.3%)	16.5N
End of transformation during unloading	11N (-26.7%)	15N
Permanent deformation	-	0.1mm

6.8 Modelling bending using the flexural modulus as input parameter

The flexural modulus of austenite was calculated earlier using experimental data; it was approximately 59GPa at 22°C and 72GPa at 37°C. Results presented in the previous sections showed that Abaqus does not capture correctly these values, as the stiffness was underestimated. Therefore, the elastic modulus of austenite (Parameter 1) was replaced by the flexural modulus, and the simulations of Figure 6-11 and Figure 6-14 in the previous section, were repeated in order to examine whether the predicted bending responses can be improved.

Results are presented in Figure 6-15 and Tables 6-9 and 6-10. At both temperatures, the flexural stiffness of austenite is in very good agreement with the bending data. At 22°C, the predicted flexural modulus (58.5GPa) is only 0.9% smaller than the experimental one. Similarly, the flexural modulus of the 37°C FEA curve is closer to the experimental value.

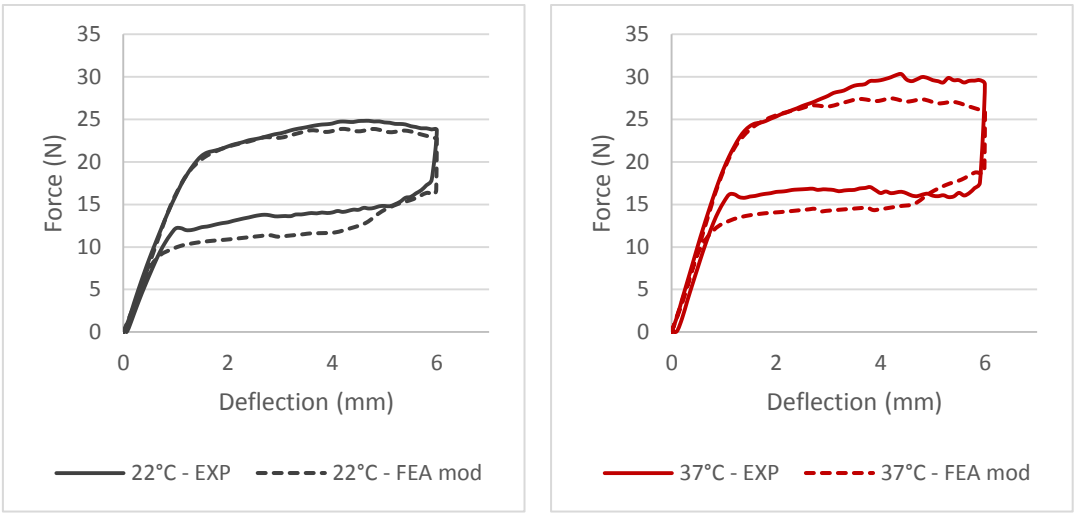

(a) (b)

Figure 6-15 Using the flexural modulus of austenite as input parameter, to improve the computational response of the 1mm Nitinol wire subjected to three-point bending, beyond the superelastic range at 22°C (a) and 37°C (b).

Table 6-9 Comparison between computational (FEA) and experimental (EXP) results obtained from Figure 6-15(a). The percentage difference between FEA and EXP results is shown in brackets.

22°C	FEA with mod E_A	EXP
Austenite flexural modulus	58.5GPa (-0.9%)	59GPa
Start of transformation during loading	21N at 1.7mm	21N at 1.6mm
Max force	23.9N at 4.3mm (-3.6%)	24.8N at 4.3mm
Load drop upon unloading	6.4N (10.3%)	5.8N
Start of transformation during unloading	12N (-21.6%)	15.3N
End of transformation during unloading	7.5N (-34.8%)	11.5N
Permanent deformation	-	0.06mm

Table 6-10 Comparison between computational (FEA) and experimental (EXP) results obtained from Figure 6-15(b). The percentage difference between FEA and EXP results is shown in brackets.

37°C	FEA with mod E_A	EXP
Austenite flexural modulus	69GPa (-4.2%)	72GPa
Start of transformation during loading	23.8N at 1.5mm	23.8N at 1.4mm
Max force	27.5N at 4.3mm (-8.3%)	30N at 4.3mm
Load drop upon unloading	7.3N (-37.1%)	11.6N
Start of transformation during unloading	15.3N (-7.3%)	16.5N
End of transformation during unloading	11N (-26.7)	15N
Permanent deformation	-	0.1mm

By using the flexural modulus, the loading path of the FEA curves is now shifted to smaller deflections. Consequently, the transformation region is improved in terms of the deflection levels it takes place. This can be seen by comparing the (Start of transformation during loading) results of Tables 6-5 and 6-6 (section 6.6) with the results of Tables 6-9 and 6-10.

The loading paths are almost the same up to a deflection of approximately 3mm. Beyond that point, the computational responses are still improved, especially

for the 22°C case. However, the unloading path remained unaffected by the use of the flexural modulus. It is still not represented correctly since the unload transformation regions take place at exactly the same force levels as the results of the previous section. This was expected since the initial stiffness affects mainly the loading path.

6.9 Modelling torsion

Figure 6-16 presents the computational and experimental response of the 1.8mm wire when rotated to 80 degrees, at 22°C. Upon loading, the torsional stiffness of the material is slightly underestimated in the predicted torque-rotation curve. The calculated torsional modulus of austenite was 15GPa in the FEA curve instead of 16.9GPa in the experimental one. Subsequently, the upper transformation region starts at somewhat lower torque levels, approximately 0.45Nm, compared to 0.5Nm in the experiment. At the end of the loading path the maximum load is 0.58Nm instead of 0.7Nm in the experiment. These results are also presented in Table 6-11.

Upon unloading from 80 degrees, the unloading modulus of martensite is in good agreement with the experimental result: 12.5GPa in FEA compared to 12.2GPa in the experiment. Therefore, the predicted modulus was 2.5% greater than the experimental one, as seen in Table 6-11.

Transformation during unloading takes place at lower torque levels. In the computational response, this region starts at approximately 0.3Nm and finishes at 0.2Nm. By comparison, reverse transformation during the experiment starts at 0.5Nm and finishes at 0.25Nm. The linear regions that correspond to the elastic deformation of austenite during loading and unloading, share the same path in the FEA curve. On the contrary, these regions are represented by different slopes in the experimental results.

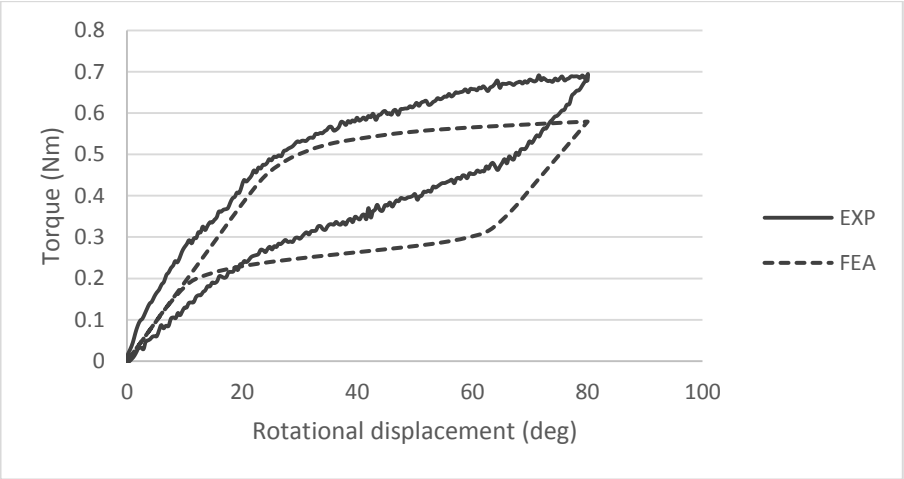

Figure 6-16 Comparison between computational and experimental responses of the 1.8mm Nitinol specimen subjected to 80 degrees rotation, at 22°C.

Table 6-11 Comparison between computational (FEA) and experimental (EXP) results obtained from Figure 6-16. The percentage difference between FEA and EXP results is shown in brackets.

	FEA	EXP
Austenite torsional modulus	15GPa (-11.2%)	16.9GPa
Start of transformation during loading	0.45Nm (-10%)	0.5Nm
Max torque at 80 degrees	0.58Nm (-17.1%)	0.7Nm
Martensite torsional modulus	12.5GPa (2.5%)	12.2GPa
Start of transformation during unloading	0.3Nm (-40%)	0.5Nm
End of transformation during unloading	0.2Nm (-20%)	0.25Nm

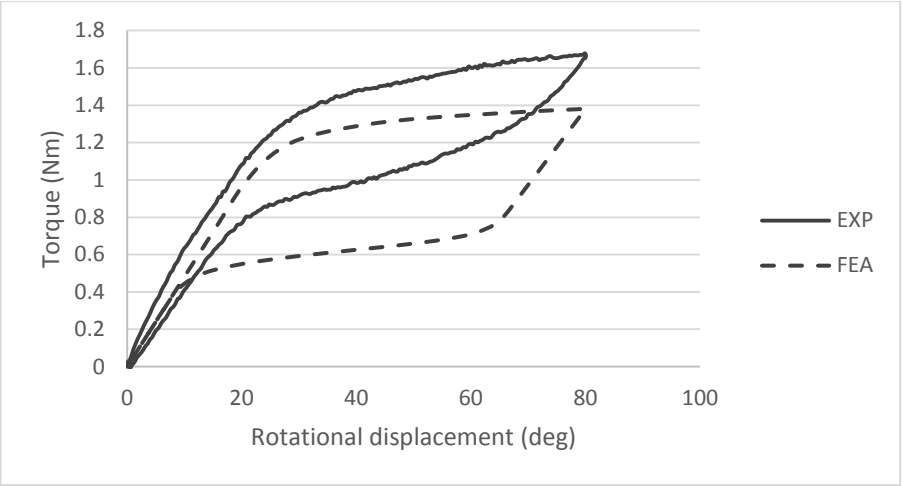

Figure 6-17 Comparison between computational and experimental responses of the 2.4mm Nitinol specimen subjected to 80 degrees rotation, at 22°C.

Greater discrepancy between computational and experimental torsional responses is seen when comparing results for the 2.4mm Nitinol specimen. The predicted torque-rotation curve is compared with the experimental one in Figure 6-17. Transformation during loading and unloading in this case takes place at noticeably different torque levels compared to the experimental curve. This was expected since the 2.4mm specimen had a lower A_f temperature, hence different properties compared to specimens that were used to identify the input parameters for the finite element simulations. Additionally, this specimen did not meet the required specifications as mentioned in section 4.1.1.

This is the reason that quantitative analysis using the results from the 2.4mm diameter wire was not performed. In the next section, results from combined tension-torsion simulations are compared with the experimental ones on a qualitative basis.

6.10 Modelling torsion under different tensile pre-loads

In this section, results from combined tension-torsion simulations are presented and discussed on a qualitative basis. Figure 6-18 presents the

computational tensile and torsional responses of the 2.4mm Nitinol wire, when subjected to combined low tensile-large torsional deformation. Results are compared with the pure tensile and pure torsional curves produced by FEA. In this simulated scenario, the specimen is initially displaced by 0.1mm under tension. Subsequently, the axial displacement is kept constant while the specimen is rotated by 80 degrees. A small load drop is observed in the force-displacement curve during this process, which is recovered when the rotational displacement is removed. Thereafter, the axial displacement is removed completing the loading sequence.

The qualitative features of combined loading can be reproduced computationally by the Abaqus Nitinol model: the force-displacement curve is similar to the pure tensile response except for the load drop, while the torsional response is shifted to slightly lower torque levels compared to the pure torsional response.

However, the computational responses are not in agreement with the experimental ones, as seen in Figure 6-19. Note that the experimental data seen here were also presented earlier in Figure 5-32 (section 5.20). After the load drop is recovered in the FEA tensile response, the curve follows the same initial path during unloading. On the contrary, the loading and unloading paths differ in the experimental tensile response. Also, the torque-rotation curve is not predicted correctly. However, this was expected considering the differences between computational and experimental results identified in the previous section.

Similarly, Figure 6-20 presents the computational tensile and torsional responses of the 2.4mm Nitinol wire, when subjected to combined large tensile-large torsional deformation. Results are again compared with the pure tensile and pure torsional curves produced by FEA. Initially, the specimen is displaced axially by 1mm. The axial displacement is then kept constant while the specimen is rotated by 80 degrees. During this process, a noticeable load drop is observed in the force-displacement curve, which is recovered when the rotational displacement is removed. Subsequently, unloading is completed with the removal of the axial displacement.

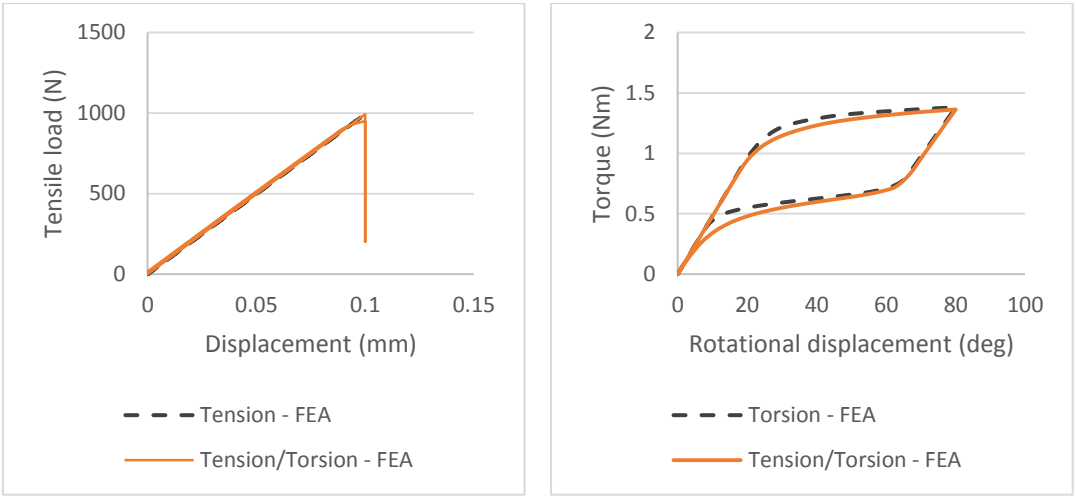

(a) (b)

Figure 6-18 Computational tensile and torsional responses of the 2.4mm Nitinol wire subjected to combined low tensile deformation-large torsional deformation: comparison with pure tensile (a) and pure torsional (b) computational responses.

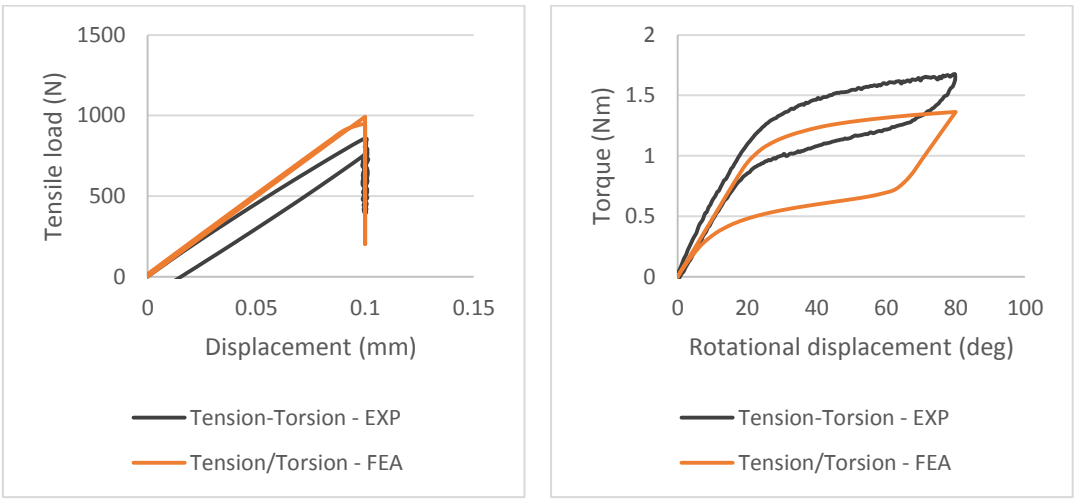

(a) (b)

Figure 6-19 Computational tensile and torsional responses of the 2.4mm Nitinol wire subjected to combined low tensile deformation-large torsional deformation. Comparison with experimental tensile (a) and torsional (b) responses under the same combined deformation conditions.

The force-displacement curve is again similar to the pure tensile response except for the load drop. Although this is not clearly seen in Figure 6-20 (a), it alters the unloading path. The predicted torsional response under these loading conditions, is shifted towards lower torque levels compared to the one shown when only a

rotational displacement is applied. The curve exhibits nearly linear loading and unloading paths with some slight hysteresis.

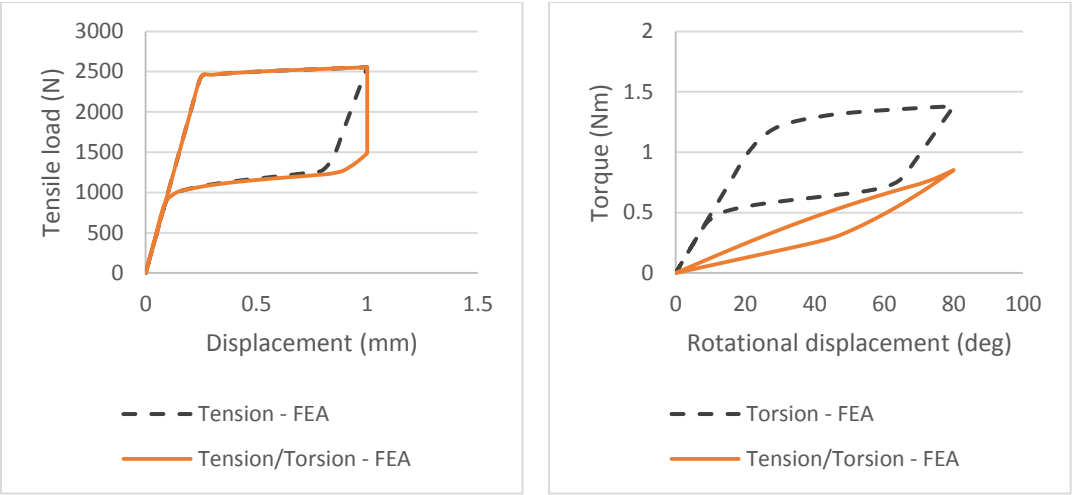

(a) (b)

Figure 6-20 Computational tensile and torsional responses of the 2.4mm Nitinol wire subjected to combined large tensile deformation-large torsional deformation: comparison with pure tensile (a) and pure torsional (b) computational responses.

Similar features were described earlier in the experimental data of Figure 5-33 (section 5.20). However, the FEA responses do not agree with the experimental ones, as seen in Figure 6-21. The computational force-displacement curve over-estimates the start of the transformation during loading and the following load plateau.

The torque-rotation curve exhibits nearly linear loading and unloading paths whereas the experimental one exhibits a short upper transformation region from approximately 65 to 80 degrees. The FEA curve is also shifted towards lower torque levels compared to the experimental response. The plastic strains produced during the analysis are in the order of 10^{-4}, thus not high enough to alter the macroscopic responses.

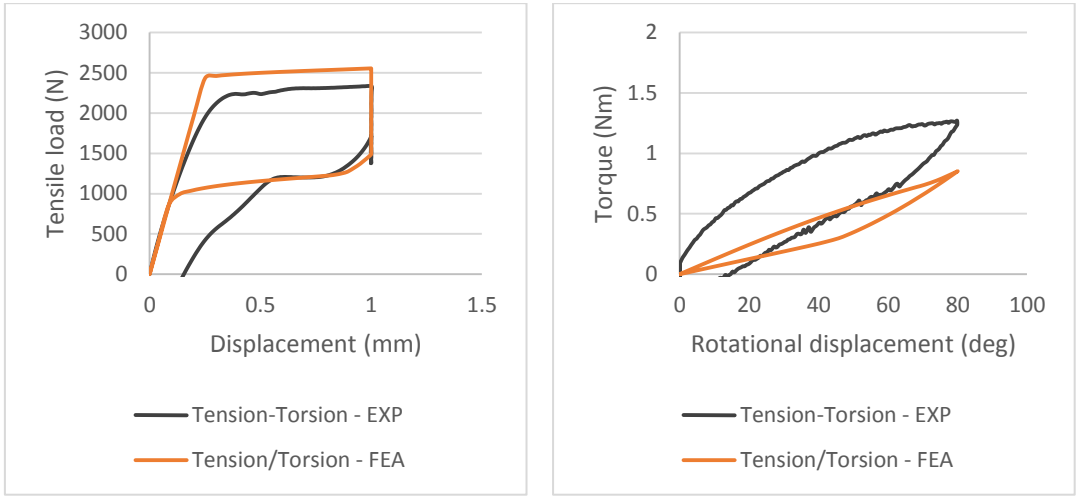

(a) (b)

Figure 6-21 Computational tensile and torsional responses of the 2.4mm Nitinol wire subjected to combined large tensile deformation-large torsional deformation. Comparison with experimental tensile (a) and torsional (b) responses under the same combined deformation conditions.

Chapter 7 Discussion

The following sections discuss the methodology, results and findings of the present work. Recommendations relating to the design of medical devices are introduced and suggestions for future work are proposed.

7.1 Assessment of the experimental methodology

7.1.1 Specimens employed for testing

The material examined in the present work is medical grade Nitinol that is used in the manufacture of cardiovascular stents. The properties of Nitinol materials depend on several factors, including the alloy composition. A change of 1% in the nickel to titanium ratio can alter the A_f temperature by 100°C [35]. Heat treatments and processing techniques can also alter the final A_f of Nitinol specimens [37, 145]. Several studies in the literature have revealed that wires of the same nominal dimensions, made from different Nitinol materials, behave differently when tested under the same conditions [146-148].

Therefore, it is crucial that all Nitinol specimens meet the same specifications when comparing test results and identifying material properties. Nitinol studies in the literature often compare wires with tubes or sheet specimens. Even though such specimens can be made to meet the same specifications, the manufacturing method (drawing, forging, rolling) will be different as explained in section 3.1.1. In addition, tubes are only used in laser-cut stents while sheet specimens are not used directly in cardiovascular devices. The majority of stent-graft devices are made of a Nitinol wireframe sewn onto a fabric graft. Therefore, studies that include wire testing are of direct interest to stent-graft manufacturers.

Testing in the present work was conducted using wires which were supplied by a single manufacturer (FWM). All specimens were made from the same ingot type

(NiTi#1) and were required to meet the same specifications. These specifications included key mechanical properties, as outlined in section 4.1.1. The chemical composition of the specimens was also required to comply with the requirements of ASTM F2063 [39].

The wires were subjected to tension, compression, bending and torsion. Testing Nitinol wires of the same specifications in various loading modes is unique in the literature. This was performed because Nitinol wires are the main component of stent-grafts which are subjected to high-strain multi-mode loading conditions during compaction and subsequent deployment in-vivo. Therefore, when developing test methods and designing a device, one should consider the different modes of deformation the device might be subjected to. Regulatory agencies have also recognized the above and have updated their guidelines accordingly. The ISO standard 25539 [123] states that if applicable, the structural integrity of an endovascular device should be evaluated under axial, bending and torsional loading.

Moreover, when submitting computational analyses reports to a regulatory agency, it is required under the same ISO guidelines, to confirm that the material model used for the simulations represents the behaviour of the materials under the applicable loading mode. The material parameters for FEA were based only on the four NiTi#1-SE specimens that complied with the required specifications. The large diameter 2.4mm specimen, which did not meet the required specifications, was only employed to examine the rate effects on the torsional response and the qualitative features of combined loading. The 0.22mm diameter USN® wire was also mainly used to investigate its high-strain deformation properties.

Variations can still exist between different diameter specimens as shown earlier in Figure 5-13 (section 5.6). These could be attributed to the slightly different processing technique that was required to manufacture each specimen. As explained in section 3.1.1, the raw material is subjected to a series of drawing and annealing cycles to reduce its diameter down to the desired specimen. This process is inevitably slightly different for different diameter specimens which is also evident by the different diameter tolerances, as shown in Table 4-1 (section 4.1.1). All specimens

were superelastic during testing which was conducted using the 'as-received' wires without any additional processing.

7.1.2 Tensile test method

Tensile testing was performed by following the ASTM standard [128] guidelines and adapting them when necessary to fit the needs of the present work. Type I testing was used to identify the tensile constitutive parameters and was conducted as described in section 4.1.2. The accurate measurement of strain is crucial in such testing, especially when results are used to identify the majority of the FEA input parameters.

Strain calculations based on the extension of the machine's crosshead is not accurate since stress concentrations near the grips can affect the transformation of the material. High stress regions, due to gripping forces become preferred sites for the formation of martensite domains. Zhang et al. [52] and Shaw and Kyriakides [53] observed the formation of localised transformation domains near the gripped ends of their specimens during tensile testing.

In the latest (2018) update of the ASTM standard for the tensile testing of Nitinol wires [149], the use of an extensometer became a requirement. In the past, this was only a recommendation. The use of clip-on extensometers on wires is challenging and can lead to testing difficulties by inducing stress concentrations on fine specimens. Therefore, a non-contact video extensometer was employed to measure strain in the present work. The benefit of measuring strain using a video extensometer can be seen in Figure 7-1 which shows the tensile strain measured by the extensometer against the crosshead extension.

During the initial elastic loading of the specimen, strain increases linearly with crosshead extension. When transformation during loading takes place at approximately 1.4% strain, local straining within the gauge length stops increasing although the crosshead keeps pulling the specimen. This is associated with

martensitic transformation taking place out of the extensometer gauge length. When the crosshead is moved by approximately 6.4mm, strain starts increasing again with extension as the remaining material transforms to martensite. Note that the load plateau of the macroscopic stress-strain response is exhibited for a corresponding crosshead extension between 2.5mm and 11mm.

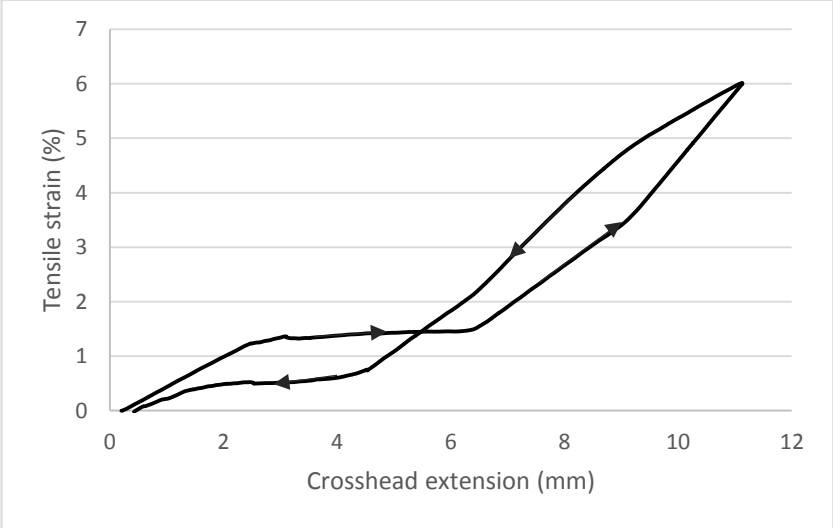

Figure 7-1 Tensile strain measured by the video extensometer against crosshead extension during tensile testing within the superelastic range.

Similarly, strain and extension during unloading are initially proportional until the remaining martensite outside the gauge length starts transforming back to austenite. During the elastic unloading of the specimen, strain decreases linearly with extension. Note that strain returns to zero whereas the extension does not. Thus, if strain is calculated based on crosshead movement, some residual deformation will appear in the stress-strain response. Similar observations were made by Shaw and Kyriakides [54] by comparing strain measurements based on crosshead movement and miniature extensometers.

Tensile tests were very repeatable as shown in section 5.7. The testing equipment was calibrated according to the ASTM standards requirements and since systematic errors and random errors were low, minor differences were observed between identical experimental results. The maximum relative error of the results, i.e. the total error as a percentage of the mean, was around 1%.

The current test method can be extended in future studies by acquiring the Instron DIC software. This software works in a post-processing mode using data obtained by the video extensometer which is already a component of the experimental configuration. DIC will provide strain and displacement field images allowing researchers to study the transformation characteristics of the specimens and examine the differences, if any, between the NiTi#1-SE and USN® materials.

7.1.3 Compression test method

The compression test method was developed to accommodate the testing of the small diameter wires used in tension. Characterisation of Nitinol materials requires the deformation of specimens to superelastic strains. Considering the issue of specimen buckling, which is often present during compression testing, a small length to diameter ratio was needed to prevent this effect.

Therefore, the 1mm diameter Nitinol wires were machined into 3mm long specimens by electrical discharge. This type of machining is recommended for fabricating small specimens as there is no direct contact between the tools and the work piece. The short specimens were then tested using a miniature compression stage mounted onto a SEM. The test method proposed in the present work is unique in the literature.

Strain was measured based on the crosshead movement, assuming the full length of the specimen was compressed uniformly. The magnified SEM images of Figure 5-17 (section 5.10) showed that this assumption was valid. The use of high load capacity lubricant minimized the friction between the compressive plattens and the specimen and thus prevented the specimen from barrelling. In addition, the fixed displacement accuracy of 0.01mm is lower than the requirement of the ASTM E2309 [135].

However, although the displacement error is very small as an absolute number, it is still large if compared to the maximum displacement the specimen

experienced in these tests. The relative error of the measured displacement was approximately 5.5%, as shown in section 5.11. Moreover, crosshead movement of only 0.03mm corresponded to 1% engineering strain for the short specimens. The above also show why compression studies of Nitinol wires are so scarce in the literature. By using a small specimen, we can overcome the issue of buckling at superelastic strains but at the same time the testing machine becomes a crucial factor in the accuracy of the results.

Due to the small specimen size, the use of a conventional DIC method is difficult. However, a few researchers have successfully combined DIC software with SEM images, eliminating the need to apply a synthetic speckle onto the surface of the specimens [150, 151]. The feasibility of this method could be explored in future work for more accurate strain measurements.

In terms of FEA simulations, the Nitinol model in Abaqus requires only one input parameter to be obtained from compression tests: the transformation stress during loading. The accurate measurement of this parameter depends only on the load cell of the testing machine, which as shown earlier produces small force errors under repeatability conditions. Therefore, the current test method is suited for identifying the input parameter that is used in the finite element model.

Although the compression stage could be used outside the SEM chamber, compression tests at 37°C were not conducted since the machine was not suitable for use at high temperatures. However, the Deben machine can be customised by the manufacturer to withstand higher temperatures. This would make it suitable for use with a universal or custom-built environmental chamber, due to its small size. Therefore, this option could be explored in future work to allow compression testing at 37°C.

This experimental configuration would also suit researchers who are interested in studying the phase transformation characteristics of Nitinol under the SEM. Similar studies have examined the tensile deformation [56, 152, 153] but are scarce for compression. However, the aforementioned studies noted the importance

of having a grain size in the order of nanometres. The grain size in typical industrial Nitinol is in the order of nanometres which is not suitable for microscopy studies.

7.1.4 Three-point bend test method

Three-point bending was performed to investigate the bending characteristics of Nitinol wires because it is a simple and straightforward test that makes comparisons with other studies easy. The thicker 1mm diameter wire was used for these tests because it was compatible with the available 450N load cell. Due to the fourth-power dependence on thickness, the second moment of area of a round wire affects the bending results for a given experimental setup. As results showed in Figure 5-24 (section 5.15), testing of the smaller 0.45mm wire introduced 'noise' or ‘oscillation’ in the force-deflection curve.

In addition, the 1mm wire could be deformed to high superelastic strains under small deflections which made the experiments easier to conduct since the specimen was less likely to slide on the supports. This was confirmed by FEA simulations, which showed that the maximum strains at 2.5mm were 6.26% and 6.12% in the tensile and compressive side of the specimen respectively.

Bend tests were very repeatable as shown in section 5.17. The equipment was calibrated to exceed the ASTM standards and systematic errors as well as random errors were low. Small differences were observed between identical experimental tests. The maximum relative error of the measured forces was around 1.4% while the relative error of the measured displacement was higher at approximately 2.7%.

The tips of the supports and the deflector were formed into cylindrical bars with a diameter of 1.3mm. Different types of supports were briefly examined when configuring the experimental set-up, as these are known to affect the bending response [154]. Preliminary tests were conducted using another two pairs of supports with tips formed into 4mm diameter bars and knife-edges, but these were quickly abandoned. With the 4mm diameter supports, the loading path was shifted

towards higher force levels compared to the other two cases, as seen in Figure 7-2. The curve was characterised by a steep slope where at approximately 5.2mm, a force drop took place probably due to abrupt specimen sliding. The knife-edge supports were also not used for any other testing due to concerns regarding kinking of the wire when it was displaced under the thrust of a knife-edge tip.

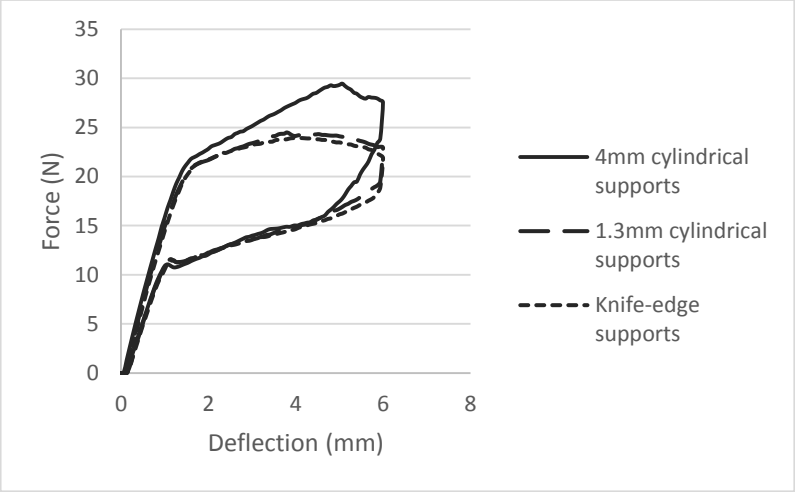

Figure 7-2 Force-deflection response of the 1mm wire when subjected to three-point bending using different support types. The span between the supports was the same for all cases.

Future testing with the current experimental set-up should be conducted to a maximum deflection of 4mm in order to avoid the negative stiffness in the force-deflection curve. By doing so, issues regarding specimen sliding would be avoided while the material would still be deformed in the post-transformation region. This was validated by FEA simulations, which showed that the maximum strain is beyond 8% at 4mm of deflection. An additional benefit would be the decrease in FEA time as a result of the less demanding analysis due to the reduced involvement of contact interactions.

7.1.5 Torsion test method

The testing machine that was employed for torsional testing was coupled with load cells that didn't feature the desired sensitivity for use with small diameter wires. Therefore, specimens with a larger diameter (1.8mm and 2.4mm) were sourced. The length of these wires was short to ensure the specimens could reach superelastic shear strains without excessive rotation. Torsion tests were repeatable as shown in section 5.21. The equipment was calibrated according to ASTM standards while the calculated errors were low. The maximum relative error of the results was around 1.8%.

Literature findings have shown that stress concentrations near the gripped ends of a specimen affect the martensitic transformation, as mentioned earlier. Although these findings were based on tensile results, the short gauge length can be a cause of worry in torsion testing too. The effect of this could not be examined here as multiple specimens with different lengths would be required to do so. However, the linear elastic region of the torque-rotation curve is not affected by the above. Therefore, the moduli that were used to determine the Poisson's ratios for the FEA input parameters were identified correctly.

Note that the torsional deformation of a solid wire is characterised by a non-uniform state of stress and strain. This is the reason the calculated moduli were termed torsional and not shear moduli in the present work. Torsion testing was only conducted at 22°C since the machine did not feature higher temperature testing capabilities.

For future studies, the torsional capabilities of other testing machines should be explored including a load cell that can accommodate the testing of smaller diameter wires with greater gauge length. The use of drill style chuck grips for thinner wires could also be investigated. In addition, future testing at 37°C would shed some light into the assumption that the Poisson's ratios of austenite and martensite remain the same at 22°C and 37°C.

7.2 Comparison between loading modes

The tensile stress-strain response is depicted macroscopically by two linear elastic regions and two nearly flat plateaus. The upper, load plateau corresponds to the transformation of austenite to martensite whereas the lower, unload plateau corresponds to the transition of martensite back to austenite. Transformation in tension is considered non-homogeneous. It is characterised by the localised formation of martensite or austenite domains, during loading and unloading respectively, which propagate along the specimen.

When temperature is increased from 22°C to 37°C, the austenitic phase of the material becomes more stable. Therefore, higher loads are required for transformation, shifting the macroscopic response towards higher stress levels. This observation agrees with the almost linear dependence of the transformation stresses on temperature. The initial elastic stiffness of the material is increased since the volume fraction of austenite is higher at 37°C.

However, the unloading modulus of martensite at 6% engineering strain, is approximately the same at 22°C and 37°C, as shown in section 5.1. This could be explained by assuming the material is completely transformed. Martensite is stable under load; therefore, the material is minimally affected by temperature at this state. Similar behaviour is exhibited by the elastic modulus of austenite which remains almost the same at temperatures between 37°C and 55°C in Figure 5-2 (section 5.2).

The compressive response is manifested macroscopically by a sigmoidal stress-strain curve where the transformation stresses during loading and unloading are higher compared to uniaxial tension. The material enters the post-transformation region beyond 4% compressive strain. Consequently, unloading from 6% strain results in residual strain while hysteresis is smaller. Asymmetry between tension and compression is not uncommon. Most published studies present responses with macroscopic traits similar to the ones mentioned here. The difference between these loading modes is often attributed to the transformation mechanism. Tension is influenced by the localised formation of transformation domains which then

propagate along the specimen. On the contrary, compression is characterised by a homogenous, uniform distribution of transformation domains across the specimen, without localisations and subsequent propagation.

Tension-compression asymmetry is often considered an inherent feature of the material. However, research has revealed that the asymmetry of single-crystal Nitinol is altered based on the grain orientation of the material [155, 156]. Different orientations resulted in different stress-strain responses. Studies investigating the crystallographic texture of Nitinol also showed that the orientation dependence is often carried over to the polycrystalline material [157, 158]. Tension-compression asymmetry was exhibited by textured polycrystalline Nitinol, whereas the un-textured material containing randomly oriented grains, showed lower levels of asymmetry. Industrial materials are usually textured polycrystallines, subjected to complex processing and often contain precipitates and undesirable oxides. Hence, they exhibit varying asymmetric responses which are different from single-crystal theory [159].

Results showed a greater tension-compression asymmetry compared to literature findings. This could be attributed to the underlying influence of the crystallographic texture, as mentioned above. The asymmetry might also be associated with the low ratio between length and width of the compression specimens. He and Sun [160] examined the effect of specimen geometry on the evolution of the tensile transformation by testing specimens with different aspect ratios. According to their results, long and narrow specimens exhibited non-homogeneous transformation influence by the localised nucleation of martensite domains. On the contrary, short and wide specimens favoured a near homogeneous transformation that was characterised by the simultaneous formation of multiple domains. In this case, the macroscopic stress-strain response exhibited a positive slope transformation region. Although these findings are based on the tensile deformation, the specimen geometry could have influenced the phase transformation during the compression tests of the present work.

The bending response of the material is influenced by the asymmetry between tension and compression. Literature findings have shown that transformation in the tensile side of the specimen is non-homogeneous, characterised by strain localisations. On the contrary, transformation in the compressive side is near-homogeneous and progresses without any strain localisations. This is possibly the reason the bending curve is marked by positive slope transformation regions like compression, as shown in Figure 5-19 (section 5.12).

The torsional response exhibited macroscopic traits of a near homogeneous transformation similar to bending. It was depicted by positive slope transformation regions unlike the flag-shaped tensile curve. Transformation during loading in torsion takes place at around 0.5Nm of torque for the 1.8mm diameter specimen which is equivalent to approximately 450MPa of maximum shear stress. Note that transformation during loading started at 540MPa in tension and at 720MPa in compression. Hence, the transformation stress takes its highest value in compression, its lowest in torsion, while the tensile transformation stress falls in-between the other two values. This finding is in agreement with the observations of Orgeas and Favier [60] and Adler et al. [72]. The value that was calculated for the torsional modulus of austenite also agrees with other studies in the literature [71, 73].

7.3 Considerations relating to the design of a stent-graft

7.3.1 High-strain post-transformation loading of Nitinol wires

When a stent-graft is compacted, its Nitinol components are deformed beyond the superelastic range. According to the results of section 5.3, the tensile response of the material depends on the applied post-transformation strain. During unloading, the stiffness of the material is not constant at high strains. Instead, the unloading modulus of martensite is increased from 8% to 11% engineering strain. It

reaches a value of approximately 49.8GPa at 11% strain and is then decreased at higher strains, as seen in the results of Table 5-2 and Figure 5-4. Although a similar finding has also been observed by Duerig [161], the cause for this increase remains unclear.

When deformation takes place up to 8% strain, the unload plateau differs only marginally from the one exhibited when straining the material within the superelastic range. This might be attributed to the complex deformation mechanisms that occur within Nitinol's microstructure. Brinson and her co-workers [56] investigated the full phase transformation characteristics of Nitinol by subjecting sheet specimens to post-transformation tensile strains while observing the microstructure of the material with an optical microscope. Their results revealed that full transformation remains incomplete at high strains. Microscope images showed that at 10% strain the specimen was only partially transformed and according to the authors it contained only around 60% martensite.

Similar conclusions were derived by Tan et al. [152] who used transmission electron microscopy to examine the phase transformation of 3mm diameter solid wires. Their results showed that there was residual austenite in the specimen even after deforming it beyond the load plateau region. Moreover, they observed the presence of twinned martensite domains within the stress-induced state of their material which was unexpected since austenite is believed to transform directly into detwinned martensite under load. Wu et al. [153] also studied the stress-induced transformation in tension using SEM. They deformed superelastic specimens cut from rolled strips to 6% strain and detected austenite within the material at the end of the macroscopic load plateau.

Hence, deformation beyond the superelastic region does not take place through a single-mechanism process. It consists of further transformation of austenite, elastic deformation of the already formed detwinned martensite, plastic deformation and also detwinning of twinned martensite, if present. Therefore, in the present work deformation up to 8% strain is possibly accommodated by further

transformation of residual untransformed austenite. This could explain the minimal drop of the unload plateau stress and the negligible residual strain.

Loading beyond 8% strain induces plasticity and defect sites within the material microstructure, which are characterised by fields of increased stress that assist the transformation during unloading. Consequently, the unload plateau is shifted towards progressively lower stress levels. The decrease of the unload plateau with increasing pre-strain is almost linear as shown in Figure 5-5 (section 5.3). The residual strain is also increased but only gradually up to 10% pre-strain. However, with applied pre-strains greater than 10%, the residual strain starts increasing quickly in an almost linear manner, as seen in Figure 5-6 (section 5.3). Therefore, if a combination of high unload plateau and low residual strain is desired the pre-strain should not exceed 10%.

The above phenomena should not be confused with the behaviour of the material when unloading it from progressively higher displacement increments but still within the superelastic range. Such examples include the compressive responses up to 5% strain and the torsional responses of Figure 5-30 (section 5.18). As the material is deformed to higher strains, the unloading path changes and the exhibited damping or mechanical hysteresis increases. This is associated with the increased volume fraction of transformed martensite and the greater internal friction of the material. Internal friction is defined as the dissipation of mechanical energy within a solid material and is different from tribological friction [162, 163]. It is usually associated with deviations from Hookean elasticity.

7.3.2 High-strain post-transformation cycling during compaction

<u>High strain cycling of the NiTi#1-SE wire</u>

Stent-graft devices can be subjected to more than one compaction attempts in industry. Although as few as three attempts are often conducted, repeated high strain loading and unloading of the material can affect its properties as seen in the

results of section 5.4. Cycling in the post-transformation region results in decreased elastic modulus of austenite, decreased transformation stresses and increased residual strain.

Note that high strain testing represents a worst-case scenario as only a few regions of the wires experience such post-transformation strains. In fact, only part of the material of a deformed ring-stent wire is actually in a martensitic state [164]. The FEA image of Figure 7-3, shows a Nitinol ring-stent model deformed to an approximate compaction state. The displayed contour plot shows the martensite level of the material. Fully transformed martensite is represented by the red contour colour, while material remaining purely austenitic is at the blue end of the contour scale. As seen in Figure 7-3, only the areas near the peaks and valleys of the Nitinol ring-stent are experiencing superelastic strain levels. The rest of the wire material between peak and valley remains in a near elastic austenite state. However, the regions of high stress and strain are usually susceptible to failure. Therefore, it is considered good practice to investigate the high-strain deformation of the material. The influence of application-related post-transformation straining on the material behaviour has not been studied extensively.

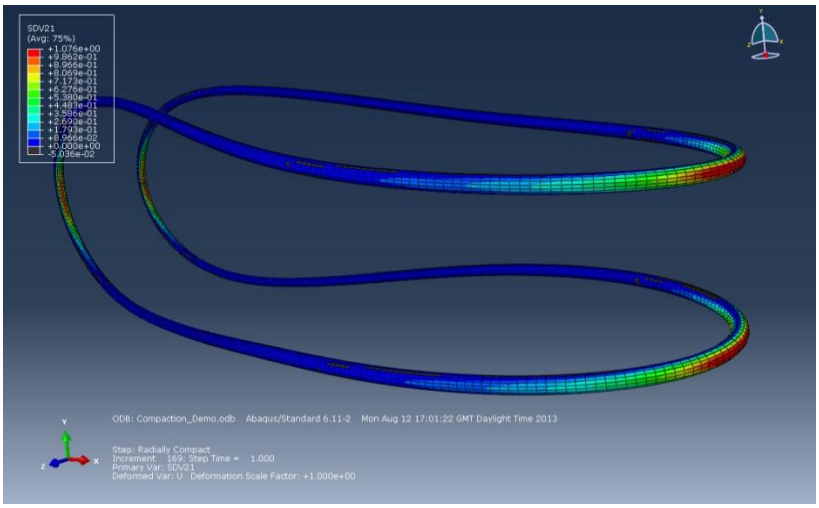

Figure 7-3 FEA image showing a Nitinol ring-stent deformed to an approximate compaction shape. The illustrated contours show the martensite level in the material; red corresponds to 100% martensite and blue to 0% martensite. Image reproduced from Bow [164].

Similar experiments were conducted by Schlun et al. [59] who tested bone-shaped specimens made from tubing. Specimens were cycled twice up to 9% strain, with increasing 1% strain increments. In the present study, three cycles were conducted up to 12% strain in order to represent a more severe case of compaction, and smaller strain increments were investigated. Deformation beyond 9% strain represents a more realistic scenario considering the design of new generation stents is directed towards a very low-profile [165].

According to Figure 5-7 (section 5.4), the initial stiffness of the material upon loading is sensitive to high strain cycling. When a higher pre-strain was applied during the first cycle, the elastic modulus of austenite exhibited a greater decrease in subsequent cycles. This observation can be seen in Table 5-3 which presents the quantitative results of Figure 5-7. The austenitic modulus in the third cycle during loading to 10% strain (50GPa) is approximately 47% and 92% higher compared to that seen in the third cycle during loading to 10.5% (34GPa) and 11% strain (26GPa) respectively. In addition, plastic deformation due to high strain cycling introduces fields of increased stress into the microstructure of the material which assist the transformation. Therefore, transformation during loading takes place at a lower stress after the first cycle. The reduced stiffness and load plateau of the material are features that can be beneficial for the compaction process of the stent-graft, since they would make the material less resistant to deformation, and thus easier for operators to compact.

The unload plateau is also affected by the pre-strain level, although the changes between the consecutive cycles are less pronounced compared to the load plateau. The unload plateau stress affects the stent's radial force which is responsible for the sealing of the device. The decrease of the unload plateau is often inevitable during compaction where high strain deformation is taking place, because as shown in Figure 5-5 (section 5.3), the unload plateau is decreased in an almost linear manner with increasing pre-strain. However, a recommendation can be made based on the results of section 5.3 and section 5.4 to limit the compaction strain to 10%, if possible. This is because if more than one compaction attempts take place at 10% strain, the

effect on the unload plateau will be small. The unload plateau stress exhibited in the third cycle after unloading from 10% strain (190MPa) is greater compared to that seen in the first cycle when unloading from 10.5% (165MPa) and 11% strain (140MPa). These quantitative results are shown in Table 5-3 (section 5.4).

In addition, up to 10% compaction strain there is only a small, gradual increase of residual strain as seen from the results of Figure 5-6 (section 5.3). If more than one compaction attempts take place, the accumulated residual strain in the third cycle after unloading from 10% strain (0.3%) will be similar to that accumulated in the first cycle after unloading from 10.5% (0.3%) and smaller compared to the first cycle after unloading from 11% strain (0.35%).

Note that when assessing the effect of pre-strain on the mechanical behaviour of stents, the effect of pre-strain on the fatigue life needs to be taken into consideration. The fatigue life of the material is a key parameter in the design of any medical device. Nitinol exhibits a complex fatigue behaviour which depends on the A_f temperature and the material's phase among other factors [166, 167]. The influence of pre-strain on the fatigue life is difficult to determine as it depends on the sequence and mode of loading. This influence can be positive or negative depending on the sense of the pre-strain with respect to the duty cycle, i.e. the deformation the Nitinol component is experiencing in-vivo.

Senthilnathan et al. [168] examined the effect of pre-strain on the fatigue life of superelastic Nitinol wires and diamond shaped specimens. Diamond-shaped specimens were used since their deformation is representative of stent components. The extrados and intrados of the specimen, as shown in Figure 7-4, experience inverse states of stress and strain when the diamond is closed or opened. Closing the diamond specimen represents the common scenario of compacting a stent. The ends of the specimen are essentially subjected to bending when the diamond is closed. At the end of compaction, the maximum tensile stresses and strains are found in the region of the extrados while the maximum compressive stresses and strains are found in the region of the intrados (image at the lower right corner).

If compaction causes plastic deformation at the extrados, releasing the load on the diamond shaped specimen results in residual stresses of the opposite sense. This means that a stent that is deployed freely from a compaction sheath, will experience residual compressive stresses at the extrados and residual tensile stresses at the intrados. If the locations of the compressive residual stresses are exposed to tension during cycling, the fatigue life improves.

Therefore, pre-strain can create residual stresses, which can either increase or reduce fatigue life. The diamond shaped specimens of this study were subjected to both tensile and compressive pre-straining to 9% strain and then subjected to cyclic loading at 3.5% mean strain. Fatigue performance was improved in all cases when the duty cycle was of the same sense as the pre-straining. For example, when tensile pre-straining was followed by a tensile duty cycle. In other words, if pre-straining leads to compressive residual stresses at the locations that will be exposed to tension during cycling, fatigue life is expected to improve.

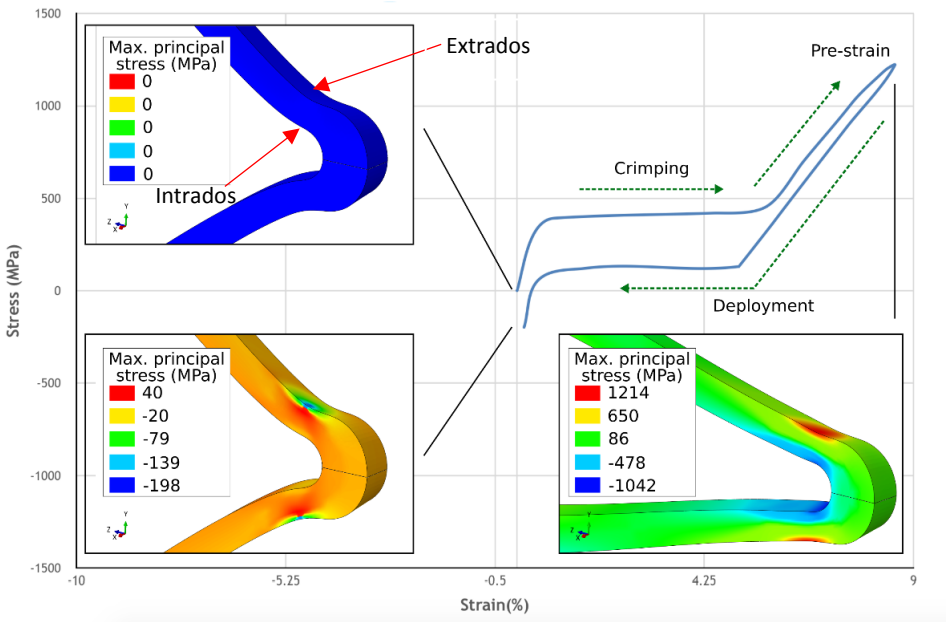

Figure 7-4 Closing the diamond shaped specimen results in tensile stresses at the extrados and compressive stresses at the intrados (lower right inset). Removing the load results in residual stresses of the opposite sense, i.e. compressive stresses at the extrados and tensile stresses at the intrados (lower left inset). The stress-strain curve represents the element that experiences the highest compaction strain. Image reproduced from Senthilnathan et al. [168].

The authors also performed tension-tension fatigue and rotary bend testing of wire specimens. Different pre-strain levels and strain amplitudes were examined. According to their results, fatigue life increased when the material was deformed plastically during pre-straining. For example, the tension-tension fatigue limit of the 9% pre-strain case was 100% greater compared to the 4% pre-strain case.

In the case of the Terumo Aortic Anaconda devices: during compaction, high bending pre-strains are applied to the ring-stents which are then constrained in a radially compressed state in-vivo. Thus, the stresses and strains at the extrados are of the same sense as the initial pre-strain since cyclic bending is taking place in the same direction as the pre-strain deformation. Based on the findings of Senthilnathan et al. [168] the fatigue life of ring-stents should improve with compaction pre-strain.

Comparison with the USN® wire

The USN® and NiTii#1 wires were both manufactured under the same required specifications. The superelastic behaviour of the USN® wire was similar to the NiTi#1-SE, as shown in Figure 5-8 (section 5.5). The main differences were the greater elastic modulus of austenite and the slightly higher unload plateau, as seen in the quantitative results of Table 5-4.

The features described earlier regarding the high-strain behaviour of the NiTi#1-SE wire were also seen in the stress-strain responses of the USN® specimens which exhibited greater stiffness upon loading, higher unload plateaus and increased residual strain compared to the standard Nitinol wire. The decrease of the unload plateau with increasing pre-strain took place at a smaller rate compared to the NiTi#1-SE wire. As seen in Figure 5-10 (section 5.5), the unload plateau experienced a very small drop between 9% and 10.5% strain and was decreased almost linearly with pre-strain only beyond 10.5%. However, the residual strain increased at a greater rate compared to the NiTi#1-SE material, as shown in Figure 5-11.

The greater stiffness and unload plateau of the USN® wire were maintained during high strain cycling. The unload plateau stress during the first cycle when unloading from 10% strain (260MPa) is approximately 24% greater compared to that

exhibited by the conventional wire under the same conditions (210MPa). The unload plateau stress of the first cycle when unloading from 11% strain (190MPa) is approximately 36% greater compared to that exhibited by the NiTi#1-SE wire at the same conditions (140MPa). These quantitative results are shown in Table 5-6 (section 5.5). The aforementioned differences between the two wires are greater in the second and third cycles since the unload plateau of the USN® wire remained practically the same.

However, the residual strain that was exhibited by the USN® wire was also increased during cycling. In the first cycle when unloading from 10% strain, residual strain was 0.45% for the USN® wire compared to only 0.12% for the NiTi#1-SE one. Moreover, the residual strain at the end of the first cycle when unloading from 11% strain was 0.8% for the USN® wire compared to 0.35% for the NiTi#1-SE wire. These differences were again greater in the second and third cycles.

The differences between the two Nitinol grades can be attributed to the slightly different compositions and processing techniques. The implementation of the USN® material into the stent design could lead to the manufacture of a lower-profile device with minimal specification changes. The wireframe of the stent and the anchoring mechanisms could potentially be made from smaller diameter wires while retaining the same overall structural rigidity. In addition, keeping the wire manufacturer and specifications the same is beneficial from a business perspective. Specification changes and/or supplier changes in the medical device industry require long approval times.

A lower profile device would then induce less trauma to patients allowing for a faster post-operative recovery. Such a device could also be employed for the treatment of patients who have smaller access vessels and tortuous anatomies, such as Asian and female patients [169-172]. Smaller hooks and barbs would cause less injury to the vessel wall, thus minimizing the inflammation and thrombus formation associated with such operations [173, 174]. More research however is required, to investigate the potential benefits and limitations of using such a material. In

particular, the impact of the increased residual strain on the long-term material behaviour is difficult to determine without fatigue tests.

Note that compaction takes place at room temperature. The tests discussed here were conducted at 37°C in order to examine the unload plateau and the stiffness during deployment. In future work, a more complete investigation of the compaction process could include: loading to the post-transformation region at room temperature, increasing the temperature to 55°C while the specimen is held at a deformed state to simulate sterilization, and then unloading at 37°C to represent in-vivo deployment.

7.3.3 Load rate effects of Nitinol wires

The compaction of a stent-graft device is often performed manually, under operator-control where load rate effects might affect the deformation of the material. The rate sensitivity of the material is determined by the rate heat is released or absorbed by the specimen and the rate of heat exchange with the environment. The first depends on the load rate and the type of transformation, whereas the second depends on the ability of the ambient medium to dissipate or supply heat fast enough at high loading rates.

Transformation from austenite to martensite during loading is exothermic. Heat is released which does not dissipate quickly at high load rates, raising the specimen's temperature and therefore increasing the transformation stresses. Consequently, when loading is taking place under a high rate in air, the exhibited forces are higher. This is seen in the force-deflection curves of Figure 5-20 (section 5.13) and Figure 5-21 (section 5.14) where the loading path of the curves is shifted towards higher force levels compared to the low rate cases.

The steeper slope of the loading path could also be influenced by the deformation modes involved in bending. At low rates, the positive slope of the bending response is attributed to the homogeneous transformation of the

compression side. At higher rates, the tensile transformation becomes also near-homogenous according to the literature which could potentially influence the slope of the loading path. In addition, at very high rates the martensitic transformation cannot keep up with the increased rate. Elastic deformation of the already formed martensite starts taking place before the transformation is complete, hence possibly further modifying the macroscopic bending response.

The transformation from martensite to austenite during unloading is endothermic causing heat absorption, thus lowering the specimen's temperature. Normally, one would expect the unloading path of the macroscopic force-deflection curve to shift towards lower forces when the load rate is increased. That would be the case if the rate was only slightly faster than the quasi-static experiment. Such an example is seen in Figure 3-9(a) (section 3.2.1) that reproduced the results of He et al. [55]: the unloading path of the 6x10-4/s curve takes place at lower force levels compared to the 4x10-5/s test.

When unloading at a high rate of 1mm/s as shown in Figure 5-21 (section 5.14), the first part of the unloading path is moved upwards. This is because there is not enough time for the heat that was generated during loading to dissipate. The heat still affects the specimen at the beginning of the unloading path increasing the forces macroscopically. However, as unloading proceeds under a high rate, the specimen's temperature is lowered rapidly shifting the last part of the curve towards lower forces compared to the 0.1mm/s case. When testing is paused before unloading, as seen in Figure 5-22 (section 5.14), there is enough time for the heat to dissipate causing the whole unloading path to take place at lower force levels. Its first part is similar to the 0.1mm/s case but the last one is shifted downwards as heat is released faster this time due to the high rate.

Note that during a tensile deformation, the stress required for the formation of the first martensite domains is higher than the stress required to continue the transformation. At low rates during loading, there is enough time for the domains to move after nucleation and the high stress is relaxed. Therefore, a stress overshoot or peak is often observed at the onset of the transformation region during loading. At

high rates however, the domains move quickly after nucleation, there is not enough time for relaxation and the macroscopic small load drop is not seen. Similar features are observed in the force-deflection curves of Figure 5-20 (section 5.13) and Figure 5-21 (section 5.14) between low- and high-rate loading cases. During loading at 0.1mm/s there is a small force overshoot right before the upper transformation region which disappears when the rate is increased to 1mm/s. This might suggest that the tensile deformation governs the rate effects during bending.

The formation of austenite during a tensile deformation requires a stress lower than the one to propagate the reverse transformation. Hence, a force undershoot or valley would be expected at the onset of the unload transformation regions in the force-deflection curves. However, this is not observed possibly because it is masked by the positive slope bending response. Instead, a clear force undershoot exists in the low rate case of Figure 5-21 (section 5.14) at the end of the lower transformation region, right before the final elastic unloading. This force undershoot, which disappears at high rates, could be associated with the formation of some final austenite domains in the remaining martensite regions instead of propagating the existing transforming austenite.

Load rate effects in air are pronounced when specimens are subjected to bending beyond the superelastic range. The major difference between superelastic and post-transformation bending under high load rates is the residual deformation. At the end of a superelastic load-unload cycle under a high rate, there is no permanent set. However, when deforming a specimen beyond the superelastic range at a high rate, the residual deformation increases, as shown in Table. This could potentially affect the properties of the wires during compaction as they are strained well beyond the superelastic range.

In addition, results from Figure 5-31 (section 5.19) suggest that torsional loading is also rate sensitive. This finding agrees with the work of Doare et al. [73] but not with the studies of Predki et al. [75] and Dolce and Cardone [74]. Predki et al. [75] used hollow specimens for testing at higher loading rates. However, heat transfer between air and hollow specimens is improved compared to solid

specimens. Therefore, this could be the reason that the rate effects were negligible in their results. Moreover, testing by Dolce and Cardone [74] was conducted at 25°C while the A_f of the material was 33°C. This means that their specimens were not fully austenitic and superelastic. As mentioned earlier, the rate sensitivity is due to the martensitic transformation which is exothermic for austenite to martensite transitions and endothermic for martensite to austenite transitions. Therefore, the deformation of their specimen was only partially governed by such transitions which could again explain the little rate sensitivity.

Minimal load rate sensitivity is observed when testing is conducted using water as the ambient medium. Even at high load rates, the force-deflection response is similar to the low rate result. This is due to the higher thermal conductivity of water compared to air which allows for a faster heat exchange between specimen and environment, thus minimising the load rate effects. Similar results can be found in the literature regarding the tensile behaviour of Nitinol [54, 55].

According to Figure 5-24 (section 5.15), the mechanical behaviour of small diameter wires is not affected by increased loading rates. This is due to the improved heat transfer between the thinner specimen and the ambient medium. However, ring-stents are made of multiple strands of thin wires where heat transfer could be affected. In the medical industry there is currently very little concern regarding the strain rate effects during compaction. Consequently, the loading rates during this process have not been quantified. Additionally, there are no available studies in the literature discussing rate effects in stent-grafts during manufacturing. These effects are usually ignored assuming their impact on the global material response is negligible.

Strain-rate effects are not expected during the in-vivo deformation of the material. The strain rate at this stage depends on the cardiac cycle which can be considered stable. Moreover, the rate effects are typically seen in air and not in water where the thermal conductivity is higher. Blood and water have similar coefficients of thermal conductivity [175]. Therefore, even if higher strain rates are experienced by a stent, their impact on the material properties is expected to be insignificant.

7.3.4 Sterilization and in-vivo behaviour of Nitinol wires

Following compaction, an assembled stent-graft is usually sterilized by ethylene oxide. During this process, the temperature of the Nitinol wires is raised to around 55°C for a prolonged period of time. As temperature is increased from 22°C to 55°C, the transformation stresses are also increased according to the results of section 5.2.

However, temperature sensitivity is not seen within the post-transformation region. Therefore, subjecting a compacted device to higher temperatures will not alter the stress state of the high-strained Nitinol regions. This is presumably due to the different mechanism of deformation involved. The post-transformation region is composed predominantly of martensite elastic deformation and ordinary plasticity which are not temperature sensitive like the martensitic transformation.

In the same results of Figure 5-2, the influence of the R-phase in the initial elastic loading is also evident. The presence of R-phase is minimised at 37°C and is completely diminished at 55°C. However, the material should not present any evidence of R-phase transition at these ambient temperatures, according to its A_f temperature. A similar finding has also been mentioned in the literature by Eaton-Evans et al. [176]. The authors observed the presence of R-phase during mechanical testing, although their material was expected to behave fully superelastically based on DSC results. They attributed the differences between mechanical testing and DSC to potential localised plastic deformation and/or residual martensite introduced into the material when cutting the small specimens required for the DSC analysis, thus leading to inaccurate measurements.

Note that mechanical characterisation is usually performed using straight wires where R-phase is present during initial loading. However, the strains in a deployed stent could be beyond the influence of the R-phase transition. For example, when a ring-stent is manufactured, straight Nitinol wires are subjected to bending.

Therefore, the ring component of a device is already under some small strain which could be greater than the strain levels that R-phase is present.

Deployed stents are subjected to a cyclic bending deformation in-vivo. The 1mm diameter specimen was used in a three-point bend configuration to examine the cyclic properties of the material. The response seen in Figure 5-25 (section 5.16) is characterised by features similar to those described in the literature regarding tensile cycling. These features include the reduction of the flexural modulus, the decrease of the transformation stresses and the accumulation of residual deformation with increasing cycles.

The sites where martensite nucleates are expected to increase with cycling [63]. Thus, transformation on the tensile side of the specimen becomes more homogenous, affecting the macroscopic bending response which is depicted by a steeper transformation region. Findings from the literature [56] also suggest that localised defects and plasticity gradually build up within the material microstructure as a result of the repeated load-unload cycles, even if the specimens are not strained directly beyond the superelastic range. Plasticity generates fields of increased stress which account for the lower transformation stresses, since they assist the transformation. These localised defect sites could be considered the cause of the gradually accumulated residual strain. This could also be attributed to residual martensite that builds up due to incomplete transformations as the cycle number increases.

The residual deformation during cycling is affected by the test temperature. Results showed a higher residual deformation at the end of the cyclic loading at 37°C. The rate that the residual deformation is increased is also higher at 37°C, as seen in Figure 5-28 (section 5.16), especially at the first ten cycles. However, at both temperatures the flexural stiffness and the transformation force decrease at a similar rate, as seen in Figure 5-26 and Figure 5-27. This last finding does not agree with observations regarding the tensile cycling of the material where the response is usually stabilised faster at higher temperatures [58, 177].

This could be possibly due to the different transformation mechanisms in tension compared to bending. The tensile deformation is characterised by the formation and propagation of martensite fronts. During cycling, the number of transformation fronts increases affecting the global behaviour of the material. Bending on the other hand is influenced by tension and compression. Transformation during compression is homogeneous and does not depend on the formation of single martensite fronts. Therefore, the influence of cycling on the compression response is possibly smaller.

Although such testing provides an insight into the bending behaviour under cycling, the in-vivo deformation is characterised by small amplitude cycling due to the physiological systolic-diastolic pressure. Therefore, cyclic testing should be expanded in future work to include small amplitude straining of the material. Testing should take place after unloading from the post-transformation region in order to take into account the pre-straining of the material. The investigation could also compare the behaviour of the different Nitinol grades. The small amplitude cyclic behaviour influences the fatigue life of the material which depends on several factors as mentioned earlier.

7.4 Assessment of the Abaqus Nitinol model

7.4.1 Defining the input parameters

The majority of the input parameters for the finite element simulations are identified from tensile data, as discussed earlier in section 6.1. However, there are a few parameters, such as the Poisson ratio and the transformation stress in compression, that require additional tests. Compression testing of Nitinol is a challenging task and torsional studies are scarce. Therefore, available data for these parameters are not easy to find. Because of this, researchers often use values for their input parameters, that were published in other studies [114, 115, 178].

However, the simulated material behaviour in such cases might not correspond to the application of interest, since the properties of Nitinol depend heavily on manufacturing and processing techniques. In the present work, all input parameters at 22°C were obtained though experimental testing. This is unique in the literature and allows the validation of the material model across all loading modes. To the author's knowledge, a similar study where all input parameters are identified by experimental tests does not exist.

The tensile input parameters were identified using tests that were conducted according to the ASTM F2516 guidelines [128], where the specimen was subjected to a single load-unload cycle to 6% strain and then it was loaded to failure. However, this is not what the Abaqus instructions show in Figure 3-25 (section 3.3.3). The stress-strain curve of Figure 3-25 shows loading to the post-transformation region to an arbitrary level of strain, and then removing the load. However, the standard test method is the approach that is likely to be adopted by engineers in industry.

Apart from Figure 3-25, there are currently no explicit instruction for identifying these parameters. This process is approximate since it depends on the interpretation of the stress-strain results by the Abaqus user. For example, the stress at the start of the transformations during loading was identified here as the point where the slope of the stress-strain curve starts changing right before entering the plateau. Another approach is to define this point as the intersection between the linear trendline of the elastic modulus of austenite and the load plateau.

Due to the nature of this process, fine-tuning of the parameters was required. This was accomplished by comparing the results of several trial and error simulations with the experimental data. In other words, an inverse approach was adopted that sought to identify the tensile input parameters by minimising the difference between the FEA predictions and the experimental results. The parameters that provided the best match between FEA and experiments in tension were then used to simulate the rest of the loading modes. According to the results presented in section 6.2, the identified input parameters can yield excellent results when modelling tension within the superelastic range.

7.4.2 Capturing the post-transformation tensile behaviour

The material model was extended with additional stress-strain points in order to capture the post-transformation deformation. The additional input parameters were derived from high strain tensile tests. Subsequently, simulations were performed to examine whether the high-strain tensile results can be reproduced computationally by Abaqus.

The loading path of the material to high strains was captured correctly as shown in Figure 6-3 and Figure 6-4 (section 6.3). When the material was unloaded from high strains in the experiments, the unloading modulus was also altered. However, this observation was not reproduced in the simulations. Instead, the unloading modulus of martensite remained the same regardless of the applied maximum strain. This was expected based on Figure 3-26 (section 3.3.3), as the equations of the material model do not account for such changes. The elastic modulus is calculated based on the elastic properties of austenite and martensite, and the martensitic fraction, as seen in Equation 3-12 (section 3.3.3).

The unload plateau was also insensitive to the plastic straining history incurred during loading as the material model was incapable of forecasting the sensitivity seen in the test results. The unload plateau was placed at the superelastic stress levels instead of being shifted towards lower stress levels when unloading from progressively higher strains. However, the residual strains that were exhibited in the computational responses were in close agreement with the experimental values. As seen in the quantitative results of Table 6-2 and Table 6-3 (section 6.3), the percentage difference between the two results was overall small, apart from the 11% strain case at 37°C.

The use of Fortran subroutines was explored as a method to overcome the limitation of the material model to predict the unload plateau. The purpose of the subroutines was to modify the unload plateau which was achieved by using an ‘If’ statement that altered the unload transformation stresses (parameters 11 and 12) as

a function of the plastic strain. Two separate subroutines were written, one for each set of input parameters (22°C and 37°C).

The FEA responses were improved with the subroutines, as seen in the results of section 6.4. In these simulations, the unload plateaus were in close agreement with the experimental responses and the transformation stresses matched perfectly the values observed in the experiments. This modelling approach has gained little recognition in the literature, although capturing the unload plateau after high-strain deformation has been an ongoing issue regarding Nitinol modelling. This can be useful when designing devices such as stent-grafts which are compacted into a small diameter delivery system. Only Rebelo et al. [179] have presented a similar method to simulate the varying unload plateau of Nitinol materials. The authors validated their subroutine with experimental data up to 9% strain.

Note that when the subroutines were used, the unload stresses started changing when a strain of 7% and 10.35% was reached during loading at 22°C and 37°C respectively. However, in the experimental results at 37°C, the unload plateau was shifted towards lower stress levels after deformation beyond 8% strain. The difference in the FEA results is because a high plastic strain is required for the 'if' statement that is written in the subroutine code. Therefore, the subroutine outputs are currently not sensitive at low plastic strains. In future work, an improved modelling approach could be developed, with subroutines that include more 'if' statements based on multiple high strain tests, in order to represent the material behaviour for a wide range of strain levels.

In addition, the elastic modulus of martensite was not modified by the subroutines because it is not recommended to do so. According to the Simulia Knowledge Base [104]: "although it is possible to modify the elasticity, complete consistency of the mathematical model is lost." This was very briefly explored when the subroutines were written. However, when the elastic modulus was modified in the subroutine, the analysis failed to finish. This is something that could be investigated in more detail in future work.

7.4.3 Investigating the computational tension-compression asymmetry

Tension-compression asymmetry was exhibited in the computational results of Figure 6-8 (section 6.5). Although the asymmetry was not as pronounced as in the experimental results, the predicted compression response was different from the tensile one. The initial stiffness of austenite during loading was in agreement with the experimental results, as seen in the quantitative data of Table 6-4. The elastic modulus of austenite was the same in tension and compression which was expected according to Figure 3-25 (section 3.3.3).

The start of the transformation during loading also agreed well with the experimental result. This was again expected considering it was the only input parameter that was based on compression data. The asymmetry in the material model is governed by Equation 3-17 (section 3.3.3). The constitutive model is configured to use the difference between the transformation stresses during loading in tension and compression to predict the rest of the stress parameters. The start of the transformation during loading in compression (720MPa) is approximately 33% greater than the start of the transformation during loading in tension (540MPa). Therefore, the rest of the parameters, shown in Table 6-4, were estimated accordingly based on this difference. The value of parameter a (Equation 3-17) can be calculated to approximately 0.14 using the above transformation stresses.

Assuming the transformation in compression is complete at 6% strain, the stress at that point (800MPa) is approximately 32% greater than the end of the transformation in tension (605MPa). Similarly, the start of the transformation during unloading (400MPa) in compression is greater by 33% compared to the start of the transformation during unloading in tension. Finally, the end of the transformation during unloading in compression is approximately 30% greater than the equivalent stress in tension. Note that the above values satisfy Equation 3-17.

Because of the above, the overall form of the compressive curve and its hysteresis did not agree with the experimental response. In addition, in the

experiment the post-transformation region starts after 4% strain whereas in the FEA curve the material enters the post-transformation region beyond 6%, as seen in Figure 6-9 (section 6.5). This behaviour depends on the volumetric transformation strain (input parameter 14), the value of which was set equal to the transformation strain (input parameter 5) in order to allow the material model to determine the asymmetry.

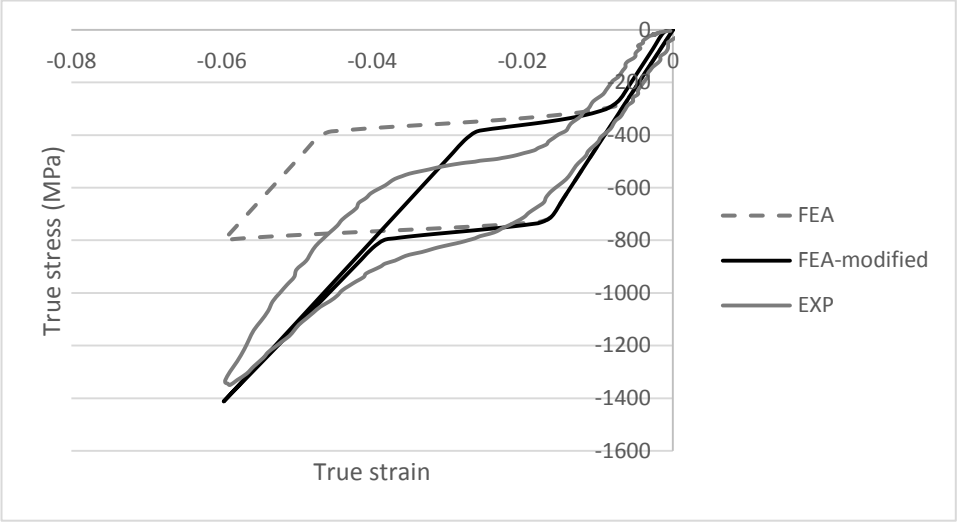

Figure 7-5 Modifiying the volumetric transformation strain to improve the computational response of the 1mm wire subjected to 6% strain in compression at 22°C.

The effect of the volumetric transformation strain on the stress-strain curve was briefly explored. Figure 7-5 shows that the short load and unload transformation regions and the faster transition to the plastic region can be reproduced when a value of 0.05 is assigned to the volumetric transformation strain. By doing so, residual strain is also produced at the end of the unloading path. However, there are currently no Abaqus instructions for calculating the volumetric strain. It is not identified from the compressive response in the same way the transformation strain is obtained from the tensile stress-strain curve. The value here was determined after several 'trial and error' simulations until the computational response matched the experimental one. Therefore, although the above results look promising, more work is required to understand the volumetric transformation strain parameter. This could be part of a future project.

7.4.4 Simulating three-point bending

The flexural stiffness of austenite is underestimated in the computational bending responses by 28.8% at 22°C and by 13.9% at 37°C. These results are presented in Table 6-5 and Table 6-6 (section 6.6). Transformation during loading starts at the same force for FEA and experimental results at both temperatures. This good agreement between the two responses is because the input parameters for the start of transformation during loading in tension and compression were configured accurately, as discussed previously. However, the transformation takes place at a different deflection due to the lower flexural stiffness. The predicted maximum force at 2.5mm was also slightly lower, by 5.8% at 22°C and by 2.6% at 37°C, compared to the experiments. A greater difference between FEA and experimental results was seen in the unload transformation forces which were underpredicted by up to 44.4%. This could be due to the unload transformation stresses in compression which were underestimated, as discussed earlier.

When the subroutine was used in bending simulations, its effect on the force-deflection curve was negligible. However, the subroutine did have an effect on the elements that experienced plastic strains as their unload transformation stresses were modified in both the tensile and compressive side of the geometry. The subroutine could probably have a greater impact on the bending response if higher plastic strains are induced during the analysis.

The computational bending response is improved when the flexural modulus of austenite is used as input parameter, instead of the elastic modulus of austenite. This observation has not been reported in the literature yet. The results of Table 6-9 and Table 6-10 (section 6.8) show that the predicted initial stiffness is lower compared to the experiment only by 0.9% at 22°C and 4.2% at 37°C. In addition, the deflection level that the transformation takes place is almost the same for computational and experimental responses. If the simulations of Figure 6-15 (section 6.8) were stopped at a deflection of 4mm, as recommended earlier, the loading paths

of computational and experimental responses would be in close agreement. However, the unloading path remained unaffected by the use of the flexural modulus.

The above findings are important since the loading nature of a ring-stent in the deployed 'saddle shape' is primarily bending [180]. If the ring-stent has a low 'saddle shape' and is almost flat, then it will experience direct compressive forces when it is radially loaded. However, if the FEA results are used for design purposes, the underpredicted unload plateau would result in a conservative design in terms of the bending force exerted by the stent, especially since devices are always oversized in practice.

A potential method to improve the bending modelling could include the partitioning of the wire into a tensile and a compressive region. Two material models could then be assigned to each region, one derived from tensile results and another from compression results. The influence of the tension-compression asymmetry on the bending response would then be better represented.

7.4.5 Simulating torsion and combined loading conditions

The computational response in torsion did not agree well with the experimental results. Although the predicted curve exhibited positive slope transformation regions like the experimental response, these regions were underestimated, especially the unloading path. As seen in the quantitative results of Table 6-11 (section 6.9), the torsional stiffness of austenite was underpredicted by 11.2% while the torsional stiffness of martensite was smaller only by 2.5% compared to the experiment. The transformation during loading was underpredicted with a similar difference, around 10%, compared to the experimental observation. However, the rest of the estimated parameters exhibited greater differences. In particular, the start of transformation during unloading was smaller by 40%

compared to the experimental result which caused the whole unloading path to take place at lower torque levels.

The impact of the above findings depends on whether torsional loads are applicable to the device of interest. Usually, a full device investigation is required to determine this. For a ring-stent that is deployed in a 'saddle shape', the predominant deformation mode is bending. Torsional loads of ring-stents are less significant in magnitude [180].

Note the pronounced differences between computational and experimental curves for the 2.4mm diameter wire. These are because the 2.4mm specimen had an A_f of 2°C whereas the one used to identify the input parameters had an A_f of around 14°C. At a given test temperature, a lower A_f material exhibits greater loads and requires higher stresses for transformation, as shown graphically in Figure 2-7 (section 2.3). The above finding also shows the sensitivity of the computational forecasts to the input parameters.

However, the model was able to reproduce the qualitative features of the combined tension-torsion deformation. Under combined loading conditions the finite element model produced results which were distinctly different from the pure tensile and torsional responses. When the specimen was rotated under a constant tensile displacement, a load drop was observed in both examined cases of combined loading. This behaviour, which was reproduced by FEA, could be associated with a lower elastic modulus as the material transforms further into its martensitic state. During the experiments, the load drop could also be attributed to a stress relaxation due to a small temperature drop while the Nitinol wire was held axially.

Additionally, in agreement with experimental observations, the hysteresis of the torsional response was decreased when the tensile pre-deformation was increased, as seen in Figure 6-21 (section 6.10). This is because as the tensile load is increased, the volume fraction of the available material for torsional transformation is decreased. Therefore, the transformation regions of the torsional responses are diminished, and the exhibited curves obtain characteristics of linear elastic loading.

The residual deformation that was seen in the experimental tensile and torsional responses under these loading conditions could be attributed to several factors. Firstly, since a high tensile deformation precedes torsion, the material is mostly transformed. Therefore, the subsequent torsional deformation could lead to mainly plastic deformation, elastic loading of the martensitic material and further transformation of any untransformed grains. In addition, the strain distribution on the cross-section of a solid specimen subjected to torsion is non-uniform. Thus, some material grains might experience incomplete transformation during unloading from high strains which could introduce some residual strain macroscopically. Stress concentrations near the grips could also affect the transformation. As discussed earlier, when measuring displacement using the crosshead movement, the corresponding macroscopic response may result in residual deformation during unloading. Since the computational model did not account for any of the above features, residual deformation was not present in the predicted responses.

Chapter 8 Conclusion

Stent-grafts are life-saving medical devices, designed to treat AAAs. The majority of these devices are composed of a Nitinol wireframe and a fabric graft. The design of next generation stent-grafts is directed towards a very low-profile when compacted. Such devices can treat narrow access vessels and tortuous anatomies while inducing less trauma to patients. Therefore, Nitinol stents are required to undergo greater deformations during manufacture without compromising the performance and durability of the medical device.

Despite these design requirements and the challenging multi-mode loading conditions stents are subjected to, there is little information on the post-transformation deformation and cycling of Nitinol wires. The bending response of Nitinol wires is usually examined under small deflections within the superelastic range with no information on the high load rate, large deflection deformation. The temperature sensitivity of Nitinol is unknown at such high strains while limited studies report on the compressive and torsional response of the material.

Medical device standards and guidelines also state that the structural integrity of endovascular prostheses should be evaluated under any applicable loading mode, including axial, bending and torsional loading. Moreover, when submitting computational analyses reports to a regulatory agency, it is required to confirm that the behaviour of the simulated materials is represented correctly by the chosen material model under the applicable loading mode.

Therefore, a methodology was developed in the present work to characterise Nitinol wires, which are the main structural component of stent-grafts, across all four basic loading modes. All wires were of the same type and were manufactured by FWM under the same specifications. A new compression test method was developed to allow the experimental characterisation of superelastic wires. To date, there is not a specific study available exploring the behaviour of Nitinol wires of the same material in tension, compression, bending and torsion. This is also necessary in order

to identify the input parameters for the computational characterisation of the material. Although the Abaqus Nitinol model is considered the industry standard, its capabilities and limitations when modelling multiple loading modes are not fully explored since there are no available studies that use experimental data from tension, compression, bending and torsion to derive the input parameters. If the input parameters are not all identified from experiments conducted with the same Nitinol material, then any comparison between FEA and experimental results would be subject to assumptions. In the present study, all input parameters at 22°C were identified from experimental data and the material model was assessed, including its superelastic-plastic modelling capabilities, by simulating the mechanical tests of all loading modes.

The experimental and computational results led to useful recommendations relating to the design of stent-grafts. Loading of the NiTi#1-SE material beyond 8% strain during compaction will result in decreased austenite stiffness, decreased load and unload plateaus and increased residual strain. These features will become more pronounced if multiple compaction attempts take place. The reduced austenite stiffness and load plateau can be beneficial for the compaction process of a stent-graft, since they would make the material less resistant to deformation.

The unload plateau was decreased in an almost linear manner with increasing pre-strain. Although this would be unavoidable during compaction, a recommendation can be made to limit the compaction strain to 10%. This is because if more than one compaction attempts take place at 10% strain, the effect on the unload plateau will be small: the unload plateau stress in the third cycle after unloading from 10% strain (190MPa) was greater compared to the stress exhibited in the first cycle when unloading from 10.5% (165MPa) and 11% strain (140MPa). In addition, up to 10% compaction strain there is only a small, gradual increase of residual strain and in the case of multiple high strain cycles, the accumulated residual strain in the third cycle after unloading from 10% strain (0.3%) will be similar to that accumulated in the first cycle after unloading from 10.5% (0.3%) and smaller compared to the first cycle after unloading from 11% strain (0.35%).

For the ultra-stiff USN® wire, the decrease of the unload plateau with increasing pre-strain took place at a smaller rate compared to the NiTi#1-SE wire. The unload plateau of the USN® wire was also greater during high strain cycling. When the wire was unloaded from 10% strain, the unload plateau stress during the first cycle (260MPa) was approximately 24% greater compared to that exhibited by the standard Nitinol wire under the same conditions (210MPa). However, the residual strain that was exhibited by the USN® wire was also greater. Therefore, limiting the compaction strain to 10%, as suggested earlier, and the compaction attempts to one only, would be beneficial for the USN® material, as this would allow design engineers to utilise the greater unload plateau of this material while minimizing the effect of the increased residual strain.

When assessing the effect of pre-strain on the mechanical behaviour of stents, the influence of pre-strain on the fatigue life also needs to be taken into consideration. This influence can be positive or negative depending on the sense of the pre-strain with respect to the duty cycle. For the ring-stents, cyclic bending will take place in the same direction as the pre-strain deformation. Therefore, the fatigue life should improve with compaction pre-strain, based on literature findings.

Compaction should also take place slowly, under a controlled manner, in order to avoid potential rate effects. Temperature sensitivity was not seen within the post-transformation region. Therefore, sterilization is not expected to have a negative impact on the stress levels experienced by Nitinol wires during this process.

Regarding the computational analyses, the Nitinol model that is implemented in Abaqus provided results that agreed well with the experiments when modelling tension within the superelastic range. Moreover, the loading path of the material under superelastic-plastic tensile deformation was predicted correctly. The material model was incapable of forecasting the sensitivity of the unload plateau to the high strain loading. This limitation of the model can be overcome by implementing Fortran subroutines that modify the transformation stresses during unloading as a function of the plastic strain reached during the simulation. In this case, the unload plateau was in close agreement with the experimental responses. Regarding the predicted

residual strains, the average absolute percentage difference of the FEA values compared to the experimental ones, was approximately 10.8%, based on the simulations of the present work.

Asymmetry between tension and compression was exhibited in the FEA results although not as pronounced as in the experimental data. The initial stiffness of austenite and the start of the transformation during loading in compression agreed well with the experimental results. However, the asymmetry is governed by essentially one value: the start of transformation during loading. The material model is configured to use the difference between the transformation stresses during loading in tension and compression to predict the rest of the stress parameters. The results of the present work showed that this approach is not accurate.

In the computational bending responses, the flexural stiffness of austenite was underestimated by up to 28.8%, although the transformation during loading started at the same force levels for FEA and experimental results. However, the unload transformation forces were underpredicted by up to 44.4%. It is advised to use the flexural modulus of austenite as input parameter in bending simulations. The loading path in such cases was significantly improved since the flexural stiffness was underpredicted by only 4.2% compared to the experimental value.

The computational response in torsion did not agree well with the experimental results. The torsional stiffness of austenite was underpredicted by 11.2% while the transformation during loading was underpredicted by approximately 10%. However, the rest of the estimated parameters exhibited greater differences such as the start of the transformation during unloading which was smaller by 40% compared to the experimental result. Although the computational response in torsion was not in agreement with the experimental results, the model was able to capture the qualitative features of the combined tension-torsion deformation.

The above findings show that while the constitutive model was able to provide a good prediction of the uniaxial tensile response of the material, it was not able to closely predict the response of the material under other loading modes. In terms of design purposes, the impact of the above findings depends on whether

these loading modes are applicable to the device of interest. For example, the torsional loads of a ring-stent are not significant in magnitude. Although there is a large number of material models proposed in the literature, these are not used by commercial finite element solvers. Since computational analyses are used to support medical device submissions, regulatory agencies require evidence of verification activities performed to establish the correctness and fidelity of the numerical algorithm. This procedure is usually effortless when a commercial solver and its built-in material database is used, as software developers comply with quality standards and they test their solvers by running benchmark problems. However, verification of a user-developed material model is time consuming and requires additional resources, which is why solvers such as Abaqus and Ansys are widely used by the medical device industry. Therefore, the present work also indicates the need for implementing a more accurate material model into commercial software or improving the current built-in model.

Detailed recommendations for future work were provided within chapter 7. The key suggestions are summarized below. The implementation of conventional DIC methods to measure strain during compression is difficult with the current experimental configuration. However, the feasibility of combining DIC software with SEM images could be explored. A universal environmental chamber could also be employed for testing at 37°C. The torsional capabilities of other testing machines and load cells that can accommodate the testing of smaller diameter wires, should be explored. A future investigation of the compaction process should include: loading of the material to the post-transformation region at room temperature, increasing the temperature to 55°C to simulate sterilization, and unloading at the in-vivo temperature of 37°C. Cyclic testing should be expanded to include small amplitude straining after unloading from the post-transformation region. Regarding the computational analyses, future subroutines should represent the material for a wider range of strain levels. Further work is also required to explore the use of the volumetric transformation strain and its effect on the predicted tension-compression asymmetry. In addition, a detailed comparison between different material models

should be performed by implementing them in Abaqus using user-defined subroutines.

In summary, the extended objectives of section 3.4 have been accomplished. Medical grade Nitinol wires were tested in tension, compression, bending and torsion and the mechanical behaviour of the material was examined under high-strain deformation. The FEA input parameters were identified from the above tests and the Nitinol model implemented in Abaqus was assessed. Useful findings relating to the design of stent-graft devices were also presented, especially regarding the compaction process and the modelling capabilities of Abaqus. Although the present work revolved mainly around AAA stent-grafts, its findings apply to other medical devices such as thoracic grafts, arterial endo-conduits and coronary-, carotid- and peripheral stents.

References

1. Aulivola B and Malinowski M. Abdominal Aortic Aneurysm. in Common Surgical Diseases: An Algorithmic Approach to Problem Solving. Springer New York. 2015. p. 77-81.
2. Forsdahl SH, Singh K, Solberg S, and Jacobsen BK. Risk factors for abdominal aortic aneurysms, a 7-year prospective study: The Tromso study, 1994–2001. Circulation. 2009. 119(16): p. 2202-2208.
3. Rodin MB, Daviglus ML, Wong GC, Liu K, Garside DB, Greenland P, et al. Middle Age Cardiovascular Risk Factors and Abdominal Aortic Aneurysm in Older Age. Hypertension. 2003. 42(1): p. 61-68.
4. Tarafdar SA and Gannon MX. Abdominal aortic aneurysm. InnovAiT. 2017. 10(5): p. 290-296.
5. Kent KC. Abdominal Aortic Aneurysms. New England Journal of Medicine. 2014. 371(22): p. 2101-2108.
6. Forsyth JM. Abdominal aortic aneurysm. InnovAiT. 2016. 9(5): p. 298-302.
7. Parodi JC, Palmaz JC, and Barone HD. Transfemoral intraluminal graft implantation for abdominal aortic aneurysms. Annals of Vascular Surgery. 1991. 5(6): p. 491-499.
8. Volodos NL, Karpovich IP, Troyan VI, Kalashnikova Yu V, Shekhanin VE, Ternyuk NE, et al. Clinical experience of the use of self-fixing synthetic prostheses for remote endoprosthetics of the thoracic and the abdominal aorta and iliac arteries through the femoral artery and as intraoperative endoprosthesis for aorta reconstruction. Vasa Supplementum. 1991. 33: p. 93-95.
9. Anaconda AAA Stent Graft System, Instructions for Use. Vascutek Limited, A Terumo Company.
10. Sicard GA, Zwolak RM, Sidawy AN, White RA, and Siami FS. Endovascular abdominal aortic aneurysm repair: Long-term outcome measures in patients at high-risk for open surgery. Journal of Vascular Surgery. 2006. 44(2): p. 229-236.
11. Dangas G, O'Connor D, Firwana B, Brar S, Ellozy S, Vouyouka A, et al. Open Versus Endovascular Stent Graft Repair of Abdominal Aortic Aneurysms: A Meta-Analysis of Randomized Trials. Journal of the American College of Cardiology: Cardiovascular Interventions. 2012. 5(10): p. 1071-1080.
12. Lederle FA, Freischlag JA, Kyriakides TC, Matsumura JS, Padberg FTJ, Kohler TR, et al. Long-Term Comparison of Endovascular and Open Repair of Abdominal Aortic Aneurysm. New England Journal of Medicine. 2012. 367(21): p. 1988-1997.
13. Schermerhorn ML, O'Malley AJ, Jhaveri A, Cotterill P, Pomposelli F, and Landon BE. Endovascular vs. Open Repair of Abdominal Aortic Aneurysms in the Medicare Population. New England Journal of Medicine. 2008. 358(5): p. 464-474.
14. Kauffman GB and Mayo I. The Story of Nitinol: The Serendipitous Discovery of the Memory Metal and Its Applications. The Chemical Educator. 1997. 2(2): p. 1-21.
15. Buehler WJ, Gilfrich JV, and Wiley RC. Effect of Low-Temperature Phase Changes on the Mechanical Properties of Alloys near Composition TiNi. Journal of Applied Physics. 1963. 34(5): p. 1475-1477.
16. Morgan NB. Medical shape memory alloy applications—the market and its products. Materials Science and Engineering: A. 2004. 378(1–2): p. 16-23.

17. MohdJani J, Leary M, Subic A, and Gibson MA. A review of shape memory alloy research, applications and opportunities. Materials & Design. 2014. 56: p. 1078-1113.
18. Thompson SA. An overview of nickel–titanium alloys used in dentistry. International Endodontic Journal. 2000. 33(4): p. 297-310.
19. Duerig T, Pelton A, and Stöckel D. An overview of nitinol medical applications. Materials Science and Engineering: A. 1999. 273: p. 149-160.
20. Duerig T, Tolomeo D, and Wholey M. An overview of superelastic stent design. Minimally invasive therapy & allied technologies. 2000. 9(3-4): p. 235-246.
21. Poncet PP. Nitinol medical device design considerations. Strain. 2000. 2(4): p. 6.
22. Santos IC, Rodrigues A, Figueiredo L, Rocha LA, and Tavares JMR. Mechanical properties of stent–graft materials. Proceedings of the Institution of Mechanical Engineers, Part L: Journal of Materials Design and Applications. 2012.
23. Anaconda™ AAA Stent Graft System. Available from: https://www.vascutek.com/products/anaconda-aaa-stent-graft-system/.
24. GORE® EXCLUDER® AAA Endoprosthesis. Available from: https://www.goremedical.com/products/excluder.
25. Tadros RO, Faries PL, Ellozy SH, Lookstein RA, Vouyouka AG, Schrier R, et al. The impact of stent graft evolution on the results of endovascular abdominal aortic aneurysm repair. Journal of Vascular Surgery. 2014. 59(6): p. 1518-1527.
26. Desai M, Eaton-Evans J, Hillery C, Bakhshi R, You Z, Lu J, et al. AAA stent-grafts: past problems and future prospects. Annals of Biomedical Engineering. 2010. 38(4): p. 1259-75.
27. Bosman WMPF, Steenhoven TJvd, Suárez DR, Hinnen JW, Valstar ER, and Hamming JF. The Proximal Fixation Strength of Modern EVAR Grafts in a Short Aneurysm Neck: An In Vitro Study. European Journal of Vascular and Endovascular Surgery. 2010. 39(2): p. 187-192.
28. Jackson CM, Wagner HJ, and Wasilewski RJ. 55-nitinol-the alloy with a memory-its physical metallurgy, properties and applications. NASA. 1972.
29. Duerig T, Melton K, Stöckel D, and Wayman CM. Engineering aspects of shape memory alloys. Butterworth-Heinemann. 1990.
30. Van Humbeeck J, Chandrasekaran M, and Delaey L. Shape memory alloys: materials in action. Endeavour. 1991. 15(4): p. 148-154.
31. Otsuka K and Wayman CM. Shape memory materials. Cambridge University Press. 1999.
32. Otsuka K and Ren X. Physical metallurgy of Ti–Ni-based shape memory alloys. Progress in Materials Science. 2005. 50(5): p. 511-678.
33. Lagoudas DC. Shape Memory Alloys: Modeling and Engineering Applications. Springer US. 2008.
34. Shaw JA, Churchill CB, and Iadicola MA. Tips and tricks for characterizing shape memory alloy wire: Part 1-Differential scanning calorimetry and basic phenomena. Experimental Techniques. 2008. 32(5): p. 55-62.
35. Pelton A, Russell SM, and DiCello J. The physical metallurgy of nitinol for medical applications. The Journal of The Minerals, Metals & Materials Society. 2003. 55(5): p. 33.
36. Plaskonka-Weisenburger K, Pelton SM, Jörn T, Hoffmann R, Keck A, Ulmer J, et al. Consideration of the Significance of Cold Work for Fatigue Behavior of Nitinol Medical Implants. in: Proceedings of the International Conference on Shape Memory and Superelastic Technologies. Konstanz, Germany, May 13-17. 2019.

37. Pelton A, Dicello J, and Miyazaki S. Optimisation of processing and properties of medical grade Nitinol wire. in: Proceedings of the International Conference on Shape Memory and Superelastic Technologies. 2000.
38. Morgan N, Painter J, and Moffat A. Mean strain effects and microstructural observations during in vitro fatigue testing of NiTi. in: SMST-2003. Proceedings of the International Conference on Shape Memory and Superelastic Technologies. Pacific Grove, CA: SMST Society. 2004.
39. ASTM F2063-18. Standard Specification for Wrought Nickel-Titanium Shape Memory Alloys for Medical Devices and Surgical Implants. ASTM International. West Conshohocken, PA. 2018. Available from: www.astm.org.
40. Forcucci SJ. Fatigue Coupon Evaluation of Ultra Fine Inclusion Nitinol Tubing. in: Proceedings of the International Conference on Shape Memory and Superelastic Technologies. Konstanz, Germany, May 13–17. 2019.
41. Xu Y, Cao H, Tripathy S, and Wu M. Impact of Inclusions on Fatigue of Medical-Grade Nitinol Tubing in: Proceedings of the International Conference on Shape Memory and Superelastic Technologies. Konstanz, Germany, May 13–17. 2019.
42. Nagaraja S, Stafford P, Braeuner C, Di Prima M, Sena G, Ravi V, et al. The Effects of Nitinol Purity and Surface Finish on Corrosion Susceptibility in: Proceedings of the International Conference on Shape Memory and Superelastic Technologies. Konstanz, Germany, May 13-17. 2019.
43. Frotscher M, Kiekbusch M, Davydova O, Kuhrke S, and Brennmehl C. Influence of Material Quality on the Performance of Peripheral NiTi Stents. in: Proceedings of the International Conference on Shape Memory and Superelastic Technologies. Konstanz, Germany, May 13-17. 2019.
44. Malito L, Bowers M, Briant P, Shamimi A, and Duerig T. Determination of the Critical Flaw Size for Crack Growth in Nitinol Material Used for Biomedical Applications through Focused Ion Beam Notch Fatigue. in: Proceedings of the International Conference on Shape Memory and Superelastic Technologies. Konstanz, Germany, May 13-17. 2019.
45. Adler PH, Frei R, Bowers M, Briant P, James B, and Liu C. Effects of Tube Processing on the Fatigue Life of Nitinol – Part II. in: Proceedings of the International Conference on Shape Memory and Superelastic Technologies. Konstanz, Germany, May 13-17. 2019.
46. Stehulak B. The Effect of Additions during Nitinol Melting to Improve Fatigue Performance. in: Proceedings of the International Conference on Shape Memory and Superelastic Technologies. Konstanz, Germany, May 13-17. 2019.
47. ISO 11135:2014. Sterilization of health-care products-Ethylene oxide-Requirements for the development, validation and routine control of a sterilization process for medical devices. International Organization for Standardization. Geneva, Switzerland. Available from: https://www.iso.org/obp/ui/#iso:std:iso:11135:ed-2:v1:en.
48. Stoeckel D, Pelton A, and Duerig T. Self-expanding nitinol stents: material and design considerations. European Radiology. 2004. 14(2): p. 292-301.
49. Ng KL and Sun QP. Stress-induced phase transformation and detwinning in NiTi polycrystalline shape memory alloy tubes. Mechanics of Materials. 2006. 38(1–2): p. 41-56.
50. Tobushi H, Shimeno Y, Hachisuka T, and Tanaka K. Influence of strain rate on superelastic properties of TiNi shape memory alloy. Mechanics of Materials. 1998. 30(2): p. 141-150.

51. Dayananda GN and Rao MS. Effect of strain rate on properties of superelastic NiTi thin wires. Materials Science and Engineering: A. 2008. 486(1–2): p. 96-103.
52. Zhang X, Feng P, He YJ, Yu T, and Sun QP. Experimental study on rate dependence of macroscopic domain and stress hysteresis in NiTi shape memory alloy strips. International Journal of Mechanical Sciences. 2010. 52(12): p. 1660-1670.
53. Shaw JA and Kyriakides S. On the nucleation and propagation of phase transformation fronts in a NiTi alloy. Acta Materialia. 1997. 45(2): p. 683-700.
54. Shaw JA and Kyriakides S. Thermomechanical aspects of NiTi. Journal of the Mechanics and Physics of Solids. 1995. 43(8): p. 1243-1281.
55. He YJ, Yin H, Zhou R, and Sun QP. Ambient effect on damping peak of NiTi shape memory alloy. Materials Letters. 2010. 64(13): p. 1483-1486.
56. Brinson LC, Schmidt I, and Lammering R. Stress-induced transformation behavior of a polycrystalline NiTi shape memory alloy: micro and macromechanical investigations via in situ optical microscopy. Journal of the Mechanics and Physics of Solids. 2004. 52(7): p. 1549-1571.
57. DesRoches R, McCormick J, and Delemont M. Cyclic properties of superelastic shape memory alloy wires and bars. Journal of Structural Engineering. 2004. 130(1): p. 38-46.
58. Iadicola MA and Shaw JA. The Effect of Uniaxial Cyclic Deformation on the Evolution of Phase Transformation Fronts in Pseudoelastic NiTi Wire. Journal of Intelligent Material Systems and Structures. 2002. 13(2-3): p. 143-155.
59. Schlun M, Zipse A, Dreher G, and Rebelo N. Effects of Cyclic Loading on the Uniaxial Behavior of Nitinol. Journal of Materials Engineering and Performance. 2011. 20(4): p. 684-687.
60. Orgéas L and Favier D. Stress-induced martensitic transformation of a NiTi alloy in isothermal shear, tension and compression. Acta Materialia. 1998. 46(15): p. 5579-5591.
61. Reedlunn B, Churchill CB, Nelson EE, Shaw JA, and Daly SH. Tension, compression, and bending of superelastic shape memory alloy tubes. Journal of the Mechanics and Physics of Solids. 2014. 63: p. 506-537.
62. Henderson E, Nash DH, and Dempster WM. On the experimental testing of fine Nitinol wires for medical devices. Journal of the Mechanical Behavior of Biomedical Materials. 2011. 4(3): p. 261-268.
63. Kim K and Daly S. Martensite Strain Memory in the Shape Memory Alloy Nickel-Titanium Under Mechanical Cycling. Experimental Mechanics. 2011. 51(4): p. 641-652.
64. Siddons DJ and Moon JR. Tensile and compression performance of superelastic NiTi tubing. Materials Science and Technology. 2001. 17(9): p. 1073-1078.
65. Xie Z, Liu Y, and Van Humbeeck J. Microstructure of NiTi shape memory alloy due to tension–compression cyclic deformation. Acta Materialia. 1998. 46(6): p. 1989-2000.
66. Liu Y, Xie Z, Van Humbeeck J, and Delaey L. Asymmetry of stress–strain curves under tension and compression for NiTi shape memory alloys. Acta Materialia. 1998. 46(12): p. 4325-4338.
67. ISO 15841:2014. Dentistry-Wires for use in orthodontics. International Organization for Standardization. Geneva, Switzerland. Available from: https://www.iso.org/standard/62223.html
68. Pelton A, Rebelo N, Duerig T, and Wick A. Experimental and FEM analysis of the bending behaviour of superelastic tubing. in: Proceedings of the International Conference on Shape Memory and Superelastic Technologies. 1994.

69. Iijima M, Ohno H, Kawashima I, Endo K, Brantley WA, and Mizoguchi I. Micro X-ray diffraction study of superelastic nickel-titanium orthodontic wires at different temperatures and stresses. Biomaterials. 2002. 23(8): p. 1769-74.
70. Tonner RI and Waters NE. The characteristics of super-elastic Ni-Ti wires in three-point bending. Part I: The effect of temperature. European Journal of Orthodontics. 1994. 16(5): p. 409-19.
71. Sun QP and Li ZQ. Phase transformation in superelastic NiTi polycrystalline micro-tubes under tension and torsion-from localization to homogeneous deformation. International Journal of Solids and Structures. 2002. 39(13–14): p. 3797-3809.
72. Adler PH, Yu W, Pelton A, Zadno R, Duerig T, and Barresi R. On the tensile and torsional properties of pseudoelastic NiTi. Scripta Metallurgica et Materialia. 1990. 24(5): p. 943-947.
73. Doaré O, Sbarra A, Touzé C, Ould Moussa M, and Moumni Z. Experimental analysis of the quasi-static and dynamic torsional behaviour of shape memory alloys. International Journal of Solids and Structures. 2012. 49(1): p. 32-42.
74. Dolce M and Cardone D. Mechanical behaviour of shape memory alloys for seismic applications 1. Martensite and austenite NiTi bars subjected to torsion. International Journal of Mechanical Sciences. 2001. 43(11): p. 2631-2656.
75. Predki W, Klönne M, and Knopik A. Cyclic torsional loading of pseudoelastic NiTi shape memory alloys: Damping and fatigue failure. Materials Science and Engineering: A. 2006. 417(1–2): p. 182-189.
76. McNaney JM, Imbeni V, Jung Y, Papadopoulos P, and Ritchie RO. An experimental study of the superelastic effect in a shape-memory Nitinol alloy under biaxial loading. Mechanics of Materials. 2003. 35(10): p. 969-986.
77. Andani MT, Alipour A, and Elahinia M. Coupled rate-dependent superelastic behavior of shape memory alloy bars induced by combined axial-torsional loading: a semi-analytic modeling. Journal of Intelligent Material Systems and Structures. 2013. 24(16): p. 1995-2007.
78. Andani MT and Elahinia M. A rate dependent tension–torsion constitutive model for superelastic nitinol under non-proportional loading; a departure from von Mises equivalency. Smart Materials and Structures. 2014. 23(1): p. 015012.
79. Mehrabi R, Andani MT, Kadkhodaei M, and Elahinia M. Experimental Study of NiTi Thin-Walled Tubes Under Uniaxial Tension, Torsion, Proportional and Non-Proportional Loadings. Experimental Mechanics. 2015. 55(6): p. 1151-1164.
80. Grabe C and Bruhns OT. Tension/torsion tests of pseudoelastic, polycrystalline NiTi shape memory alloys under temperature control. Materials Science and Engineering: A. 2008. 481–482: p. 109-113.
81. Mehrabi R, Kadkhodaei M, and Elahinia M. Constitutive modeling of tension-torsion coupling and tension-compression asymmetry in NiTi shape memory alloys. Smart Materials and Structures. 2014. 23(7): p. 075021.
82. Machado LG and Lagoudas DC. Thermomechanical Constitutive Modeling of SMAs. in Shape Memory Alloys: Modeling and Engineering Applications. Springer US. 2008. p. 121-187.
83. Tanaka K and Nagaki S. A thermomechanical description of materials with internal variables in the process of phase transitions. Ingenieur-Archiv. 1982. 51(5): p. 287-299.
84. Tanaka K. Thermomechanical sketch of shape memory effect: one-dimensional tensile behavior. Res Mechanica: International Journal of Structural Mechanics and Materials Science. 1986. 18(3): p. 251-263.

85. Liang C and Rogers CA. One-Dimensional Thermomechanical Constitutive Relations for Shape Memory Materials. Journal of Intelligent Material Systems and Structures. 1990. 1(2): p. 207-234.
86. Brinson LC. One-Dimensional Constitutive Behavior of Shape Memory Alloys: Thermomechanical Derivation with Non-Constant Material Functions and Redefined Martensite Internal Variable. Journal of Intelligent Material Systems and Structures. 1993. 4(2): p. 229-242.
87. Boyd JG and Lagoudas DC. Thermomechanical Response of Shape Memory Composites. Journal of Intelligent Material Systems and Structures. 1994. 5(3): p. 333-346.
88. Prahlad H and Chopra I. Comparative Evaluation of Shape Memory Alloy Constitutive Models with Experimental Data. Journal of Intelligent Material Systems and Structures. 2001. 12(6): p. 383-395.
89. Brinson LC and Huang MS. Simplifications and Comparisons of Shape Memory Alloy Constitutive Models. Journal of Intelligent Material Systems and Structures. 1996. 7(1): p. 108-114.
90. Huo Y. A mathematical model for the hysteresis in shape memory alloys. Continuum Mechanics and Thermodynamics. 1989. 1(4): p. 283-303.
91. Ortín J. Preisach modeling of hysteresis for a pseudoelastic Cu-Zn-Al single crystal. Journal of Applied Physics. 1992. 71(3): p. 1454-1461.
92. Ivshin Y and Pence TJ. A constitutive model for hysteretic phase transition behavior. International Journal of Engineering Science. 1994. 32(4): p. 681-704.
93. Macki JW, Nistri P, and Zecca P. Mathematical Models for Hysteresis. Society for Industrial and Applied Mathematics. 1993. 35(1): p. 94-123.
94. Brocca M, Brinson LC, and Bazant ZP. Three-dimensional constitutive model for shape memory alloys based on microplane model. Journal of the Mechanics and Physics of Solids. 2002. 50(5): p. 1051-1077.
95. Kadkhodaei M, Salimi MH, Rajapakse RK, and Mahzoon M. Modeling of Shape Memory Alloys Based on Microplane Theory. Journal of Intelligent Material Systems and Structures. 2007.
96. Bazant ZP. Microplane Model for Strain Controlled Inelastic Behavior. in Mechanics of Engineering Materials. John Wiley & Sons. 1984. p. 45-59.
97. Patoor E, Eberhardt A, and Berveiller M. Thermomechanical behaviour of shape memory alloys. Archives of Mechanics 1988. 40(5): p. 775-794.
98. Fischer FD and Tanaka K. A micromechanical model for the kinetics of martensitic transformation. International Journal of Solids and Structures. 1992. 29(14–15): p. 1723-1728.
99. Sun QP and Hwang KC. Micromechanics modelling for the constitutive behavior of polycrystalline shape memory alloys—I. Derivation of general relations. Journal of the Mechanics and Physics of Solids. 1993. 41(1): p. 1-17.
100. Sun QP and Hwang KC. Micromechanics modelling for the constitutive behavior of polycrystalline shape memory alloys—II. Study of the individual phenomena. Journal of the Mechanics and Physics of Solids. 1993. 41(1): p. 19-33.
101. Lexcellent C, Goo BC, Sun QP, and Bernardini J. Characterization, thermomechanical behaviour and micromechanical-based constitutive model of shape-memory CuZnAl single crystals. Acta Materialia. 1996. 44(9): p. 3773-3780.
102. Huang M and Brinson LC. A Multivariant model for single crystal shape memory alloy behavior. Journal of the Mechanics and Physics of Solids. 1998. 46(8): p. 1379-1409.

103. Reporting of Computational Modeling Studies in Medical Device Submissions. Guidance for Industry and Food and Drug Administration Staff. 2016. Available from: https://www.fda.gov/regulatory-information.
104. Simulia DS Support Knowledge Base. Question & Answer: UMAT and VUMAT routines for the elastic-plastic simulation of Nitinol. 2019. Available from: https://onesearch.3ds.com/mashup-ui/page/resultqa?id=QA00000009225e.
105. Simulia DS Support Knowledge Base. User Assistance R2019x - Superelasticity. 2019. Available from: https://help.3ds.com/2019x/English/DsDoc/SIMA3DXMATRefMap/simamat-c-superelasticity.htm?contextscope=all&search=nitinol&highlight=nitinol.
106. Abaqus 6.14 Online Documentation. Dassault Systemes of America Corp. Woodlands Hills, CA. 2014.
107. Auricchio F and Taylor RL. Shape-memory alloys: modelling and numerical simulations of the finite-strain superelastic behavior. Computer Methods in Applied Mechanics and Engineering. 1997. 143(1–2): p. 175-194.
108. Barbarino S. SMAs in Commercial Codes. in Shape Memory Alloy Engineering. Butterworth-Heinemann. 2015. p. 193-212.
109. UMAT for Superelasticity and Plasticity of Shape Memory Alloys. Dassault Systemes of America Corp. Woodlands Hills, CA.
110. Simulia DS Support Knowledge Base. User Assistance R2019x - Plasticity model for superelastic materials. 2019. Available from: https://help.3ds.com/2019x/English/DsDoc/SIMA3DXMATRefMap/simamat-c-plastsuperelastic.htm?contextscope=all&search=nitinol&highlight=nitinol.
111. Gong XY and Pelton A. ABAQUS Analysis on Nitinol Medical Applications. in: Proceedings of the ABAQUS Users' Conference. 2002.
112. Kleinstreuer C, Li Z, Basciano CA, Seelecke S, and Farber MA. Computational mechanics of Nitinol stent grafts. J Biomech. 2008. 41(11): p. 2370-8.
113. DeHerrera M and Dang N. Finite Element Analysis of a Percutaneous Stent-Mounted Heart Valve. in: Proceedings of the ABAQUS Users' Conference. 2004.
114. Auricchio F, Conti M, De Beule M, De Santis G, and Verhegghe B. Carotid artery stenting simulation: From patient-specific images to finite element analysis. Medical Engineering & Physics. 2011. 33(3): p. 281-289.
115. Demanget N, Avril S, Badel P, Orgéas L, Geindreau C, Albertini J-N, et al. Computational comparison of the bending behavior of aortic stent-grafts. Journal of the Mechanical Behavior of Biomedical Materials. 2012. 5(1): p. 272-282.
116. Zhao S, Gu L, and Froemming SR. Finite element analysis of the implantation of a self-expanding stent: impact of lesion calcification. Journal of Medical Devices. 2012. 6(2).
117. Gong XY, Pelton A, Duerig T, Rebelo N, and Perry K. Finite element analysis and experimental evaluation of superelastic Nitinol stent. in: Proceedings of the International Conference on Shape Memory and Superelastic Technologies. 2004.
118. Qidwai MA and Lagoudas DC. Numerical implementation of a shape memory alloy thermomechanical constitutive model using return mapping algorithms. International Journal for Numerical Methods in Engineering. 2000. 47(6): p. 1123-1168.
119. Zhu P, Brinson LC, Peraza-Hernandez E, Hartl D, and Stebner A. Comparison of Three-Dimensional Shape Memory Alloy Constitutive Models: Finite Element Analysis of Actuation and Superelastic Responses of a Shape Memory Alloy Tube. in: Proceedings of the ASME Conference on Smart Materials, Adaptive Structures and Intelligent Systems. 2013.

120. Stebner AP and Brinson LC. Explicit finite element implementation of an improved three dimensional constitutive model for shape memory alloys. Computer Methods in Applied Mechanics and Engineering. 2013. 257: p. 17-35.
121. Lagoudas D, Hartl D, Chemisky Y, Machado L, and Popov P. Constitutive model for the numerical analysis of phase transformation in polycrystalline shape memory alloys. International Journal of Plasticity. 2012. 32–33: p. 155-183.
122. Scalet G, Auricchio F, and Hartl DJ. Efficiency and effectiveness of implicit and explicit approaches for the analysis of shape-memory alloy bodies. Journal of Intelligent Material Systems and Structures. 2015.
123. ISO 25539-1:2017 Cardiovascular implants — Endovascular devices — Part 1: Endovascular prostheses. International Organization for Standardization. Geneva, Switzerland. Available from: https://www.iso.org/standard/66925.html
124. Nitinol #1. Fort Wayne Metals. Available from: https://www.fwmetals.com/services/resource-library/nitinol-1/.
125. USN®. Fort Wayne Metals. Available from: https://www.fwmetals.com/materials/nitinol/usn-nitinol/.
126. ASTM F2082 / F2082M-16. Standard Test Method for Determination of Transformation Temperature of Nickel-Titanium Shape Memory Alloys by Bend and Free Recovery. ASTM International. West Conshohocken, PA. 2016. Available from: www.astm.org.
127. Technical Considerations for Non-Clinical Assessment of Medical Devices Containing Nitinol. Draft Guidance for Industry and Food and Drug Administration Staff. 2019. Available from: https://www.fda.gov/regulatory-information.
128. ASTM F2516-14. Standard Test Method for Tension Testing of Nickel-Titanium Superelastic Materials. ASTM International. West Conshohocken, PA. 2014. Available from: www.astm.org.
129. Instron 3119-600 Series Environmental Chambers Brochure V4. Available from: www.instron.com.
130. Tensile Testing of Nitinol Wire in Strain Control Using the AVE. Instron Application Report. 2005. Available from: www.instron.com.
131. Instron Video Extensometer AVE and SVE. Reference Manual, M26-14185-EN, Revision E. Available from: www.instron.com.
132. Instron WaveMatrix. Software Reference Manual, M22-16102-EN, Revision C. Available from: www.instron.com.
133. Taylor J. Introduction to error analysis, the study of uncertainties in physical measurements. University Science Books. 1997.
134. ASTM E4-16. Standard Practices for Force Verification of Testing Machines. ASTM International. West Conshohocken, PA. 2016. Available from: www.astm.org.
135. ASTM E2309 / E2309M-16. Standard Practices for Verification of Displacement Measuring Systems and Devices Used in Material Testing Machines. ASTM International. West Conshohocken, PA. 2016. Available from: www.astm.org.
136. ASTM E83-16. Standard Practice for Verification and Classification of Extensometer Systems. ASTM International. West Conshohocken, PA. 2016. Available from: www.astm.org.
137. Instron 5960 Dual Column Series for Mechanical Testing. Available from: www.instron.com.
138. Instron AVE 2 Non-Contacting Video Extensometer. Available from: www.instron.com.

139. 2kN & 5kN Tensile compression and horizontal bending stage. Available from: www.deben.co.uk.
140. ElectroForce® 3200 Series II Test Instrument. in: Testing Solutions from Bose. Available from: www.bose-electroforce.com.
141. Instron ElectroPuls™ E10000 Linear-Torsion All-Electric Dynamic Test Instrument. Available from: www.instron.com.
142. Bell S. Measurement Good Practice Guide No. 11: The Beginner's Guide to Uncertainty of Measurement. National Physical Laboratory UK.
143. ISO 9001:2015 Quality management systems — Requirements. International Organization for Standardization. Geneva, Switzerland. Available from: https://www.iso.org/standard/62085.html
144. Simulia Abaqus 6.14 Analysis User's Guide Volume II: Analysis. Dassault Systemes of America Corp. Woodlands Hills, CA.
145. Favier D, Liu Y, Orgéas L, Sandel A, Debove L, and Comte-Gaz P. Influence of thermomechanical processing on the superelastic properties of a Ni-rich Nitinol shape memory alloy. Materials Science and Engineering: A. 2006. 429(1–2): p. 130-136.
146. Bartzela TN, Senn C, and Wichelhaus A. Load-deflection characteristics of superelastic nickel-titanium wires. The Angle Orthodontist. 2007. 77(6): p. 991-8.
147. Berger J and Waram T. Force levels of nickel titanium initial archwires. Journal of Clinical Orthodontics. 2007. 41(5): p. 286-92.
148. Gurgel Jde A, Kerr S, Powers JM, and Pinzan A. Torsional properties of commercial nickel-titanium wires during activation and deactivation. American Journal of Orthodontics and Dentofacial Orthopedics. 2001. 120(1): p. 76-9.
149. ASTM F2516-18. Standard Test Method for Tension Testing of Nickel-Titanium Superelastic Materials. ASTM International. West Conshohocken, PA. 2018. Available from: www.astm.org.
150. Kammers AD and Daly S. Digital Image Correlation under Scanning Electron Microscopy: Methodology and Validation. Experimental Mechanics. 2013. 53(9): p. 1743-1761.
151. Lindfeldt E, Ekh M, Cvetskovski K, and Schilke M. Using DIC to Identify Microscale Strain Fields from In-situ SEM Images of a Pearlitic Steel. Experimental Mechanics. 2014. 54(9): p. 1503-1513.
152. Tan G, Liu Y, Sittner P, and Saunders M. Lüders-like deformation associated with stress-induced martensitic transformation in NiTi. Scripta Materialia. 2004. 50(2): p. 193-198.
153. Wu M, Gong XY, Mao S, and Han X. Crystallographic study of superelastic deformation of Nitinol. in Fatigue and Fracture of Medical Metallic Materials and Devices: 2nd Volume. ASTM International. 2010. p.
154. Kasuya S, Nagasaka S, Hanyuda A, Ishimura S, and Hirashita A. The effect of ligation on the load deflection characteristics of nickel titanium orthodontic wire. European Journal of Orthodontics. 2007. 29(6): p. 578-82.
155. Gall K, Sehitoglu H, Chumlyakov YI, and Kireeva IV. Tension–compression asymmetry of the stress–strain response in aged single crystal and polycrystalline NiTi. Acta Materialia. 1999. 47(4): p. 1203-1217.
156. Sehitoglu H, Karaman I, Anderson R, Zhang X, Gall K, Maier HJ, et al. Compressive response of NiTi single crystals. Acta Materialia. 2000. 48(13): p. 3311-3326.

157. Wang YF, Yue ZF, and Wang J. The effect of grain orientation on the tensile-compressive asymmetry of polycrystalline NiTi shape memory alloy. Materialwissenschaft und Werkstofftechnik. 2007. 38(4): p. 294-298.
158. Gall K and Sehitoglu H. The role of texture in tension–compression asymmetry in polycrystalline NiTi. International Journal of Plasticity. 1999. 15(1): p. 69-92.
159. Bucsek AN, Paranjape HM, and Stebner AP. Myths and Truths of Nitinol Mechanics: Elasticity and Tension–Compression Asymmetry. Shape Memory and Superelasticity. 2016. 2(3): p. 264-271.
160. He YJ and Sun QP. Macroscopic equilibrium domain structure and geometric compatibility in elastic phase transition of thin plates. International Journal of Mechanical Sciences. 2010. 52(2): p. 198-211.
161. Duerig T. Some unsolved aspects of Nitinol. Materials Science and Engineering: A. 2006. 438-440: p. 69-74.
162. Blanter MS, Golovin IS, Neuhäuser H, and Sinning HR. Internal Friction in Metallic Materials: a Handbook Vol. 90. Berlin, Heidelberg. Springer-Verlag. 2007.
163. Yoshida I, Ono T, and Asai M. Internal friction of Ti–Ni alloys. Journal of Alloys and Compounds. 2000. 310(1): p. 339-343.
164. Bow D. Terumo Aortic R&D Report 1448, Nitinol Ring Mechanics: Investigating the Radial Strength and Material Strain Levels within Nitinol Stent Rings by Finite Element simulation. Terumo Aortic. 2014.
165. Bow D. Terumo Aortic R&D Report 1530, Micro CT Compaction Strain Analysis of Anaconda ONE-LOK. Terumo Aortic. 2015.
166. Wick A, Gong XY, Fino J, Sheriff J, and Pelton A. Bending fatigue characteristics of Nitinol. in: Proceedings of the International Conference on Shape Memory and Superelastic Technologies. 2006.
167. Pelton A, Fino-Decker J, Vien L, Bonsignore C, Saffari P, Launey M, et al. Rotary-bending fatigue characteristics of medical-grade Nitinol wire. Journal of the Mechanical Behavior of Biomedical Materials. 2013. 27: p. 19-32.
168. Senthilnathan K, Shamimi A, Bonsignore C, Paranjape H, and Duerig T. Effect of Prestrain on the Fatigue Life of Superelastic Nitinol. Journal of Materials Engineering and Performance. 2019. 28(10): p. 5946–5958.
169. Murray D, Ghosh J, Khwaja N, Murphy MO, Baguneid MS, and Walker MG. Access for Endovascular Aneurysm Repair. Journal of Endovascular Therapy. 2006. 13(6): p. 754-761.
170. Cheng SWK, Ting ACW, Ho P, and Poon JTP. Aortic Aneurysm Morphology in Asians: Features Affecting Stent-Graft Application and Design. Journal of Endovascular Therapy. 2004. 11(6): p. 605-612.
171. Masuda EM, Caps MT, Singh N, Yorita K, Schneider PA, Sato DT, et al. Effect of ethnicity on access and device complications during endovascular aneurysm repair. Journal of Vascular Surgery. 2004. 40(1): p. 24-29.
172. Banzic I, Lu Q, Zhang L, Stepak H, Davidovic L, Oszkinis G, et al. Morphological Differences in the Aorto-iliac Segment in AAA Patients of Caucasian and Asian Origin. European Journal of Vascular and Endovascular Surgery. 2016. 51(6): p. 783-789.
173. Dolmatch BL. Healing response to vascular stentgrafts. Journal of Vascular Surgery. 2000. 31(6): p. 1285-1290.
174. Wang J, Jin X, Huang Y, Ran X, Luo D, Yang D, et al. Endovascular stent-induced alterations in host artery mechanical environments and their roles in stent restenosis and late thrombosis. Regenerative Biomaterials. 2018. 5(3): p. 177-187.

175. Ponder E. The coefficient of thermal conductivity of blood and of various tissues. The Journal of general physiology. 1962. 45(3): p. 545-551.
176. Eaton-Evans J, Dulieu-Barton JM, Little EG, and Brown IA. Observations during mechanical testing of Nitinol. Proceedings of the Institution of Mechanical Engineers, Part C: Journal of Mechanical Engineering Science. 2008. 222(2): p. 97-105.
177. De la Flor S, Urbina C, and Ferrando F. Effect of mechanical cycling on stabilizing the transformation behaviour of NiTi shape memory alloys. Journal of Alloys and Compounds. 2009. 469(1–2): p. 343-349.
178. Conti M, De Beule M, Mortier P, Van Loo D, Verdonck P, Vermassen F, et al. Nitinol Embolic Protection Filters: Design Investigation by Finite Element Analysis. Journal of Materials Engineering and Performance. 2009. 18(5): p. 787-792.
179. Rebelo N, Zipse A, Schlun M, and Dreher G. A Material Model for the Cyclic Behavior of Nitinol. Journal of Materials Engineering and Performance. 2011. 20(4): p. 605-612.
180. Bow D. Mechanical Analysis and Simulation of the Nitinol Ring-Stent: Assessing the Radial Strength, Fatigue Safety and Compaction Strains. PhD Thesis. 2018. University of Strathclyde.

Appendix - Fortran Subroutines

A.1 - Fortran subroutine for 22°C input parameters

```
c
c superelastic materials user subroutine
c
      subroutine USUPERELASPLASTMOD(cmname,
     1    noel,npt,layer,kspt,CAS,CSA,
     2    eqplast,temp,RefT,EmodARef,
     3    EnuARef,EmodSRef,EnuSRef,SsASRef,SfASRef,SsSARef,
     4    SfSARef,EmodA,EnuA,EmodS,EnuS,SsAS,SfAS,SsSA,SfSA)
c
      INCLUDE 'ABA_PARAM.INC'
      character*80 cmname
c
c           Parameters passed in the subroutine as information:
c cmname        Material name
c noel          Element number
c npt           Integration point number
c layer         Layer number
c kspt          Section point number
c eqplast       Equivalent plastic strain
c temp          Current temperature
c RefT          Reference temperature at which material properties are defined
c EmodARef      Austenite elasticity defined as input parameter
c EnuARef       Austenite Poisson's ratio defined as input parameter
c EmodSRef      Martensite elasticity defined as input parameter
c EnuSRef       Martensite Poisson's ratio defined as input parameter
c SsASRef       Start of transformation stress in loading as input parameter
c SfASRef       End of transformation stress in loading defined as input parameter
c SsSARef       Start of transformation stress in unloading defined as input parameter
c SfSARef       End of transformation stress in unloading defined as input parameter
c
c           Variables defined in the subroutine:
c EmodA         Austenite elasticity
c EnuA          Austenite Poisson's ratio
c EmodS         Martensite elasticity
c EnuS          Martensite Poisson's ratio
c SsAS          Start of transformation stress in loading
c SfAS          End of transformation stress in loading
c SsSA          Start of transformation stress in unloading
c SfSA          End of transformation stress in unloading
c eqp           Equivalent plastic strain
c
```

```
c The following statements produce no modifications to the material behaviour:
c
      EnuA  = EnuARef
      EnuS  = EnuSRef
      EmodA = EmodARef
      EmodS = EmodSRef
      SsAS  = SsASRef
      SfAS  = SfASRef
      eqp = eqplast
c
c The following 'if' statements modify the material parameters 'SsSA' and 'SfSA' as a function
c of the plastic strain:
      if(eqp.lt.0.002) then
        SsSA  = SsSARef - 110000. * eqp
        SfSA  = SfSARef - 64000. * eqp
      else
        SsSA  = SsSARef - 220. - 9091.  * (eqp -0.002)
        SfSA  = SfSARef - 128. - 47273.  * (eqp -0.002)
      end if
c
c
      return
      end
c
```

A.2 - Fortran subroutine for 37°C input parameters

```
c
c superelastic materials user subroutine
c
      subroutine USUPERELASPLASTMOD(cmname,
     1    noel,npt,layer,kspt,CAS,CSA,
     2    eqplast,temp,RefT,EmodARef,
     3    EnuARef,EmodSRef,EnuSRef,SsASRef,SfASRef,SsSARef,
     4    SfSARef,EmodA,EnuA,EmodS,EnuS,SsAS,SfAS,SsSA,SfSA)
c
      INCLUDE 'ABA_PARAM.INC'
      character*80 cmname
c
c          Parameters passed in the subroutine as information:
c cmname        Material name
c noel          Element number
c npt           Integration point number
c layer         Layer number
c kspt          Section point number
c eqplast       Equivalent plastic strain
```

```
c temp          Current temperature
c RefT          Reference temperature at which material properties are defined
c EmodARef      Austenite elasticity defined as input parameter
c EnuARef       Austenite Poisson's ratio defined as input parameter
c EmodSRef      Martensite elasticity defined as input parameter
c EnuSRef       Martensite Poisson's ratio defined as input parameter
c SsASRef       Start of transformation stress in loading as input parameter
c SfASRef       End of transformation stress in loading defined as input parameter
c SsSARef       Start of transformation stress in unloading defined as input parameter
c SfSARef       End of transformation stress in unloading defined as input parameter
c
c       Variables defined in the subroutine:
c EmodA         Austenite elasticity
c EnuA          Austenite Poisson's ratio
c EmodS         Martensite elasticity
c EnuS          Martensite Poisson's ratio
c SsAS          Start of transformation stress in loading
c SfAS          End of transformation stress in loading
c SsSA          Start of transformation stress in unloading
c SfSA          End of transformation stress in unloading
c eqp           Equivalent plastic strain
c
c The following statements produce no modifications to the material behaviour:
c
    EnuA  = EnuARef
    EnuS  = EnuSRef
    EmodA = EmodARef
    EmodS = EmodSRef
    SsAS  = SsASRef
    SfAS  = SfASRef
    eqp = eqplast
c
c The following 'if' statements modify the material parameters 'SsSA' and 'SfSA' as a function
c of the plastic strain:
    if(eqp.lt.0.003) then
      SsSA  = SsSARef - 102000. * eqp
      SfSA  = SfSARef - 64000. * eqp
    else
      SsSA  = SsSARef - 254. - 10294.  * (eqp -0.003)
      SfSA  = SfSARef - 156. - 11765.  * (eqp -0.003)
    end if
c
c
    return
    end
c
```